



The
University
Of
Sheffield.

A Combined Experimental and Finite Element Modelling Study of Electrical Heterogeneity in Electroceramics

Hong Ma

A thesis submitted in partial fulfilment of the requirements for the degree of

Doctor of Philosophy

Supervised by

Prof. Derek C. Sinclair

Dr. Julian S. Dean

The University of Sheffield

Faculty of Engineering

Department of Materials Science and Engineering

May 2022

Acknowledgement

Firstly, I would like to thank Prof. Derek C. Sinclair for his outstanding supervision during my PhD. I am deeply grateful for his support, encouragement, patience and the advice provided during my research project. I would like to thank Dr. Julian S. Dean for his encouragement and the considerable effort he invested in me during my PhD that led me to the world of materials simulation. Covid-19 changed too many things and it was my greatest fortune to have you both as my supervisors, not only for my research process but also in supporting me through my decisions, so that I could survive through these difficult times.

I would like to thank Dr. Zhilun Lu, Dr Linhao Li, Dr. Ge Wang and Dr Dawei Wang who helped me with the laboratory work and taught me various experimental skills. I would also like to thank everyone in the Functional Materials group and Cleanroom in the Diamond.

Finally, thank you to my Dad for the love and support in all aspects of my life. Thank you to my wife who encouraged and supported me with her care and love through the tough times in these four years.

Abstract

The initial aim of this thesis was to investigate the electrical properties of $\text{Na}_{1/2}\text{Bi}_{1/2}\text{TiO}_3$ (NBT)-based dielectric materials. After the onset of the Covid-19 pandemic, the experimental work came to an end after a discussion with the supervisors. The research focus shifted to a simulation-based finite element modelling (FEM) study on micro-contact impedance spectroscopy (mIS) and its application on ceramic systems with defects, namely surface layers and/or cracks (physical voids).

As the pre-pandemic part of this work, solid solutions of NBT with $\text{BiMg}_{0.5}\text{Ti}_{0.5}\text{O}_3$ (BMT) and $\text{BiZn}_{0.5}\text{Ti}_{0.5}\text{O}_3$ (BZT) were explored. The NBT-BMT samples were prepared by two processing methods, hand grinding and ball milling. The hand ground NBT-BMT samples show a dramatic decrease in bulk conductivity with increasing BMT content. Obvious secondary phases can be observed for Modest levels of BMT. The ball milled NBT-BMT samples show non-systematic behaviour with increasing BMT content. The dielectric properties were also irregular when compared to a solid solution of $\text{Na}_{1/2}\text{Bi}_{1/2}\text{TiO}_3$ - $\text{BiMg}_{2/3}\text{Nb}_{1/3}\text{O}_3$ (NBT-BMN). This suggests an important role is played by Nb in the solid solution as a stabiliser for better mixing of Mg.

For NBT-BZT there is little effect on the permittivity profiles and a gradual decrease in bulk (oxide-ion) conductivity until the system becomes electrically insulating at ~ 4 mol% BZT. NBT-BZT shows conductivity behaviour is similar to that reported in the literature for NBT- $\text{BiZn}_{2/3}\text{Nb}_{1/3}\text{O}_3$ (NBT-BZN) and explained as trapping of oxygen vacancies by the B-site dopant. It appears the absence of Nb in NBT-BZT did not affect the distribution of Zn but its incorporation is at a low level. Both NBT-BMT and NBT-BZT showed large grains embedded in a small grained matrix structure which could support the grain size effect reported in the literature. Due to the limited number of compositions prepared, only a preliminary comparison of the trapping power between Mg and Zn could be made.

For the finite element modelling part of this work, the research was conducted in three sections. Firstly, a homogenous cubic model with a crack on the top surface was created, the model is assigned with the electrical properties of SrTiO_3 . Two types of cracks were constructed, a meshed region assigned with very high resistivity as a crack (MC) and a physically void region as a crack (PVC). The geometries and properties of the crack were altered to investigate their effect on the simulated impedance data. The simulated impedance data show that increasing crack width and depth results in higher measured resistance from top-top micro-contact electrode measurements on a homogenous material. The maximum increase in the measured resistance is 59%, when micro-contacts are separated by two times of contact radius which is a strong current interference set up. The spreading resistance equation (SRE) can be used to extract bulk conductivity under certain situations. The crack effect (current confinement) can counterbalance the current interference from closely placed electrodes. The calculated results are within a $\pm 10\%$ error range of the input value. As the micro-contact separation increased, the crack's confinement effect diminishes more rapidly than the decrease in current interference. The crack's effect therefore becomes less effective

in cancelling the current interference effect. When plotting the calculated bulk conductivities of models on a logarithmic scale, the effect of a crack on the conductivity value is very limited thus should not be a major concern for experimentalists.

The modelling was then advanced to a two-layer ceramic system. A resistive surface layer of thickness from 0.125 to 30 μm was then created onto a bulk substrate. A novel method called the two-layer spreading resistance equation was developed to extract surface layer electrical properties in a two-layer ceramic system. This method offers higher accuracy in correcting the results obtained, when compared to using a conventional geometry factor correction or the well-known spreading resistance equation (SRE) for microcontacts. It also has a wider applicable range in terms of surface layer thickness and surface layer to bulk material resistivity ratio, which is an improvement to the various equations presented in the literature.

The final stage of simulation is to create a crack structure in the surface layer of a two-layer model. The simulated impedance data revealed the confinement/hindrance effect of crack geometry is reduced, as current density is reduced within the resistive surface layer. The SRE was proven not to be applicable to extract surface layer properties. The two-layer spreading resistance equation, however, can extract surface layer electrical properties with less than 10% deviation from the intrinsic value of the model. The crack's length is altered to investigate its effect on the simulated impedance data. This shows that when the crack length extends more than 8 times of the micro-contact radius, the increase in the measured resistance is minimal. Next, a non-through surface layer crack is created, leaving a tunnel underneath the crack for current to flow through. The simulated results show the crack's hindrance/confinement effect is reduced.

Finally, models were created to resolve an experimental problem posed by a former PhD student (Dr Richard Veazey) on radiation damaged and subsequently annealed SrTiO_3 single crystals. The radiation damaged SrTiO_3 samples contained an amorphous surface layer and when annealed, recrystallisation and micro-cracks developed on the surface layer. Micro-contact impedance measurements revealed significantly different impedance data from areas with low and high density of surface visible cracks. The FEM simulations show the crack effect alone could not fully reproduce the impedance data from the experiment. A new hypothesis that the surface layer thickness may alter across local regions and between different micro-contact measurements is proposed. Simulations based on varying surface layer thickness in addition with the presence of a crack are used to successfully reproduce the impedance data gathered from the Veazey experiments. To fully expand the capability of our models, a selection of case studies on published micro-contact impedance experiments were conducted. Preliminary simulations show promising results in replicating the experimental impedance data.

Table of Contents

Chapter 1 : Introduction.....	7
Chapter 2 : Literature Review	10
2.1 Impedance Spectroscopy	10
2.2 Micro contact-IS (mclS) and finite element modelling (FEM)	14
2.3 Perovskites	23
2.3.1 Ferroelectrics.....	24
2.3.2 Oxygen ion conductors.....	27
2.4 $\text{Na}_{0.5}\text{Bi}_{0.5}\text{TiO}_3$ (NBT) perovskite	29
2.5 Oxide ion conduction in NBT.....	29
2.6 Ferroelectric and dielectric NBT systems	34
2.7 Multi-layer ceramic capacitors.....	36
2.8 Solid Oxide Fuel Cells.....	38
2.9 References.....	39
Chapter 3: Methods.....	46
3.1 Finite Element Modelling (FEM)	46
3.2 Three-dimensional model design.....	46
3.3 Material properties and Boundary conditions.....	49
3.4 Discretizing (meshing) the model into elements.....	50
3.5 Visual presentation of simulated data.....	58
3.6 Extraction of data from Impedance spectroscopy.....	60
3.7 Solid state synthesis	61
3.8 Powder X-ray diffraction (XRD).....	61
3.9 Scanning electron microscopy	62
3.10 LCR/Impedance Spectroscopy	62
3.11 References	63
Chapter 4: $\text{Na}_{0.5}\text{Bi}_{0.5}\text{TiO}_3$-$\text{Bi}(\text{M}_{0.5}\text{Ti}_{0.5})\text{O}_3$ Solid Solutions (M = Mg, Zn).....	64
4.1 Introduction.....	64
4.2 Results and discussion.....	68
4.2.1 $(1-x)\text{Na}_{0.5}\text{Bi}_{0.5}\text{TiO}_3$ - $(x)\text{BiMg}_{0.5}\text{Ti}_{0.5}\text{O}_3$	68
4.2.2 $\text{Na}_{0.5}\text{Bi}_{0.5}\text{TiO}_3$ - $\text{BiZn}_{0.5}\text{Ti}_{0.5}\text{O}_3$	89
4.3 Conclusions	98
4.4 References	100
Chapter 5: Finite Element Modelling of a Homogenous Model with a Crack.....	102
5.1 Introduction.....	102
5.2 Results and discussion	104
5.2.1 Current density distribution of cracked model.....	104
5.2.2 Impedance results of high interference models, $S/r=2$	110
5.2.3 Applying the spreading resistance equation.....	114
5.2.4 Impedance results of Low Interference model, $S/r=10$	117
5.2.5 Cross S/r ratio comparison.....	119
5.2.6 Crack effect versus current interference.....	124
5.2.7 Cross conductivity comparison.....	126

5.2.8 Plotting the crack effect using a \log_{10} scale.....	127
5.3 Conclusions	128
5.4 References	129
Chapter 6: Two-layer (heterogeneous) Model.....	131
6.1 Introduction.....	131
6.2 Results	134
6.2.1 Current density distribution and impedance data.....	134
6.2.2 Line scan results for $R_s = 100R_b$ models with different surface thickness.....	135
6.2.3 Data processed with the original spreading resistance equation.....	138
6.2.4 Introducing the two-layer spreading resistance equation.....	140
6.2.5 Instructions on how to use the two-layer spreading resistance equation.....	142
6.2.6 The influence of the surface to bulk layer resistivity ratio.....	143
6.3 Discussion	148
6.4 Conclusions	149
6.5 References	150
Chapter 7: Finite Element Modelling of Two-layer System with a Crack.....	151
7.1 Introduction.....	151
7.2 Results and discussion	152
7.2.1 Current density distribution and impedance results of $S/r=2$ models.....	152
7.2.2 Cross comparison between a homogenous cube and two-layer models with the same crack geometry.....	161
7.2.3 Current density and Impedance results of $S/r=10$ models.....	163
7.2.4 Cross S/r ratio comparison.....	164
7.2.5 Applying the two-layer spreading resistance equation.....	166
7.2.6 Non-through thickness crack.....	170
7.2.7 Non-through length crack.....	173
7.2.8 Simulations of real experimental results.....	176
7.3 Conclusions	180
7.4 References	181
Chapter 8: Conclusions.....	182
8.1 Conclusions.....	182
8.2 Future work and application examples.....	184
8.2.1 Resistive $BaZrO_3$ grain boundary characterisation: MTT.....	185
8.2.2 Conductive dislocation enhanced local conductivity: MTT.....	189
8.2.3 Effect of crack on impedance in zirconia polycrystals: MTT.....	192
8.2.4 Electrical property changes and crack generation in thermal barrier coating: MTT.....	195
8.2.5 Crack and thin layer characterisation in thermal barrier coating: MTMB.....	199
8.2.6 Thin layer characterisation and micro-contact size effects: MTFB.....	201
8.2.7 Dislocation enhanced local conductivity with 2D FEM simulation: MTFB.....	203
8.3 References	206

Chapter 1: Introduction

The $\text{Na}_{0.5}\text{Bi}_{0.5}\text{TiO}_3$ perovskite (NBT), mainly as a parent compound in solid solutions, has received lots of research interest due to its potential applications as a lead-free piezoelectric or dielectric material [1] [2] [3]. Apart from having attractive dielectric properties, recent research has revealed NBT to exhibit three types of electrical behaviour, *i.e.* oxide-ion conduction (type I), mixed ionic–electronic conduction (type II) and insulating/dielectric (type III) based on various defect mechanisms [4] [5]. The different electrical behaviours in the NBT lattice are related to the high mobility of oxide ions which can be fine-tuned to optimise or suppress ionic conduction.

Several acceptor doping studies have been conducted on NBT (*i.e.* A-site = Sr^{2+} and B site = Mg^{2+} , Zn^{2+} , Ga^{3+}) in attempts to improve its ionic conductivity. A minor amount of Mg^{2+} or Sr^{2+} into the structure has improved the bulk conduction close to the theoretical limit based on the oxygen-vacancy diffusion coefficient in a perovskite lattice, [6] but NBT tolerates only small amounts (<5 at%) of most single acceptor dopants. However, it has been reported that NBT can form solid solutions with other perovskites at higher solid solution limits, such as BaAlO_3 , $\text{BiMg}_{0.5}\text{Ti}_{0.5}\text{O}_3$ and $\text{BiZn}_{0.5}\text{Ti}_{0.5}\text{O}_3$ [7] [8] [9] [10] [11]. Most research on the NBT-perovskite solid solutions has focused on the ferroelectric or piezoelectric applications and little information on the oxide-ion conductivity was investigated. It is worthy to investigate how changes in the Na/Bi ratio can affect the electrical behaviour of NBT. Also, it is of particular interest to compare the oxygen vacancy trapping power of the dopants in the solid solution, such as Al, Mg and Zn.

The aim of this work consists two parts. First, to gather more information on the oxide-ion conduction behaviour of NBT solid solutions. To achieve this, the structure and electrical properties of NBT-based solid solutions with two Bi-based perovskites, NBT- $\text{BiMg}_{0.5}\text{Ti}_{0.5}\text{O}_3$ (NBT-BMT) and NBT- $\text{BiZn}_{0.5}\text{Ti}_{0.5}\text{O}_3$, (NBT-BZT) are studied.

Covid 19 pandemic disrupted the progress of the entire project, where limited numbers of NBT-BMT and NBT-BZT samples were prepared and examined. As the laboratories were closed for months and experimental work could not be carried out, the focus of this thesis shifted to finite element modelling (FEM) of micro-contact impedance spectroscopy (mclS). This FEM study could be conducted without accessing the campus in person and thus the research progress was not hindered by the pandemic.

Being a powerful characterisation tool, conventional Impedance Spectroscopy measurements gather an average electrical response across the entire sample [12]. In contrast, mclS receives 75% of the electrical responses from a region that extends 4 times the micro-contact radius from the surface, thus mclS has particular advantage in probing any area or feature(s) of interest on the sample surface [13]. mclS has been widely used in extracting local electrical properties within grains and across single grain boundaries of electro-ceramics and in thin films, thermal barrier coatings and many other materials [14] [15] [16]. In situations where the sample surface contains defects such as cracks, the impedance response gathered is different

from a defect free sample. It is of particular interest to investigate how such defects can affect the impedance data. Finite element modelling is a powerful tool to simulate the electrical response in electro-ceramics. Some successful examples of FEM based mIS simulations are based on defect free ceramic structures. Adding structural defects like cracks into the models can expand the scope of this research and the application of mIS.

The second part of this work is to construct FEM models that can simulate various experimental set ups containing structural defects such as microcracks and apply mIS to investigate how the dimensions and electrical properties of the crack structure can affect the impedance responses. To achieve this, FEM models with different types of cracks and surface layers were created and examined.

Chapters 2 and 3 provide the background for this work. Chapter 2 consists of a review of impedance spectroscopy, micro-contact impedance spectroscopy and finite element modelling. It also contains a review of the literature on NBT and its potential applications. Chapter 3 describes the experimental methods and the finite element modelling approach used in this work. In Chapter 4 the electrical properties of solid solutions between NBT and $\text{BiMg}_{0.5}\text{Ti}_{0.5}\text{O}_3$ or $\text{BiZn}_{0.5}\text{Ti}_{0.5}\text{O}_3$ are explored.

In Chapter 5, micro-contact simulations were conducted where a crack is present in a ceramic cube, using an inhouse finite element software package. The effect of the crack's dimensions on the impedance data is studied. A spreading resistance equation is used to extract local conductivities. In Chapter 6, an additional resistive layer is added to the ceramic cube model, without a crack in the structure. A novel method to extract surface layer conductivity at high accuracy is presented. Chapter 7 presents the model with combined features of chapter 5 and 6, which contains a resistive surface layer and a crack in the top layer. Different crack set ups were examined and a successful attempt to simulate experimental data from radiation damaged SrTiO_3 is made.

Chapter 8, presents conclusions of this work. Multiple experimental examples of where the FEM models developed in this thesis can be applied are explored. Preliminary simulations were conducted and the results look promising. Also, future work to complement the NBT solid solutions is discussed, and other features that should be added into the FEM models are considered.

1.1 References

- [1] E. Aksel and J. L. Jones, "Advances in Lead-Free Piezoelectric Materials for Sensors and Actuators," *Sensors*, 10(3), pp. 1935-1954, 2010.
- [2] D. Damjanovic, N. Klein, J. Li and V. Porokhonsky, "What can be expected from lead-free piezoelectric materials," *Functional Materials Letters*, 3 (1) pp. 5-13, 2010
- [3] K. Reichmann, A. Feteira and M. Li, "Bismuth Sodium Titanate Based Materials for Piezoelectric Actuators," *Materials*, 8, pp. 8467-8495, 2015.

- [4] M. Li, M. J. Pietrowski, R. A. De Souza, H.-R. Zhang, I. M. Reaney, S. N. Cook, J. A. Kilner and D. C. Sinclair, "A family of oxide ion conductors based on the ferroelectric perovskite $\text{Na}_{0.5}\text{Bi}_{0.5}\text{TiO}_3$," *Nature Mater*, 13, pp. 31–35, 2014.
- [5] F. Yang, J. S. Dean, Q. Hu, P. Wu, E. Pradal-Velázquez, L. Li and D. C. Sinclair, "From insulator to oxide-ion conductor by a synergistic effect from defect chemistry and microstructure: acceptor-doped Bi-excess sodium bismuth titanate $\text{Na}_{0.5}\text{Bi}_{0.51}\text{TiO}_{3.015}$," *J. Mater. Chem. A*, 8, pp. 25120-25130, 2020.
- [6] R. A. De Souza, "Oxygen Diffusion in SrTiO_3 and Related Perovskite Oxides," *Adv. Funct. Mater.*, 25, pp. 6326-6342, 2015.
- [7] F. Yang, P. Wu and D. C. Sinclair, "Suppression of electrical conductivity and switching of conduction mechanisms in 'stoichiometric' $(\text{Na}_{0.5}\text{Bi}_{0.5}\text{TiO}_3)_{1-x}(\text{BiAlO}_3)_x$ ($0 \leq x \leq 0.08$) solid solutions," *J. Mater. Chem. C*, 5, pp. 7243-7252, 2017.
- [8] H. Yu and Z.-G. Ye, "Dielectric, ferroelectric, and piezoelectric properties of the lead-free $(1-x)(\text{Na}_{0.5}\text{Bi}_{0.5}\text{TiO}_3)_x\text{BiAlO}_3$ solid solution," *Appl. Phys. Lett*, 93, pp. 112902, 2008.
- [9] C. Chen, H. Zhang, X. Zhao, H. Deng, L. Li, B. Ren, D. Lin, X. Li, H. Luo, Z. Chen and J. Su, "Structure, Electrical, and Optical Properties of $(\text{Na}_{1/2}\text{Bi}_{1/2})\text{TiO}_3$ -1.5at.%Bi($\text{Zn}_{1/2}\text{Ti}_{1/2}$) O_3 Lead-free Single Crystal Grown by a TSSG Technique," *J. Am. Ceram. Soc*, 97, pp. 1861-1865, 2014.
- [10] J.-H. Wang, Y. Li, N.-N. Sun, J.-H. Du, Q.-W. Zhang and X.-H. Hao, "Bi($\text{Mg}_{0.5}\text{Ti}_{0.5}$) O_3 addition induced high recoverable energy-storage density and excellent electrical properties in lead-free $\text{Na}_{0.5}\text{Bi}_{0.5}\text{TiO}_3$ -based thick films," *J. Eu. Ceram. Soc*, 39, pp. 255-263, 2019.
- [11] E. Pradal Velazquez, "Structure-property relations in Sodium-Bismuth Titanate related materials," PhD Thesis, University of Sheffield, 2019.
- [12] J. T. S Irvine, D. C. Sinclair and A. R. West, "Electroceramics: Characterization by Impedance Spectroscopy," *Adv. Mater*, 2, pp. 132–138, 1990.
- [13] J. Fleig, "Local conductivity measurements on AgCl surfaces using microelectrodes.," *Solid State Ionics*, 85, pp. 9–15, 1996.
- [14] M. Shirpour, R. Merkle, C. Lina and J. Maier, "Nonlinear electrical grain boundary properties in proton conducting Y-BaZrO_3 supporting the space charge depletion model," *Phys. Chem. Chem. Phys.*, 14, pp. 730-740, 2012.
- [15] J.-S. Lee, J. Fleig, J. Maier, D.-Y. Kim and T.-J. Chung, "Local Conductivity of Nitrogen-Graded Zirconia," *J. Am. Ceram. Soc*, 88, pp. 3067-3074, 2005.
- [16] N. Wu, K. Ogawa, M. Chyu and S. X. Mao, "Failure detection of thermal barrier coatings using impedance spectroscopy," *Thin Solid Films*, 457(2), pp. 301-306, 2004.

Chapter 2: Literature Review

2.1 Impedance Spectroscopy

When undertaking two electrode dc measurements on electro-materials, the generated response is a combination of electrical properties of different components in the tested materials, e.g., bulk and grain boundaries, core and shell grain components and electrode effects. Applying an alternating voltage over a wide frequency range instead of applying a direct voltage over the electro-material can provide information on these different electro-active components and therefore allows their individual properties to be established and differentiated from one another [1].

The pioneering approach of using Impedance Spectroscopy (IS) on electro-ceramics was performed by Bauerle. An ac voltage was applied over yttria-stabilised zirconia ceramics and the data analysed using an equivalent circuit based on two parallel resistor-capacitor elements connected in series. One element to represent the grain (bulk) response and the other for the grain boundary response. Bauerle was therefore able to identify the bulk and grain boundary resistances from the experimental results obtained [2]. Equivalent circuit analysis is central in analysing impedance data. Equivalent circuits mostly consist of resistors (R) and capacitors (C) connected in series and/or parallel to model the IS response from a ceramic when an ac voltage is applied. The configuration of the equivalent circuit is related to the electro-active microstructure and sample/electrode contacts. It is used to model the physical conduction/charge storage processes occurring in the ceramics and at the electrodes.

Beekmans and Heyne proposed a brick layer model (BLM) that consisted of conductive grains surrounded by a resistive secondary phase or grain boundaries, which can be used to describe the equivalent circuit Bauerle used in his experiments [3]. A schematic illustration of the brick layer model is shown in Figure 2.1 (a).

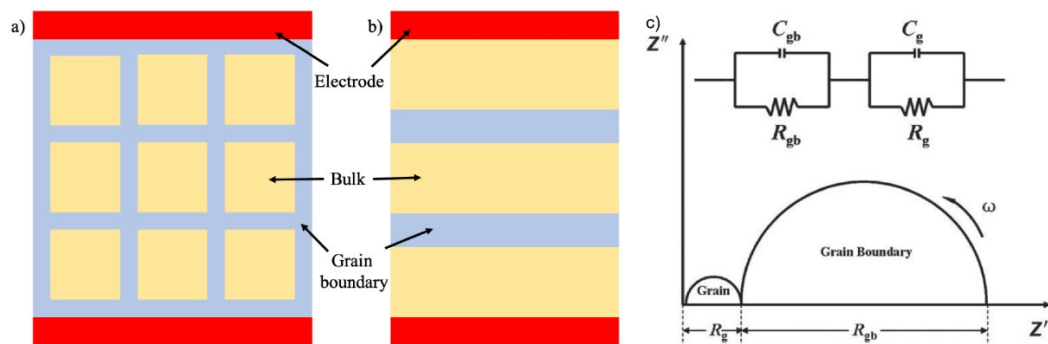


Figure 2.1, a) Illustration of the brick layer model and b) Beekmans boundary layer model [4] c) a schematic illustration of a complex impedance plot generated from the equivalent circuit [5].

Considering low frequencies, it is the nature of current to always take the pathway of least resistance through a system. The current in the BLM would prefer to take a pathway via the bulk instead of the grain boundary on the basis that the grain boundaries are more resistive than the grains. The current will therefore take the shortest pathway that connects the

electrodes with the least grain boundary proportion, resulting in a simplified model that is identical to the Beekmans and Heynes boundary layer model shown in Figure 2.1(b) [6]. An equivalent circuit of two parallel RC elements connected in series can generate two semi-circles in a complex impedance plot, shown in Figure 2.1(c). The plot can be used to simulate the IS response originated from the structure shown in Figure 2.1(b), by extracting R and C values from the individual arcs generated.

Bulk and grain boundary conductivity σ , and relative permittivity ϵ_r values can be calculated from the extracted R and C values using the equations below.

$$R = \frac{GF}{\sigma} \text{ (Equation 2.1)}$$

$$C = \frac{\epsilon_0 \epsilon_r}{GF} \text{ (Equation 2.2)}$$

The geometric factor (GF) is a term related to the geometry of the sample through which the current flows. In a typical experimental set up in Figure 2.1(b), the geometric factor to be used is shown below

$$GF = \frac{l}{A} \text{ (Equation 2.3)}$$

where l is the thickness of the sample and A is the surface area of the sample covered by an electrode.

The brick layer model (BLM) has been widely used due to its simplicity, however Fleig and Maier reported the BLM does not represent the microstructure of real-world ceramics [7]. They used two-dimensional finite element modelling (FEM) as a tool to study current flow based on a change in the shape(s) of the grains from simple cubic to triangular, hexagonal, zig-zag and sloping shapes. They concluded that the grain boundary pattern can alter the impedance response associated with the grain boundaries. As shown in the impedance complex plane, Z^* , plot in Figure 2.2, the data obtained from the BLM model does not match either of those obtained from hexagonal and triangular grain models. They did concede, however, that the brick layer model still holds up to generate acceptable results as different effects can cancel out. For example, only a 10% difference in the grain boundary response was observed in Z^* plots between a realistic grain boundary pattern and the brick layer model [7], Figure 2.3. In the same study, they proposed a discovery named the “detour-effect”. They describe how current detours around the more resistive grain boundaries to lower the impedance and that increasing the grain boundary area (i.e. creating larger grains in the microstructural model) results in a decrease in the grain boundary resistance.

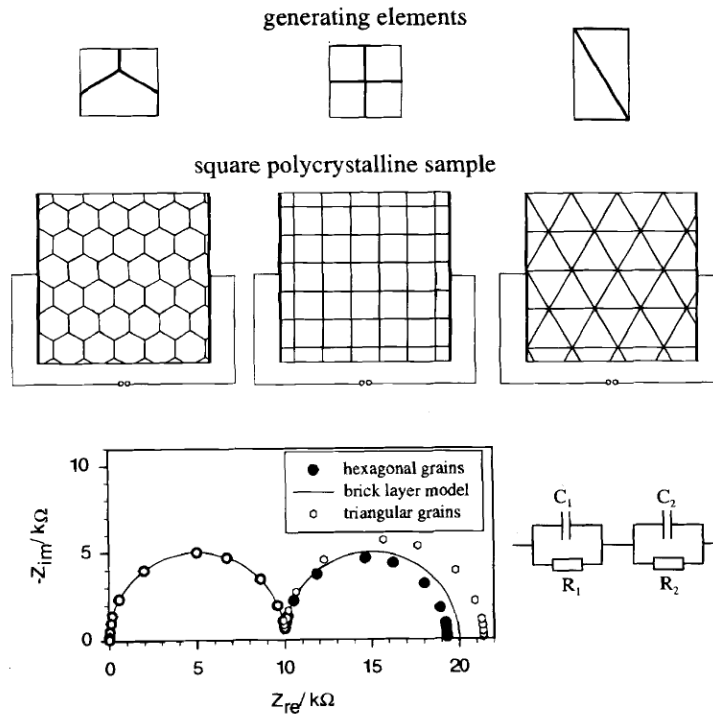


Figure 2.2. 2D FEM impedance simulation with different grain patterns. The brick layer model result does not match with triangle and hexagonal shaped grains [7].

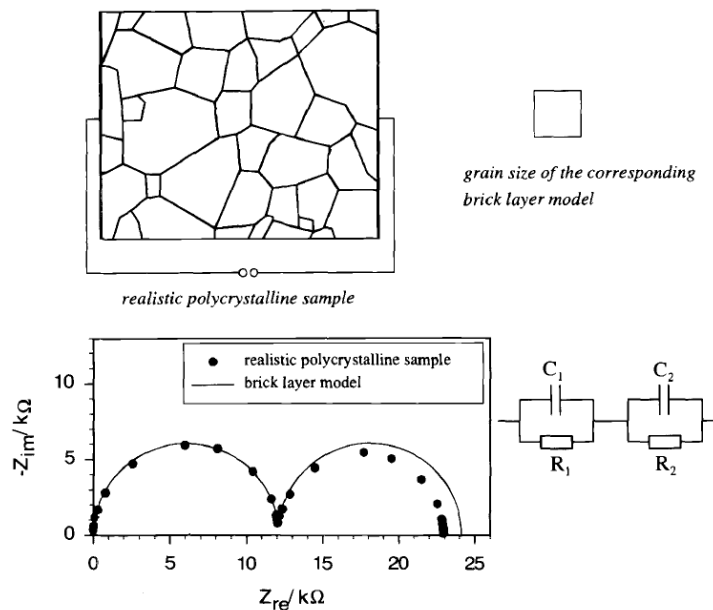


Figure 2.3. A simulation comparison of a realistic polycrystalline microstructure and the BLM model. The difference in the grain boundary response in the Z^* plot is only 10% [7].

In follow up studies, Fleig created sample models with inhomogeneous grain size distribution [8]. As shown in Figure 2.4, the model has 12 large square grains and 4 agglomerates with 49 small grains. Since the grain boundary has higher resistivity than the bulk material, the volume with higher density of grain boundaries had a lower level of current density. In other words, a high density of small grains is more resistive than large grains even when the volume

occupied is the same.

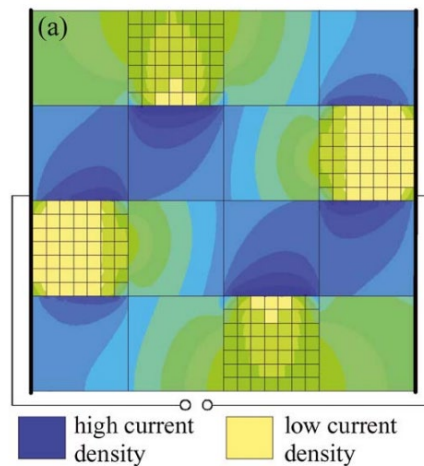


Figure 2.4. Illustration of dc current density in a simulated 2D microstructural array containing small and large grains. The grain boundary has higher resistivity than the bulk material and therefore areas with high density of small grains have low levels of current density [8].

Core-shell grain structures also revealed similar 'detour-effects' [9] based on models where the shell was more resistive than the grains. Heath et al. [9] reported the preferred current pathway within the material is through cores that have higher conductivity than the shells. Later Dean et al [10] conducted an FEM simulation approach on a related topic. They created models with the same grain core and grain shell volume fractions, but one type of model features a layered (Maxwell, series model) structure whereas the other has a grain core encased in a resistive shell as shown in Figure 2.5 (a) and (b), respectively. The simulated impedance responses (plotted in the form of complex electric modulus, M^* plots) from the two types of models are very different even though both models have the same volume fraction of core and shell, Figures 2.5 (c) and (d). They consider the distortion from the ideal Debye semi-circles was due to the heterogeneous electrical microstructure that was established with current detours [10].

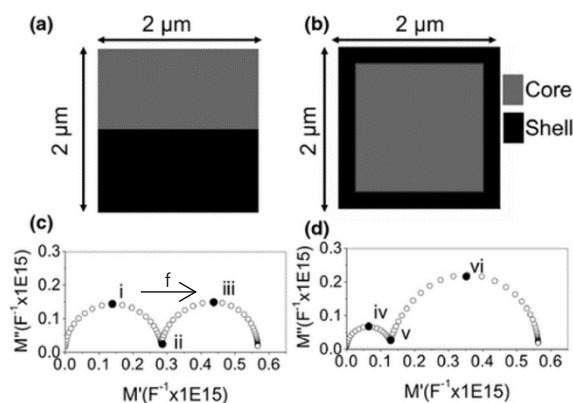


Figure 2.5. Simulation set up for a series of core-shell models. The complex modulus response (shown in (d) of the core-shell model shows a decrease in the shell region response, as the semi-circle at lower frequency is smaller compared to the same component in (c) [9].

2.2 Micro contact-IS (mCIS) and finite element modelling (FEM)

The micro-contact method has been used to probe specific regions such as surface layers, individual grains and grain boundaries in ceramics and for thin films [11-19].

Conventional IS uses a geometric factor to correct the data for the influence of sample geometry. The fact that micro-contact impedance takes place in much finer regions of the sample surface induces more complexity into data correction and analysis as the conventional geometric factor must be modified to be used in micro-contact experiments.

The general derivation of a micro-contact specific geometric factor is as follows; first consider two hemi-spherical contacts that cover the two sides of a sample, one is a micro contact with radius r_{mc} , the counter electrode has radius r_{ce} , as shown in Figure 2.6. The bulk resistance of the sample is obtained by integrating the infinitesimal resistances of the hemi-spherical shells of radius dr which is between r_{ce} and r_{mc} .

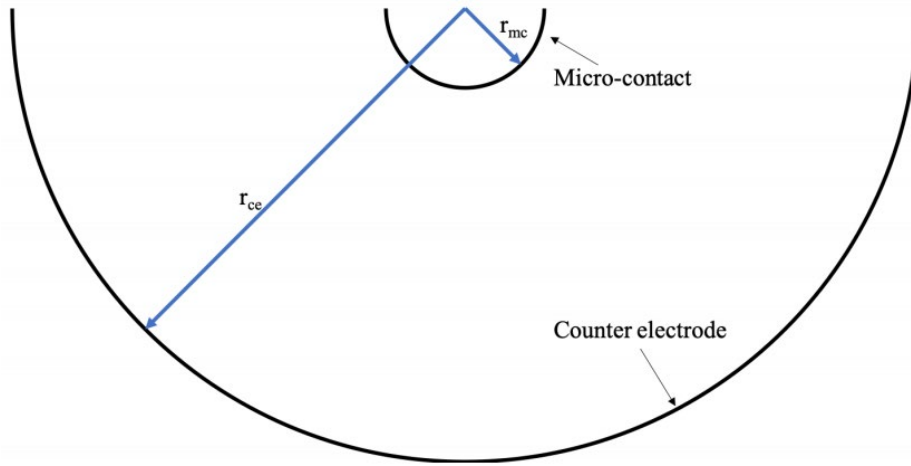


Figure 2.6. Illustration of a sample with two hemi-spherical electrodes [4].

$$R = \int_{r_{mc}}^{r_{ce}} \frac{1}{\sigma \cdot 2\pi r^2} dr \quad (\text{Equation 2.4})$$

Then

$$R = \frac{1}{2\pi r_{mc} \sigma} \left(1 - \frac{r_{mc}}{r_{ce}}\right) \quad (\text{Equation 2.5})$$

The total spreading resistance from one hemi-spherical micro-contact is calculated when $r_{ce} \rightarrow \infty$, because the measured resistance from hemi-spherical shells decreases as the separation between them increases, the equation evolves into

$$R_{spr} = \frac{1}{2\pi r_{mc} \sigma} \quad (\text{Equation 2.6})$$

Changing the hemi-spherical micro-contact to a flat circular micro-contact will transform Equation 2.6 to the equation below [12]

$$R_{spr} = \frac{1}{4r_{mc} \sigma} \quad (\text{Equation 2.7})$$

The R_{spr} is the actual resistance measured by the probe and σ is the calculated conductivity, thus the geometric factor for micro-contact impedance is

$$GF = \frac{1}{4r_{mc}} \text{ (Equation 2.8)}$$

Two requirements to use this modified geometric factor are; (i) there is no highly resistive extrinsic regions between the micro-contact and counter electrode, which would block the current flow; (ii) the size of the micro-contact is much smaller than the size of the sample [13]. The deduced geometric factor is applicable for a micro-contact on a top surface and a large counter electrode on the bottom side. When both electrodes are micro-contacts, the equation derived has to change as the number of micro-contacts is doubled, therefore

$$R_{spr} = \frac{1}{2r_{mc}\sigma} \text{ (Equation 2.9)}$$

It is worth noting that apart from the requirements of Equation 2.8, an additional requirement has to be met to use Equation 2.9 and that is the separation between the micro-contacts is at least 10 times the radius of the micro-contact [4].

Electrodes for conventional impedance measurements are usually pasted conductive metal slurry on the whole sample surface that are later cured at elevated temperature. For micro-contact experiments, the micro-contacts can be created by placing sharp probes into the sample surface [14] [15], or by printing a metal contact array onto the sample surface [16], Figure 2.7. The prepared sample is then loaded onto a probe station which has an optical microscope to zoom in on the micro-contact area to facilitate probe allocation.

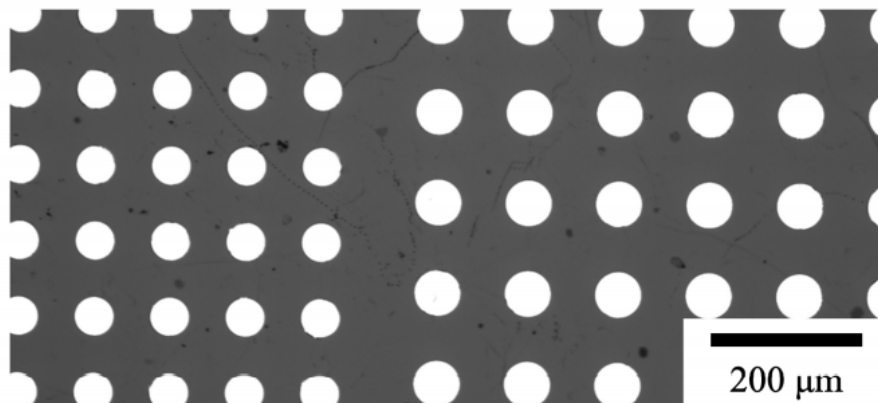


Figure 2.7. Array of micro-contacts with radii of 20 and 30 μm printed by photolithography [4].

Experiments of micro-contact impedance on radiation damaged SrTiO_3 samples have been performed by a former PhD student, Dr Richard Veazey, in the department. After the samples were irradiated by 5 MeV Au ions, he used photolithography to print Au micro contacts with 20 and 30 μm diameter on single crystal SrTiO_3 samples. The minimal separation, s , between electrodes is 1x the electrode diameter. When performing micro-contact impedance measurements, the separation between the probes can be multiplied by factors of the electrode diameter, as the interested area may be across various micro-contacts.

In the impedance experiments conducted by Veazey, SrTiO_3 samples were covered with printed arrays of micro-contacts. The sample was loaded onto a probe station with a heating stage. The probes were placed in contact with the micro-electrodes and connected to an

impedance analyser via cables, Figure 2.8.

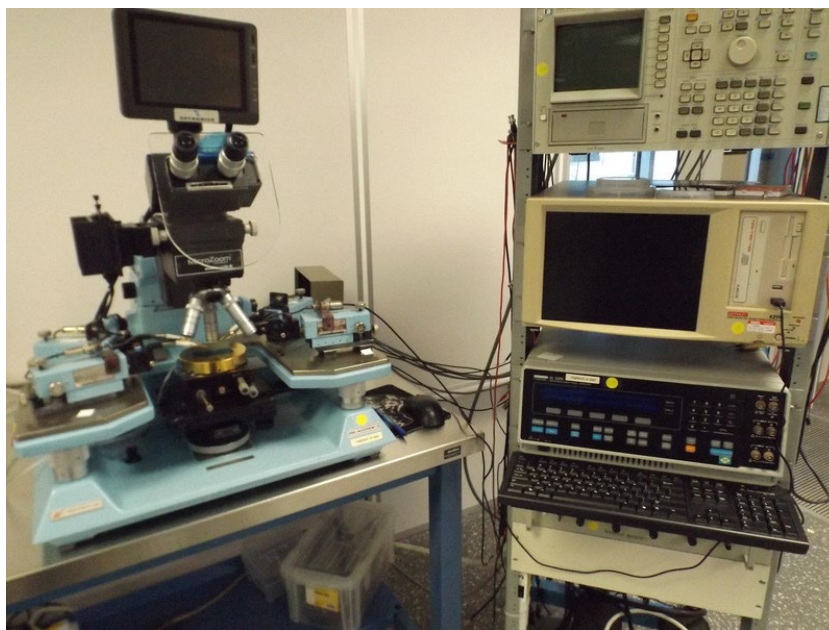


Figure 2.8. Example of a probe station for samples to be mounted on. The probes are connected to an impedance analyser for characterisation [17].

One technical aspect to note when using a heating stage in a probe station is asymmetrical heating, resulting in a temperature gradient across the sample. In addition, the probes in contact with the sample can also act as a heat sink, adding further inaccuracy in the temperature measured. Equation 2.10 is needed to make an estimation of the actual sample temperature [18] [19].

$$T_{spr} = \frac{E_a}{k_B \cdot \ln(\sigma_0 4T_{mc} R)} \quad (\text{Equation 2.10})$$

where E_a is the activation energy of charge carriers in the bulk material, k_B is the Boltzmann constant. R is material's bulk resistance retrieved from the high frequency arc intercept on the real axis in the complex impedance plots. σ_0 is the macroscopic conductivity of the material (established by using conventional IS).

As mentioned above, prior to impedance measurements, the pristine SrTiO_3 samples (both undoped and doped with Fe (wt%)) were subjected to 5 MeV Au irradiation. This induced an amorphous surface on the samples which were subsequently heated (annealed) at higher temperatures to crystallise the amorphous layer. Figure 2.9 (a) shows a radiation damaged sample prior to heat treatment, a smooth surface can be observed. Figure 2.9 (b) shows the samples developed crack features on the surface after 500 °C heat treatment. Veazey [4] used TEM to study the cross section of the radiation damaged Fe-doped SrTiO_3 samples. An XTEM micrograph image and selected area electron diffraction patterns (SAEDP) of a 0.2 wt% Fe sample are shown in Figure 2.10. The radiation damaged region B penetrated $1.47 \pm 0.04 \mu\text{m}$ into the sample surface and this region is completely amorphous.

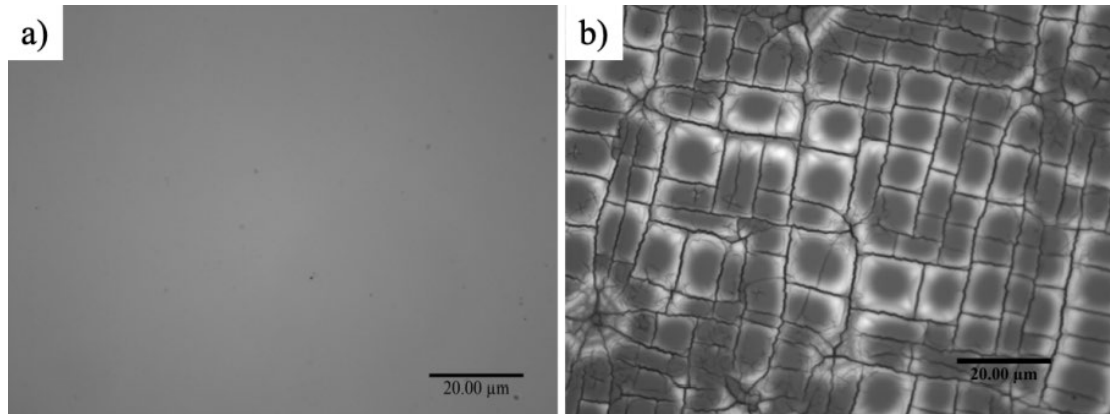


Figure 2.9. Optical microscope image of a) damaged and b) damaged and annealed (at 500 °C) 0.02 wt% Fe-doped single crystal sample at 100x magnification. Other samples showed similar features [4].

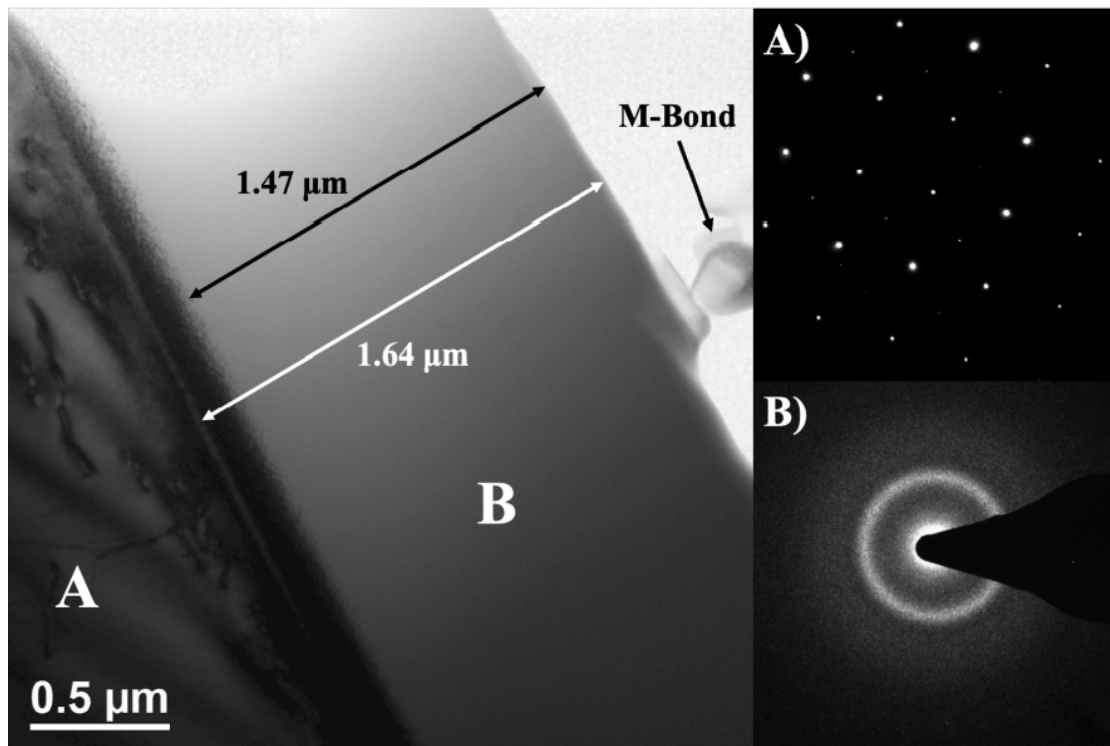


Figure 2.10, Bright-field XTEM micrograph image of a 0.2 wt% Fe-doped SrTiO₃ sample with the selected area electron diffraction patterns taken from the regions labelled A (crystalline) and B (amorphous surface) [4].

Figure 2.11 shows a bright-field XTEM image of a 1wt% Fe-doped sample irradiated and heat treatment at 500 °C. Region B was measured to be $1.52 \pm 0.10 \mu\text{m}$ thick, slightly thicker than that found for the irradiated 0.2wt% Fe-doped sample. The cracks in region B have various depth and should be assigned to the crack features shown in Figure 2.9 (b).

To determine the effect of the cracks on the impedance response, Veazey conducted micro-contact impedance measurements in the region shown in Figure 2.12. Measurement A took place where the number of visible surface cracks is small and measurement B took place in a region with significantly higher surface crack density. The impedance response was plotted in

the same figure.

The cracks in the surface layer of the sample caused the impedance response from region A and B to be significantly different. When there is a low level of cracks between the micro-contacts, the two peaks at high and intermediate frequencies in the M'' spectra have similar magnitude. However, for a high level of cracks between the micro-contacts, the high frequency M'' peak increased and the intermediate frequency response decreased. The Z'' impedance plot reveals that increasing crack density results in a decrease in the measured impedance.

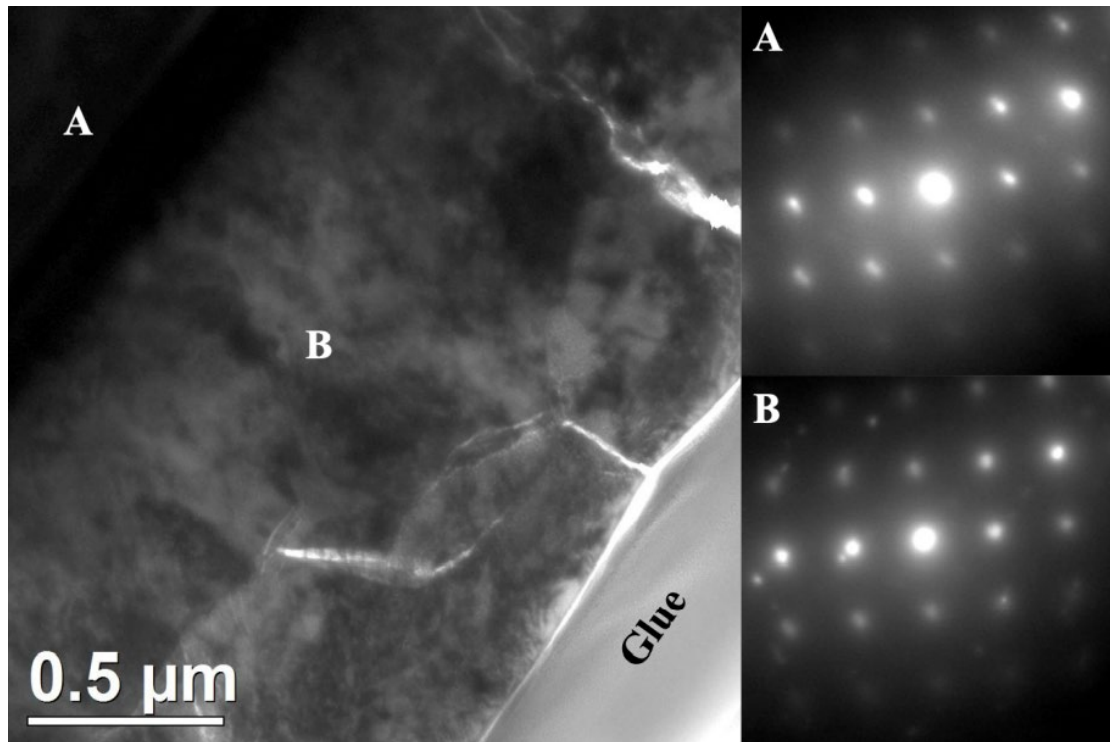


Figure 2.11. Bright-field XTEM micrograph image of a 1 wt% Fe-doped SrTiO₃ single crystal. SAEDPs are labelled according to their origin with an A or B on the image. Also shown is the M-bond glue used to create the cross-section [4].

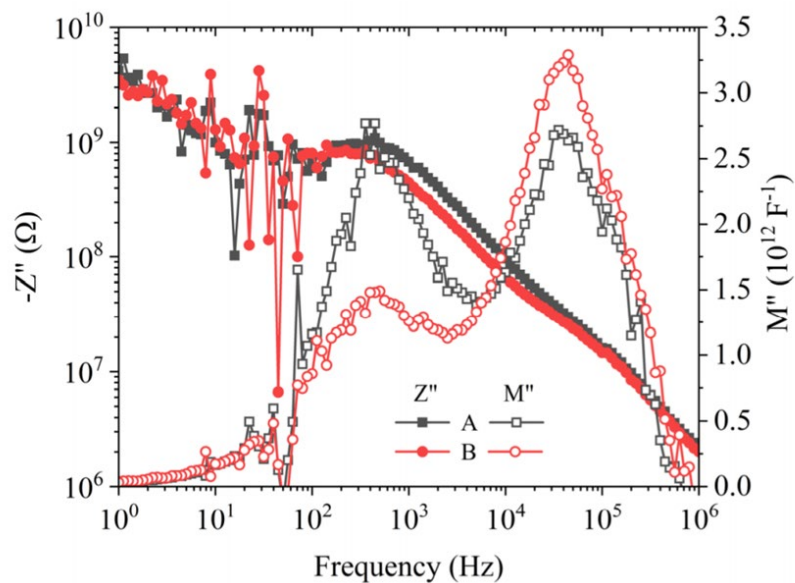
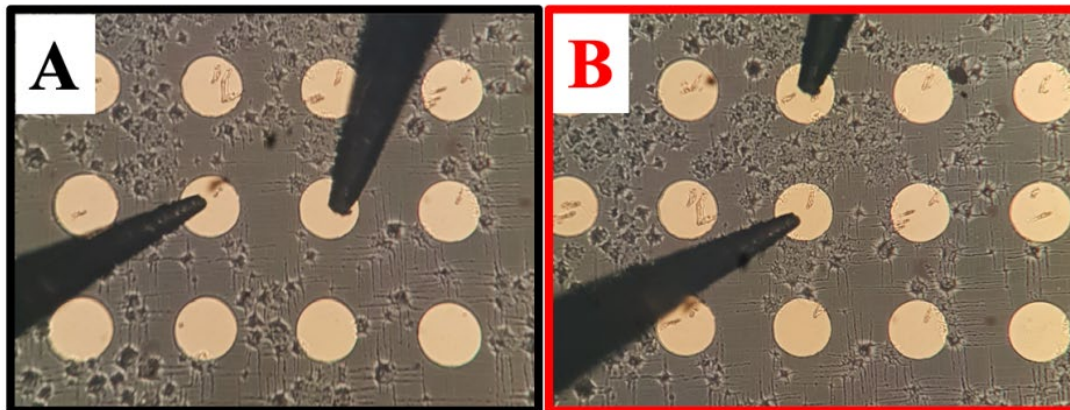


Figure 2.12. Veazey's impedance results from measurements A and B. Measurement A took place in a region with a low density of visible surface cracks, whereas measurement B took place in a region with a high density of visible surface cracks. The radius of micro-contact is $10\ \mu\text{m}$ and the temperature of measurement was held at $310\ \text{°C}$ [4].

To explain the different results between measurements A and B, Veazey [4] proposed an assumption that a crack in the resistive surface layer would drive the current down to the conductive bulk material layer, causing the total impedance response contribution from the surface layer to drop (low frequency M'' peak to decrease in height) and the response from bulk layer to increase (high frequency M'' peak to increase in height), Figure 2.13.

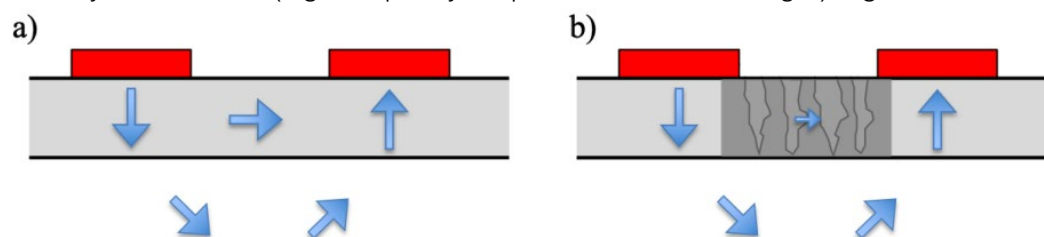


Figure 2.13. Schematic illustration of the proposed flow of current in the sample. a) Damaged sample prior to heat treatment, an intact resistive layer on top of a conductive crystalline bulk.

b) After heat treatment, cracks formed between the micro-contacts, hinder the current flow in the surface layer between the micro-contacts [4].

Based on the experimental results, Veazey et al investigated how to obtain accurate conductivity values when using micro-contacts [20]. They used FEM to create various two electrode configurations on single crystals of undoped and Fe-doped SrTiO₃. As shown in Figure 2.14, the first configuration on the left has a micro-contact on the top surface of the sample, and a conventional electrode on the bottom surface. The second configuration on the right has two micro-contacts on the same (upper) surface of the sample. The major findings reported were: (i) when current flow through the sample is homogenous, the geometric factor (Equation 2.3) returns accurate bulk conductivity values. When current flow is heterogenous in the sample, the spreading resistance equation (Equation 2.9) gives the most accurate conductivity values; (ii) in the case of two micro-contacts on the sample surface, if the separation between the two electrodes is low (less than $S/r = 8$), the high current density volume underneath each electrode overlaps and causes an overestimation of conductivity of the material (this is called 'interference'); (iii) when the sample size is small enough to confine the current from spreading out, confinement occurs and an underestimation of conductivity occurs. However, the effect of confinement and overestimation of current can cancel each other out at some S/r settings.

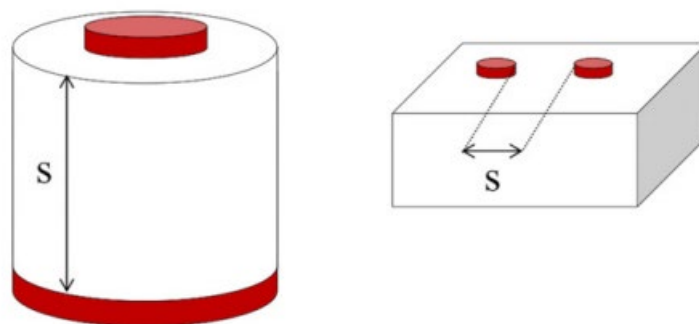


Figure 2.14, schematic illustration of FEM models created by Veazey et al to study micro-contact impedance [20].

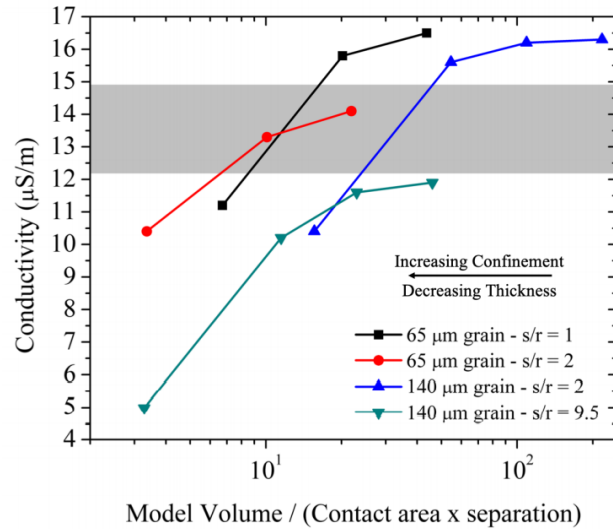


Figure 2.15, calculated conductivity using the spreading resistance equation (Equation 2.9) plotted against confinement provided by the size of the model. The grey box represents a region of $\pm 10\%$ of the input conductivity. Simulations shown are from models with a single grain size of 65 and 140 μm , with S/r ratios of 1, 2 and 9.5 to investigate how the S/r and confinement affect the accuracy based on the spreading resistance equation. The simulations show when confinement is high in samples with small volume, low separation between the electrodes (low S/r) provides more accurate results when using the spreading resistance equation [20].

In follow-up research by Veazey et al. [21], they continued to investigate how to calculate accurate conductivity values of a material with micro-contacts. In this study they added an additional surface layer of higher resistivity on top of the bulk layer material to simulate the amorphous layer observed in the experiment (Figure 2.10), however no crack feature(s) were added to their model.

For two micro-contacts on the same surface of the sample, they gave boundary conditions of when the geometric factor (Equation 2.3) or spreading resistance equation (Equation 2.9) should be used: (i) when the surface layer thickness was more than 10 times the radius of the micro-contact, the spreading resistance equation can provide the surface layer conductivity with acceptable accuracy; (ii) when the surface layer thickness was 10 times smaller than the radius of the micro-contact radius, the geometric factor gives the best calculated surface layer conductivity. However, the boundary conditions limited the applicability of their reported methods to be used in wider experimental set ups. Their results are summarised in Figure 2.16 below. For a thick and resistive surface layer where the thickness is at least 10 times the electrode radius (left hand diagram) there is a suitable equation for the surface layer conductivity, σ_s but there is no suitable equation for the bulk conductivity, σ_b . For a thin resistive layer (right hand diagram) where the layer thickness is 10 times smaller than the electrode radius there are suitable equations for both σ_s and σ_b . When the surface layer thickness is between 0.1 and 10 times the radius of the electrode, no equation(s) were provided to calculate material conductivity values.

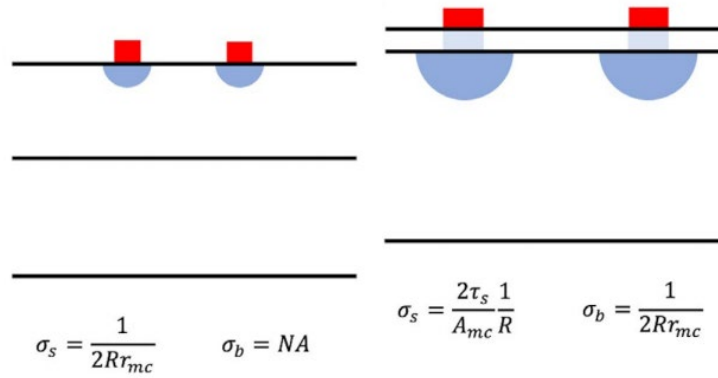


Figure 2.16. Equations used to calculate bulk (σ_b) and surface layer (σ_s) conductivity under different experimental set ups. When a surface layer thickness is more than 10 times the radius of the electrode (left), and when a surface layer thickness is less than 10 times the radius of the electrode (right). Note that when the surface layer thickness is between 0.1 and 10 times of the radius of the electrode, no equations were provided to calculate material conductivity [21].

There also exist various studies on extracting conductivity via the micro-contact impedance spectroscopy (mc-IS) method and their results provide insightful reference to this study. Rodewald et al. [22] compared the measured bulk conductivity from micro-contact and conventional impedance methods of the same Fe-doped SrTiO₃ polycrystalline sample. The results from both methods were very close. The major difference between them came from the low frequency electrode response which overestimated the measured resistance from the micro-contact due to the small size of the electrodes [22].

Wachter-Welzl et al. [23] monitored the change in surface region conductivity of Li₇La₃Zr₂O₁₂ after being exposed in air for extended periods. The measured resistance increased after exposure in air for 3 weeks, and the increase in resistance was greatest for micro-contacts with smaller radius. This indicates the degradation occurred at the sample surface, since micro-contacts can pick up responses from the surface region. Also, conventional impedance results show the conductivity is 3.3x10⁻⁴ S/cm, whereas the micro-contact impedance values show a range from a maximum surface conductivity of 6.3x10⁻⁴ S/cm to a minimum of 2.6x10⁻⁴ S/cm. They considered the change in measured conductivity was due to compositional gradients in the surface region. Therefore the micro-contact impedance measurements revealed local compositional changes in the surface region of the sample after exposure in air in contrast to an averaged value from conventional measurements.

Rettenwander et al. [24] investigated the properties of single crystal Li_{1+x}Al_xTi_{2-x}(PO₄)₃ embedded in epoxy with mc-IS and utilized FEM to facilitate analysis. The aim of their simulations was to investigate how confinement can affect impedance measurements. They created 10 cases with different grain sizes and shapes and the position of the micro-contacts. They reported that the deviations in conductivity due to differently sized single crystals or different microelectrode positions are generally in the 10% range. The most confined model's calculated conductivity was 27% inaccurate. The simulations supported their experimental

results.

Fleig [11] set up innovative work in using mc-IS to investigate surface layer thickness and measured conductivity. A AgCl single crystal sample studied had a mechanically produced surface layer with higher conductivity than the underlying bulk material. Utilizing the ability of mc-IS to pick up the surface layer response, the impedance response of the surface layer could be readily detected. Since the surface layer was more conductive, the measured resistance of the bulk layer was smaller compared to the directly measured bulk layer because the surface layer can increase the effective diameter of the micro-contact instead of the actual micro-contact size. By comparing 'effective' differences in diameter with the actual diameter of the micro-contacts, the surface layer thickness and conductivity can be calculated based on known baseline values for the bulk. In the case of AgCl, the activation energy of the surface layer conductivity was 0.42 eV, which is in good agreement with that known for higher dimensional defects in AgCl, confirming the effectiveness of the mc-IS technique.

2.3 Perovskites

Perovskite is a crystal structure named after the Russian mineralogist Lev Perovski, as German mineralogist Gustav Rose discovered the mineral calcium titanium oxide (CaTiO_3) in 1839. The perovskite structure can be described by a common formula ABX_3 , where A and B are generally cations and X is an anion. The ideal perovskite has a cubic unit cell with space group $Pm\bar{3}m$. The A site is a large cation which occupies the cubo-octahedral interstice site, surrounded by twelve X anions. The B site has a medium sized cation that occupies the octahedral site, surrounded by six anions. Visual illustrations of the perovskite structure are shown in Figure 2.17.

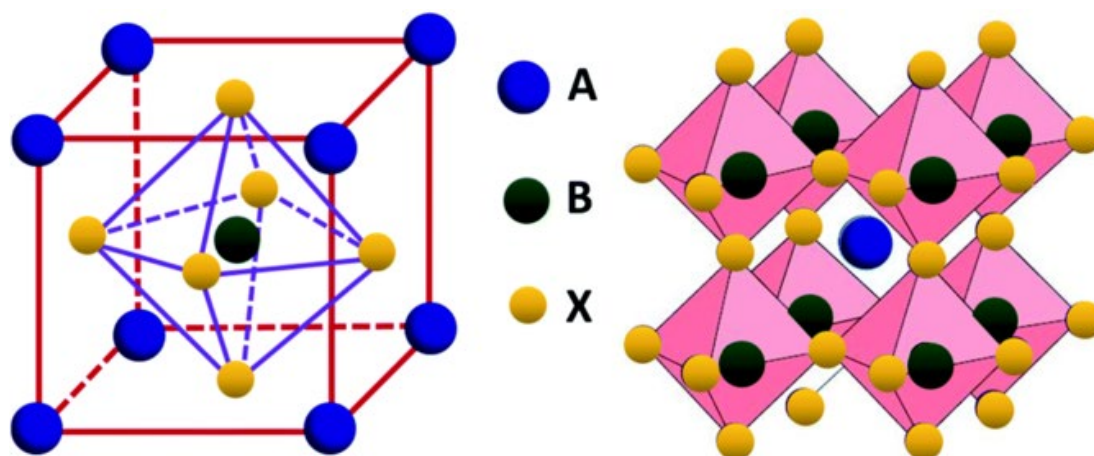


Figure 2.17. Illustrations of the perovskite structure with general formula ABX_3 [25].

The anions in the X sites of ABX_3 perovskite are generally halogens and/or oxygen. In this project, the focus is limited to oxide perovskites. Thus, the balanced combined oxidation states of cations in the ideal structure is 6. This allows multiple combinations of cations with different charges, such as $\text{A}^{1+}\text{B}^{5+}\text{O}_3$, $\text{A}^{2+}\text{B}^{4+}\text{O}_3$ and $\text{A}^{3+}\text{B}^{3+}\text{O}_3$ [26]. When more than one type of cation is present in a crystallographic site, the perovskite structure can be identified as a complex perovskite. Examples can be $(\text{AA}')\text{BO}_3$, $\text{A}(\text{BB}')\text{O}_3$ or $(\text{AA}')(\text{BB}')\text{O}_3$ [26] [27].

For the ideal cubic perovskite structure, Goldschmidt proposed the A-cation should fit into the 12-coordinated site [28]. Thus, the unit cell face-diagonal has length of $2(R_A + R_O)$, where R_A and R_O are the ionic radii of the A and O ions, respectively. Therefore, the unit cell edge length is $\sqrt{2}(R_A + R_O)$. The unit cell edge can also be represented by $2(R_B + R_O)$, where R_B is the ionic radius of B site cation. An ideal cubic perovskite structure should fulfil the relationship of the following equation.

$$2(R_B + R_O) = \sqrt{2}(R_A + R_O) \quad (\text{Equation 2.11})$$

Since the ideal situation is limited to very few numbers of combinations of A and B site cations the term tolerance factor, t , is introduced to allow distortions in the structure. The equation is rearranged to

$$t = \frac{R_A + R_O}{\sqrt{2}(R_B + R_O)} \quad (\text{Equation 2.12})$$

When $t=1$, the ideal cubic perovskite structure is obtained, otherwise it is distorted. If the value of t deviates significantly away from 1, the perovskite structure would not form since it is unstable. In most situations the perovskite structure will be formed between $0.8 < t < 1.06$ [29]. When $t < 1$, the A site cation is too small to sit in the ideal 12 fold co-ordination with 12 equal A-O bond lengths. Tilting of BO_6 octahedra therefore takes place to reduce the A-site co-ordination number, thus creating shorter and longer A-O bond lengths. When $t > 1$, the B site cation is too small for the ideal octahedral environment, the B-site cations can displace from their central position and/or BO_6 octahedra become distorted [29] [30] [31].

2.3.1 Ferroelectrics

Ferroelectric materials exhibit spontaneous polarisation within the structure in the absence of an electric field. When an electric field is applied, the dipoles in the material are forced to align and polarisation is achieved. When the external electric field is removed, some polarisation remains [32]. To be classified as a ferroelectric material, it should meet two essential conditions: the existence of spontaneous polarisation and a demonstrated reorienting of polarisation [33].

Using BaTiO_3 as an example of a ferroelectric perovskite-based material, the phase transition sequence of BaTiO_3 is shown Figure 2.18. Tetragonal BaTiO_3 is ferroelectric but cubic BaTiO_3 is paraelectric with no net dipole moment [34]. The difference originates from the position of the Ti^{4+} ions in the TiO_6 octahedra. In tetragonal BaTiO_3 , the central Ti^{4+} ions are displaced from their centrosymmetric position towards one of the six apical oxygen ions, causing a spontaneous polarisation [34] [35]. Whereas in cubic BaTiO_3 , the Ti^{4+} ions are at the centrosymmetric position, thus no net charge displacement. These two different states are illustrated in Figure 2.19. The phase transition from cubic to tetragonal BaTiO_3 occurs (on cooling) at $\sim 130^\circ\text{C}$ [36].

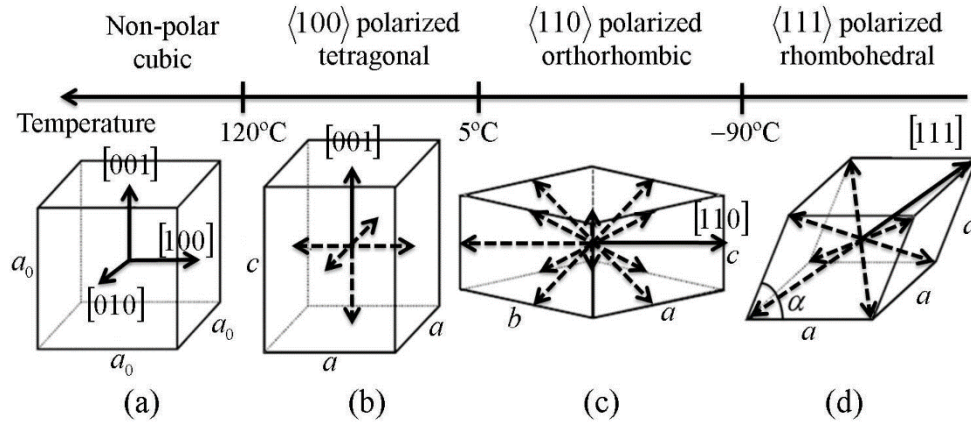


Figure 2.18. Phase transformation of BaTiO₃, (a) cubic crystal system; (b) tetragonal system with 6 crystal variants; (c) orthorhombic system with 12 variants; (d) rhombohedral system with 8 variants [37].

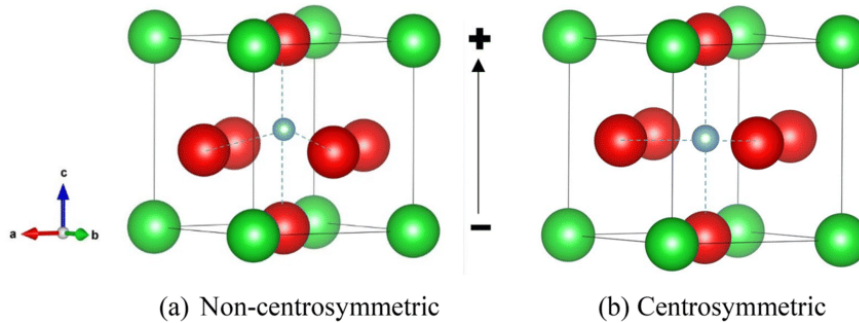


Figure 2.19. Illustration of non-centrosymmetric tetragonal BaTiO₃ (a) and centrosymmetric cubic BaTiO₃ (b) [38].

When adjacent electric dipoles align in the same direction, ferroelectric domains are formed. When domains are not in the same direction, domain walls are formed and separate the domains. The overall result in the material is an electrically neutral state with the electrostatic energy within the material being minimised. An illustration of ferroelectric domains is shown in Figure 2.20 [34] [39] [40].

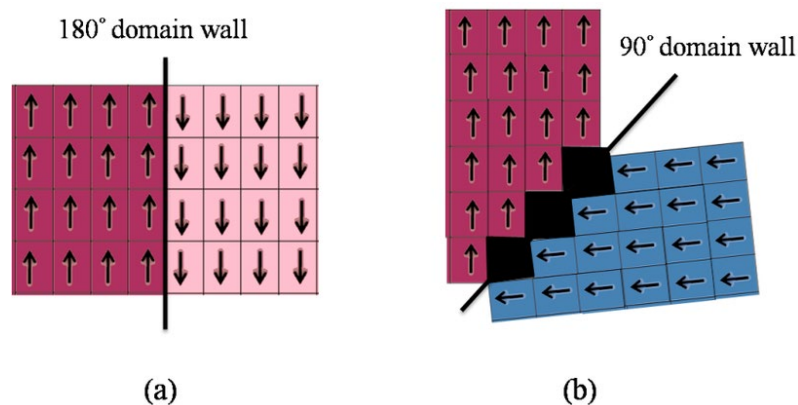


Figure 2.20. Illustration of (a) a 180° domain wall and (b) a 90° domain wall [41] in tetragonal BaTiO₃.

In BaTiO₃, the phase transition from a polar ferroelectric state to non-polar paraelectric state occurs at 130 °C and this temperature is called the Curie temperature (T_c). In the process of

losing spontaneous polarisation, a first or second order phase transition occurs. When a second order transition occurs, the Curie Weiss temperature T_0 equals the Curie temperature T_C and T_0 defines the maximum of the dielectric constant of the material [42].

In the paraelectric state, a ferroelectric material obeys the Curie-Weiss (CW) law:

$$\epsilon_r - 1 = \frac{C}{T - T_0} \quad (\text{Equation 2.13}),$$

where ϵ_r is the relative permittivity, C is the Curie constant and T_0 is the Curie-Weiss temperature. Equation 2.13 can be further simplified, if considering the relative permittivity of a ferroelectric material is much larger than 1, e.g. BaTiO_3 has maximum relative permittivity of about 10,000, Equation 2.13 becomes,

$$\epsilon_r = \frac{C}{T - T_0} \quad (\text{Equation 2.14}).$$

T_0 can be retrieved by plotting the Curie-Weiss law as $1/\epsilon_r$ vs T . An illustration is shown in Figure 2.21.

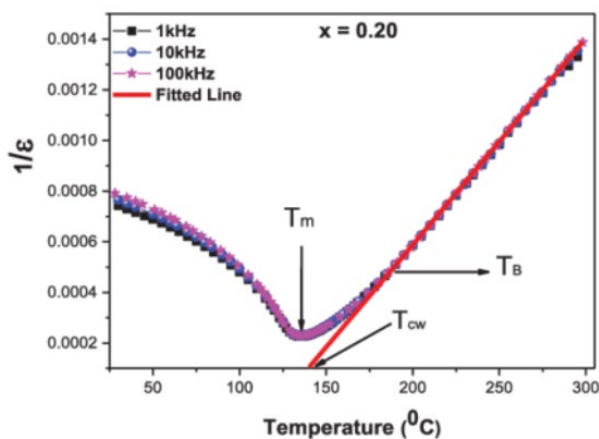


Figure 2.21. Application of the Curie-Weiss law on a sol-gel prepared $\text{Ba}_{0.8}\text{Ca}_{0.2}\text{TiO}_3$ sample. $1/\epsilon'$ is plotted against temperature. The material's T_0 (T_{cw}) is extracted by extrapolation [43].

A polarisation against electric field (P-E) hysteresis loop reveals the domain alignment process in ferroelectric materials. An example P-E hysteresis loop for a BaTiO_3 sample is shown in Figure 2.22 [43] [44]. When an electric field is applied to a ferroelectric, the domains in the same direction as the field would remain unchanged, the domains at directions different from the electric field would change their orientation when electric field strength is high enough. The polarisation increases and will reach saturation. When the electric field is reduced to zero, some domains retain polarisation in the direction of the applied field and thus the material has remanent polarisation [45]. Applying an electric field in the reverse direction will set the polarisation to zero and then generate saturation polarisation in the opposite direction. A P-E hysteresis loop can be completed by removing the reverse electric field. The coercive field E_c is defined as the field required to reduce polarisation to zero.

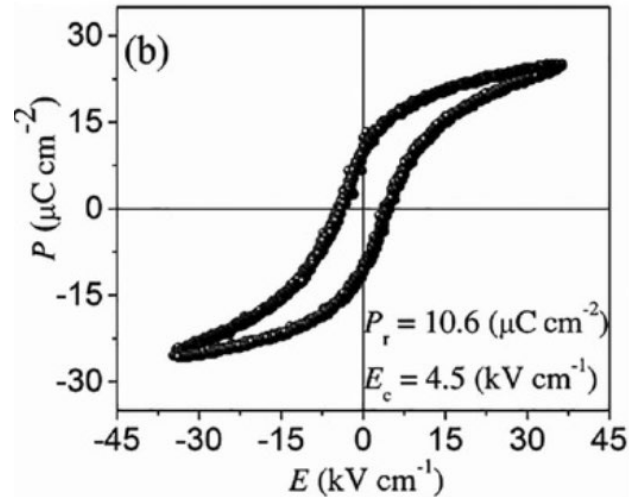


Figure 2.22. Ferroelectric P-E hysteresis loops of a BaTiO₃ ceramic sintered at 1300 °C, plotted as polarisation against applied field [46].

2.3.2 Oxygen ion conductors

When charge carriers migrate in a material, electrical conduction occurs. The type of charge carrier (electron, electron hole, cation or anion) and host material determines the conduction mechanism. Electrical conductivity σ can be calculated by the equation

$$\sigma = nq\mu \quad (\text{Equation 2.15})$$

where n is the number of charge carriers, q is the electrical charge of the carrier and μ is the mobility of the charge carrier. If more than one charge carrier exists, the total conductivity is the sum of all types of conduction combined.

Some oxides exhibit high levels of oxygen ion conductivity. The charge carrier is therefore the oxygen ion. There exists intense interest in oxygen ion conductors as solid state electrolytes or oxygen separation membranes that can be used for solid oxide fuel cells (SOFC), or oxygen sensors, respectively [47] [48].

In oxygen ion conductors, the current flow is achieved by the hopping of thermally activated oxygen ions when an electric field is applied. The oxygen ion can migrate in the structure via interstitial sites or oxygen vacancies. In the latter method, two conditions must be satisfied, structurally, there exists unoccupied lattice sites that are the same type as the oxygen ions already occupy. Energetically, the barrier for the hopping process should be low, a typical energy barrier for an oxide ion conductor is less than 1 eV. When the temperature is high, the charge carrier concentration rises thus high ionic conductivity is achievable. Another way to increase charge carrier concentration is by acceptor doping, which will generate oxygen vacancies in the lattice. For example, in Y₂O₃ doped ZrO₂ (YSZ), introducing Y³⁺ to replace Zr⁴⁺ generates oxygen vacancies in the fluorite structure [49]. One particular aspect to be aware of, is the trapping of oxygen vacancies by the dopants, lowering the mobility of the vacancies and hence lowering the ionic conductivity, as shown in Figure 2.23 [50]. Skinner et al reported that the oxide ion conductivity in acceptor-doped ceria solid solutions reaches a maximum when the dopant concentration is ~8 mole percent. Further increasing the dopant level has

an adverse effect on the conductivity. Computer simulations based on energy minimisation techniques and atomic lattice simulations suggest the trapping of oxygen vacancies by dopants is due to the size mismatch of dopant and host ions, where elastic strain will occur. For example, in CeO_2 , Gd^{3+} is proven to have the smallest binding energy and other dopant ions with larger ionic radii (La^{3+}) or smaller ionic radii (Sc^{3+} , Fe^{3+} , Ga^{3+} , Al^{3+}) would have higher binding energy, thus lowering the oxide ion conductivity [51] [52].

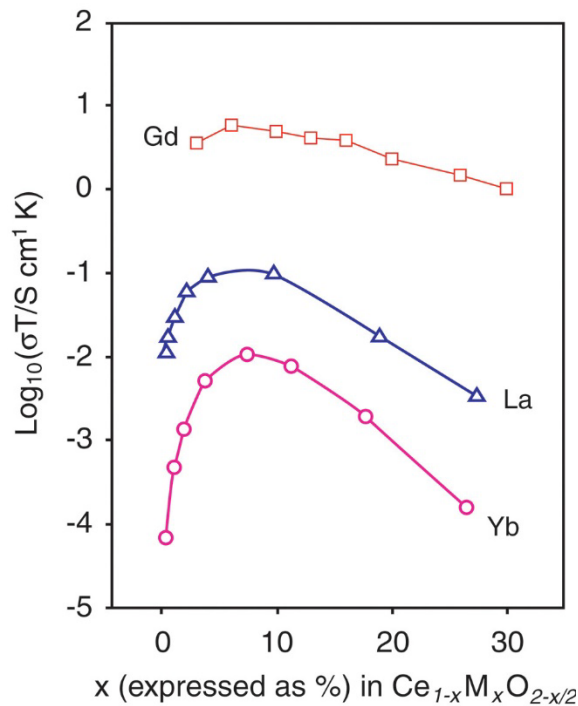


Figure 2.23. The isothermal conductivity of some ceria solid solutions at temperatures close to 200 °C. When the doping level of the Gd, La and Yb exceeds 8%, the bulk conductivity decreases [50].

Some oxygen ion conductors have already been utilized in applications such as SOFC. Ytria-stabilised zirconia (YSZ) has been widely used in high temperature SOFC as the electrolyte. Gadolinium-doped ceria (GDC) also shows good potential to be commercialised in intermediate temperature SOFCs, since it shows high oxygen ion conductivity at a working temperature near 550 °C [53] [54]. Strontium and magnesium co-doped LaGaO_3 (LSGM) is another competitive candidate for intermediate temperature SOFCs [55]. Lastly, Sodium bismuth titanate $\text{Na}_{0.5}\text{Bi}_{0.5}\text{TiO}_3$ has also been reported to show very high oxygen ion conductivity and therefore has potential in SOFC applications. A conductivity comparison of some typical oxide ion conductors is shown in Figure 2.24 [56] [57].

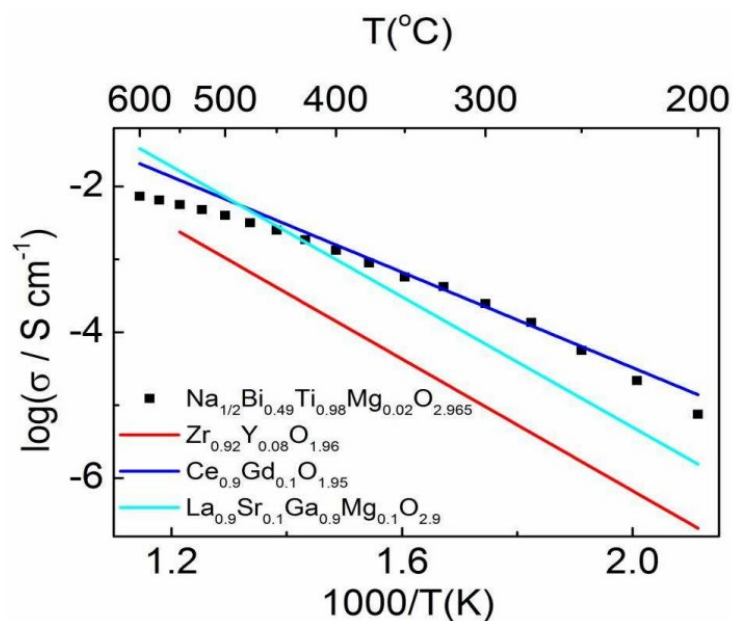


Figure 2.24. Comparison of bulk oxide ion conductivity in the range ~200–600 °C of the nominal composition $\text{Na}_{0.5}\text{Bi}_{0.49}\text{Ti}_{0.98}\text{Mg}_{0.02}\text{O}_{2.965}$ and YSZ ($\text{Zr}_{0.92}\text{Y}_{0.08}\text{O}_{1.96}$), GDC ($\text{Ce}_{0.9}\text{Gd}_{0.1}\text{O}_{1.95}$) and LSGM ($\text{La}_{0.9}\text{Sr}_{0.1}\text{Ga}_{0.9}\text{Mg}_{0.1}\text{O}_{2.9}$) [57].

2.4 $\text{Na}_{0.5}\text{Bi}_{0.5}\text{TiO}_3$ (NBT) perovskite

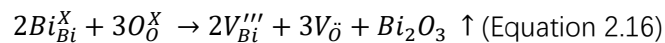
$\text{Na}_{0.5}\text{Bi}_{0.5}\text{TiO}_3$ (NBT) perovskite was first reported by Smolenskii et al in 1960 [58]. This ferroelectric material is mainly known as a lead-free piezoelectric material and a dielectric material at elevated temperatures. Perovskites generally have a common formula of ABX_3 , with AX_3 constructing a fcc type of lattice with B cations located in octahedral sites in the lattice. Levin and Reaney's TEM study revealed that in NBT, sodium and bismuth cations occupy the A cation's position with no observable ordering and titanium ions are located in the B cation's position. The NBT structure at room temperature is extremely complex, octahedral tilting and cation disorder have been observed. An average anti-phase octahedral tilting $a^-a^+c^-$ is concluded from the mix of short ranged in-phase tilting $a^-a^+c^+$ and long range anti-phase tilting $a^-a^+c^-$. [59].

NBT undergoes a series of phase changes with increasing temperature. Dorcet et al reported the phase transformation process using a combination of transmission electron microscopy and electron diffraction. Below 200°C, NBT has a rhombohedral-type structure. From 200 to 280 °C, orthorhombic sheets start to form in the structure and increases in volume percentage until no rhombohedral phase remains. On further heating to 320 °C, the orthorhombic phase converts to a tetragonal phase. Dorcet et al claimed that A site ordered P42/mm nanodomains can be observed above 400 °C. After 520 °C, the tetragonal phase transforms to a cubic phase [60] [61].

2.5 Oxide ion conduction in NBT

In 2014, Li et al reported NBT is an excellent oxide ion conductor which can be used as an

electrolyte in solid oxide fuel cells [57]. Later in 2015, Li et al revealed that the exceptionally high oxide ion conductivity in NBT ceramics originates from the highly polarizable bismuth ion and weak Bi-O bond, which allows oxygen vacancies to diffuse through the structure [56]. Prior to this finding, the oxide ion conductivity in NBT was generally assumed to be the result of loss of Bi_2O_3 during the sintering process, as shown in Equation 2.16. Oxygen vacancies generated in the volatilization of Bi_2O_3 are mobile under elevated temperature and act as the main charge carrier in NBT ceramics [62] [63]. These researchers investigated the origin of oxygen vacancies, however they did not illustrate how the charge carriers migrate through the lattice.



Alongside with the discovery of the origin of oxide ion conductivity in NBT, these series of studies also investigated other factors that can influence the conductivity in NBT samples. These included, donor and acceptor doping on the A and B sites of NBT, as well as sodium and bismuth non-stoichiometry [57] [56] [64].

A review by Yang et al concluded some trends in tailoring the properties of NBT ceramics [65]. NBT samples that are sodium-deficient or bismuth-rich in starting composition are electrically insulating and therefore have good dielectric and piezoelectric performance since the current leakage is low. In contrast, Na_2O rich or Bi_2O_3 deficiency in the starting materials will produce highly ionic conductive NBT samples with oxide-ion transport numbers close to 1. The detailed results are shown in Figure 2.25. Li et al concluded that the Na/Bi ratio of the initial NBT composition has a fundamental influence on its conductivity. When Na/Bi is more than 1, ceramics are conductive, and when the Na/Bi ratio is less than 1, they are insulating. It is worth mentioning that excessive amounts of Bi_2O_3 in the starting compositing can reintroduce conductivity into the ceramics. In this case, samples are mixed conductors with both ionic and electronic conduction mechanisms being present.

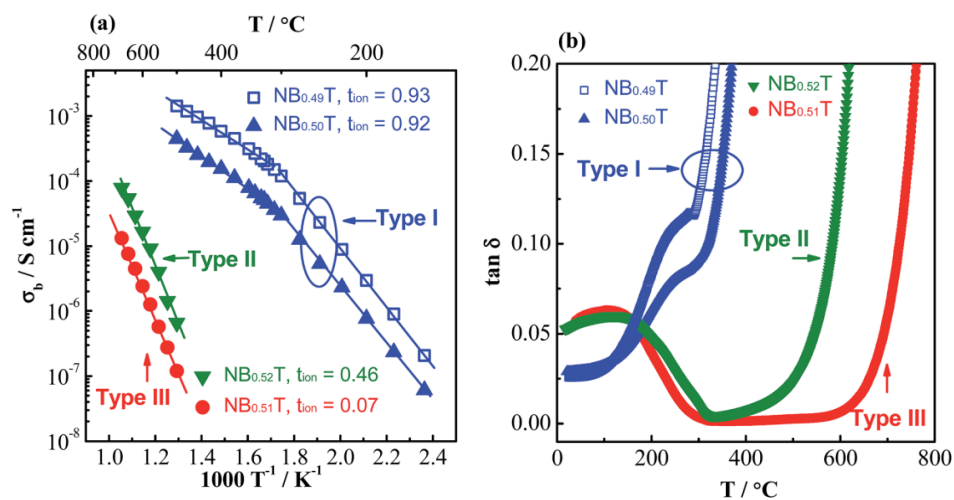


Figure 2.25. (a) Arrhenius plot of bulk conductivity, σ_b and (b) dielectric loss, $\tan \delta$, at 1 MHz versus temperature for NBT with various A-site Bi nonstoichiometry: $\text{Na}_{0.5}\text{Bi}_{0.49}\text{TiO}_{2.985}$, $\text{NB}_{0.49}\text{T}$; $\text{Na}_{0.5}\text{Bi}_{0.5}\text{TiO}_3$, $\text{NB}_{0.50}\text{T}$; $\text{Na}_{0.5}\text{Bi}_{0.51}\text{TiO}_{3.015}$, $\text{NB}_{0.51}\text{T}$; $\text{Na}_{0.5}\text{Bi}_{0.52}\text{TiO}_{3.03}$, $\text{NB}_{0.52}\text{T}$ [65].

Acceptor doping on the A-site to replace Bi^{3+} with Ca^{2+} , Sr^{2+} and Ba^{2+} shows improvement in

conductivity. Acceptor doping on the B-site with magnesium to replace titanium also showed improved conductivity. Both doping mechanisms are similar in that they generate oxygen vacancies by introducing lower valence cations. It is also important to point out that only low levels of dopants are accepted by the NBT lattice, increasing the doping level results in the formation of secondary phases with no improvement in overall conductivity.

Experimental results have shown that donor doping NBT, such as using Nb^{5+} to replace Ti^{4+} , can fill up the oxygen vacancies generated and hence the ionic conductivity is reduced. With increasing levels of doping, the ceramic transforms into an insulator from a mixed ionic-electronic conductor. The level of donor doping however is similar to the acceptor doping mentioned above. Only a low level of aliovalent dopant (<2 at%) is generally accepted in the structure. The Arrhenius plot in Figure 2.26 shows the relationship between bulk conductivity and Nb doping level.

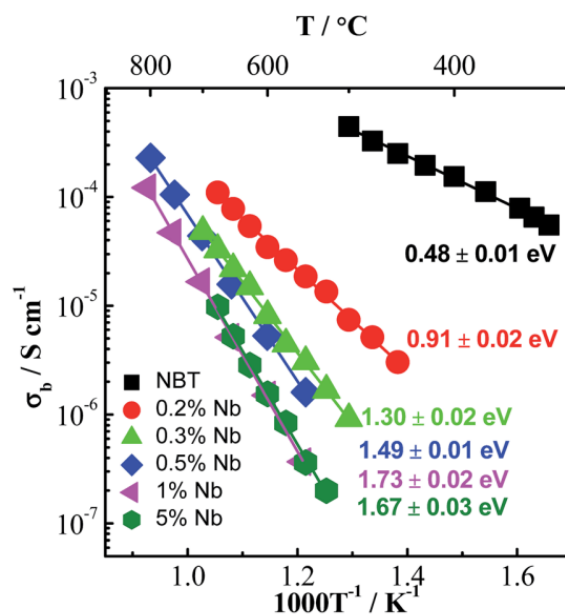


Figure 2.26. Arrhenius plot of the bulk conductivity, σ_b , of Nb-doped NBT with a nominal composition $\text{Na}_{0.5}\text{Bi}_{0.5}\text{Ti}_{1-x}\text{Nb}_x\text{O}_{3+0.5x}$. Activation energy for each composition is indicated in the figure [65].

Isovalent doping on the A-site leads to a local perspective to look at the conduction mechanism in NBT. Saiful Islam in 2000 proposed that for an oxide ion conducting perovskite, the oxide ions migrate through the structure in a specific pathway, which is through a triangle structure consisting of two A-site cations and one B-site cation (A-A-B) called a saddle point [66]. In the case of the NBT perovskite structure, He and Mo used first principles calculations to investigate the oxide ion diffusion mechanism in NBT [67]. Their calculations revealed that the different saddle point configurations have different activation energies. The Bi-Bi-Ti configuration has the lowest energy barrier which is 0.22 eV, the Na-Na-Ti saddle point has the highest activation energy (1.0 – 1.3 eV), and the Na-Bi-Ti path has an intermediate value of 0.6 to 0.85 eV. Their calculations agree well with the fact that bismuth ions are highly polarizable. Also, they claimed that the oxide ions will not go through the Na-Na-Ti path with

highest activation energy, that leaves the Na-Bi-Ti path being the rate limiting path for oxide ion conduction. In the same work, He and Mo's simulation results agree well with the experiment results from Li et al on Mg doped NBT, hence their theory on the NBT saddle points should be valid and useful as a guideline for further studies on NBT ceramics.

The effects of isovalent doping have been demonstrated in the review by Yang et al. Partial replacement of Na with K on the A-site reduced the oxide-ion conductivity, mainly due to K being more volatile than Na and more K is lost during the sintering process. This results in NKBT being Bi-rich on the A-site, thus the Na/Bi ratio is lower than 1 therefore the overall conductivity is suppressed. Using Y^{3+} or La^{3+} to replace Bi^{3+} also produces NBT with decreased conductivity. Yang et al reasoned that both Y and La are less polarizable than Bi, while both have stronger bonding strength with oxygen than Bi. The bulk conductivity of NBT is therefore suppressed again. On the B-site, replacing Ti with Zr results in less conductive NBT, even though Zr has highly polarizability than Ti, the Zr-O bond is stronger than the Ti-O bond, therefore the trapping power of Zr is stronger on the B-site [68].

In summary, numerous experiments have been performed to improve the bulk conductivity of NBT ceramics, among which, acceptor doping has shown positive effects on the oxide-ion conductivity, yet only low levels of dopants can be substituted into the A- and B-sites. Two reasons have been proposed by Yang et al. First, the low level of doping is restricted by the limited solubility of dopants in the NBT solid solution. Second, excessive amounts of acceptor dopants in the matrix effectively trap the oxide-ions from moving, lowering the diffusivity of oxide-ions [67]. Combined with the theory reported by De Souza, which claimed there is an upper limit of oxide-ion diffusivity in perovskite structured ceramics, Yang et al believe the optimization of NBT in regard of oxide-ion conductivity has been achieved [69] [70].

$BiMg_{0.5}Ti_{0.5}O_3$ was first reported as a high pressure lead-free dielectric material which could only be prepared under high temperature and pressure [71]. Other and similar perovskites include $BiZn_{0.5}Ti_{0.5}O_3$, and $BiAlO_3$ [72] [73]. There are also reports showing this type of high-pressure phases can form solid solutions with NBT at atmospheric pressure, however these reports focused mainly on properties other than oxide-ion conductivity [74] [75].

With the formation of a solid solution of NBT- $BiMO_3$, (M can be Mg, Zn or Al), the Na/Bi ratio within the ceramic would decrease. According to the work by Li et al, bismuth rich compositions of NBT would decrease the bulk conductivity, yet if applying the theory proposed by He and Mo, where the Na-Bi-Ti saddle point (activation energy 0.6 -0.85 eV) is the rate limiting step in the conduction process, increasing the amount of Bi will result in more Bi-Bi-Ti saddle points with a lower activation energy barrier, thus enhancing the overall conductivity. It is also important to point out that He and Mo calculated the barrier energy if acceptors like Mg are placed on the B-site, since due to the predicted strong trapping power of Mg, the Na-Bi-Mg and Na-Na-Mg pathways will have significantly higher activation energies of 1.0 – 1.3 eV and around 2.1 eV respectively, compared with stoichiometric NBT.

Yang et al and Pradal-Velázquez have done pioneering work to investigate the electrical

properties of NBT-BiAlO₃ (NBT-BA), NBT-BiMg_{1/3}Nb_{2/3}O₃ (NBT-BMN) and NBT- BiZn_{1/3}Nb_{2/3}O₃ (NBT-BZN) solid solutions [76] [77]. In their work, the bulk conductivity of the solid solutions gradually decreases with an increasing amount of the BA, BMN and BZN high-pressure phase. The bulk conductivities of the three solid solutions are shown in Figure 2.27. The ionic transport number also decreases and the solid solutions transform from excellent oxide-ion conductors to mixed conductors then to dielectric materials with a low level of electronic conduction. They concluded that the acceptors added to the B-site act as oxide-ion vacancy traps, decreasing the mobility of oxide-ions and suppressing bulk conductivity.

Besides the chemical doping method, ceramics microstructure also has significant effect over the NBT-based materials electrical conduction behaviour, revealed by Yang et al [78]. It is reported that NB_{0.51}T ceramics with very low levels of acceptor doping on the Ti site will present an inhomogeneous microstructure with randomly distributed large grains surrounded by a small grained matrix. SEM images were used to reveal the grain distribution, Figure 2.28 [78]. Considering the large grains as a conductive phase and small grains as an insulating phase, the ceramics can be treated as a two-phase composite. Increasing the doping level leads to more conductive large grains in the structure. Oxide-ion transport number measurements were performed and the results agreed with the trend of increasing fraction of large grains. Furthermore, this electrical two-phase model has been supported by finite element modelling by re-creating the microstructure. Thus, it is very important to identify the microstructure of the samples when impedance measurements are performed.

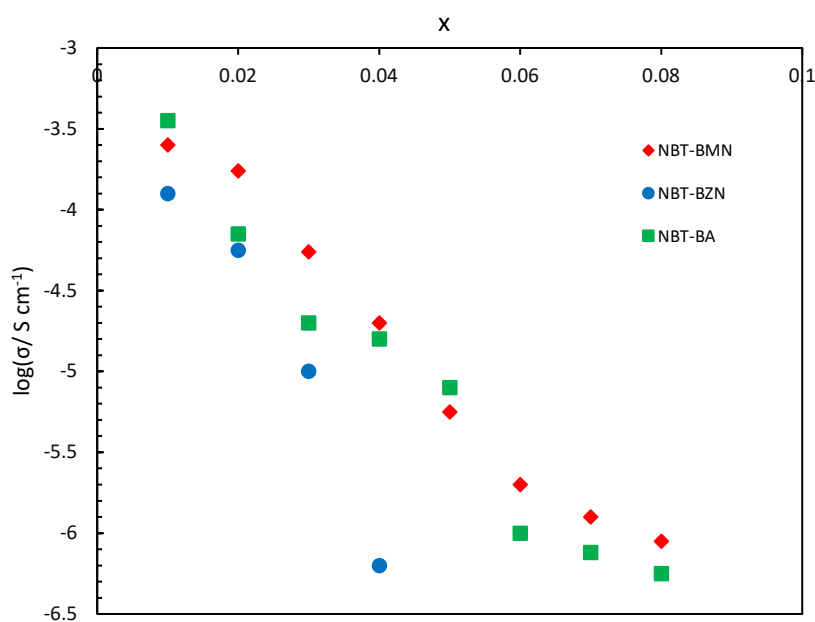


Figure 2.27 Bulk conductivities of solid solutions of (1-x)NBT-(x)BMN, (1-x)NBT-(x)BZN and (1-x)NBT-(x)BA compared at 550 °C [76].

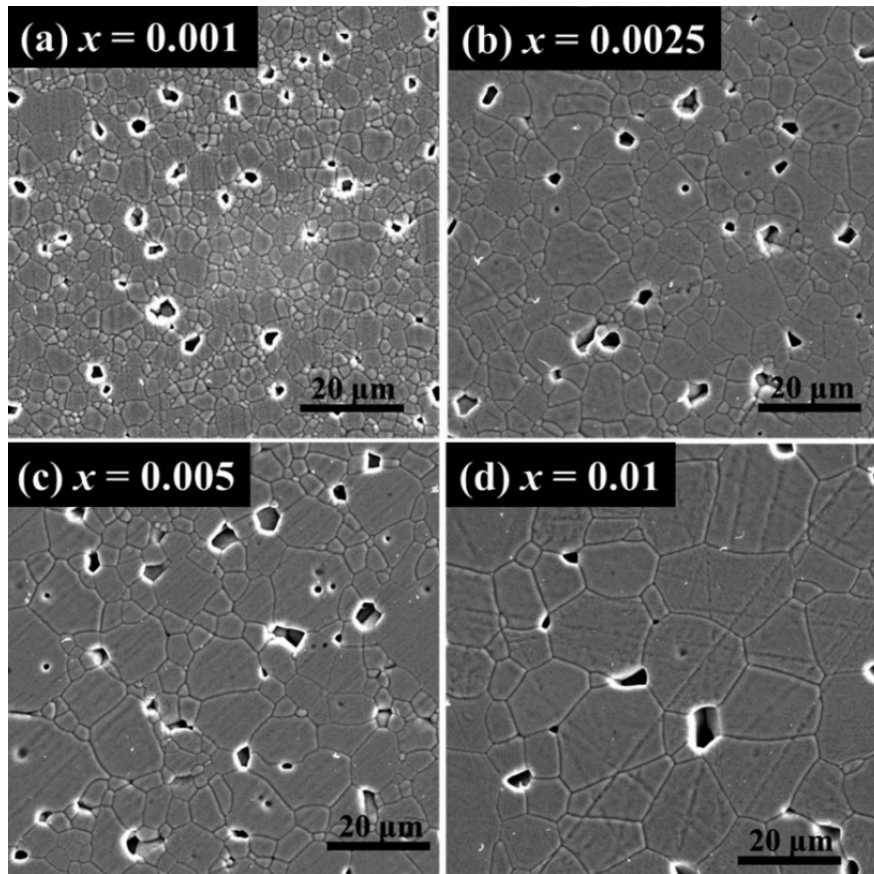


Figure 2.28. SEM micrographs of thermally-etched surfaces of $\text{Na}_{0.5}\text{Bi}_{0.51}\text{Ti}_{1-x}\text{Mg}_x\text{O}_{3.015-x}$ ceramics. (a) $x = 0.001$; (b) $x = 0.0025$; (c) $x = 0.005$; (d) $x = 0.01$. When the doping level is low, a two-phase composite microstructure with large grains embedded in a small grain matrix is formed [78].

2.6 Ferroelectric and dielectric NBT systems

Ferroelectricity is a macroscopic phenomenon caused by the long range ordered alignment of electric dipoles. In NBT, the ferroelectricity comes from the combined effect of off-centred titanium ions in the octahedra and displaced bismuth ions on A-site positions.

Li et al reported NBT's dielectric properties are strongly influenced by the starting composition. As shown in Figure 2.29, Na-rich and Na-deficient NBT was tested. The relative permittivity of NBT is modestly influenced by the Na nonstoichiometry in terms of magnitude and temperature. In contrast, the dielectric loss is heavily influenced by the change in Na composition. NBT and $\text{Na}_{0.51}\text{BT}$ shows high levels of dielectric loss at $\sim 300^\circ\text{C}$ with $\tan \delta > 0.05$. $\text{Na}_{0.49}\text{BT}$ has the lowest dielectric loss of less than 0.005 across a temperature range of $300\text{-}600^\circ\text{C}$. $\text{Na}_{0.49}\text{BT}$ also has the lowest relative permittivity of 2700. As the Na content increases, the relative permittivity also increases: NBT has $\epsilon_{r,\text{max}}$ of 3000 and $\text{Na}_{0.51}\text{BT}$ has the highest value of 3200 with T_m at 315°C .

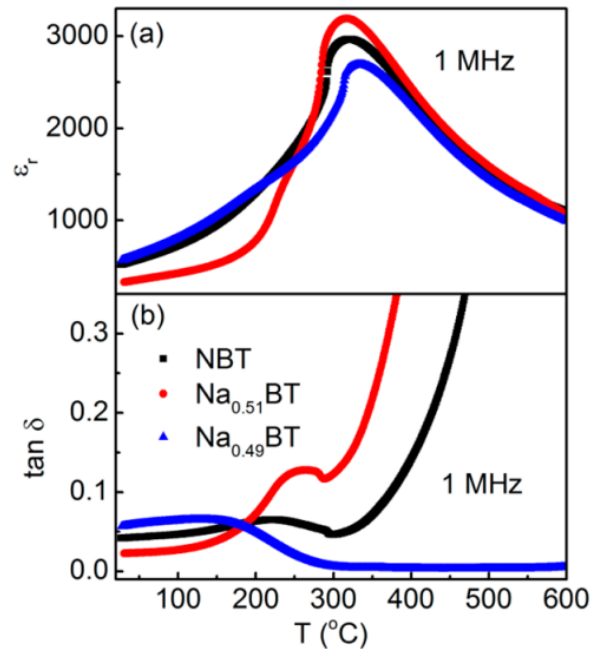


Figure 2.29. Temperature dependence of (a) ϵ_r and (b) $\tan \delta$ at 1 MHz for NBT, Na_{0.51}BT, and Na_{0.49}BT [56].

Results from P-E hysteresis loops agree with the trend discovered in the dielectric loss of nonstoichiometric NBT. Samples with Na-deficient and/or Bi-rich compositions show lower remnant polarisation whereas samples with Na-rich and/or Bi-deficient compositions fail to reach a saturated state due to high leakage current [79] [80]. The results are presented in Figure 2.30.

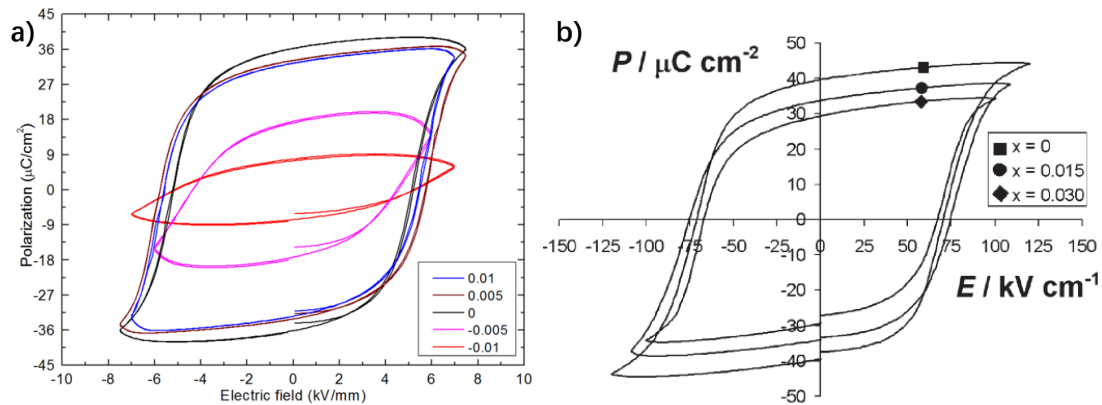


Figure 2.30. Polarisation-Electric field hysteresis loops for a) $\text{Na}_{(0.5-x)}\text{Bi}_{(0.5+x)}\text{TiO}_{(3+x)}$ and b) $\text{Na}_{0.5-x}\text{Bi}_{0.5}\text{TiO}_{3-x/2}$. [80] [79]

As a dielectric material, NBT's biggest issue is the high current leakage, due to its high intrinsic oxide-ion conductivity, which has been discussed in the previous section. In addition, stoichiometric NBT's d_{33} value is around 100 pC/N, compared to 500 pC/N of Lead Zirconate-Titanate (PZT) which is widely used in industry. The piezoelectric properties of NBT are clearly inferior to that of PZT [81]. Still, prior to the discovery of NBT's oxide ion conductivity by Li et al, NBT received most of its research attention as a possible lead-free piezoelectric material to replace PZT, because PbO's production and utilization involves health concerns [82].

2.7 Multi-layer ceramic capacitors

Multi-layer ceramic capacitors (MLCC) are a type of capacitor made by stacking multiple thin layered dielectric materials with internal electrodes in parallel and then contacted via terminal surfaces. An illustration of the internal structure of an MLCC is shown in Figure 2.31.

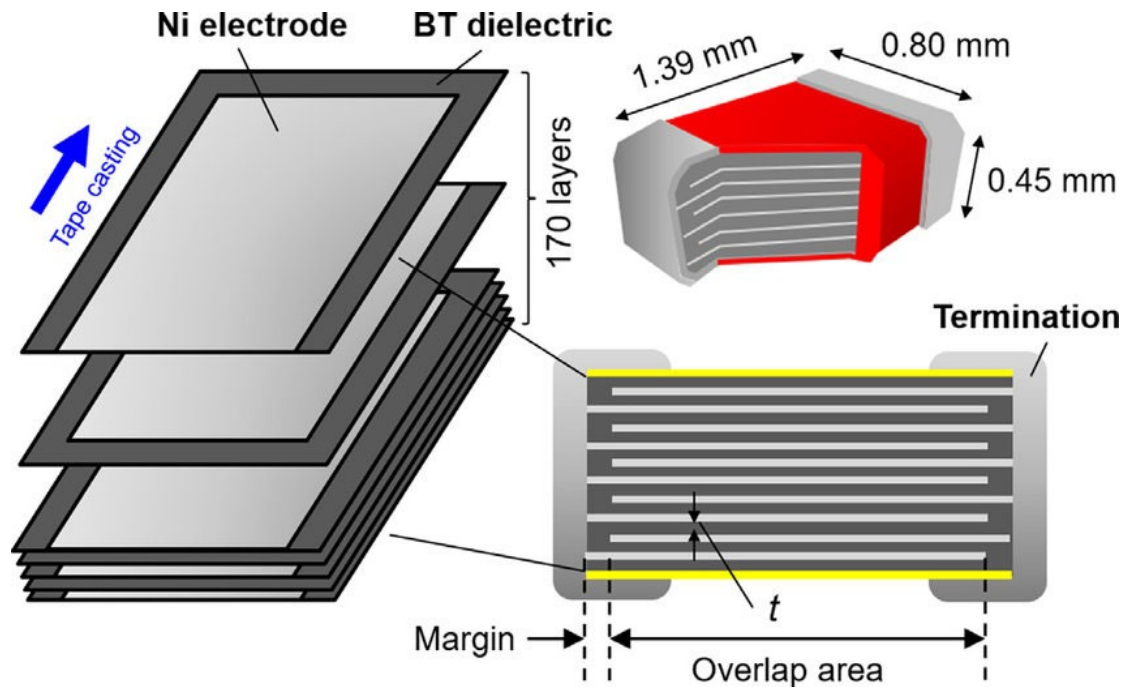


Figure 2.31. Schematic illustration of the internal structure within an MLCC using BaTiO_3 as the dielectric material [83].

Multiple steps are required to manufacture MLCCs, an illustration is given in Figure 2.32. The ceramic slurry is first prepared by mixing dielectric powder with solvents, dispersant, plasticizers and binders. The homogenous suspension is then tape cast into a thin sheet of uniform thickness. Electrode paste is screen printed on the dried thin sheet with designed patterns. The printed layers are stacked together and pressure is applied to the stack for lamination. After dicing and cutting, the green MLCCs will burn out the organic binder and plasticizers first, then during the sintering stage the dielectric layers and metal electrodes form a dense body. The last step is applying metal terminations on the two opposing ends on the MLCC to allow the internal electrodes to be connected to external circuits [84].

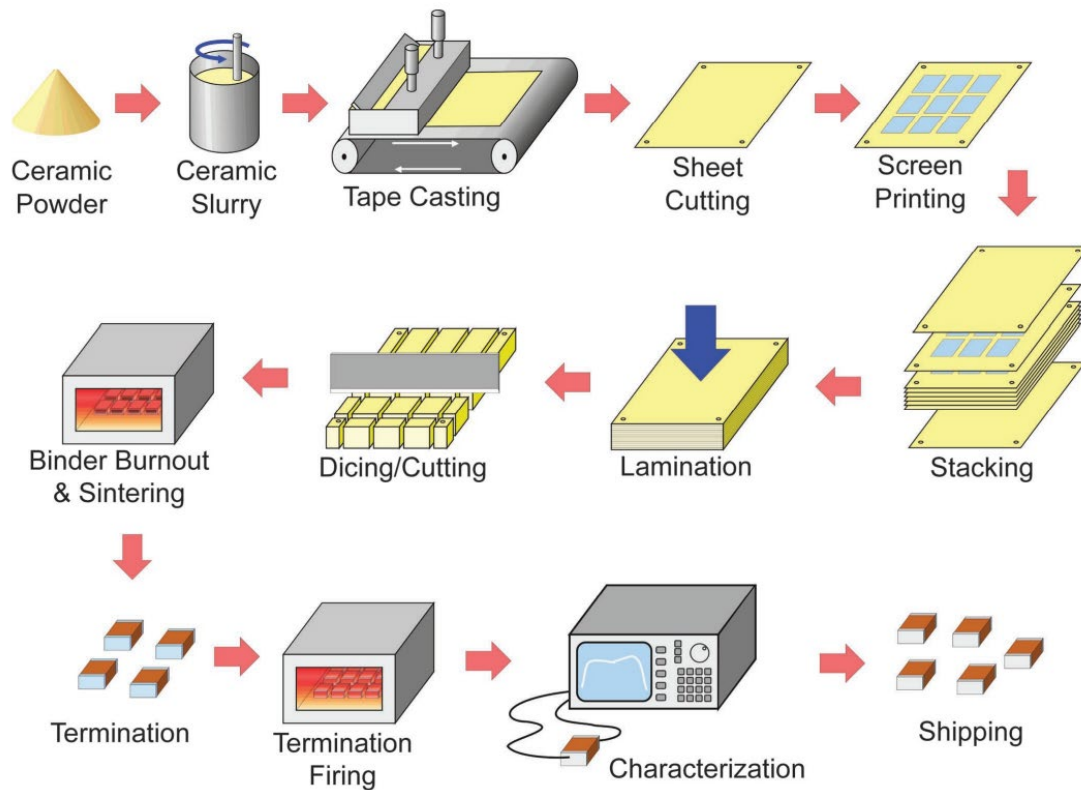


Figure 2.32. A schematic illustration of steps to fabricate MLCCs [84].

Modern electronic industry demands the miniaturization of MLCCs. This can be achieved by reducing the thickness of the dielectric material and/or increasing the permittivity of the dielectric material.

One of the major dielectric materials used in MLCCs is rare-earth doped BaTiO_3 . These dopants have ionic radii that are intermediate between Ba and Ti, such as Dy, Y and Ho [85] [86] [87] [88] [89] [90]. These elements can fit into both the A and B sites. This is called the donor-acceptor rare earth-doping mechanism, which can induce two major improvements in MLCCs, high resistance and long service life [91] [92] [93]. High resistance allows MLCC layers to be reduced in thickness. Another benefit is the oxygen vacancy concentration is reduced, since donor (A site) and acceptor (B site) doping happens at the same time, self-compensation does not create additional oxygen vacancies, preventing oxygen ion conduction occur in the dielectric material, achieving good electrical insulation. A typical material used in MLCCs is $\text{BaTiO}_3\text{-MgO-R}_2\text{O}_3$, where R is a rare earth ion [94] [84]. Besides the BT based family of materials, other series of ceramics also attract intense research attention, such as those based on $\text{K}_{0.5}\text{Na}_{0.5}\text{NbO}_3$, BiFeO_3 , AgNbO_3 and NaNbO_3 . $\text{Na}_{0.5}\text{Bi}_{0.5}\text{TiO}_3$ has also showed great potential to be used as a dielectric material, the distorted perovskite structure naturally favours large polarization. The drawback of NBT in dielectric applications, as mentioned above, is the high leakage and novel doping methods are needed to improve the breakdown strength of NBT for successful capacitor applications [95].

2.8. Solid Oxide Fuel Cells

Solid Oxide Fuel Cells (SOFC) are a type of electrochemical conversion device that generates electricity from the oxidation of various fuel types. Since it is not an Internal Combustion Engine (ICE), its overall efficiency in the generation of electricity is not limited by the Carnot cycle. If combined with gas turbines to utilize the hot exhaust gas of the cell, a SOFC-turbine system can reach an overall efficiency of ~ 80% [96].

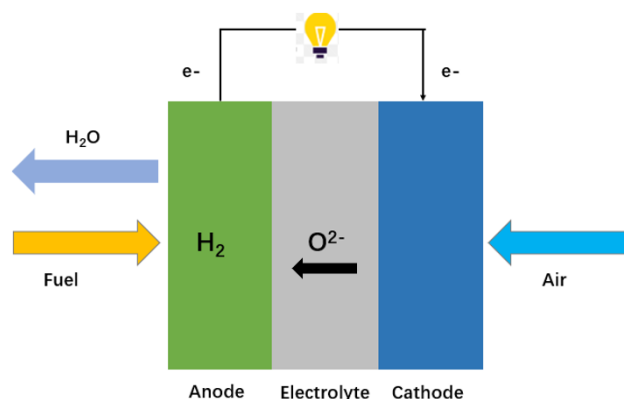
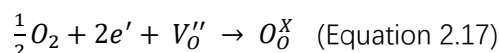
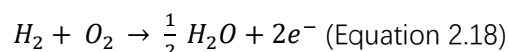


Figure 2.33 Basic schematic structure of a Solid Oxide Fuel Cell.

A typical SOFC consists of three different layers, an anode, cathode and electrolyte, as shown in Figure 2.33. The cathode's role is to reduce oxygen molecules from air into oxide ions as shown in Equation 2.17. The material used in the cathode should be a mixed conductor of electrons/holes and oxide-ions in order to fulfil its role. Currently, Lanthanum Strontium Manganite (LSM) is used commercially to manufacture SOFC stacks, mainly due to its thermal expansion coefficient matching well with zirconia-based electrolytes and it remains chemically non-reactive with the electrolyte at the operating temperature [97].



The electrolyte serves as an oxide-ion conductor that allows the oxide-ions generated at the cathode to diffuse towards the anode for a complete reaction cycle. The electronic conductivity of the electrolyte should be minimal so that no internal short circuit occurs. Yttria-stabilized Zirconia (YSZ), Scandia stabilized Zirconia (ScSZ) and Gadolinium doped Ceria (GDC) are the common materials used in commercial grade SOFCs [98]. The anode is where the oxide-ions and fuel react, producing water as a by-product, as shown in Equation 2.18. Common material used today is a mixture of Nickel metal particles and a YSZ ceramic matrix [97].



The SOFC could also serve as an auxiliary power unit (APU) in mobile applications, such as heavy-duty trucks and airplanes, prototypes of such APUs have been put into field test [99] [100]. However, many challenges must be addressed before full scale commercialization can occur.

One of the biggest challenges is the low power density of the fuel cell stack. The components in commercial grade SOFCs are chosen as a balance between performance and service life time, yet the conductivity of the ceramic layers within the SOFC is the bottleneck that limits

the overall power density of the SOFC. High power density ceramics with high oxide-ion conductivity must be used in order to compete with proton-exchange membrane fuel cells (PEMFC). Another challenge is the high operation temperature (800 °C) of SOFCs. The high operating temperature is needed for the oxide-ion conductors to have enough energy to overcome the activation energy, yet it disables the possibility of rapid start-up and shut down, which is a crucial feature required in any mobile application. Researchers have been dedicated to discover intermediate temperature SOFCs that operate at lower temperatures, typically between 500 – 700 °C [99] [97].

The literature review itself can be grouped into two major sections: (i) micro-contact impedance spectroscopy and finite element modelling; and (ii) experimental work on NBT based materials. The results chapters in this thesis also consists of two major sections, corresponding to the literature review here. For the first section (Chapter 4), experimental work was conducted on NBT based solid solutions. This was an attempt to increase the oxide ion conductivity or achieve low current leakage, creating NBT based materials with the required properties for applications. Furthermore, an attempt to establish the trapping power of Mg and Zn ions in NBT based solid solutions. For the second section (Chapters 5 -7), various finite element models were created and mc-IS data simulated to determine the bulk and/or surface layer electrical properties, in order to gain a better understanding of how crack-like features can affect the measured (experimental) results from mc-IS.

2.9 References

- [1] K. S. Cole and R. H. Cole, "Dispersion and absorption in dielectrics I. Alternating current characteristics," *J. Chem. Phys.*, 9, pp.341–351, 1941.
- [2] J. E. Bauerle, "Study of solid electrolyte by a complex admittance," *J. Phys. Chem. Solids*, 30, pp. 2657–2670, 1969.
- [3] N. M. Beekmans and L. Heyne, "Correlation Between Impedance, Microstructure and Composition of Calcia-Stabilized Zirconia," *Electrochim*, 21, pp. 303–310, 1976.
- [4] R. A. Veazey, "Probing Radiation Damage in Fe-doped SrTiO₃ using Micro-contact Impedance Spectroscopy," PhD Thesis, The University of Sheffield, 2019.
- [5] A. Chaouchi and S. Kennour, "Impedance spectroscopy studies on lead free (Ba_{0.85}Ca_{0.15})(Ti_{0.9}Zr_{0.1})O₃ ceramics," *Processing and Application of Ceramics*, 6 [4] pp. 201–207, 2013.
- [6] N. J. Kidner, N. H. Perry, T. O. Mason and E. J. Garboczi, "The brick layer model revisited: Introducing the nano-grain composite model.," *J. Am. Ceram. Soc.*, 91, pp. 1733–1746., 2008.
- [7] J. Fleig and J. Maier, "A Finite Element Study on the Grain Boundary Impedance of Different Microstructures," *J. Electrochem. Soc*, 145, p. 2081, 1998.
- [8] J. Fleig, "Impedance spectroscopy on solids: The limits of serial equivalent circuit models," *J. Electroceramics*, 13, pp. 637–644, 2004.
- [9] P. Heath, J. S. Dean, J. H. Harding and D. C. Sinclair, "Simulation of Impedance Spectra for Core-Shell Grain Structures Using Finite Element Modeling.," *J. Am. Ceram Soc*, 98, pp. 1925–1931, 2015.

- [10] J. S. Dean, J. H. Harding and D. C. Sinclair, "Simulation of Impedance Spectra for a Full Three-Dimensional Ceramic Microstructure Using a Finite Element Model.," *J. Am. Ceram. Soc.*, 97, pp. 885-891, 2014.
- [11] J. Fleig, "Local conductivity measurements on AgCl surfaces using microelectrodes.," *Solid State Ionics*, 85, pp. 9-15, 1996.
- [12] R. Holm, *Electric Contacts*, Springer, 1967.
- [13] J. Fleig, in *Advances in Electrochemical Science and Engineering*, Wiley-VCH, 2002, pp. 1-79.
- [14] J. Fleig, "Microelectrodes in solid state ionics.," *Solid State Ionics*, 161, pp. 279-289, 2003.
- [15] H. Lauret and A. Hammou, "Localization of oxygen cathodic reduction zone at lanthanum manganite/zirconia interface.," *J. Eur. Ceram. Soc.*, 16, pp. 447-451, 1996.
- [16] S. Rodewald, J. Fleig and J. Maier, "Microcontact Impedance Spectroscopy at Single Grain Boundaries in Fe-Doped SrTiO₃ Polycrystals.," *J. Am. Ceram. Soc.*, 84, pp. 521-530, 2001.
- [17] GBITest, [Online]. Available: <http://www.gbit.net.cn/index.php?c=show&id=86>. [Accessed 20 11 2020].
- [18] A. K. Opitz and J. Fleig, "Investigation of O₂ reduction on Pt/YSZ by means of thin film microelectrodes: The geometry dependence of the electrode impedance," *Solid State Ionics*, 181, pp. 684-693, 2010.
- [19] T. M. Hube, A. K. Opitz, M. Kubicek, H. Hutter and J. Fleig, "Temperature gradients in microelectrode measurements: Relevance and solutions for studies of SOFC electrode materials.," *Solid State Ionics*, 268, pp. 82-93, 2014.
- [20] R. A. Veazey, A. S. Gandy, D. C. Sinclair and J. S. Dean, "Modeling the influence of two terminal electrode contact geometry and sample dimensions in electro-materials," *J. Am. Ceram. Soc.*, 102 (6), pp. 3609-3622, 2018.
- [21] R. A. Veazey, A. S. Gandy, D. C. Sinclair and J. S. Dean, "Finite element modeling of resistive surface layers by micro-contact impedance spectroscopy.," *J Am Ceram Soc.*, 103, pp. 2702- 2714, 2020.
- [22] S. Rodewald, J. Fleig and J. Maier, "Measurement of conductivity profiles in acceptor doped strontium titanate.," *J. Eur. Ceram. Soc.*, 19, pp. 797-801, 1999.
- [23] A. Wachter-Welzl, R. Wagner, D. Rettenwander, S. Taibl, G. Amthauer and J. Fleig, "Microelectrodes for local conductivity and degradation measurements on Al stabilized Li₇La₃Zr₂O₁₂ garnets.," *J. Electroceramics*, 38, pp. 176-181, 2017.
- [24] D. Rettenwande, A. Welzl, S. Pristat, F. Tietz, S. Taibl, G. J. Redhammer and J. Fleig, "A microcontact impedance study on NASICON-type Li_{1+x}Al_xTi_{2-x}(PO₄)₃ (0 ≤ x ≤ 0.5) single crystals.," *J. Mater. Chem. A*, 4, pp. 1506-1513, 2016.
- [25] Z.-J. Yi, N. H. Ladi, X.-X. Shai, H. Li, Y. Shen and M.-K. Wang, "Will organic-inorganic hybrid halide lead perovskites be eliminated from optoelectronic applications?," *Nanoscale Adv*, 1, pp. 1276-1289, 2019.
- [26] K. Graham and P. M. Woodward, "Cation ordering in perovskites," *J. Mater. Chem*, 20, pp. 5785-5796, 2010.
- [27] M. L. López, A. L. Veiga and C. Pico, "Cation ordering in distorted perovskites (MLa)(MgTe)O₆, M = Na, K," *J. Mater. Chem*, 4, pp. 547-550, 1994.

- [28] V. M. Goldschmidt, "Die Gesetze der Krystallochemie," *Naturwissenschaften*, 14, pp. 477–485, 1926.
- [29] A. R. West, *Solid State Chemistry*, John Wiley & Sons, Ltd, 2014.
- [30] A. M. Glazer, "The classification of tilted octahedra in perovskites," *Acta Crystallogr. Sect. B Struct. Crystallogr. Cryst. Chem*, 28, pp. 3384–3392., 1972.
- [31] A. M. Glazer, "Simple ways of determining perovskite structures," *Acta Crystallogr. Sect. A*, 31, pp. 756–762, 1975.
- [32] K. J. Pascoe, *Properties of Materials for Electrical Engineers*, New York, N.Y.: J. Wiley and Sons, 1973.
- [33] G. H. Haertling, "Ferroelectric ceramics: history and technology," *J. Am. Ceram. Soc*, 82, p.797, 1999.
- [34] A. J. Moulson and J. M. Herbert, *Electroceramics - Materials, Properties, Applications*, London, UK: Chapman & Hall, 1990.
- [35] D.-H. Yoon, "Tetragonality of barium titanate powder for a ceramic capacitor application," *J. Ceram. Process. Res*, pp. 7, 343–354, 2006.
- [36] J. Ravez, "Ferroelectricity in solid state chemistry," *C. R. Acad. Sci. Paris. Ser. IIC, Chim./Chem.*, 3, pp. 267–283., 2000.
- [37] Y. C. Shu and K. Bhattacharya, "Domain patterns and macroscopic behaviour of ferroelectric materials.," *Philos. Mag. B*, 81, pp. 2021–2054, 2001.
- [38] K. Muhsen, R. Osman and M. S. Idris, "The effects of Ca, Zr and Sn substitutions into a ternary system of BaTiO₃–BaSnO₃–BaZrO₃ towards its dielectric and piezoelectric properties: a review," *Journal of Materials Science: Materials in Electronics*, 27. p. 10.1007, 2021.
- [39] E. C. Subbarao, M. C. McQuarrie and W. R. Buessem, "Domain Effects in Polycrystalline Barium Titanate," *J. Appl. Phys*, 28, pp. 1194–1200, 1957.
- [40] T. Hiramatsu, T. Tamura, N. Wada, H. Tamura and Y. Sakabe, "Effects of grain boundary on dielectric properties in fine-grained BaTiO₃ ceramics," *Mater. Sci. Eng.B*, 120, pp. 55–58, 2005.
- [41] P. Potnis, N.-T. Tsou and J. Huber, "A Review of Domain Modelling and Domain Imaging Techniques in Ferroelectric Crystals," *Materials*, 4, pp. 417–447, 2011.
- [42] J. G. Webster, *The Measurement, Instrumentation, and Sensors Handbook*, Boca Raton, FL: CRC Press published in cooperation with IEEE Press, 1999.
- [43] M. Shandilya, R. Rai, A. Zeb and S. Kumar, "Modification of structural and electrical properties of Ca element on barium titanate nano-material synthesized by hydrothermal method," *Ferroelectrics*, 520(1), pp. 93-109, 2017.
- [44] N. Wongdamnern, K. Kanchiang, A. Ngamjarrojana, S. Ananta, Y. Laosiritaworn, A. Charoenphakdee, S. Gupta, S. Priya and R. Yimnirun, "Crystal-structure dependent domain-switching behavior in BaTiO₃," *Smart Mater. Struct.*, 23, p. 085022, 2014.
- [45] T. Lee and I. A. Aksay, "Hierarchical structure– ferroelectricity relationships of barium titanate particles," *Cryst. Growth Des*, 1, pp. 401–419, 2001.
- [46] V.-o. Do, D.-v. Le, V.-c. Truong, A.-q. Dao and T.-t. Vo, "Study on the synthesis and application of BaTiO₃ nanospheres," *International Journal of Materials Research*, 112(6), pp. 448-456, 2021.
- [47] B. C. Steele and A. Heinzl, "Materials for fuel-cell technologies," *Nature*, 414, pp. 345–

352, 2001.

- [48] E. D. Wachsman and K. T. Lee, "Lowering the Temperature of Solid Oxide Fuel Cells," *Science*, 334, pp. 935–939, 2011.
- [49] T. Ishihara, "Oxide ion conductivity in defect perovskite, Pr_2NiO_4 and its application for solid oxide fuel cells," *Journal of the Ceramic Society of Japan*, 122, pp. 179–186, 2014.
- [50] S. J. Skinner and J. A. Kilner, "Oxygen ion conductors," *Mater. Today*, 6, pp. 30–37, 2003.
- [51] V. Butler, C. R. Catlow, B. E. Fender and J. H. Harding, "Dopant ion radius and ionic conductivity in cerium dioxide," *Solid State Ionics*, 8, pp. 109–113, 1983.
- [52] L. Minervini, "Defect cluster formation in M_2O_3 -doped CeO_2 ," *Solid State Ionics*, 116, pp. 339–349, 1999.
- [53] B. C. Steele, "Oxygen ion conductors and their technological applications," *Mater. Sci. Eng. B*, 13, pp. 79–87, 1992.
- [54] J. Kilner, "Fast oxygen transport in acceptor doped oxides," *Solid State Ionics*, 129, pp. 13–23, 2000.
- [55] K. Huang, "Electrode Performance Test on Single Ceramic Fuel Cells Using as Electrolyte Sr- and Mg-Doped LaGaO_3 ," *J. Electrochem. Soc.*, 144, pp. 3620–3624, 1997.
- [56] M. Li, H. Zhang, S. N. Cook, L. Li, J. A. Kilner, I. M. Reaney and D. C. Sinclair, "Dramatic Influence of A-Site Nonstoichiometry on the Electrical Conductivity and Conduction Mechanisms in the Perovskite Oxide $\text{Na}_{0.5}\text{Bi}_{0.5}\text{TiO}_3$," *Chem. Mater*, 27, pp. 629–634, 2015.
- [57] M. Li, M. J. Pietrowski, R. A. De Souza, H. Zhang, S. N. Cook, J. A. Kilner and D. C. Sinclair, "A family of oxide ion conductors based on the ferroelectric perovskite $\text{Na}_{0.5}\text{Bi}_{0.5}\text{TiO}_3$," *Nat. Mater.*, 13, pp. 31–51, 2014.
- [58] G. A. Smolenskii, V. A. Isupov, A. I. Agranovskaya and N. N. Krainik, "New ferroelectrics with complex compounds IV," *Soviet Phys. -Solid State*, 2, pp. 2651–2654, 1961.
- [59] I. Levin and I. M. Reaney, "Nano- and Mesoscale Structure of $\text{Na}_{1/2}\text{Bi}_{1/2}\text{TiO}_3$: A TEM Perspective," *Adv. Funct. Mater*, 22, pp. 3445–3452, 2012.
- [60] V. Dorcet, G. Trolliard and P. Boullay, "Reinvestigation of Phase Transitions in $\text{Na}_{0.5}\text{Bi}_{0.5}\text{TiO}_3$ by TEM . Part I : First Order Rhombohedral to Orthorhombic Phase Transition," *Chem. Mater*, 20, pp. 5061–5073, 2008.
- [61] G. Trolliard and V. Dorcet, "Reinvestigation of Phase Transitions in $\text{Na}_{0.5}\text{Bi}_{0.5}\text{TiO}_3$ by TEM. Part II : Second Order Orthorhombic to Tetragonal Phase Transition," *Chem. Mater*, 20, pp. 5074–5082, 2008.
- [62] H. Nagata, "Electrical properties and tracer diffusion of oxygen in some Bi-based lead-free piezoelectric ceramics," *J. Ceram. Soc. Japan*, 116, pp. 271–277, 2008.
- [63] Y. S. Sung, J. M. Kim, J. H. Cho, T. K. Song, M. H. Kim and T. G. Park, "Effects of Bi nonstoichiometry in $(\text{Bi}_{0.5+x}\text{Na})\text{TiO}_3$ ceramics," *Appl. Phys. Lett*, 98, p. 012902, 2011.
- [64] L. Li, "Oxide Ion Conduction in A-site Bi-containing Perovskite-type Ceramics," Thesis presented for the degree of doctor of philosophy, University of Sheffield, 2016.
- [65] F. Yang, M. Li, L. Li, P. Wu, E. Pradal-Velázquez and D. C. Sinclair, "Review: Defect chemistry and electrical properties of sodium bismuth titanate perovskite," *J. Mater. Chem. A*, 6, pp. 5243–5254, 2018.
- [66] S. Islam, "Ionic transport in ABO_3 perovskite oxides: a computer modelling tour," *J. Mater. Chem*, 10, pp. 1027–1038., 2000.
- [67] X.-F. He and Y.-F. Mo, "Accelerated Materials Design of $\text{Na}_{0.5}\text{Bi}_{0.5}\text{TiO}_3$ Oxygen Ionic

- Conductors Based on First Principles Calculations," *Phys. Chem. Chem. Phys.*, 17, pp. 18035–18044, 2015.
- [68] Y. R. Luo, *Comprehensive Handbook of Chemical Bond Energies*, Boca Raton: CRC Press, 2017.
- [69] F. Yang, M. Li, L. Li, P. Wu, E. Pradal-Velázquez and D. C. Sinclair, "Optimisation of oxide-ion conductivity in acceptor-doped $\text{Na}_{0.5}\text{Bi}_{0.5}\text{TiO}_3$ perovskite: Approaching the limit?," *J. Mater. Chem. A*, 5, pp. 21658–21662, 2017.
- [70] R. A. De Souza, "Oxygen Diffusion in SrTiO_3 and Related Perovskite Oxides," *Adv. Funct. Mater.*, 25, pp. 6326–6342, 2015.
- [71] Y. Yasuhiro, S. Hiroyuki, Y. Kenji and N. Takashi, "Growth and Characterization of Bismuth Magnesium Titanate $\text{Bi}(\text{Mg}_{1/2}\text{Ti}_{1/2})\text{O}_3$," *Key Engineering Materials*, 421–422, pp. 30–33, 2010.
- [72] A. A. Belik, T. Wuernisha, T. Kamiyama, K. Mori, T. Nagai, M. Male, Y. Matsui and E. Takayama-Muromachi, "High-pressure synthesis, crystal structures, and properties of perovskite-like BiAlO_3 and pyroxene-like BiGaO_3 ," *Chem. Mater.*, 18, pp. 133–139, 2006.
- [73] A. A. Belik, T. Yokosawa, K. Kimoto and Y. Matsui and E. Takayama-Muromachi, "High-Pressure Synthesis and Properties of Solid Solutions between BiMnO_3 and BiScO_3 ," *Chem. Mater.*, 19, pp. 1679–1689, 2007.
- [74] H. Nagata and T. Takenaka, "Lead-free piezoelectric ceramics of $(\text{Bi}_{1/2}\text{Na}_{1/2})\text{TiO}_3$ -1/2. $(\text{Bi}_2\text{O}_3$ center dot Sc_2O_3) system," *Jpn. J. Appl. Phys.*, 36, pp. 6055–6057, 1997.
- [75] H. Yu and Z.-g. Ye, "Dielectric, ferroelectric, and piezoelectric properties of the lead-free $(1-x)(\text{Na}_{0.5}\text{Bi}_{0.5}\text{TiO}_3-x\text{BiAlO}_3$ solid solution," *Appl. Phys. Lett.*, 93, p. 112902, 2008.
- [76] F. Yang, P. Wu and D. C. Sinclair, "Suppression of electrical conductivity and switching of conduction mechanisms in stoichiometric' $(\text{Na}_{0.5}\text{Bi}_{0.5}\text{TiO}_3)_{1-x}(\text{BiAlO}_3)_x$ ($0 < x < 0.08$) solid solutions," *J. Mater. Chem. C*, 5, pp. 7243–7252, 2017.
- [77] E. Pradal-Velázquez, "Structure-property relations in Sodium-Bismuth Titanate related materials," Phd Thesis, University of Sheffield, 2019.
- [78] F. Yang, J. S. Dean, Q.-d. Hu, P. Wu, E. Pradal-Velázquez, L. Li and D. C. Sinclair, "From insulator to oxide-ion conductor by a synergistic effect from defect chemistry and microstructure: acceptor-doped Bi-excess sodium bismuth titanate $\text{Na}_{0.5}\text{Bi}_{0.51}\text{TiO}_{3.015}$," *J. Mater. Chem. A*, 8, pp. 25120, 2020.
- [79] J. Carter, E. Aksel, T. Iamsasri, J. Forrester, J. Chen and J. L. Jones, "Structure and ferroelectricity of nonstoichiometric $(\text{Na}_{0.5}\text{Bi}_{0.5})\text{TiO}_3$," *Appl. Phys. Lett.*, 104, pp. 0–4, 2014.
- [80] M. Spreitzer, M. Valant and D. Suvorov, "Sodium deficiency in $\text{Na}_{0.5}\text{Bi}_{0.5}\text{TiO}_3$," *J. Mater. Chem.*, 17, pp. 185–192, 2007.
- [81] J. Rödel, W. Jo, K. T. Seifert, E. M. Anton, T. Granzow and D. Damjanovic, "Perspective on the development of lead-free piezoceramics," *J. Am. Ceram. Soc.*, 92, pp. 1153–1177, 2009.
- [82] S. O. Leontsev and R. E. Eitel, "Progress in engineering high strain lead-free piezoelectric ceramics," *Sci. Technol. Adv. Mater.*, 11, pp. 044302, 2011.
- [83] G. Okuma, N. Saito, K. Mizuno, Y. Iwazaki, H. Kishi, A. Takeuchi, M. Uesugi, K. Uesugi and F. Wakai, "Microstructural evolution of electrodes in sintering of multi-layer ceramic capacitors (MLCC) observed by synchrotron X-ray nano-CT," *Acta Materialia*, 206, p. 116605. 10.1016, 2021.

- [84] M.-J. Pan, "A Brief Introduction to Ceramic Capacitors," *Electrical Insulation Magazine*, IEEE, 26, pp. 44 - 50, 2010.
- [85] K.-j. Park, C.-h. Kim, Y.-j. Yoon, S.-m. Song, Y.-t. Kim and K.-h. Hur, "Doping behaviors of dysprosium, yttrium and holmium in BaTiO₃ ceramics," *J. Eur. Ceram. Soc*, 29, pp. 1735–1741, 2009.
- [86] C.-H. Kim, K.-J. Park, Y.-J. Yoon, M.-H. Hong, J.-O. Hong and K.-H. Hur, "Role of yttrium and magnesium in the formation of core-shell structure of BaTiO₃ grains in MLCC," *J. Eur. Ceram. Soc*, 28, pp. 1213–1219, 2008.
- [87] Z. Tian, X. Wang, H. Gong, T.-H. Song, K. H. Hur and L. Liz, "Core-shell structure in nanocrystalline modified BaTiO₃ dielectric ceramics prepared by different sintering methods," *J. Am. Ceram. Soc.*, 94, pp. 973–977, 2011.
- [88] H. Kishi, N. Kohzu, J. Sugino, H. Ohsato, Y. Iguchi and T. Okuda, "The effect of rare-earth (La, Sm, Dy, Ho and Er) and Mg on the microstructure in BaTiO₃," *J. Eur. Ceram. Soc.*, 19, pp. 1043–1046, 1999.
- [89] J. Nishikawa, T. Hagiwara, K. Kobayashi, Y. Mizuno and H. Kishi, "Effects of microstructure on the Curie temperature in BaTiO₃-Ho₂O₃-MgO-SiO₂ system," *Jpn. J. Appl. Phys., Part 1*, 46, pp. 6999–7004, 2007.
- [90] C.-C. Chou, C.-S. Chen, I. N. Lin, W.-C. Yang and H.-F. Cheng, "Development of X7R type base-metal-electroded BaTiO₃ capacitor materials by Co-doping of MgO/Y₂O₃ additives," *Ferroelectrics*, 332, pp. 35–39, 2006.
- [91] H. Kishi, Y. Mizuno and H. Chazono, "Base-metal electrode-multilayer ceramic capacitors: Past, present and future perspectives," *Jpn. J. Appl. Phys*, 42, pp. 1-15, 2003.
- [92] H. J. Hagemann and D. Hennings, "Reversible Weight Change of Acceptor-Doped BaTiO₃," *J. Am. Ceram. Soc*, 64, pp. 590–594, 1981.
- [93] K. Albertsen, D. Hennings and O. Steigelmann, "Donor-Acceptor Charge Complex Formation in Barium Titanate Ceramics: Role of Firing Atmosphere," *J. Electroceramics*, 2, pp. 193–198, 1998.
- [94] H. Saito, H. Chazono, H. Kishi and N. Yamaoka, "X7R Multilayer Ceramic Capacitors with Nickel Electrodes," *Jpn. J. Appl. Phys*, pp. 2307-2310, 1991.
- [95] P.-Y. Zhao, Z.-M. Cai, L.-W. Wu, C.-Q. Zhu and L.-T. Li, "Perspectives and challenges for lead-free energy-storage multilayer ceramic capacitors," *J Adv Ceram*, 10, pp. 1153–1193, 2021.
- [96] Y. Kobayashi, K. Tomida, M. Nishiura, K. Hiwatashi and K. Takenobu, "Development of Next-Generation Large-Scale SOFC toward Realization of a Hydrogen Society," *Mitsubishi Heavy Industries Technical Review*, 52, 2, pp. 111-114, 2015.
- [97] F. Tietz, "Solid Oxide Fuel Cells," in *Encyclopedia of Materials: Science and Technology (Second Edition)*, pp. 1-8, 2008.
- [98] L. Rose, M. Menon, K. Kammer, O. Kesler and P. H. Larsen, "Processing of Ce_{1-x}Gd_xO_{2-δ} (GDC) thin films from precursors for application in solid oxide fuel cells," *Advanced Materials Research*, 15–17, pp. 293–298, 2006.
- [99] M. D. Fernades, S. T. P. Andrade, V. N. Bistrizki, R. M. Fonseca, L. G. Zacarias, H. N. Goncalves, A. F. Castro, R. Z. Domingues and T. Matencio, "SOFC-APU systems for aircraft: A review," *International Journal of Hydrogen Energy*, 43(33), pp. 16311-16333, 2018.
- [100] J. Rechberger, A. Kaupert, J. Hagerskans and L. Blum, "Demonstration of the First

European SOFC APU on a Heavy Duty Truck," *Transportation Research Procedia*, pp. 3676-3685, 2016.

- [101] A. V. Pushkarev, N. M. Olekhovich and Y. V. Radyush, "High-pressure $\text{Bi}(\text{Mg}_{1-x}\text{Zn}_x)_{1/2}\text{Ti}_{1/2}\text{O}_3$ perovskite solid solutions," *Inorg. Mater*, 47, pp. 1116–1119, 2011.
- [102] S. Bhandari and B. Kumar, "Effect of Structural Modification by MnO_2 Addition on the Electrical Properties of Lead Free Flux Grown $(\text{Na}_{0.5}\text{Bi}_{0.5})\text{TiO}_3$ - $(\text{K}_{0.5}\text{Bi}_{0.5})\text{TiO}_3$ Single Crystals," *Crystal Growth & Design*, 15, pp. 867–874, 2015.

Chapter 3: Methods

3.1 Finite Element Modelling (FEM)

In its most simplistic form, finite element modelling (FEM) is a method that subdivides a complex problem in space in time, into numerous small, simpler pieces, known as finite elements. Each element is assigned a material property and its behaviour described with comparatively simple, differential, equation known as a governing equation. In a simple example, each element could represent the simulation of current flowing through it using $V=IR$ (Ohm's law). Here the measured current, I from an applied potential different V , is linearly dependent upon the assigned material properties R . The complexity of the governing equation and material properties required, are defined by the physics of the system being simulated.

FEM was originally developed for applications in mechanical, civil, and aeronautical engineering, providing approximate solutions to complex systems through transforming the governing differential equations into a set of linear equations, which can be solved [1] [2].

To simulate dielectric materials, which possess both a resistive and capacitive effect, we use an in-house developed package called ElCer [3]. This package uses a time-domain finite element method based on Maxwell's equations to approximate the electric potential as a function of space and time. This allows the electrical response to be calculated including impedance spectra, electric fields and current density vector maps. The strength of ElCer is its capability of calculating the impedance response of three-dimensional objects such as combinations of irregular grains and grain boundaries along with changes in electrodes configurations. Each region can be assigned electrical properties (conductivity and permittivity) and the effective electrical response predicted without the need for an equivalent circuit or equivalent circuit analysis. An in-depth description of the working mechanism of ElCer can be found in Dean et al [3].

The FEM process requires the design of a three-dimensional system discretised into elements through a process known as meshing. Material properties and boundary conditions are assigned to appropriate volumes and surfaces, resulting in a model that can be solved for its electrical response using our finite element package. The final process is to visualize the resulting information to provide microstructure-property relationships. These processes are discussed in more detail below.

3.2 Three-dimensional model design

The models are drawn and meshed through a scripting process, using the open source CAD software Gmsh [4]. For all the models used in this thesis, they share a basic structure. As shown in Figure 3.1 below, a model is generated of a cube with a side length of $200\ \mu\text{m}$. Two electrodes are formed of radius, $r = 5$ or $10\ \mu\text{m}$. These are placed on the top surface of the cube with separation S .

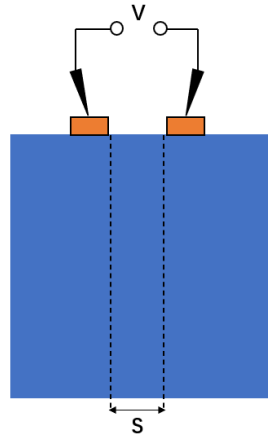


Figure 3.1. Schematic illustration of the basic experimental set up used in this project, side view [5].

At first, a homogenous cube is created with the described dimensions. A crack structure is then placed on the top surface of the model. There are two approaches to simulate the crack. The first is to mesh the crack region and assign it with very high resistivity and low permittivity, simulating air. The second is to remove the volume of material associated with the crack and create a void in the model, which represents it as a complete void. We designate the first approach as a "meshed crack" (MC) and the second as a "physical void crack" (PVC).

The width and depth of the crack can be controlled through variables in the scripting. The total width of the crack is limited to the edge of the electrodes and the maximum depth of crack created is 50 μm from the top surface.

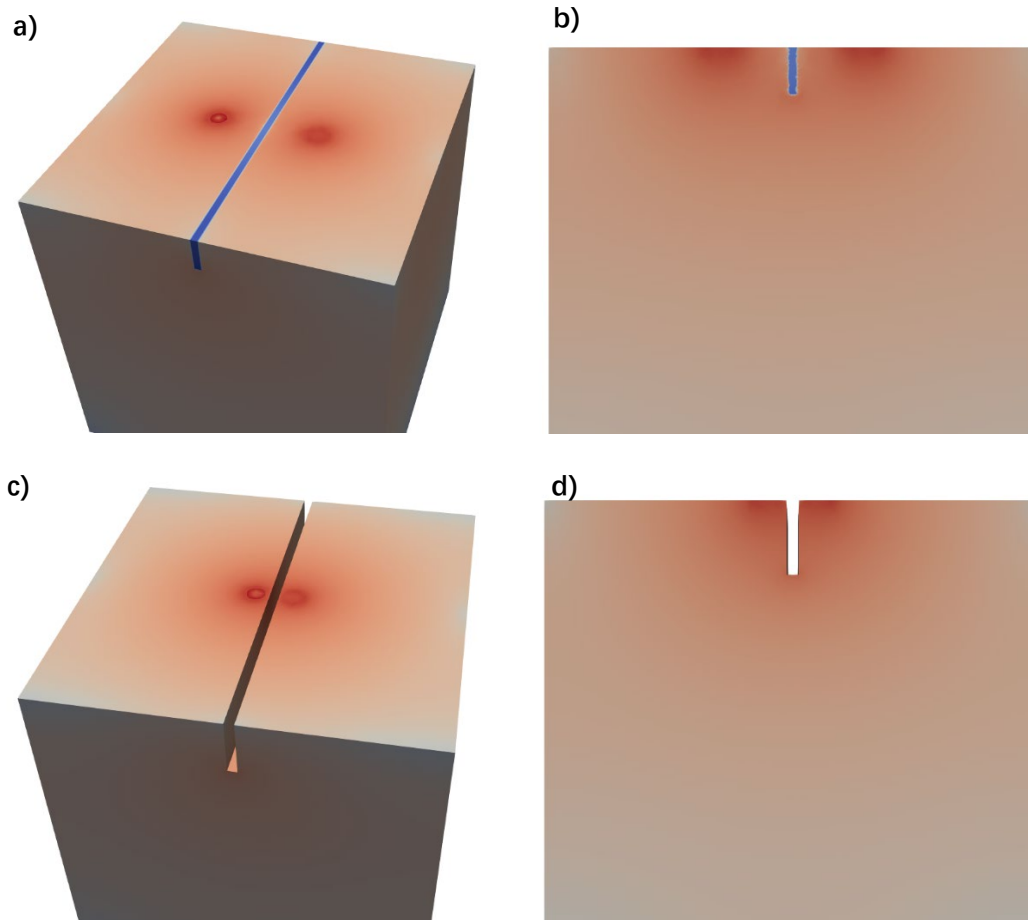


Figure 3.2. Illustration of homogenous cubic model with a meshed and unmeshed crack, MC and PVC models, top and bottom, respectively. Red indicates high current density whereas blue indicates low current density. (a) Angled view of the top surface of a model with a meshed crack. The two dense red circles are micro-contacts, the blue coloured region is a meshed crack with conductivity 1.355×10^9 S/m. (b). Cross section view along the Y axis of the same model in (a). (c), Angled view of the top surface of a model with a physical void crack. (d), Cross section view of the PVC model.

Next, we aim to develop a better method of extracting surface layer conductivity in a two-layer ceramic system. Previous studies [5] based on an amorphous layer developed on single crystals of SrTiO_3 after radiation damage revealed a limited set of solutions on how to accurately calculate conductivity values. At this stage, no crack feature(s) were added to the cubic model but an additional resistive layer was added to fully develop the complexity of the initial two-layer simulations.

To achieve this goal, the homogenous cube is separated into two layers; a surface layer and a bulk layer. The bulk layer has been assigned a conductivity of 1.355×10^{-5} S/m and relative permittivity $\epsilon_r = 162$. These values are obtained by conventional IS data on a SrTiO_3 single crystal measured at a temperature of 300 °C [6]. The surface layer of interest is assigned with varying resistivity values of 2, 5, 10, 100 and 1000 times more resistive than the bulk layer for each model. The permittivity value is set the same as the bulk layer.

Another variable is the thickness of the surface layer, T , which is set at different ratios to the electrode radius, r . An additional volume is placed on top of the surface layer as a reference layer for simulation purposes, which is considered as a pure resistor. The entire model is meshed by Gmsh, with the size of the tetrahedral elements being controlled by various input values.

Finally, after results have been obtained from the homogenous model that contains a crack and the two-layer model with no crack, the model is extended into its final form, a two-layer model with a crack on the surface layer, which fits our assumption of Veazey's experimental measurements. The resistive surface layer's thickness is equal to the depth of the crack, therefore the crack penetrates through the surface layer. The surface layer has an initial conductivity of 1.355×10^{-7} S/m, 100 times less conductive than the bulk material. The relative permittivity of both the bulk and surface layer is 162.

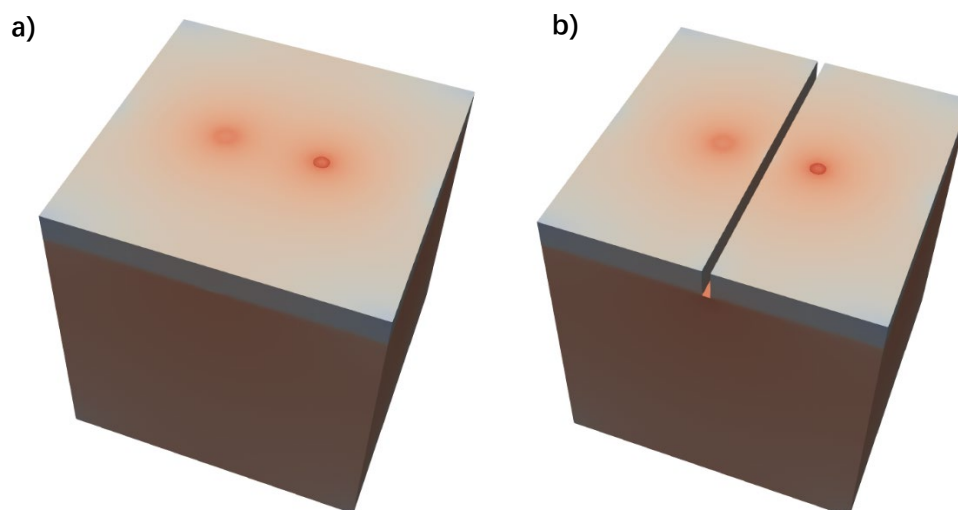


Figure 3.3. Illustration of the 2-layer model with crack region meshed (a) and unmeshed (b). The red circles on the top surface are micro-contacts. The surface layer shows blue/grey colour as it has lower current density than the more conductive (underlying) bulk layer.

3.3 Material properties and Boundary conditions

To be able to solve the model, boundary conditions and material properties are assigned to the surfaces and volumes of the models, respectively. Neumann boundary conditions are applied to the external surfaces, setting the current density on these surfaces to be zero so that a confined environment is constructed and current does not leak out the sides of the mode. The electrode regions are subjected to Dirichlet-type boundary conditions, assigning a time dependent voltage to them. In order to generate an impedance response, a sinusoidal voltage of peak-to-peak amplitude of 0.1 V is assigned to one of the electrodes, whilst the other is assigned as the ground.

For each frequency, a sine wave response of the applied voltage and resulting current is produced. The phase difference between the applied voltage and measured current response from the reference layer mentioned earlier is calculated, along with its magnitude. The

impedance of the material at that particular frequency can be calculated, and a complete impedance spectrum can be constructed by repeating this process over the desired frequency range and by combining the results from each frequency step.

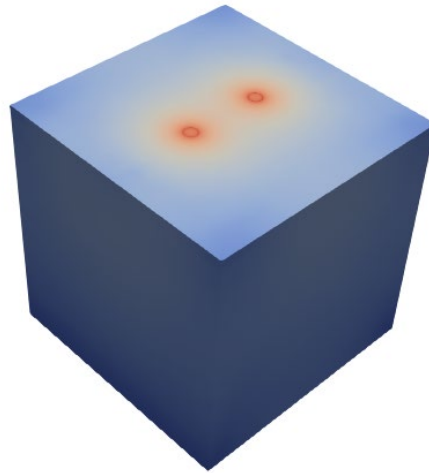


Figure 3.4. Illustration of the boundary conditions. The side line of the cube is 200 μm .

3.4 Discretizing (meshing) the model into elements

To discretize the model into a set of linear equations, the models are divided into tetrahedra. The points of the tetrahedra are commonly known as nodes which connect the vertices of the shape together which in turn is known as an element. To ensure that the model is not dependent on the meshing elements but on the physics of the system a convergence study is performed. Convergence is achieved when a increase in the number of elements or a decrease in the size of the mesh no longer gives changes in the results. In this work, we are interested in the influence of the mesh size in particular regions on the impedance results.

It is reasonable to anticipate that the mesh size of the model has a significant impact on the final generated IS data. The ideal scenario would be to have a very fine mesh over the entire model. A fine mesh would lead to a significantly large number of elements in the system and while the results would converge to a greater precision, there are computational limitations on memory and time. The high performance cluster (HPC)'s work node assigned to simulations has sufficient memory to be able to run models with approximately three million elements. It is therefore crucial to know how and where to assign finer meshed regions in the model to achieve a balance between high simulation accuracy and computational limit.

One solution is to use a Gmsh inbuilt function called a 'mesh attractor'. As shown in Figure 3.5, an attractor has three defining values. The location of the centre point, a length characteristic (L_c) that sets a minimum meshing size, $L_{c_{min}}$ and a maximum $L_{c_{max}}$. These are applied as concentric spheres, where $L_{c_{min}}$ sets the mesh size at the minimum radius, and $L_{c_{max}}$ sets the mesh size at the larger radius. Within this volume the size of mesh gradually decreases from $L_{c_{min}}$ to $L_{c_{max}}$.

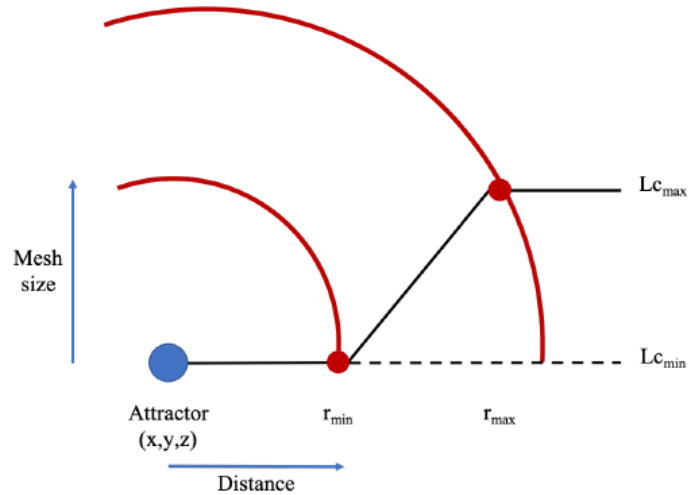


Figure 3.5. Top view illustration of Attractor's set up, the distance between Lc_{max} and Attractor centre is called Distance max, which will be optimised in a convergence study [5].

As the models created can be divided into two categories, with and without cracks, we decided to initially conduct a convergence study of models without a crack. Then to apply the mesh optimisation obtained from the non-cracked model as a foundation for cracked models, as adding a crack into the structure brings complexity into the convergence study.

First, we present how the mesh setting is progressed in the two-layer model without a crack, despite it containing a resistive surface layer, its physical structure is the simplest. It has been reported that in a micro electrode set up, 75% of the current density is located in a zone of 4 times the radius of the micro electrode and centred in the micro electrode [7]. Therefore, attractor centre points are fixed on the top surface's centre point to maximize the number of elements in the high current density zone, leaving the outer region with a coarser mesh. A visual illustration in Figure 3.6 shows how the attractors'-controlled mesh size is varied across the model. A series of 6 attractors with the same centre point location are placed within the model, each attractor has its unique Lc value, as labelled. Attractor 1 (A1) sets the background mesh, which is the coarsest. From Attractor 2 to Attractor 4, the controlled zone gradually moves towards the micro-electrode with decreasing mesh size. Attractors 5 and 6 control the region directly within the electrode's radius and this is the region with the finest mesh size.

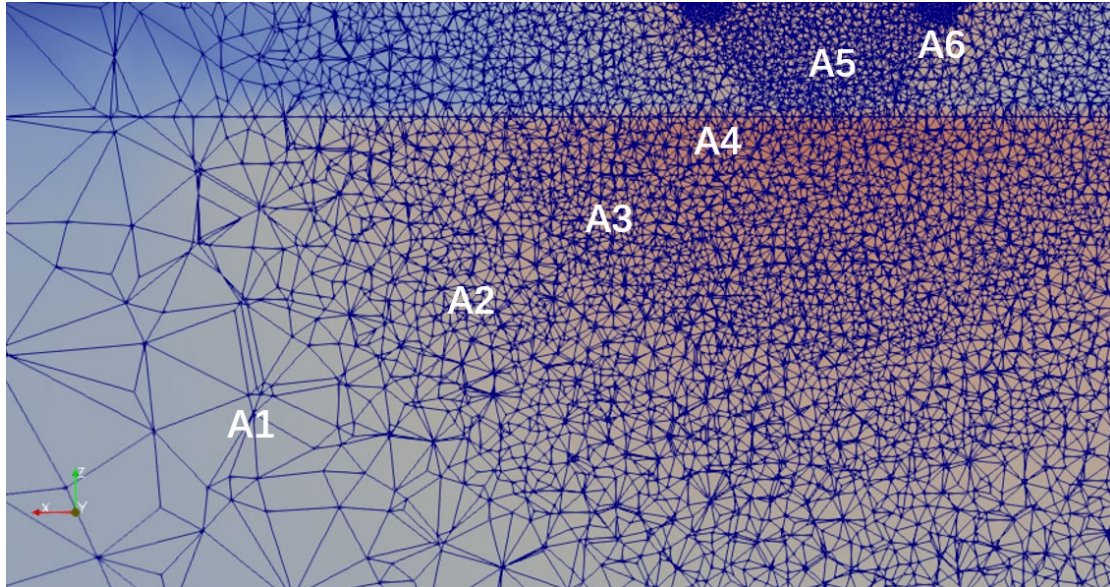


Figure 3.6. Mesh size distribution and attractor-controlled area. Here the attractor values are assigned as such, A1=20 μm , A2=1.5 μm , A3=1 μm , A4=0.8 μm , A5=0.5 μm and A6=0.2 μm to allow control of the finer mesh regions around the electrically contacted areas.

The ideal mesh size should be less than half the surface layers thickness¹. For example, if the surface layer thickness is set at 1.25 μm , A6 should be set at 0.3 μm or smaller to ensure greater accuracy in the results. A convergence study showing how the mesh size of A6 input can affect the impedance results is shown in Figure 3.7. Three different values of 0.3 μm , 0.5 μm and 0.8 μm were assigned to A6 for three models. Increasing the A6 value from 0.3 to 0.8 decreased the number of elements along with a decrease in the Z'' peak value from 594 to 531 G Ω . The inaccuracy induced by increasing the mesh size is 10%. Therefore, it is an important process to determine each attractor value to achieve convergence before conducting extensive simulations.

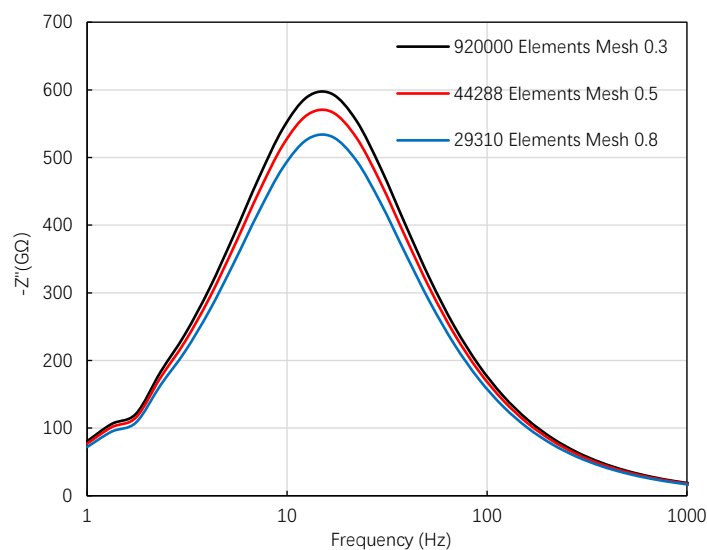


Figure 3.7. Z'' spectra of different mesh setting and its effect on raw data.

¹ Personal communication with R Veazey

As a reference, for a typical two-layer model with surface layer thickness of 1.25 μm , the attractor values are assigned as such, $A_1=20 \mu\text{m}$, $A_2=1.5 \mu\text{m}$, $A_3=1 \mu\text{m}$, $A_4=0.8 \mu\text{m}$, $A_5=0.5 \mu\text{m}$ and $A_6=0.2 \mu\text{m}$, each model should have a number of elements above two million.

Next, in models where cracks are presented in the cubic system, the attractor setting previously described is insufficient to cover the electroactive regions. As shown in Figure 3.8, a PVC model is created with the basic attractor setting from the 2-layer cubic model. It is obvious that only the centre of the top surface has a sphere of high current density. Since the crack has the same length of the cube crossing the entire surface between the electrodes the original attractor setting cannot assign more elements near the crack in regions away from the top surface centre. This could lead to loss of simulation accuracy. This has been proven in the Impedance spectroscopy simulations from a series of tests.

In Figure 3.9, a series of Z'' spectra for PVC models with different crack depths (3- 50 μm) is plotted. When the crack depth is at 3 μm (model D3), the model has the highest Z'' value and therefore resistance (R). When the crack depth increased to 10 μm (model D10), the Z'' value and therefore R is the lowest. Crack depths of 7 and 50 μm show similar Z'' and therefore R values. The randomness in the result indicates a convergence study is needed and the primary method is to add-in attractors.

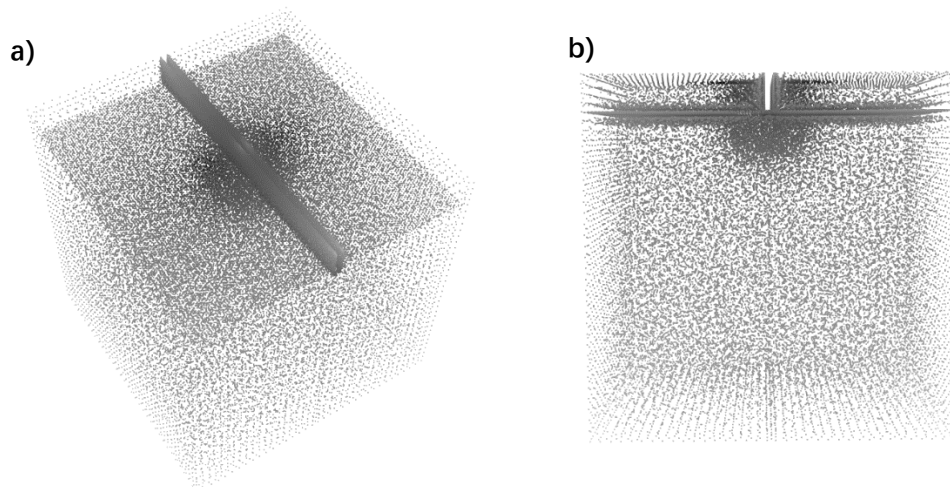


Figure 3.8. Point gaussian illustration of the cracked model with a basic 2-layer model's attractor set up. (a) Angled top view. (b). Side view. The data files are shown as points processed with gaussian distribution function. The dense grey dots indicate high current density, while lighter grey dots represent volume of lower current density.

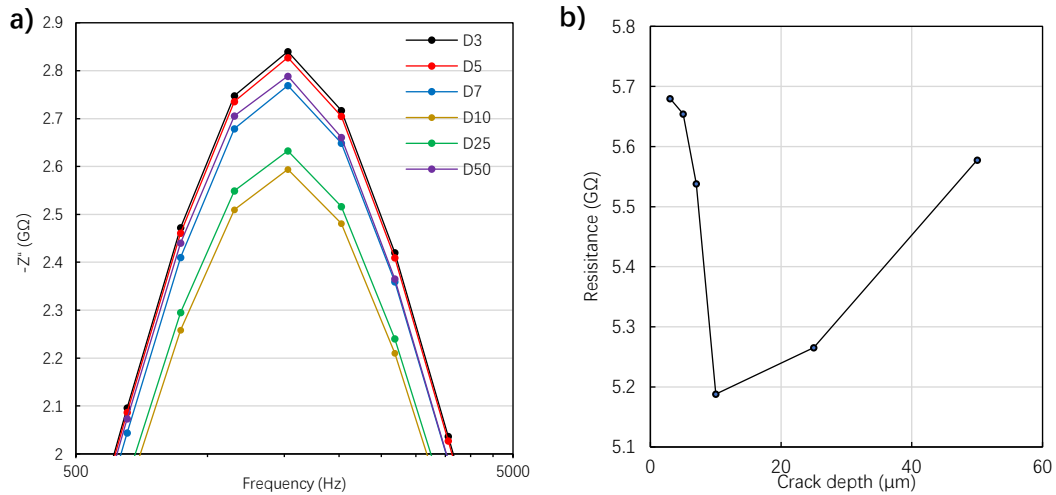


Figure 3.9(a), Variation in Z'' spectra with crack depth in the PVC model from IS simulations with the default set up. The letter D and the following number is the depth of crack in microns. Figure 3.9(b), measured resistance of models in Figure 3.9(a) versus crack depth. Line shown to guide the eye.

The first step is to establish the number of additional attractors needed. A model with one additional attractor placed on the crack bottom's surface centre is called PVC1A. This new attractor is set to move with the crack's surface at the same depth. This model does not generate the mesh of the crack volume, so it is a physical void crack.

Next, we created a model with 5 additional attractors. The 5 attractors are fixed to the surface of the crack bottom, 4 of them are at the centre of perpendicular bisector lines of the crack bottom's plane. The fifth attractor is the same position as the additional attractor in PVC1A, however this model generates the crack's mesh, so it is a meshed crack model and denoted as M5A.

The last model has 6 attractors. Based on the 5-attractor model, an additional attractor fixed at the point (100, 100, 25) is added to enhance the number of elements in the region between the electrodes, especially when the crack is deep into the model and the other 5 attractors are away from the electrodes. In Figure 3.10, the attractors are labelled from 1 to 6 to illustrate their position. The model presented is denoted as PVC6A with the crack region unmeshed.

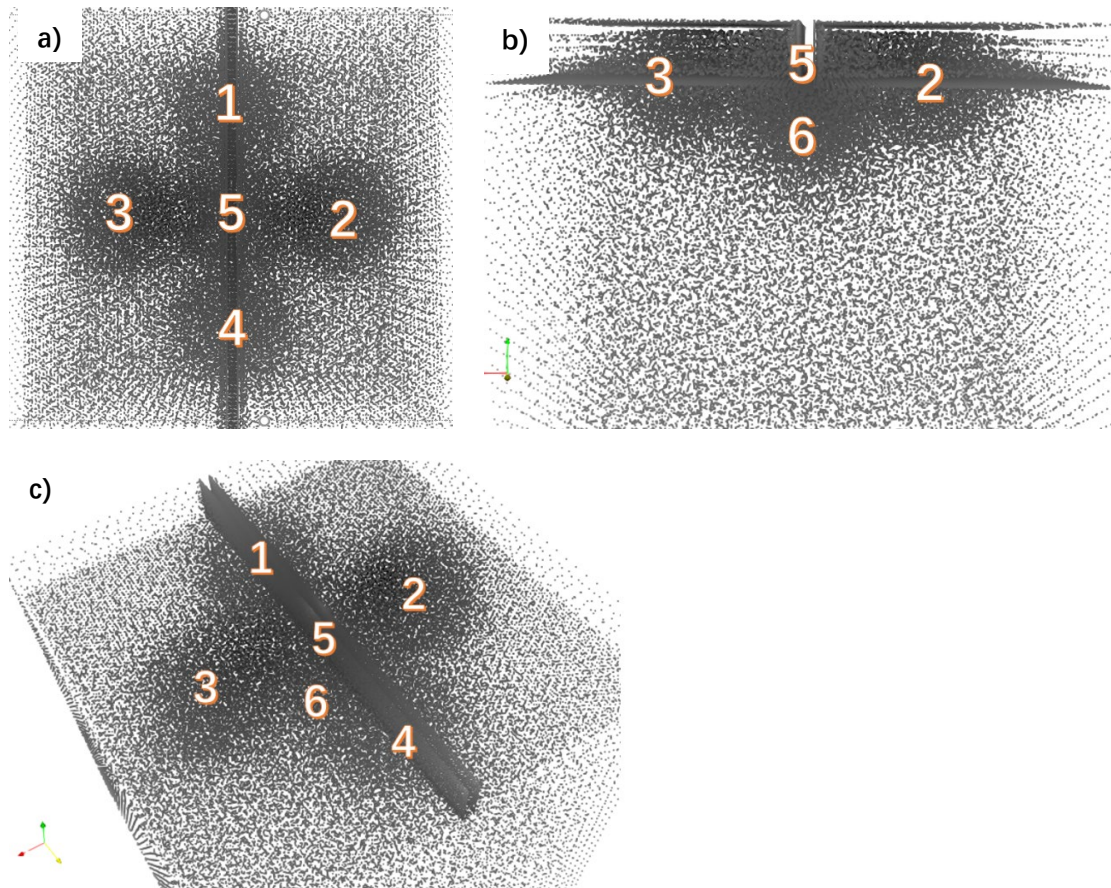


Figure 3.10, illustration of the positions of 6 new attractors in a PVC6A model. (a) Top view, (b) side view and (c) angled top view.

The impedance data of the models listed above are shown in Figure 3.11. All of the models have a crack depth of $20\ \mu\text{m}$ into the surface. The cube has side length of $200\ \mu\text{m}$, electrode radii are set to $5\ \mu\text{m}$ and the electrode separation is $50\ \mu\text{m}$ to avoid interference. As shown in Figure 3.11, the one attractor model (PVC1A) has the lowest raw Z'' value. Increasing the number of attractors to 5 brings an increase in the Z'' value (M5A). Both 6-attractor models with the crack volume meshed (M6A) and unmeshed (PVC6A) have the same Z'' peak value and are the highest among all models tested. Two conclusions can be drawn. First, the 6 attractors model gives the highest Z'' and therefore R value, and, second, whether a crack region is meshed or not it does not affect the impedance results, as long as the meshed crack region is assigned low conductivity and low relative permittivity ($1.355 \times 10^{-9}\ \text{S/m}$ and 1, respectively).

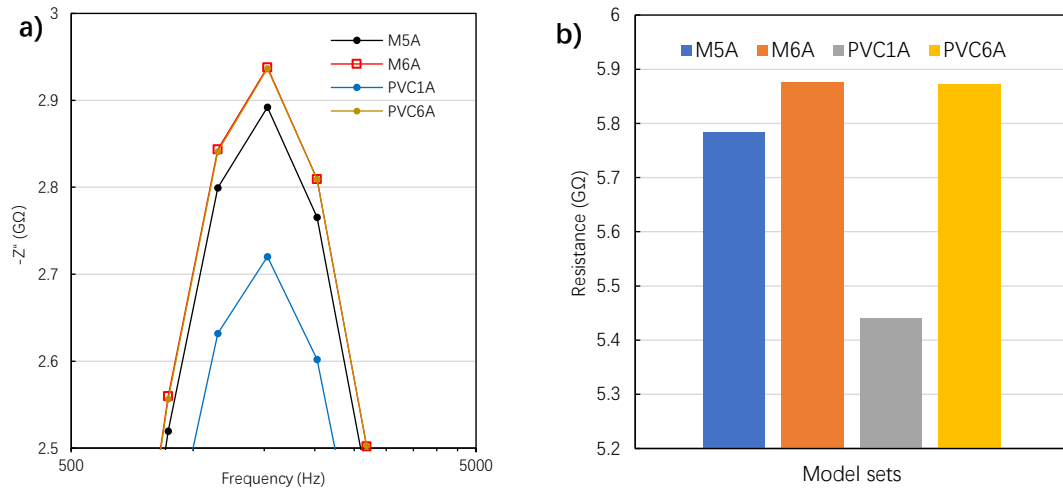


Figure 3.11. Simulated impedance spectroscopy (a) and the extracted resistance values (b) of models with different attractor settings. The models are meshed crack model with 5 and 6 attractors (M5A and M6A respectively) and physical void crack model with 1 and 6 attractors (PVC1A and PVC6A respectively). At a crack depth of 20 microns the 6 attractors setting shows the highest resistance. Whether or not the crack is meshed has negligible impact on Z'' and therefore R values. Only the number of attractors can influence the measured Z'' values.

With the attractor positions fixed, it is necessary to investigate the attractor field's size. The parameter determining the attractor's range is called Distance Max which is equal to the attractors field radius. The 6 new attractor's Distance Max were set to 30, 75 and 100 microns for comparison.

With crack depth set to 20 μm in all models, a model with Distance Max of 30 microns has 73968 elements. With a Distance Max of 75 microns it has 93942 elements and a Distance Max of 100 microns increases the number of elements in the model to 107526. Therefore, the radius of the attractor field can be extended to 100 μm without excessively increasing the number of elements as the processing time of each model is highly correlated to the number of elements. In terms of Impedance spectroscopy data, as shown in Figure 3.12, the size of the attractor field showed a minor influence from the size of the attractor field at a crack depth of 20 μm . A Distance Max of 30 microns gives the lowest Z'' peak value, the difference between Distance Max values of 75 and 100 microns is within $\sim 1\%$, Figure 3.12 (b). Therefore, convergence has been achieved. A Distance Max of 100 microns was used for all models.

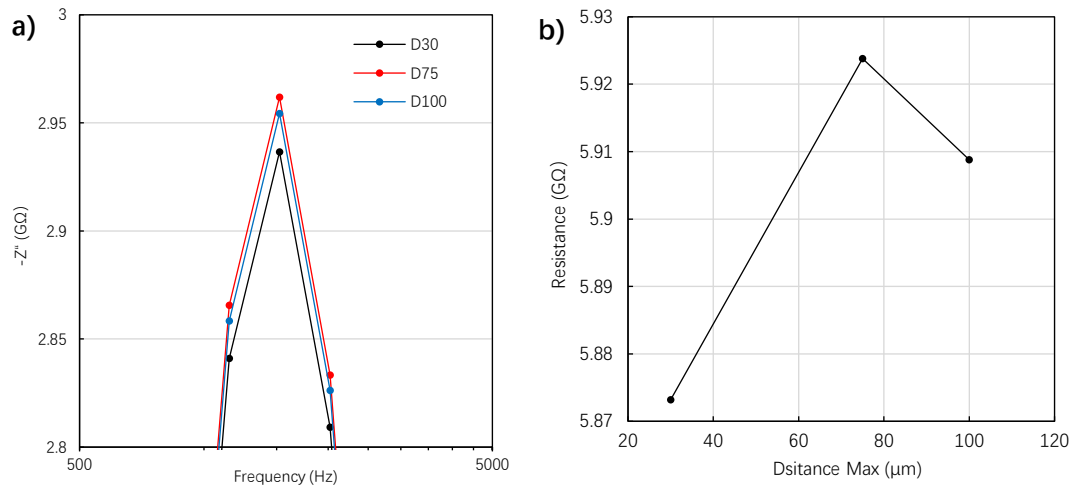


Figure 3.12. (a) Zoomed view of impedance spectra of models with attractor sizes of 30, 75 and 100 microns. (b) The difference in resistance values between D75 and D100 is as small as 1.18%.

Finally, we tried to achieve a balance between mesh size and processing time, as each attractor can be controlled separately. The mesh size of the 6 new attractors were set to 2.5, 2 and 1.5 microns. With a background mesh size of 2.5 microns, the model has around 120k elements leading to a processing time over 48 hours. Decreasing the background mesh size to 2.0 microns, the number of elements in the model increased to 140k and the processing time to ~ 60 hours. Finally, when the background mesh size is reduced to 1.5 microns, the number of elements in the model is 220k and requires over 86 hours to process. This is the upper limit of elements we can run. If the crack geometry is changed, this could increase the number of elements in the model. As such the background mesh size of 1.5 microns is not applicable for the project and consistency between models. The impedance results for the 3 settings with reducing mesh size are shown Figure 3.13. The Z'' peak value and therefore R steadily increases with reduced mesh size. For an increase in the fineness of the background mesh size from 2.0 to 1.5 microns, there is a 3.17% increase in Z'' value, but requires 57% extra elements and thus the processing time needed has been increased by 33%. Therefore, a mesh size of 2 microns was used to achieve a balance of processing time and convergence of data. The relationship between processing time and the number of elements is summarised in Table 3.1.

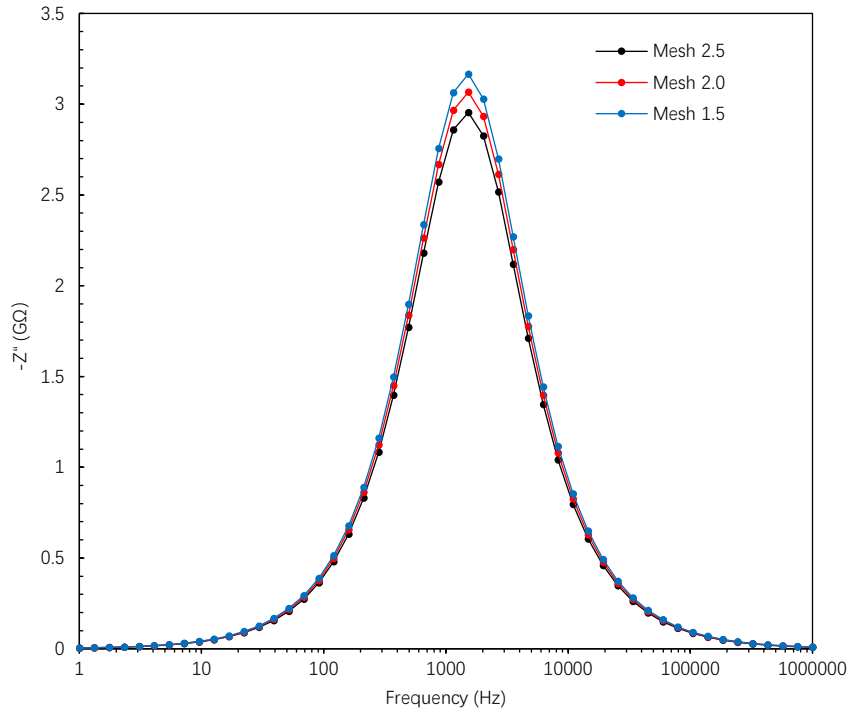


Figure 3.13. Impedance results of models with attractor mesh size of 2.5 (Black), 2 (Red) and 1.5 (Blue) microns. The smallest mesh size leads to the largest number of elements in the blue model and it has the highest Z'' peak value.

	Attractor mesh size (μm)	No. of elements (1000's)	Z'' value (G Ω)	Resistance (G Ω)	Processing time (hrs)
Model 1	2.5	120	3.17	6.34	48
Model 2	2	140	3.07	6.14	60
Model 3	1.5	220	2.94	5.88	86

Table 3.1. Summary of the attractor mesh size affecting the processing time and resistance value.

3.5 Visual presentation of simulated data

The Elcer software not only generates impedance data of varying frequency but it can also simulate a static (DC) response, where a DC bias is applied over the model and the simulated result is generated to show the distribution of the current density.

Paraview [8] is used for visualization of simulated static data in this project. After loading the static current distribution files into Paraview, one can adjust the presentation format for optimized illustration of the results. For example, the default viewing set up is shown in Figure 3.14(a). The cubic model is presented by portraying the surfaces of the cube and the electrodes, the colour change from red to blue indicating a decrease in current density. Alternatively, one can change the surface presentation to point gaussian with small radii to look through the surfaces without using filters such as slice.

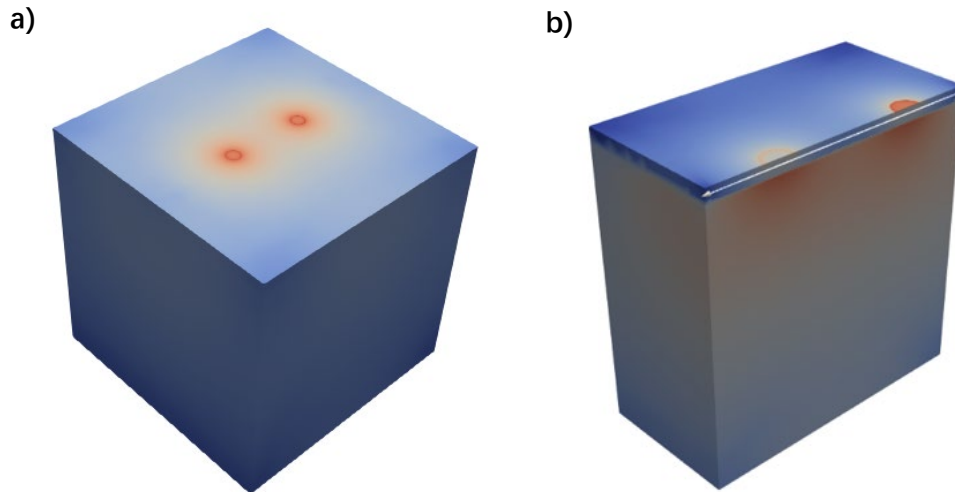


Figure 3.14. (a) Static current density distribution of simulated result with surface presentation. (b) Cross-sectional view of the bi-layer model with a surface layer thickness of 10 μm . The white line is the line scan across the x axis at 1 μm below the top surface of the cube.

In addition to qualitative presentation, Paraview can be used to extract data by using filter functions to analyse current density within the model. Filters are functional units that process the data to generate, extract, or derive features from the data. Filters are attached to readers, sources, or other filters to modify the data in some form. In Figure 3.14(b), a plot over line filter is applied to a model where the surface layer is 100 times more resistive than the bulk and the scan depth is set at 1 μm below the top surface of the cube along the x axis. The line scan result is shown in Figure 3.15. The current density is lowest at the edge of the model and increases to a maximum at the edge of the electrodes. The plot over line function allows the current density in any direction and at any depth within the model to be probed.

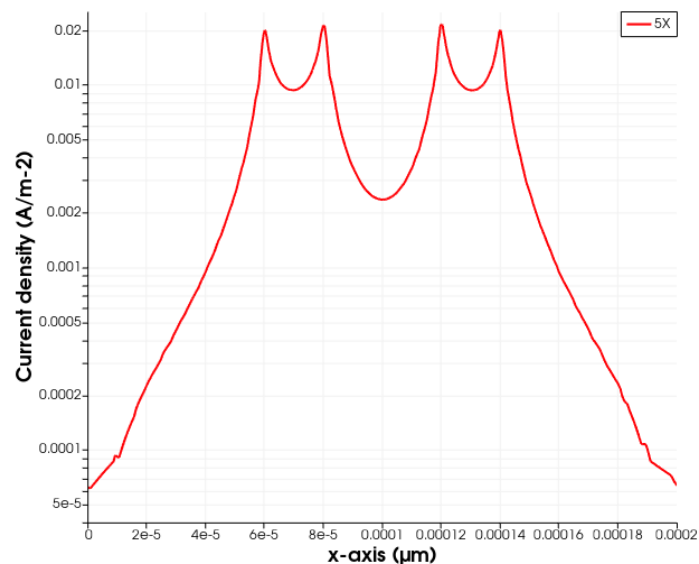


Figure 3.15. Line scan of a bi-layer model at the depth of 1 μm below the top surface of the cube along the x axis.

3.6 Extraction of data from Impedance spectroscopy

A detailed introduction on IS has been given in the literature review, hence we limit our discussion to the application of IS when micro-contacts are used.

In our two-layer models, it is necessary to calculate the surface and bulk layer properties separately. The magnitude of the Debye peaks in Z'' and M'' spectroscopic plots are used to calculate resistance (R) and capacitance (C) values for each layer, using Equations 3.1 and 3.2, respectively.

$$-Z''_{max} = \frac{R}{2} \quad (\text{Equation 3.1})$$

$$M''_{max} = \frac{1}{2C} \quad (\text{Equation 3.2})$$

Equation 3.3 is used to extract R values from M'' spectra, f_{max} is the frequency value where the maximum of the Debye peak is located. This is particularly useful when two peaks are present in the same M'' plot. The R value of each peak can be calculated and differentiated by their different peak frequency values.

$$f_{max} = \frac{1}{2\pi RC} \quad (\text{Equation 3.3})$$

Now the R and C values of each layer can be extracted from the equations listed above, the intrinsic properties of each layer can be calculated. In a conventional impedance measurement, where the electrodes cover the entire measured top and bottom surface, a geometric factor as shown in Equation 3.4, is used, where l is the thickness of the sample and A equals to the surface area of electrode.

$$GF = \frac{l}{A} \quad (\text{Equation 3.4})$$

This equation is only valid for impedance measurements where the electrode covers the entire top and bottom surfaces of the sample being measured. In this situation, the current flows homogeneously from the top towards the bottom surface. With micro electrodes, the current has to spread across the top surface and flow towards the other electrode heterogeneously and a different correction factor is required [9]. Veazey et al had stated for each micro electrode used, a new geometric factor, Equation 3.5, is used when two micro contacts are on the same surface. The r_{mc} is the radius of the electrode.

$$GF = \frac{1}{2r_{mc}} \quad (\text{Equation 3.5})$$

Therefore, the capacitance and resistivity of each layer can be calculated with the geometric factors added in the following equations.

$$R = GF \cdot \frac{1}{\sigma} \quad (\text{Equation 3.6})$$

$$C = \frac{\epsilon_r \epsilon_0}{GF} \quad (\text{Equation 3.7})$$

Although the geometric factor used by Veazey et al has been proven to be relatively accurate within a set of boundary conditions [6], we have made improvements on their findings in this project and will discuss the process in the next section.

3.7 Solid state synthesis

Known as the conventional ceramic synthesis method, solid state synthesis is a common technique used to prepare ceramics. To make oxide ceramics, precursors are mixed and heated at elevated temperature. In this process, thermal energy allows the ions in the reagents to diffuse and react. Intermediate mixing and milling are required because as the ions react at the interface of reactants, the products formed hinder further reaction between the precursors. Additional milling creates new reaction sites and therefore ensures the reaction can proceed and the desired phase can be synthesized. To examine the electrical properties, powders are pressed into pellets and sintered at high temperature to form dense and uniform ceramics.

The samples in this project are prepared by solid state synthesis. The starting materials were Na_2CO_3 , Bi_2O_3 , TiO_2 , MgO and ZnO , the supplier of each reagent and their drying conditions are listed in Table 3.2. The precursors were dried and weighed to the calculated amount, after that they are either hand ground in a pestle and mortar or ball milled in HDPE bottles with Ytria stabilized Zirconia in isopropanol as the milling media. The mixed reactants then were then subjected to a two stage calcination process, first at 800°C for two hours, then the powder is hand ground or ball milled again, and followed by another two hours of calcination at 800°C . The powder is hand ground or ball milled for another time and XRD is conducted to monitor the phase purity of the reactants. Prior to sintering, the powders are added with 5 wt% PVA solution as a binder. The powders are then pressed by uniaxial press in a 10 mm diameter die to form green pellets. The pellets are placed in alumina crucibles and buried with sacrificial powders to minimize the loss of volatile materials during sintering, the sintering temperature is held at 1150°C for 2 hours, the ramp rate of furnace was set at 5K per minute for calcination and sintering.

Reagent	Supplier	Purity (%)	Drying temperature ($^\circ\text{C}$)	Drying time (hrs)
Na_2CO_3	Fisher	99.5	300	12
Bi_2O_3	Acros Organics	99.9	300	12
TiO_2	Sigma Aldrich	99.9	900	6
MgO	Honeywell	99.0	900	12
ZnO	Sigma Aldrich	99.9	600	12

Table 3.2 Details of the chemicals used in this project.

3.8 Powder X-ray diffraction (XRD)

The various properties of a material are determined by the arrangement of the atoms inside it. For crystalline materials like ceramics, the atoms are packed in periodic order. High energy electromagnetic radiation such as X-rays interact with the atomic planes in the crystal structure at certain angles and give a specific set of diffraction patterns via constructive interference. The XRD is applied in the sintering stage to monitor the reaction process, and used to investigate the phase purity of the sintered product, lattice parameters can also be extracted if XRD is conducted at very high resolutions.

A Bruker D2 Phaser diffractometer was used to obtain the XRD patterns of different samples.

A Cu source with wavelength of 1.54 Å was used and the scan range was between 10 to 90° with a scan rate of 0.2 to 0.5s/step. The retrieved XRD patterns were then identified and analyzed using the ICDD PDF-4+ data base, by comparing the sample's pattern with entries in the database.

3.9 Scanning electron microscopy

To investigate the microstructure of prepared samples and gather information about the elemental distribution within the ceramics, different modes of scanning electron microscopy (SEM) were used.

The Secondary Electron (SE) mode was used to study the surface topography of the prepared ceramics. The Back Scattered Electron (BSE) mode was used to investigate the element distribution in the samples. BSE images can show the distribution of different elements and it is valuable to investigate if secondary phases or element aggregation is present, however BSE cannot be used to identify the elements. Energy dispersive X-ray spectroscopy (EDS) was used to address the limitation of the BSE mode.

In this work, ceramic samples were polished with different grades of silicon carbide paper or thermally etched at 90% of the sintering temperature, then coated with a thin layer of carbon or gold (around 20 nm) to prevent the buildup of electrons on the surface, which will interfere with observation. The microscope used was a FEI Inspect F50, the field emission gun was operating at a range between 10 kV to 20 kV, with the aperture of 3.5 or 4.0. EDS images were gathered and analyzed via Oxford Software's Aztec package.

3.10 LCR/Impedance Spectroscopy.

This work combines micro-contact impedance spectroscopy with FEM and conventional impedance measurement on NBT-BMT/BZT samples. For the conventional impedance measurement, Equation 3.4 is used to correct the geometric differences between different sample pellet dimensions. Then Equation 3.6 and 3.7 are used to extract the desired electrical properties of the sample measured.

The measured NBT based solid solution sample pellets had electrodes painted with gold paste fired at 850°C for 2 hours. Impedance spectra were measured between room temperature and 750°C under air used an Agilent 4980A precision LCR meter in the frequency range 20 Hz ~ 1 MHz, applying 0.1 V. When measured under Nitrogen or Oxygen, a Solartron SI 1260 impedance analyser was used measuring between 10 mHz and 1 MHz with 0.1 V. The impedance data was analyzed with the Zview software from Scribner Associates Inc [10].

3.11 References

- [1] A. Hrennikoff, "Solution of problems of elasticity by the framework method," *Journal of applied mechanics*, 8.4, pp. 169–175, 1941.
- [2] R. Courant, "Variational methods for the solution of problems of equilibrium and vibrations," *Bulletin of the American Mathematical Society*, 49, pp. 1–23, 1943.
- [3] J. S. Dean, J. H. Harding and D. C. Sinclair, "Simulation of Impedance Spectra for a Full Three-Dimensional Ceramic Microstructure Using a Finite Element Model.," *J. Am. Ceram. Soc.*, 97, pp. 885–891, 2014.
- [4] C. Geuzaine and J.-F. Remacle, "Gmsh: a three-dimensional finite element mesh generator with built-in pre- and post-processing facilities.," *International Journal for Numerical Methods in Engineering*, 79(11), pp. 1309–1331, 2009.
- [5] R. A. Veazey, "Probing Radiation Damage in Fe-doped SrTiO₃ using Micro-contact Impedance Spectroscopy," PhD Thesis, The University of Sheffield, 2019.
- [6] R. A. Veazey, A. S. Gandy, D. C. Sinclair and J. S. Dean, "Finite element modeling of resistive surface layers by micro-contact impedance spectroscopy.," *J Am Ceram Soc.*, 103, pp. 2702– 2714, 2020.
- [7] J. Fleig, "Microelectrodes in solid state ionics.," *Solid State Ionics*, 161, pp. 279–289 (2003).
- [8] Kitware Inc, "Paraview," [Online]. Available: <https://www.paraview.org/>. [Accessed 20 1 2022].
- [9] R. A. Veazey, A. S. Gandy, D. C. Sinclair and J. S. Dean, "Modeling the influence of two terminal electrode contact geometry and sample dimensions in electro-materials," *J. Am. Ceram. Soc.*, 102, pp. 3609– 3622, 2018.
- [10] Scribner Associates Inc, "ZView® For Windows," [Online]. Available: <https://www.scribner.com/software/68-general-electrochemistr376-zview-for-windows/>. [Accessed 5 2022].

Chapter 4: $\text{Na}_{0.5}\text{Bi}_{0.5}\text{TiO}_3\text{-Bi}(\text{M}_{0.5}\text{Ti}_{0.5})\text{O}_3$ Solid Solutions (M = Mg, Zn)

4.1 Introduction

The first part of the research work in this thesis is focused on ($\text{Na}_{1/2}\text{Bi}_{1/2}\text{TiO}_3$, NBT) solid solutions. NBT has received considerable research interest due to its high Curie temperature ($T_c \sim 325^\circ\text{C}$), relatively high remnant polarisation ($P_r = 38 \mu\text{C cm}^{-2}$) and piezoelectric constant ($d_{33} = 73 \text{ pC N}^{-1}$). These properties show its potential as a lead-free piezoelectric material to replace lead zirconium titanate (PZT) [1] [2] [3]. The major hindrance of utilising NBT as a dielectric material is the high electrical conductivity, high dielectric loss and therefore leakage current. Previous studies from the functional materials and devices group at TUOS revealed NBT can have very different electrical behaviour depending on the nominal starting stoichiometry of the composition. Bi-deficient NBT shows high oxide-ion conductivity and Bi-rich NBT shows insulating behaviour with low levels of electronic and ionic conduction and therefore dielectric loss [4].

Many studies have tried to improve NBT's dielectric properties, by forming solid solutions with other perovskites such as NBT-BiAlO₃, NBT-BiScO₃, NBT-Bi($\text{Mg}_{1/2}\text{Ti}_{1/2}$)O₃ and NBT-Bi($\text{Zn}_{1/2}\text{Ti}_{1/2}$)O₃ [5] [6] [7] [8] [9] [10]. For example, Wang et al used a sol-gel method to grow $(1-x)\text{Na}_{0.5}\text{Bi}_{0.5}\text{TiO}_3\text{-xBiMg}_{0.5}\text{Ti}_{0.5}\text{O}_3$ thick films on LaNiO₃ substrates. Compared to undoped NBT thick films, the addition of BMT at $x=0.4$ increased the recoverable energy-storage density to 40.4 J/cm^3 when $E=2400 \text{ kV/cm}$, which is an improvement of more than 4 times. A high breakdown strength field was also measured at 2440 kV/cm for $x=0.4$ [8]. Chen et al reported single crystal $\text{Na}_{0.5}\text{Bi}_{0.5}\text{TiO}_3\text{-1.5 at.}\% \text{ BiZn}_{0.5}\text{Ti}_{0.5}\text{O}_3$ to have enhanced electrical properties compared to undoped NBT. The piezoelectric constant increased to 121 pC/N for an NBT-1.5 at.% BZT sample, compared with 62 pC/N for undoped NBT ceramics [9]. Liu et al reported negative temperature coefficient (NTC) behaviour of NBT-BZT. The obtained ρ_{600} , ρ_{900} , and $B_{600/900}$ constants of the NBT-ZBT NTC thermistors were approximately 5.92×10^6 to $3.01 \times 10^4 \Omega \text{ cm}$, 7.03×10^3 to $7.60 \times 10^2 \Omega \text{ cm}$ and $2.3 \times 10^4\text{-}1.3 \times 10^4 \text{ K}$, respectively.

Although these discoveries of NBT-based solid solutions are very important and inspirational, there is no information on the mentioned compositions' electrical/ionic conduction properties. As discussed in the literature review on NBT materials, the Bi-Bi-Ti saddle point for oxide-ion conduction has the lowest activation energy of 0.22 eV [11]. It is interesting to know how any excess Bi and Ti in the starting composition may affect the bulk properties. Also, it is important to determine the trapping power of any dopant elements in NBT solid solutions. Yang et al conducted a study over the NBT-BiAlO₃ (NBT-BA) solid solution and reported that a systematic decrease in the conductivity occurred with increasing BA content, shown in Figure 4.1. The transport mechanism changed from predominantly ionic to mixed ionic-electronic and then predominantly electronic as the BA content increased. They considered the Aluminium (acceptor) ions trapped oxygen vacancies and formed $(\text{Al}'_{\text{Ti}} - \text{V}_\text{O}^{\bullet\bullet})^\cdot$ complexes, and as a consequence the carrier concentration and mobility of the oxygen vacancies were reduced. Atomic simulations supported these conclusions [5] [12].

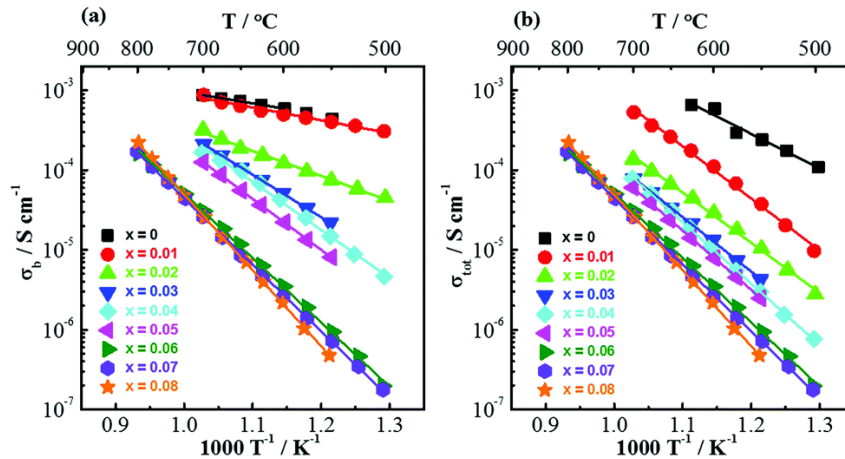


Figure 4.1. Arrhenius plots for (a) bulk conductivity and (b) total conductivity of the $(1-x)(\text{Na}_{0.5}\text{Bi}_{0.5}\text{TiO}_3)\text{-}(x)\text{BiAlO}_3$ ($0 \leq x \leq 0.08$) solid solutions measured in air [5].

A former PhD student of the functional materials and devices group, Emilio Pradal-Velazquez conducted a study on $\text{Na}_{0.5}\text{Bi}_{0.5}\text{TiO}_3\text{-BiMg}_{2/3}\text{Nb}_{1/3}\text{O}_3$ (NBT-BMN) and $\text{Na}_{0.5}\text{Bi}_{0.5}\text{TiO}_3\text{-BiZn}_{2/3}\text{Nb}_{1/3}\text{O}_3$ (NBT-BZN) solid solutions as part of his thesis [13]. For the NBT-BMN system, the solid solution limit was established to be $\sim 6\%$. The bulk conductivity decreased with increasing BMN content, accompanied with the reduction of oxide ion conduction, Figure 4.2. The dielectric loss at high temperature gradually decreased with increasing dopant concentration; however, the maximum relative permittivity of the solid solution also decreased. After comparing the conductivity data, Pradal-Velazquez considered the trapping power of Mg to be stronger than Al at low concentrations in the NBT-BA solid solution presented by Yang et al [5]. But at higher concentrations, Al ions show stronger trapping power due to the stronger Al-O bond. For the NBT-BZN system, a low solid solution limit of 4% was determined as secondary phases were observed at this level. The conductivity of the NBT-BZN system showed a greater decrease than NBT-BMN and NBT-BA, as the concentration of dopant increased. Also, the dielectric loss was suppressed to very low levels with lower dopant concentration, when compared to NBT-BMN and NBT-BA. For a solid solution with 4% BZN the bulk conductivity dropped to similar levels as insulating NB0.51T, Figure 4.3. This is a sign that Zn is a stronger trap for oxygen vacancies than Mg and Al, however the addition of Nb^{5+} ions might also have an influence over the bulk conductivity since the solid solution limit was low and limited Zn^{2+} ions enter into the perovskite structure. It is therefore important to identify the role of the Nb^{5+} ions in the solid solution. One approach is to form NBT solid solutions without any Nb content, such as NBT-BMT and NBT-BZT where the trapping powers of oxygen vacancies by Mg and Zn ions can be further investigated and compared.

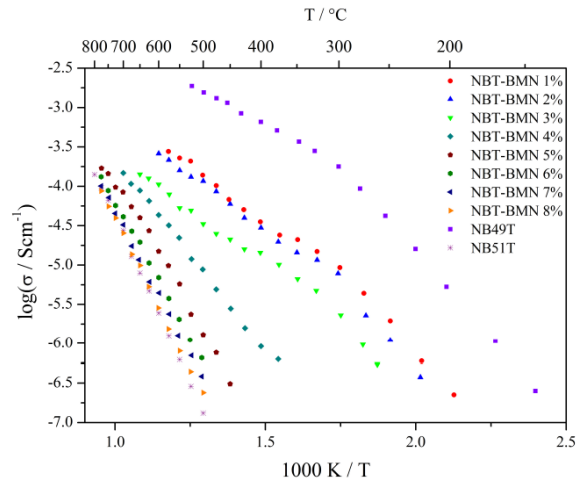


Figure 4.2. Arrhenius plots of bulk conductivity for NBT-BMN compositions from 1 to 8% BMN. All impedance data extracted from M'' plots [13].

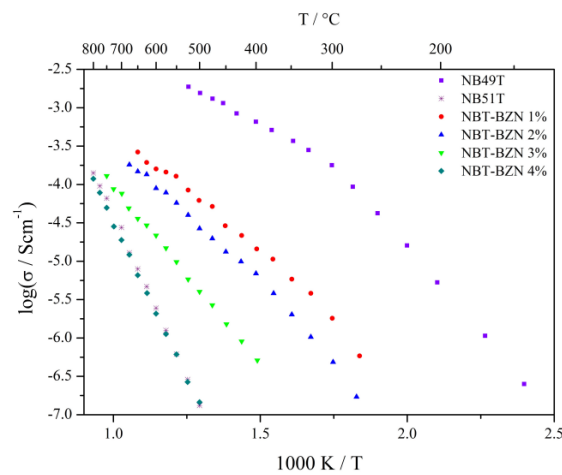


Figure 4.3. Arrhenius plots of bulk conductivity for NBT-BZN with BZN compositions from 1 to 4%. All impedance data extracted from M'' plots [13].

In addition to the compositional-electrical property analysis, in the latest research on NBT materials, Yang et al reported a relationship between grain size and electrical properties which had not been reported previously. An inhomogeneous microstructure with randomly distributed large grains embedded in a small grained matrix was reported for $\text{NaBi}_{0.51}\text{TiO}_3$ (NB0.51T) ceramics with very low levels of doping [14]. This type of microstructure is considered as a two-phase composite with large grains ($d > 3.5 \mu\text{m}$) as a non-percolative conductive phase and small grains ($d < 3.5 \mu\text{m}$) as the insulating phase, Figure 4.4. The grain size of $3.5 \mu\text{m}$ is critical to determine the grain conductivity behaviour in the matrix. Moreover, through statistical review of various literature, they showed the conductive large grains' fraction in the ceramics agrees with the oxide-ion transport number. In conclusion, the electrical conduction behaviour in acceptor-doped NB0.51T is affected by the defect chemistry and the ceramic microstructure. This study reveals the significance of microstructure on the electrical conduction behaviour in NBT-based materials, which is an important aspect to consider when characterising NBT samples in this thesis.

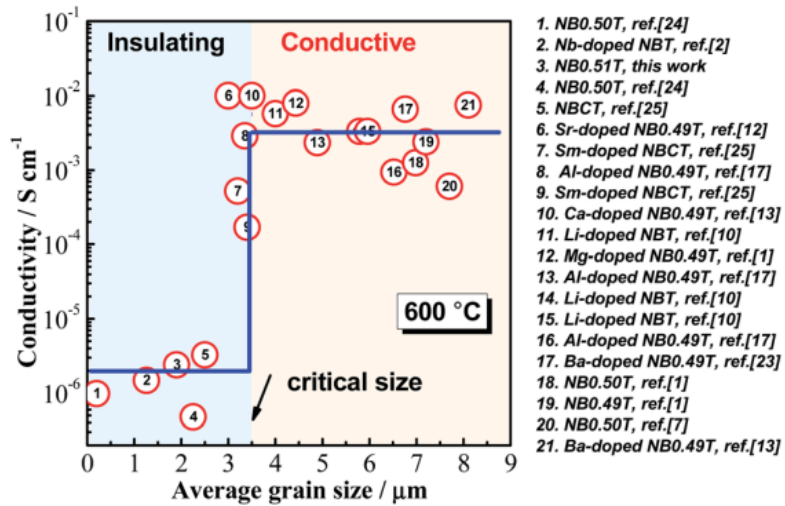


Figure 4.4. Conductivity-average grain size relationship of nonstoichiometric and doped NBT ceramics [14].

Solid solutions of $\text{Na}_{0.5}\text{Bi}_{0.5}\text{TiO}_3$ - $\text{BiMg}_{0.5}\text{Ti}_{0.5}\text{O}_3$ (NBT-BMT) and $\text{Na}_{0.5}\text{Bi}_{0.5}\text{TiO}_3$ - $\text{BiZn}_{0.5}\text{Ti}_{0.5}\text{O}_3$ (NBT-BZT) have been prepared and their electrical properties investigated. The focus is to determine if the B-site acceptor dopants (Mg, Zn) will act as oxide-ion traps and lower the conductivity.

4.2 Results and discussion

4.2.1 $(1-x)\text{Na}_{0.5}\text{Bi}_{0.5}\text{TiO}_3-(x)\text{BiMg}_{0.5}\text{Ti}_{0.5}\text{O}_3$

A series of NBT-BMT for $x = 0.01$ to 0.08 were prepared by two different processing techniques, hand grinding and ball milling. The hand grinding method was proven to be insufficient to achieve a homogenous distribution of the reactants in the samples. Ball milling was then chosen as the mixing method. Selected results below explain how this decision was made. For the hand ground samples, the weighed reactants of the compositions were ground by pestle and mortar for 1 hour with isopropanol. The powder was then calcined twice at $800\text{ }^\circ\text{C}$ for two hours with an intermediate grinding step. Pressed pellets buried in sacrificial powder of the same composition were then sintered at $1150\text{ }^\circ\text{C}$ for two hours. The sintered pellets were over 93% dense.

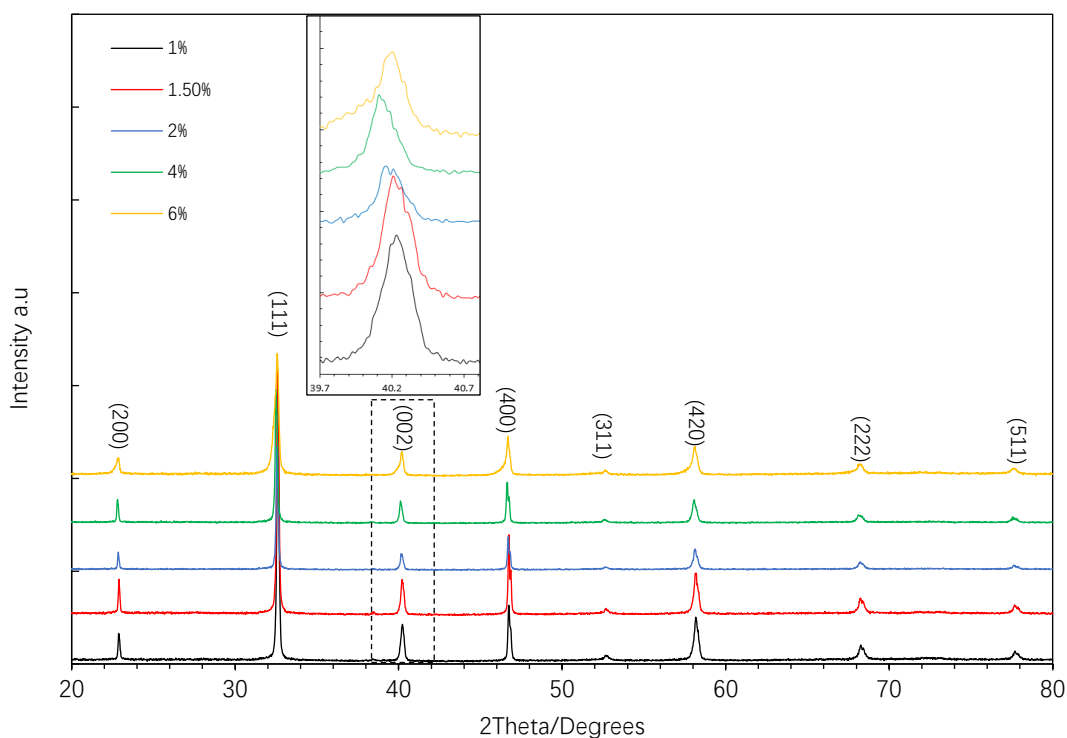


Figure 4.5. XRD patterns of hand ground NBT-BMT samples sintered at $1150\text{ }^\circ\text{C}$.

As shown in Figure 4.5, different compositions of NBT-BMT were examined using XRD to establish if they were single phase. The results show no additional peaks up to 6% BMT, and therefore no trace of secondary phases being present. A systematic decrease in the diffraction angles (see inset) for the peaks indicates the unit cell is expanding with increasing BMT content from 1 to 4%, as expected from the larger ionic radius of Mg^{2+} (72 pm) compared to Ti^{4+} (60.5 pm). The diffraction angle increased when the BMT concentration reached 6%, a possible sign that the solid solution limit has been reached. It was not possible to obtain high resolution XRD data for lattice parameter determination of these samples (or any others in this thesis) as the Covid 19 pandemic resulted in a long-term closure of the XRD laboratory.

SEM images reveal the microstructure of the hand ground NBT-BMT samples, Figure 4.6. The 1% BMT sample shows very low concentration of Bi in the grain analysed. In the 2% BMT sample,

large aggregates of a Ti-rich and Bi-deficient composition can be observed as the darker regions in the BSE image. The solid solution limit of BMT in NBT seems lower than BA in NBT-BA which is 8% and also lower than BMN in NBT-BMN which was estimated at ~6% [5] [13]. A possible BMT solid solution limit for the hand ground NBT-BMT samples could be as low as ~2 or 3%.

In terms of grain size, the 1% BMT sample shows large grains with a relatively uniform size distribution but for the 2% BMT sample the large grains were separated by a small grain matrix. The 8% BMT sample has a very evident heterogenous grain size distribution. In the study presented by Yang et al, they reported NB.51T samples contain an insulating small grain matrix with a few large conductive grains embedded within the matrix. This results in low bulk conductivity behaviour in the ceramics, forming a composite-like microstructure [14]. This might also be the case for the hand ground NBT-BMT samples as the 1% BMT sample shows predominantly large grains whereas the 8% sample shows a few large grains surrounded by small grains. Impedance measurements should determine if the NBT-BMT samples support Yang et al's hypothesis. Also, the presence of large Mg-rich aggregates suggests an uneven mixture of reactants and therefore inhomogeneous mixing from this processing method.

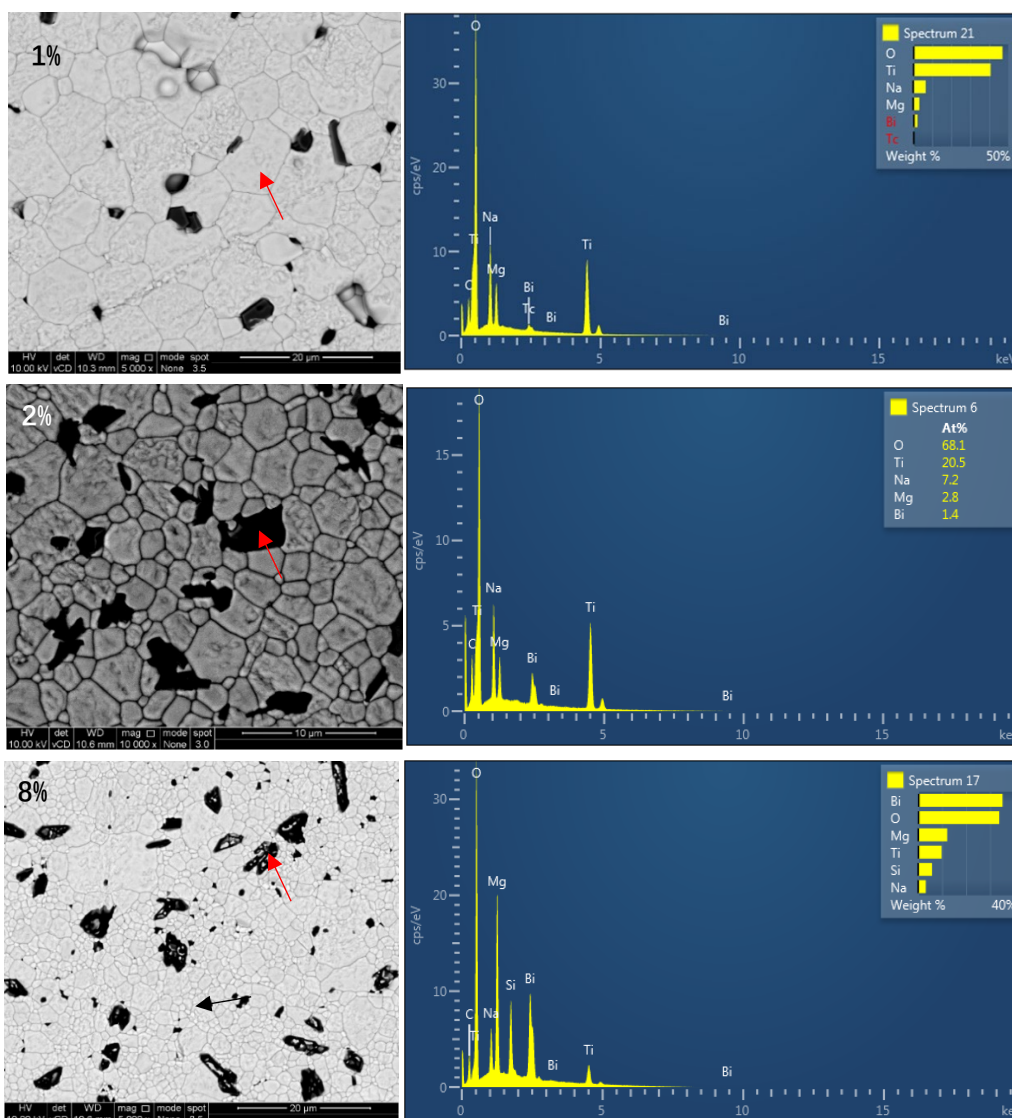


Figure 4.6. Back-scattered electron SEM images of 1% (top), 2% (middle), and 8% (bottom) of thermally etched surfaces (at 90% of the sintering temperature, 1035°C) of hand ground NBT-BMT samples. EDX analysis of highlighted (arrowed) regions shown on the right, respectively. Note that for 1% and 8% EDX analyses, the unit used is weight percentage but for 2% it is in atomic percentage.

The relative permittivity and dielectric loss data for 1, 2, 4 and 8% NBT-BMT samples are shown in Figure 4.7. A maximum relative permittivity of 3070 at $T_{max} \sim 316^\circ\text{C}$ is obtained for the 1% BMT sample, whereas T_{max} increased to $\sim 350^\circ\text{C}$ for 2, 4 and 8% samples, but the relative permittivity decreased with increasing BMT content. The 1% NBT-BMT sample has the highest dielectric loss across the entire measured temperature range. The 2 and 4% samples show similar dielectric loss behaviour as the 1% sample, but when the temperature exceeds 425°C the 2 and 4% have the lowest dielectric loss. For the 8% sample, it has the lowest dielectric loss below 290°C but then exhibits higher leakage than the 2 and 4% samples when the temperature exceeds 290°C . The shift in T_{max} is a very distinctive feature of the hand ground NBT-BMT samples. In NBT-BA, the relative permittivity decreased with increasing dopant concentration but T_{max} and peak shape were not as heavily influenced. [5] In the NBT-BMN system, the peak in relative permittivity also became broader with increasing dopant concentration but T_{max} showed little variation, unlike the hand ground NBT-BMT samples [13]. Also, the non-systematic behaviour of the dielectric loss data suggests impedance measurements are required to further analyse the electrical properties of the NBT-BMT system. When considering Mg^{2+} ions as an oxygen vacancy trap, increasing the concentration of BMT should further reduce the mobility of oxygen vacancies in the material and suppress the dielectric loss but the 8% NBT-BMT sample does not support this hypothesis, which might be related to the presence of second phase in the sample .

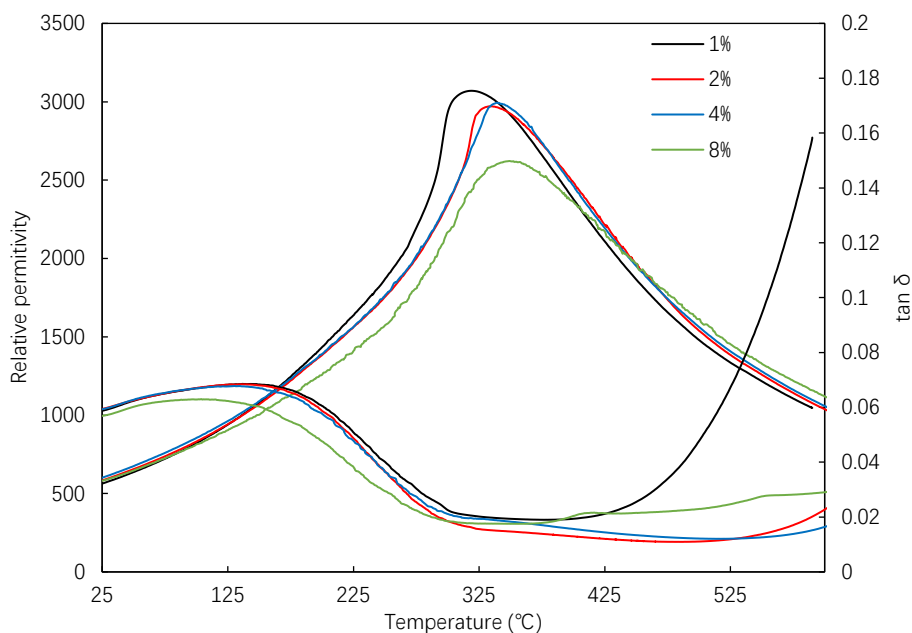


Figure 4.7. Relative permittivity and dielectric loss of hand-ground NBT-BMT 1, 2, 4 and 8% samples, measured at 1 MHz.

Selected examples of Z'' and M'' spectroscopic plots and the corresponding complex impedance plots for samples of 1 and 2 % BMT are shown in Figures 4.8 and 4.9, respectively. The data are analysed using 2 parallel RC elements connected in series. For the 1% sample, the M'' plot shows a single response at high frequency, whereas the Z'' plot shows one peak with a hump at the high frequency which is overlapping with the M'' peak, indicating the presence of two electroactive regions with comparable resistivities. The M'' peak can be assumed to be the bulk response of the ceramic, or the conductive grain response (capacitance of 2.26×10^{-10} F/cm), whereas the major Z'' peak (lower frequency) indicates it might be a grain boundary or a resistive grain type response (capacitance of 8.41×10^{-10} F/cm). In the complex impedance plots for the 1% sample, two distorted semi-circles and a low frequency spike can be observed, with the latter being an indicative sign of ionic conduction. The arc at higher frequency which is on the left has a capacitance value of 2.26×10^{-10} F/cm, for the arc on the right it is 8.41×10^{-10} F/cm.

The 2% NBT-BMT sample shows a single response in the Z'' and M'' spectra, indicating the presence of only one electro-active response with little evidence for a low frequency spike in the Z'' plots, Figure 4.8 (b). Further information can be obtained from complex impedance plots, Figure 4.9 (b). Only one semi-circle can be observed for the 2% sample, which has capacitance of 9.97×10^{-11} F/cm, which is a reasonable value for the bulk response. Furthermore, there is no evidence of a low frequency spike in the Z'' plot. The 4 and 8% samples have very similar impedance responses as the 2% sample and are therefore not presented. When compared with the NBT-BMN system, low BMN concentrations of 1 and 2% resulted in similar impedance responses, where two electro-active regions could be identified. This is not the case for hand ground NBT-BMT samples, where the impedance response of low (2%), medium (4%) and high (8%) dopant concentrations are very similar.

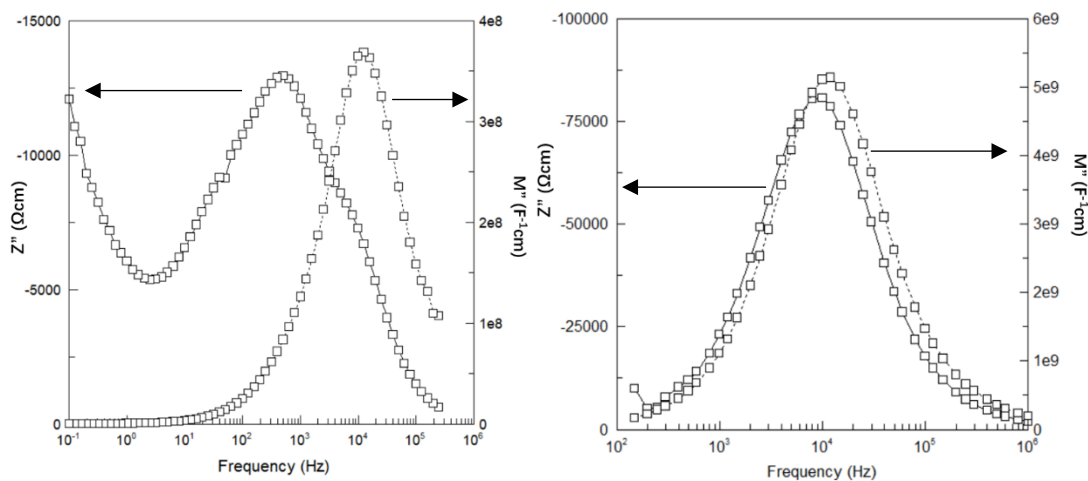


Figure 4.8. Z'' and M'' spectra of hand ground NBT-BMT ceramics sintered at 1150 °C. (a) NBT-BMT 1% sample measured at 405 °C. (b) NBT-BMT 2% sample measured at 610 °C.

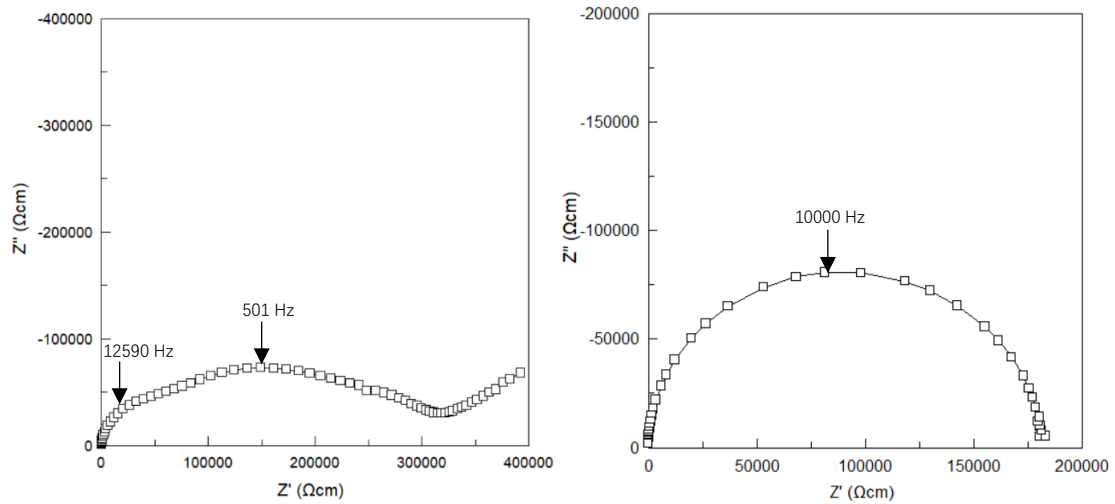


Figure 4.9. Z^* plots of hand ground NBT-BMT ceramics sintered at 1150 °C. (a) NBT-BMT 1% sample measured at 350 °C. (b) NBT-BMT 2% sample measured at 610 °C.

The relative permittivity extracted from 1% and 2% NBT-BMT samples' M'' and Z'' spectra were compared with the LCR data, in order to understand any relationship between the electrical response and the microstructure. Curie Weiss type plots of 1% and 2% NBT-BMT hand ground samples are shown in Figure 4.10. The 1% M'' extracted data has a gradient of 3.53×10^{-6} K and T_0 of 580 K. The 2% M'' extracted data has a gradient of 2.91×10^{-6} K and T_0 of 560 K. The $1/\text{relative permittivity}$ data extracted from M'' of both 1% and 2% are very close to the LCR measurements, showing strong temperature dependence. This indicates both can be assumed to be a bulk (paraelectric) material response. The 1% Z'' extracted data has a gradient of 1.37×10^{-6} K and T_0 of 590 K, with less temperature dependence, suggesting it might be a grain boundary type behaviour or resistive grain behaviour. For the 2% Z'' extracted data, the gradient is 3.23×10^{-6} K and T_0 of 610 K. The capacitance extracted from 2% sample's M'' and Z'' spectra are very similar to the LCR data and have similar gradient, indicating the bulk material response is dominating the LCR response. In contrast, for the 1% sample, a bulk response and a possible grain boundary response or resistive grain response exists at the same time. Although the SEM images reveal no obvious secondary phase, the dopant concentration may not be uniform within the grains.

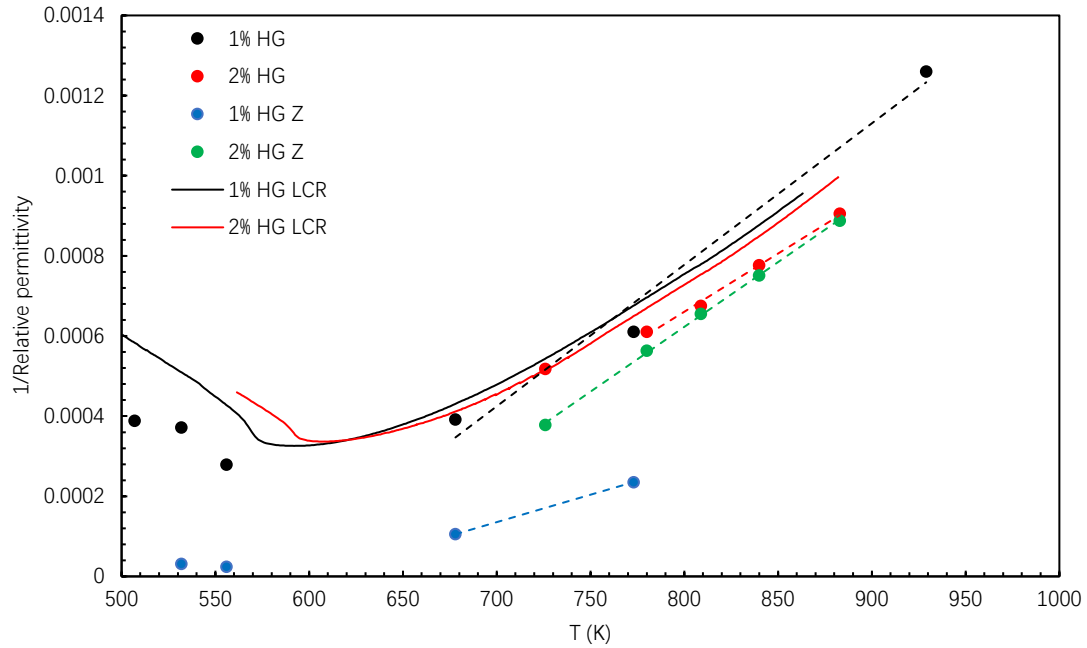


Figure 4.10. 1/relative permittivity versus temperature plots for 1% and 2% NBT-BMT hand ground samples. Relative permittivity data extracted from M'' and Z'' spectra were overlaid with the 1 MHz LCR data (solid lines).

An Arrhenius plot of bulk conductivity constructed from M'' spectra of different samples is shown in Figure 4.11 to summarise the results. To extract the conductivity from M'' spectra, F_{max} of the M'' peak representing the bulk response was located and then Equation 3.3 was used to extract an R value and substituted into Equation 3.6 to calculate the corresponding conductivity. For reference, Li et al's NBT and NB0.51T bulk conductivity data are reproduced to represent conductive and insulating undoped NBT, respectively [4]. It is obvious that after 2% BMT the conductivity of the ceramics decreases to the extent where the increment of percentage of BMT does not result in a substantial change in the conductivity. The 8% NBT-BMT sample showed lower conductivity than insulating NB0.51T. The activation energy based on the bulk conductivity also increased dramatically from 1% to 2% BMT content (0.71 to 1.21 eV), and only a small increment occurred on further additions of BMT content. This decrease in bulk conductivity is more dramatic than that shown by Yang and Pradal-Velázquez' in solid solutions of NBT-BiAlO₃, NBT-Bi(Mg_{1/3}Nb_{2/3})O₃ and NBT- Bi(Zn_{1/3}Nb_{2/3})O₃, where the conductivity decreased gradually with an increasing percentage of the high pressure Bi-based perovskite phase [5]. The solid solution limit of BMT in NBT could be very low at ~3 % when processed by hand grinding.

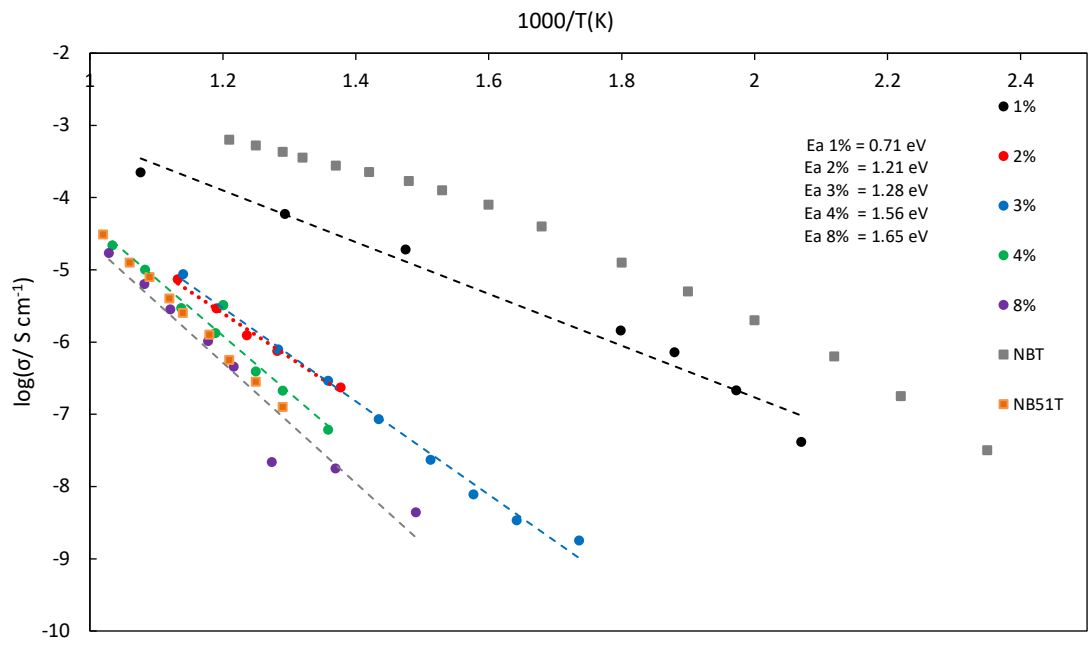


Figure 4.11. Arrhenius plots of bulk conductivity for hand ground NBT-BMT samples. Data obtained from M'' spectra of impedance measurements. Conductivity for insulating NB0.51T and conductive NBT from work by Li et al [4] are included for comparison.

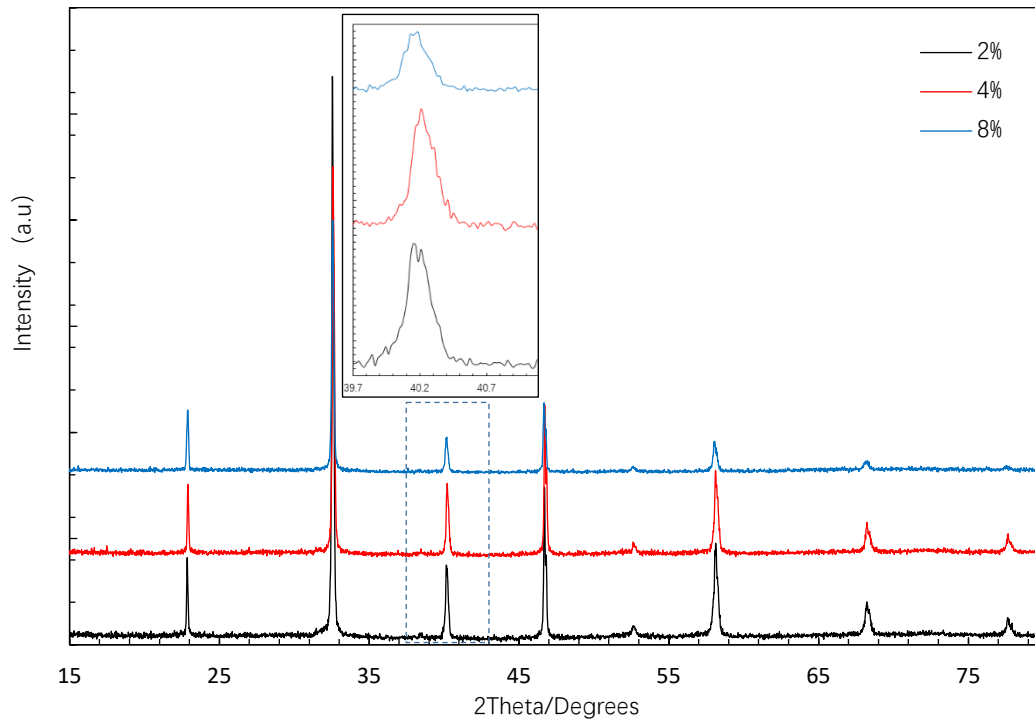


Figure 4.12. XRD patterns of ball milled NBT-BMT samples sintered at 1150 °C.

After the characterisation of hand ground samples, $(1-x)\text{NBT}-x\text{BMT}$ solid solution ceramics were prepared by ball milling as described in Chapter 3. Ball milling was implemented for better mixing of the reactants. The ball milling consisted of two stages. First, after the reactants had been dried in the drying ovens and weighed and, second, after the first calcination at 800 °C. Each milling stage lasted 6 hours. Compositions of 2, 4 and 8 at% of NBT-BMT samples were sintered at 1150 °C and investigated via multiple characterisation methods. The relative density of the ceramics was > 90%. The XRD results show no additional peaks up to 8%, Figure 4.12. A decrease in the diffraction angles (see inset) indicates the unit cell is expanding with increasing BMT concentration from 2 to 8%, but the 4% sample did not show a decrease in diffraction angle compared to the 2% sample. This is a possible sign that mixing of the reagents is still a problem with the ball mill processing method.

Electron microscopy reveals the microstructure of ball milled NBT-BMT solid solution samples, Figure 4.13. Only two of the compositions prepared via ball milling were studied under SEM prior to the pandemic lockdown. For $x = 0.04$, the NBT-BMT sample shows a homogenous matrix across the pellet and has no sign of secondary phases. When the doping level increased to 6 at%, an obvious secondary phase can be observed via the back-scattered mode. The dark squares and sheets appear to be Mg- and Ti-rich regions (and Bi-deficient), Figure 4.14; interestingly, no additional peaks in XRD patterns were observed at 8 at%, which is nominally a higher doping level.

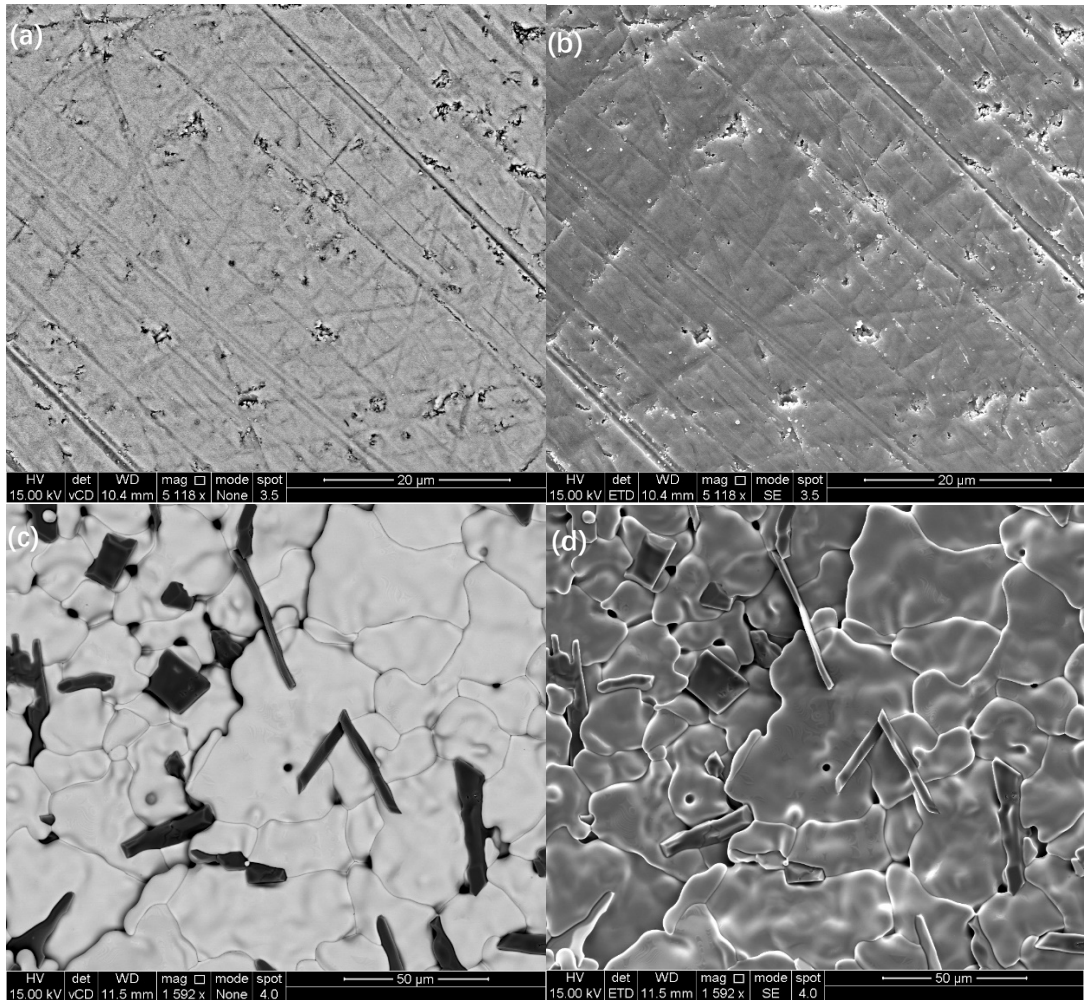


Figure 4.13. Back-scattered electron and secondary electron images of 4% NBT-BMT (a) and (b) with polished surface. 6% NBT-BMT (c) and (d) with as sintered surface. Obvious secondary phase can be observed in the 6 at% NBT-BMT sample.

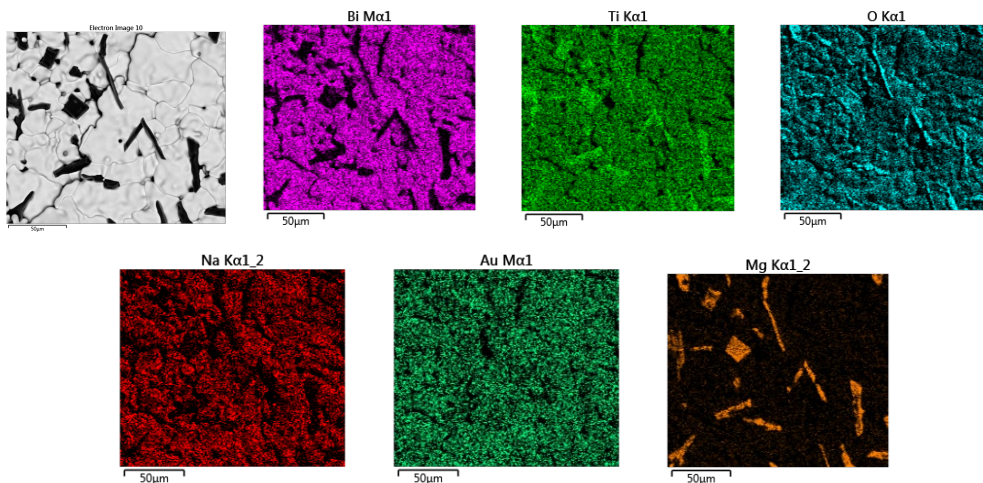


Figure 4.14. EDS shows the darker region in 6% NBT-BMT is a secondary phase with rich Mg and Ti content and Bi deficient.

Figure 4.15 shows the relative permittivity and dielectric loss properties of 2, 4 and 8% ball milled NBT-BMT samples measured at 1 MHz. The maximum relative permittivity at $T_{max} \sim 330^\circ\text{C}$ decreased when x increased from 0.02 to 0.08 but otherwise the responses look similar. For the dielectric loss of the samples, 8% BMT has the lowest values at higher temperatures, but the 4% BMT sample has higher loss than the 2% sample, which is unexpected. As for the hand ground NBT-BMT samples, non-systematic dielectric properties were obtained with increasing BMT content. Switching the processing method from hand grinding to ball milling did not resolve this issue. The origin of the non-systematic electrical property changes may be beyond the mixing method used during the processing of the ceramics and may be linked to other parameters. For example, the particle size and distribution of the reagents used and/or the processing temperatures and times.

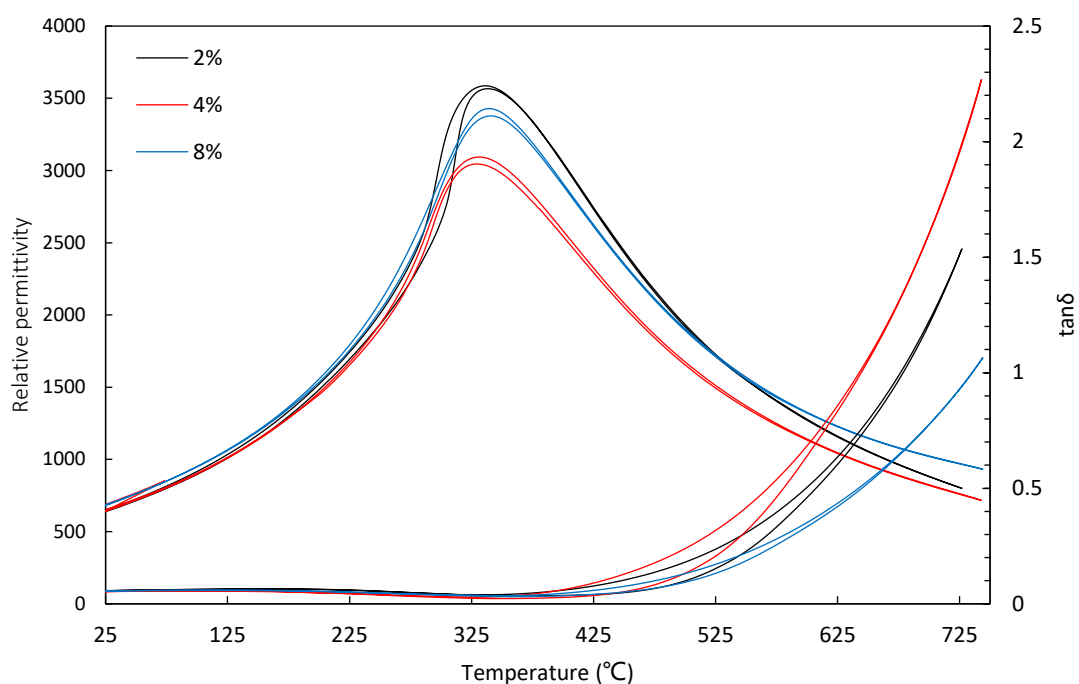


Figure 4.15. Relative permittivity and dielectric loss of NBT-BMT 2, 4 and 8% samples, measured at 1 MHz on heating and cooling.

Impedance spectroscopy was then conducted on ball milled NBT-BMT 2 and 8% samples. Z'' and M'' spectra and complex impedance plots are shown in Figures 4.16 and 4.17, respectively. The data are analysed using 2 parallel RC elements connected in series. For the 2% sample, the M'' plot shows a single response at high frequency, whereas the Z'' plot shows two peaks with different heights (one of the peaks is overlapping with the M'' peak) indicating the presence of an element with higher resistivity and one with lower resistivity. The M'' peak can be assumed to be the bulk response of the ceramic, whereas the larger Z'' peak (lower frequency) may indicate a grain boundary response. In the complex impedance plots for $x = 0.02$, two semi-circles are observed. The arc at higher frequency which is on the left has a capacitance value of 8×10^{-10} F/cm and is consistent with a bulk response and for the arc on the right it is 8×10^{-9} F/cm. which is consistent with a grain boundary response.

The 8% sample shows a different response with two M'' and one Z'' peaks in the spectra but again indicating the presence of two electro-active responses. Usually, the larger M'' peak is used to calculate the bulk response from samples but given the similar sizes of the 2 M'' peaks such as assignment may not be valid. Considering the smaller peak at 600 Hz is another electroactive region, then the M'' plot is portraying two capacitors of similar magnitude connected in series. As the M'' peak is broader and the peak value could be underestimated, therefore using the high frequency M'' peak value to calculate the 'bulk' capacitance would result in overestimation of capacitance.

Further information can be obtained from complex impedance plots, one large arc and a very small and distorted arc can be observed for the 8% sample. The large arc in the low frequency region has a capacitance of 1.08×10^{-9} F/cm, and the capacitance of the small arc is around 2.78×10^{-9} F/cm. These values indicate the small arc may correspond to a bulk-type (grain/core) response within the ceramic and the large arc is the response from a second electro-active region that maybe a resistive grain shell effect, secondary phase, or another matrix of NBT material. Alternatively, this might be evidence of large conductive grains embedded within small and resistive grain matrix. At this stage, the identity of this region is unclear and is under further investigation.

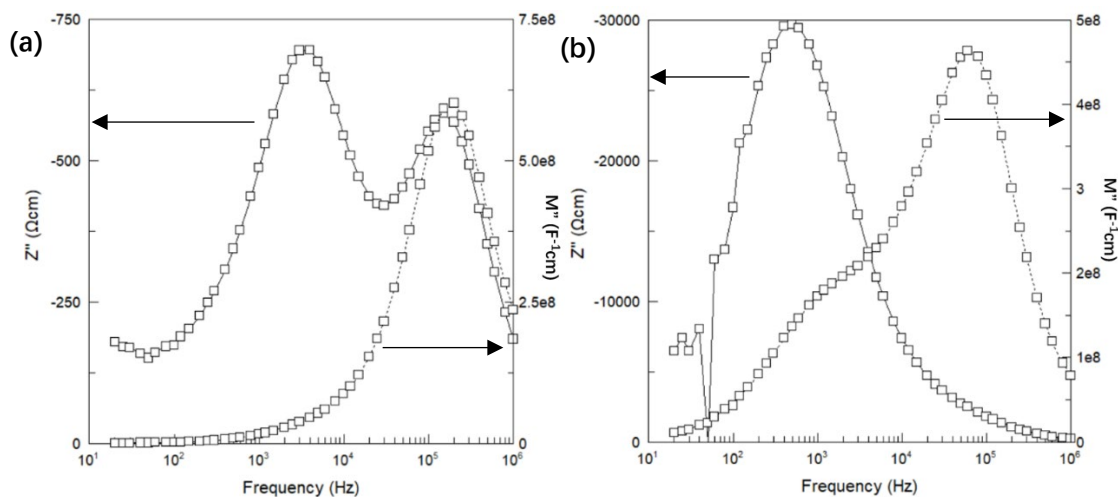


Figure 4.16. Plots of the imaginary components of the impedance and the electric modulus for NBT-BMT 2% (a) and 8% (b), measured at 499 °C.

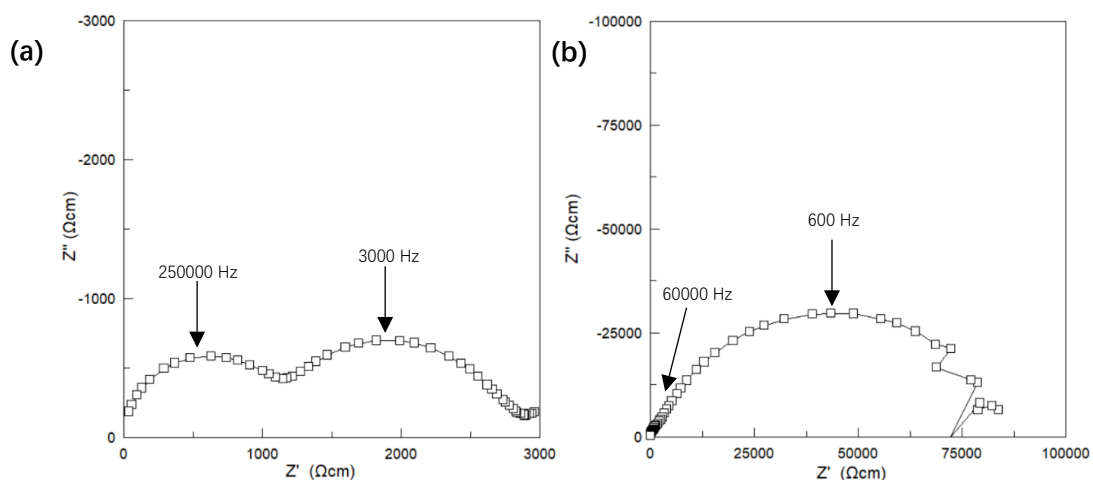


Figure 4.17. Complex impedance plot (Z') of 2% (a) and 8% (b) NBT-BMT, measured at 499 °C.

The relative permittivity extracted from 2% and 8% NBT-BMT samples' M'' and Z'' spectra were compared with the LCR data, in order to reveal any potential relationship between the electrical response with the microstructure. The 1/relative permittivity versus temperature plots of 2% and 8% NBT-BMT ball milled samples are shown in Figure 4.18. The 2% M'' extracted data has a gradient of 2.10×10^{-6} K and T_0 at 480 K, the 8% M'' extracted data has a gradient of 1.79×10^{-6} K and T_0 at 440 K. The 1/relative permittivity data extracted from M'' of both 2% and 8% are very similar to the 1 MHz LCR data showing strong temperature dependence and therefore indicating both can be attributed to a bulk material response. The 2% Z'' extracted data has gradient of 2.01×10^{-7} K and T_0 at 440 K, with less temperature dependence, suggesting a possible grain boundary type behaviour. For the 8% Z'' extracted data, the gradient is 1.03×10^{-6} K and T_0 at 640 K. It shows strong temperature dependency and Curie Weiss-type behaviour, suggesting the Z'' spectra of 8% NBT-BMT ball milled sample captured a bulk type behaviour (possibly shell) from possibly another type of NBT material with a different composition from the bulk material dominated 8% NBT-BMT sample's M'' spectra. This is in agreement with the impedance analysis results above. Thus, based on the Curie Weiss analysis, the 2% NBT-BMT ball milled sample shows grain and grain boundary type behaviour, but the 8% sample may contain two types of NBT based material, forming a composite structure.

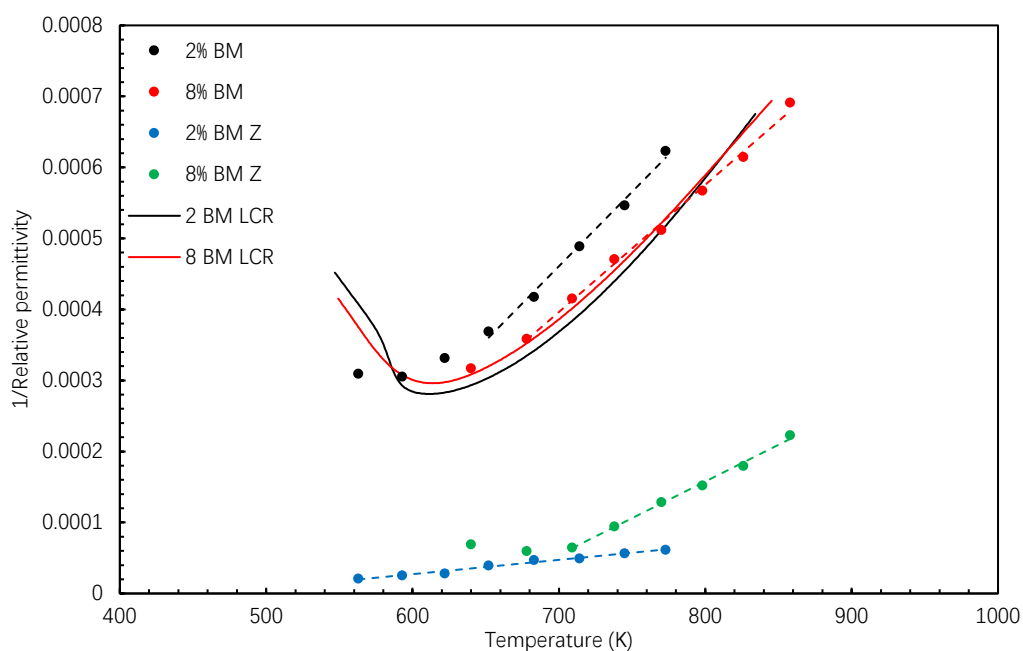


Figure 4.18. 1/relative permittivity versus temperature plots for 2% and 8% NBT-BMT ball milled samples. Relative permittivity data extracted from M'' and Z'' spectra were overlaid with the 1 MHz LCR data.

An Arrhenius plot of conductivity is presented based on data extracted from M'' and Z'' spectra of the samples, shown in Figure 4.19. For the NBT-BMT 2% sample, the conductivity retrieved from Z'' and M'' plots are separated by less than one order of magnitude, which is in agreement with the fact that Z'' plots show two peaks of different height. Again, (based on the magnitude of the extracted capacitance values) the M'' plots are assumed to be the grain

response and data from Z'' is from the grain boundary response. The M'' data show the bulk to be conductive, although the conductivity is lower than undoped NBT. Considering the Na/Bi ratio in the NBT-BMT, the NBT-BMT system is actually forming Bi-rich NBT. According to Li et al's discovery of insulating NB0.51T [4], this could be the scenario of insulating Bi-rich NBT matrix and conductive Mg-doped NBT forming a composite ceramic. For the 8% sample, the conductivity data retrieved from the Z'' peak is much lower than that from the larger M'' peak. The Z'' data clearly indicate a more resistive response that is closer to insulating NB0.51T, whereas the M'' data indicate a conductive region that is very similar in magnitude to the bulk response of the 2% sample.

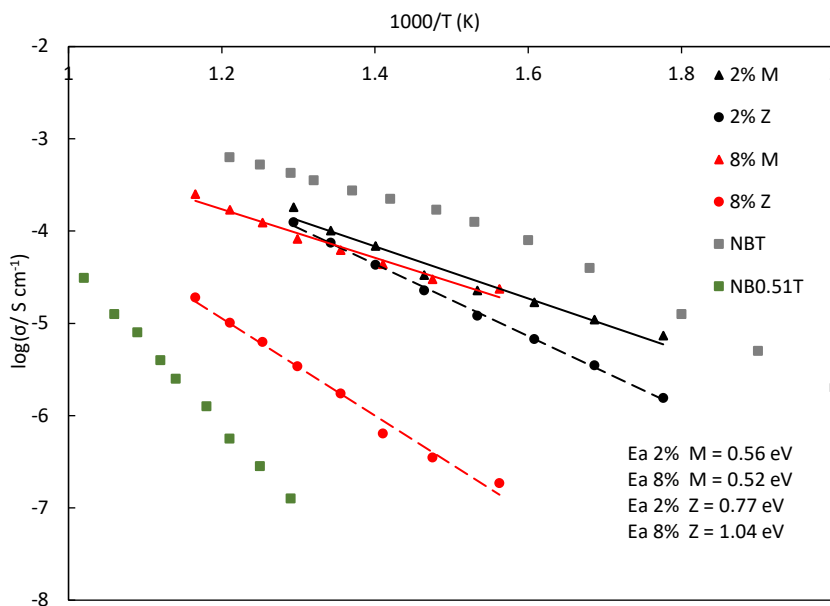


Figure 4.19. Arrhenius plots of conductivity for ball milled NBT-BMT samples. Data calculated from the Z''(Z) and M''(M) peaks in the impedance data. Conductivity for insulating NB0.51T and conductive NBT from work by Li et al [4] are included for comparison.

Comparison between hand ground and ball milled samples

The conductivity of hand ground and ball milled samples at the same BMT percentage is compared, as shown in Figure 4.20. Both hand ground samples have inferior bulk conductivity and much higher activation energy values than their ball milled counterparts. The 8% BMT hand ground sample shows lower conductivity than the insulating NB0.51T composition. The ball milled samples have very similar bulk conductivity close to the conductive NBT value, regardless of the BMT percentage. The vast difference of conductivity between the two types of NBT-BMT samples is possibly due to the processing method, which was unexpected.

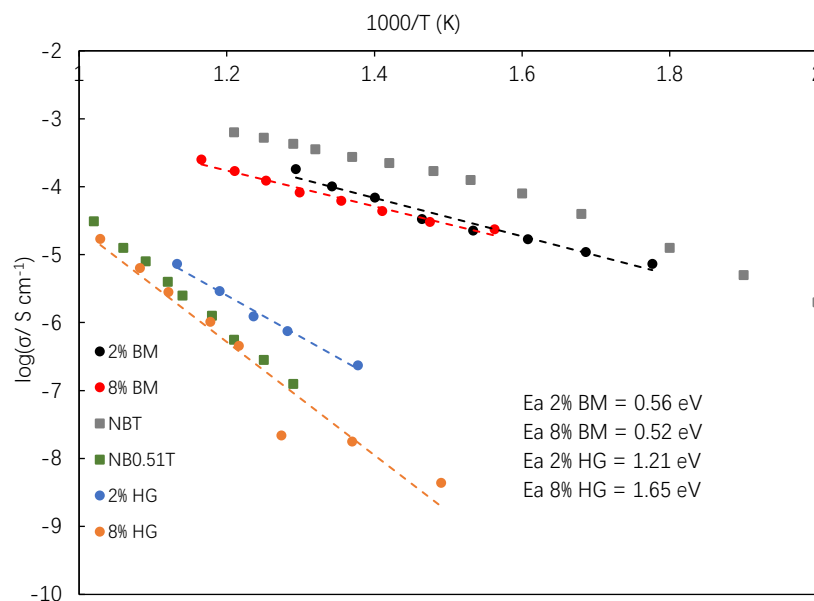


Figure 4.20. Arrhenius plots of conductivity for hand ground and ball milled NBT-BMT samples of the same composition with data extracted from M'' peaks. Conductivity for insulating NB0.51T and conductive NBT from work by Li et al [4] are included for comparison. Activation energy values are calculated based on extracted M'' bulk conductivity values.

The F_{\max} analysis from the high frequency M'' peaks is shown as $\log(F_{\max})$ versus $1000/T$ plots for the hand ground and ball milled NBT-BMT samples at 2 and 8%, Figure 4.21. The F_{\max} differences between 2 and 8% NBT-BMT bulk responses are relatively small, regardless of the processing method, suggesting the compositional change between the 2 and 8% bulk material are small. As the hand ground NBT-BMT SEM images revealed, secondary phase appeared when the BMT content reached 2%. The solid solution limit of BMT in NBT could be very low, thus the small F_{\max} difference between the 2 and 8% bulk responses. However, the F_{\max} difference between hand ground and ball milled samples is large, indicating the processing method could be the origin of the different electrical properties for these samples.

The hand ground samples used coarse pellets of MgO as a reactant, and ball milled samples used a finer powder form of MgO. It is possible the particle size difference of the starting reactant could be associated with the different electrical properties of the sintered products. In the case of ball milling and finer reagents, the MgO is better distributed and incorporated into the grains and this results in larger F_{\max} values and is consistent with a higher level of

ionic conduction, as observed for Mg-doped NBT. In contrast, poor mixing and incorporation of MgO for the hand ground samples indicates that Na/Bi ratio may play a more important role. Thus, the grains are Bi-rich and the samples are electrically insulating.

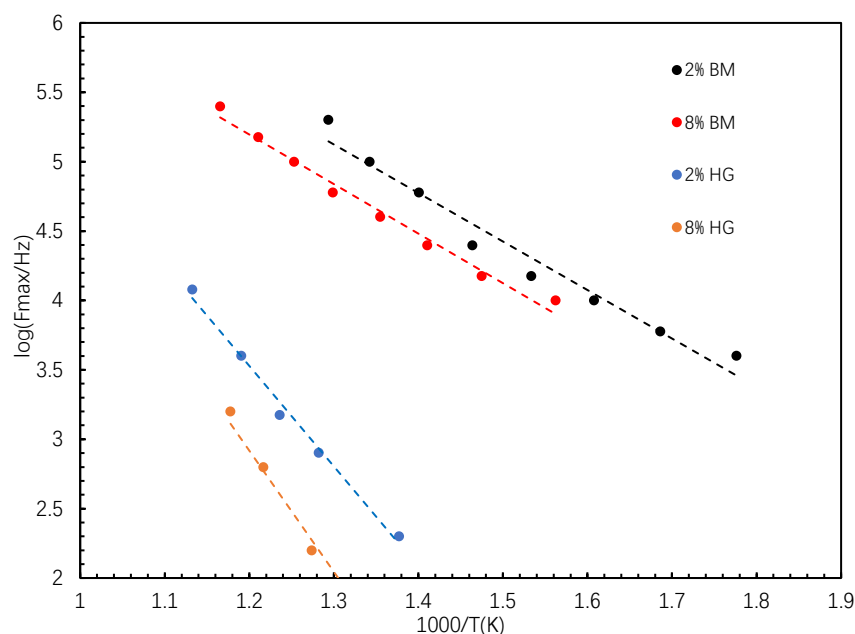


Figure 4.21. $\log(F_{\max})$ versus $1000/T$ plot for hand ground (HG) and ball milled (BM) NBT-BMT samples of the same composition. The F_{\max} value is located from the peak position in M'' spectra of the corresponding samples.

NBT-BMT sintering temperature dependence

With the bulk conductivity of 2% and 8% ball milled NBT-BMT samples (based on M'' plots) being very similar, more samples and compositions are required to establish any trends that may be present in the ball milled samples. Hence 6% BMT samples were prepared at different sintering temperatures and characterised with impedance spectroscopy. This shows how the sintering temperature may affect the electrical properties of NBT-BMT.

6% BMT samples were sintered at 1100 and 1150 °C, the pellets had relative density over 90% for both temperatures. SEM was used to reveal the microstructure of the samples. In Figure 4.22, the BSE SEM for the 1150 °C samples show light-coloured grains and dark coloured secondary phase embedded in the grain boundaries. Compositional analysis shows the secondary phase contains very high Mg concentration at 17 at.%. The grains contain low Mg concentration at 0.8 at.%. For the 1100 °C sample, only light-coloured grains can be observed, no secondary phase is present and there are minor voids between the grains. The compositional analysis shows the Mg concentration in the grains is ~0.5 at. %, shown in Figure 4.23. It is peculiar as there is no trace of a Mg-rich phase being present and the Mg concentration within the grains is well below the 6% BMT in the nominal starting composition.

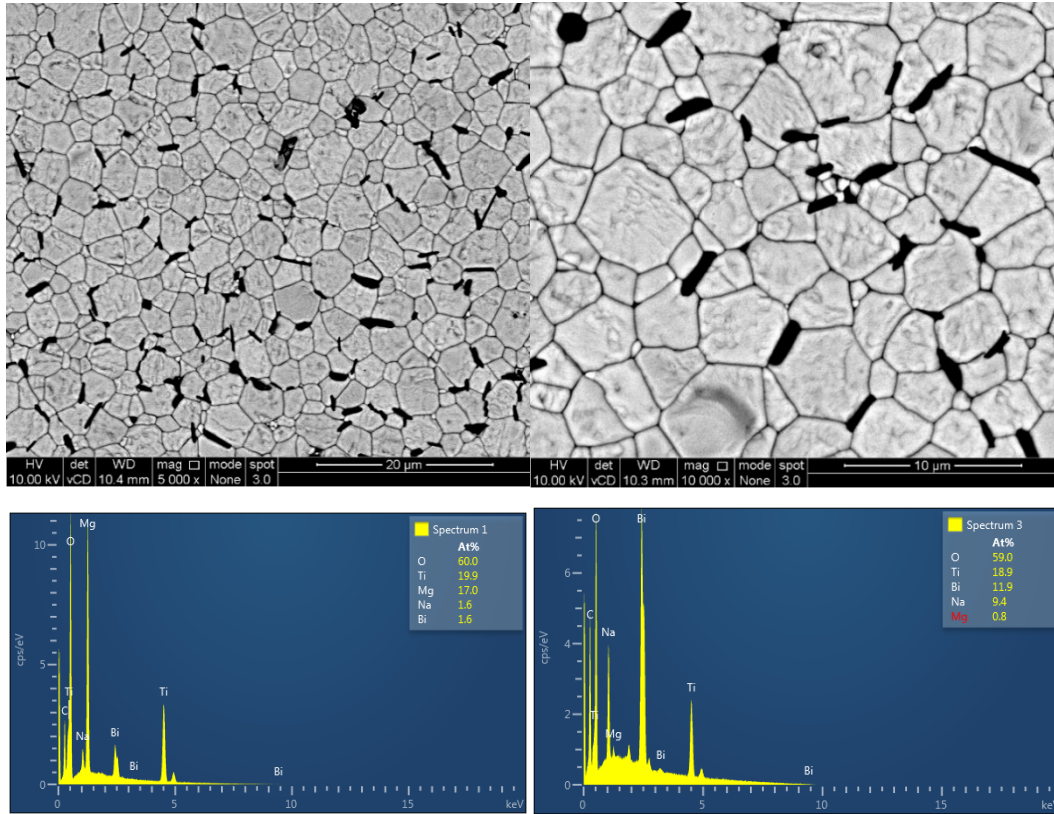


Figure 4.22. Back-scattered electron SEM images of a 6% BMT sample sintered at 1150 °C where a dark secondary phase appeared between the grain boundaries. Compositional analysis on the dark area (Spectrum 1) shows high Mg concentration, the light-coloured grains (Spectrum 3) show very low Mg concentration.

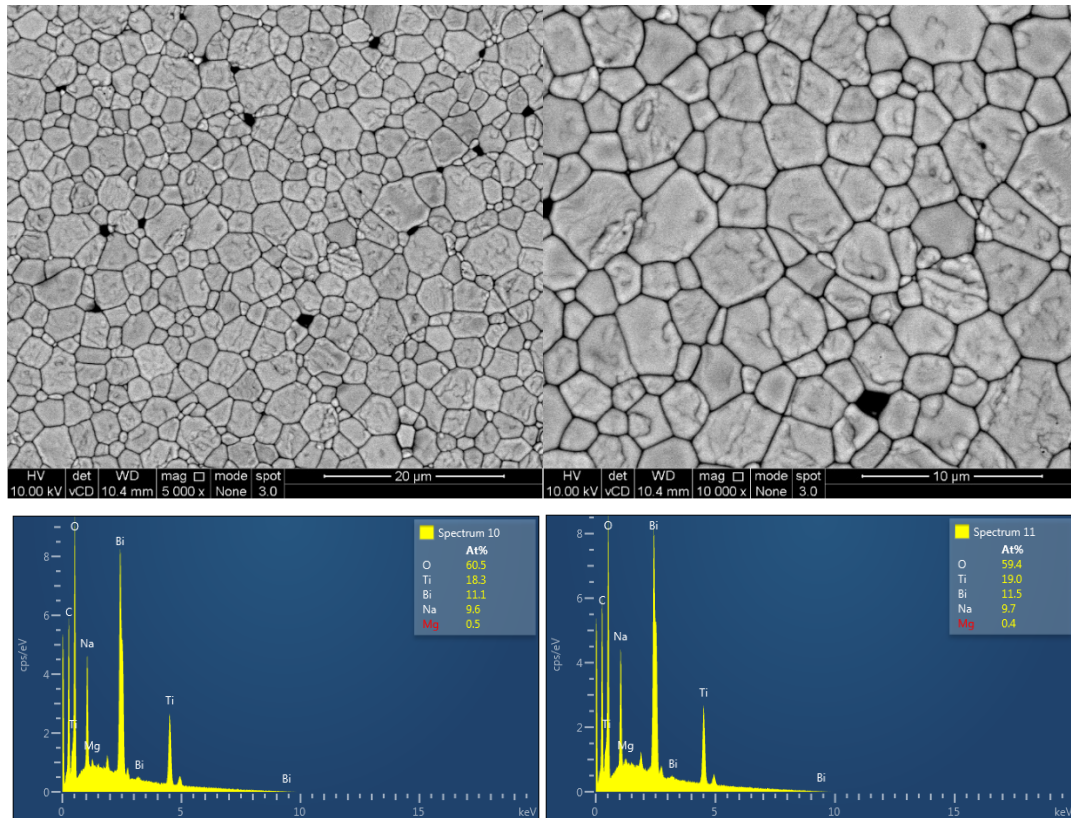


Figure 4.23. Back-scattered electron SEM images of a 6% BMT sample sintered at 1100 °C where no dark secondary phase is observed. Compositional analysis on the grains shows low Mg concentration in multiple locations. Two examples are shown in Spectra 10 and 11.

The impedance data for samples at the two sintering temperatures are dramatically different, which is expected as the microstructures of the 1100 and 1150 °C samples revealed by SEM are very different, Figure 4.24 and Figure 4.25, respectively. Similar to the hand ground and previous ball milled samples, the data are analysed using 2 parallel RC elements connected in series. For the 1150 °C sample, a single response is shown in the M'' plot at high frequency, whereas two peaks with different heights (the high frequency peaks is overlapping with the M'' peak) are observed in the corresponding Z'' plot, suggesting two electroactive regions with high resistivity and low resistivity, Figure 4.24(a). According to the extracted capacitance of the M'' peak at 5.97×10^{-10} F/cm, it can be assumed to be the bulk response of the ceramic, whereas the larger Z'' peak at lower frequency has capacitance of 2.48×10^{-9} F/cm, which could be a grain boundary or another type of NBT based material with higher resistivity. In the complex impedance plots for the 1150 °C sample, two semi-circles can be observed. The arc at higher frequency which is on the left has a capacitance value of 5.97×10^{-10} F/cm and for the arc on the right it is 2.48×10^{-9} F/cm.

The 1100 °C sample shows two very poorly resolved responses in M'' and Z'' spectra, Figure 4.24(b). From complex impedance plots, a very distorted small arc at high frequency and a large arc at low frequency can be observed, Figure 4.25(b). The small arc is difficult to separate from the large arc. The capacitance extracted from M'' and Z'' are very close too with values of 4.51×10^{-10} F/cm and 6.95×10^{-10} F/cm, respectively. These are reasonable values for a bulk

response, thus two NBT type material could co-exist in the sample, Figure 4.24(b).

Arrhenius plots for the two samples are shown in Figure 4.26 where conductivity values are extracted from M'' and Z'' peak values, respectively. The 1150 °C sample has higher conductivity than the 1100 °C sample based both on M'' and Z'' spectra data. The calculated activation energy for the 1150 °C bulk material (1150 M) is 0.49 eV and the 1100 °C bulk material (1100 M) has a value of 0.79 eV.

F_{max} analysis in the form of $\log(F_{max})$ versus $1000/T$ plots for 6% NBT-BMT samples sintered at 1150 and 1100 °C was constructed by locating the F_{max} of each sample from their M'' spectra and Z'' spectra, Figure 4.27. The F_{max} values extracted from M'' spectra for 1100 and 1150 °C samples overlap, suggesting the bulk composition of both samples are almost the same. The F_{max} values extracted from the Z'' spectra for both samples deviated slightly, also suggesting the secondary electro-active region's composition are very similar. The $1/\text{relative permittivity}$ versus temperature plot in Figure 4.28 shows the relative permittivity extracted from M'' and Z'' spectra for the 1100 and 1150 °C samples. The M'' spectra data for the 1100 °C sample has a gradient of 5.97×10^{-7} K and T_0 at 520 K. The Z'' spectra data of the same sample has a gradient of 6.64×10^{-7} K and T_0 at 650 K. For the 1150 °C sample, the M'' spectra extracted $1/\text{relative permittivity}$ data has a gradient of 4.16×10^{-7} K and T_0 at 530 K, and the Z'' spectra extracted data has a gradient of 3.54×10^{-7} K, T_0 at 600 K.

Both M'' and Z'' extracted data show strong temperature dependent Curie Weiss type behaviour indicating the electrical responses captured by the M'' and Z'' spectra are all bulk behaviour of NBT type materials. It is possible that both 1100 and 1150 °C samples contain conductive and insulative grains of different compositions, which can be supported by the impedance analysis. A possible scenario could be the formation of Mg-doped NBT which is more conductive and Bi-rich NBT which is more resistive, due to the difference in the distribution of the ions in NBT-BMT. More data are required to have a better understanding of this issue. At present, we know that the ball milled NBT-BMT system is sensitive to the sintering temperature and close attention should be paid when preparing samples for each composition. Again, sintering temperature sensitivity was not reported for the NBT-BMN system. The presence of Nb^{5+} ions in the structure could potentially benefit the homogenous distribution of Mg and the NBT-BMN system is less sensitive to sintering conditions.

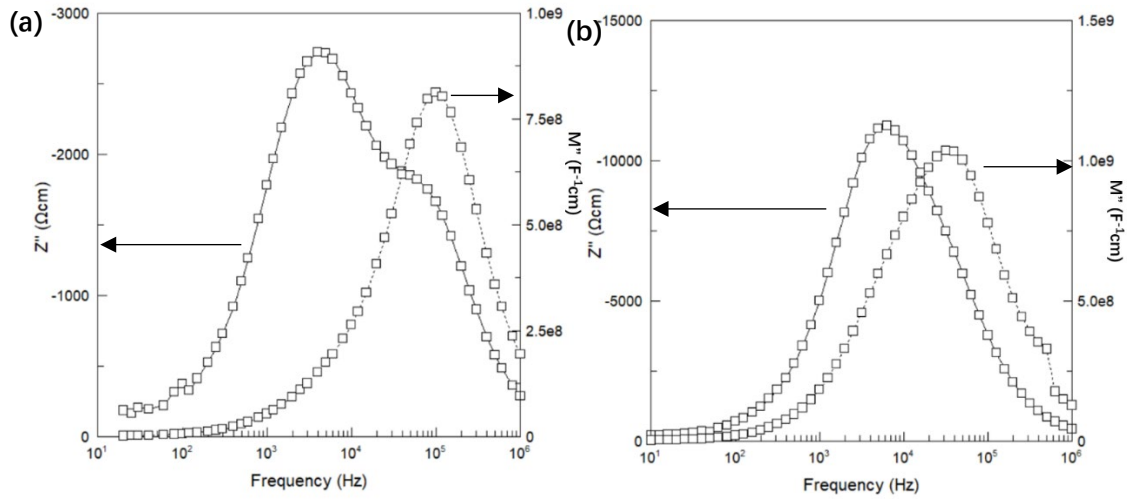


Figure 4.24. M'' and Z'' spectra for 6% NBT-BMT ball milled samples sintered at different temperatures. (a) 1150 °C sample measured at 560°C. (b) 1100 °C sample measured at 565 °C.

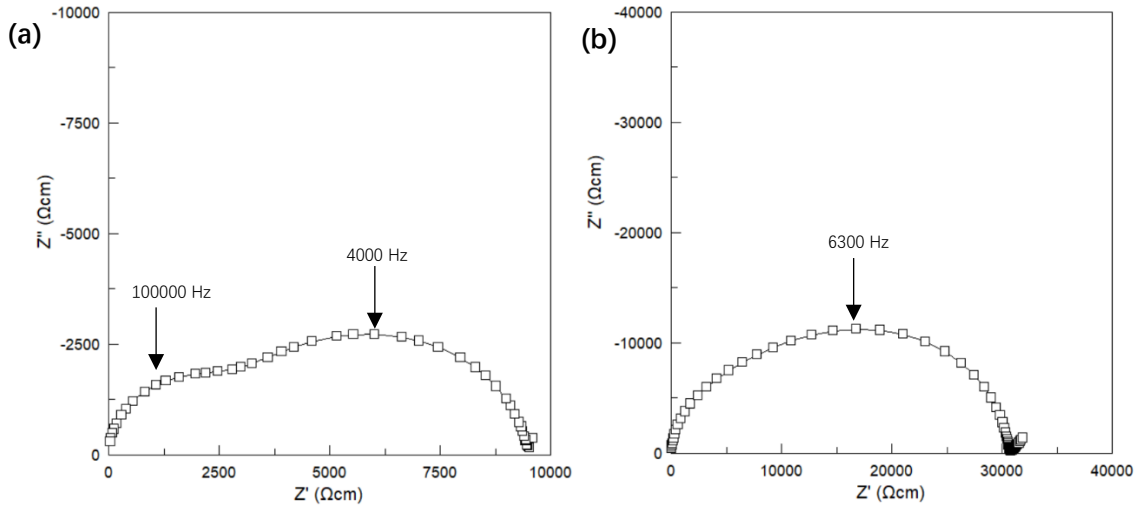


Figure 4.25. Complex impedance spectra for 6% NBT-BMT ball milled samples sintered at different temperatures. (a) 1150 °C sample measured at 560 °C. (b) 1100 °C sample measured at 565 °C.

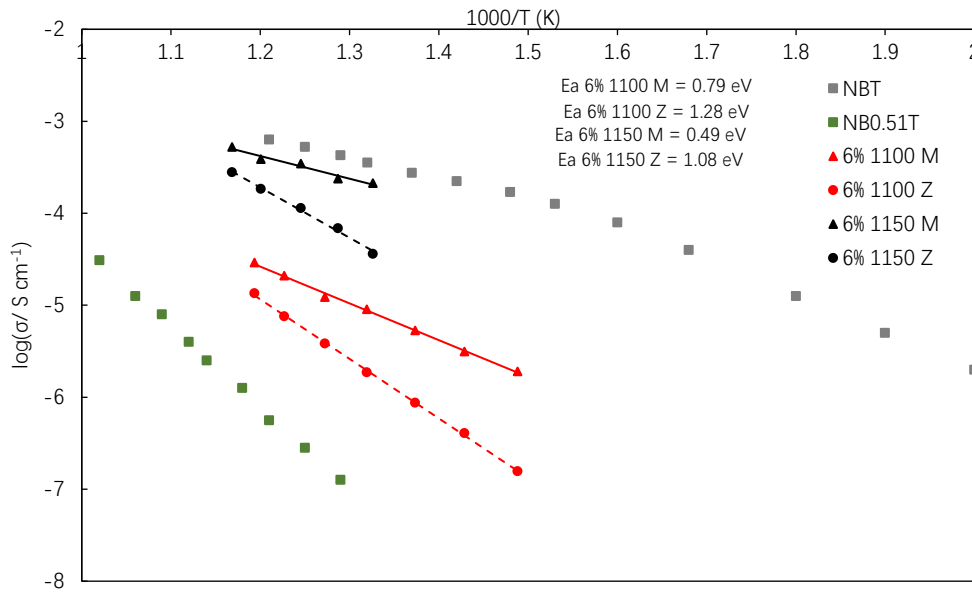


Figure 4.26. Arrhenius plots of 6% BMT samples sintered at 1100 and 1150 °C with conductivities calculated from the Z''(Z) and M''(M) peaks in the impedance data. Conductivity for insulating NBO.51T and conductive NBT from work by Li et al [4] are included for comparison.

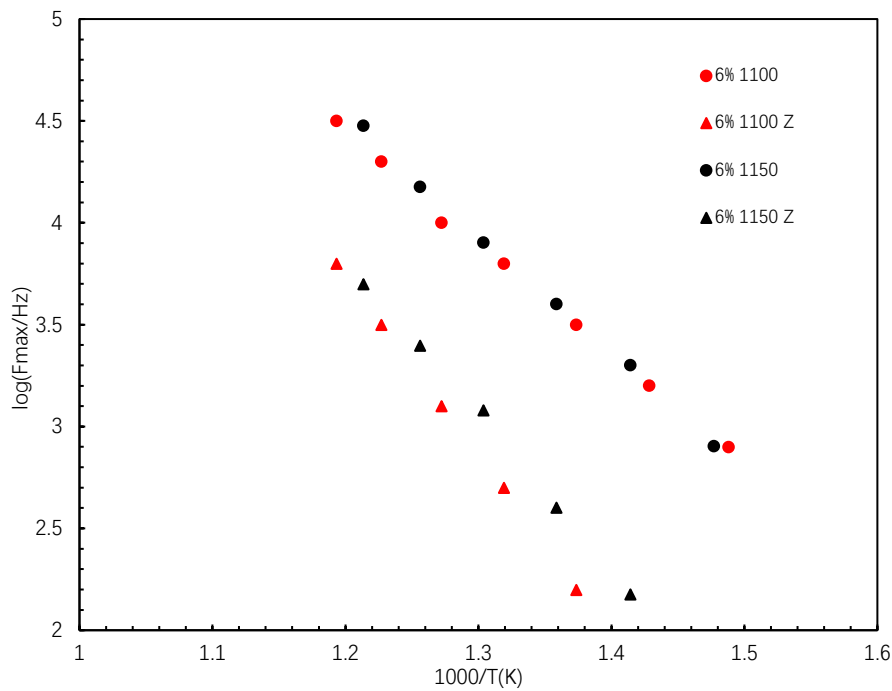


Figure 4.27. $\log(F_{max})$ versus $1000/T$ plot for 6% NBT-BMT samples sintered at 1100 (red) and 1150 °C (black). The F_{max} value is located from the peak position in M'' and Z'' spectra of the corresponding samples.

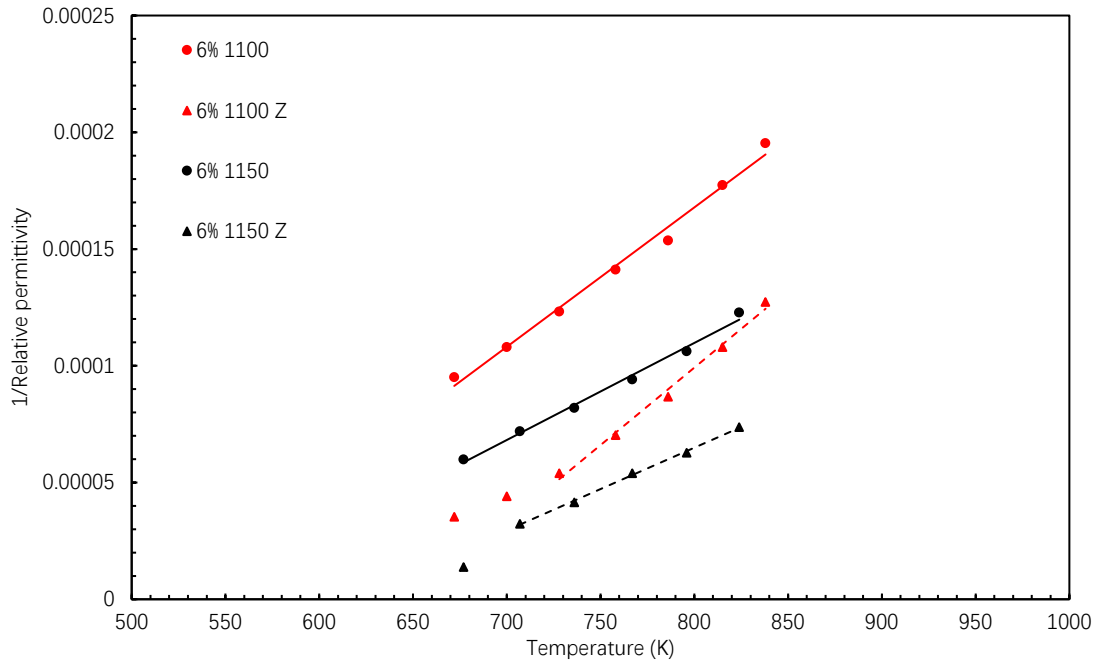


Figure 4.28. 1/relative permittivity versus temperature plot for 6% NBT-BMT samples sintered at 1100 (red) and 1150 °C (black). The relative permittivity values are extracted from the M'' and Z'' spectra of the corresponding samples.

4.2.2 $\text{Na}_{0.5}\text{Bi}_{0.5}\text{TiO}_3\text{-BiZn}_{0.5}\text{Ti}_{0.5}\text{O}_3$

Pellet samples of (1-x) NBT-xBZT solid solution were prepared using the same ball milling processing details as described in the previous section. Similar to NBT-BMT samples, ball milling was implemented after a few months of hand grinding, therefore the number of compositions prepared was limited in a short period of time. From the XRD patterns shown in Figure 4.29, the NBT-BZT sample at 8% doping shows 4 additional peaks at lower angles, suggesting the presence of a secondary phase.

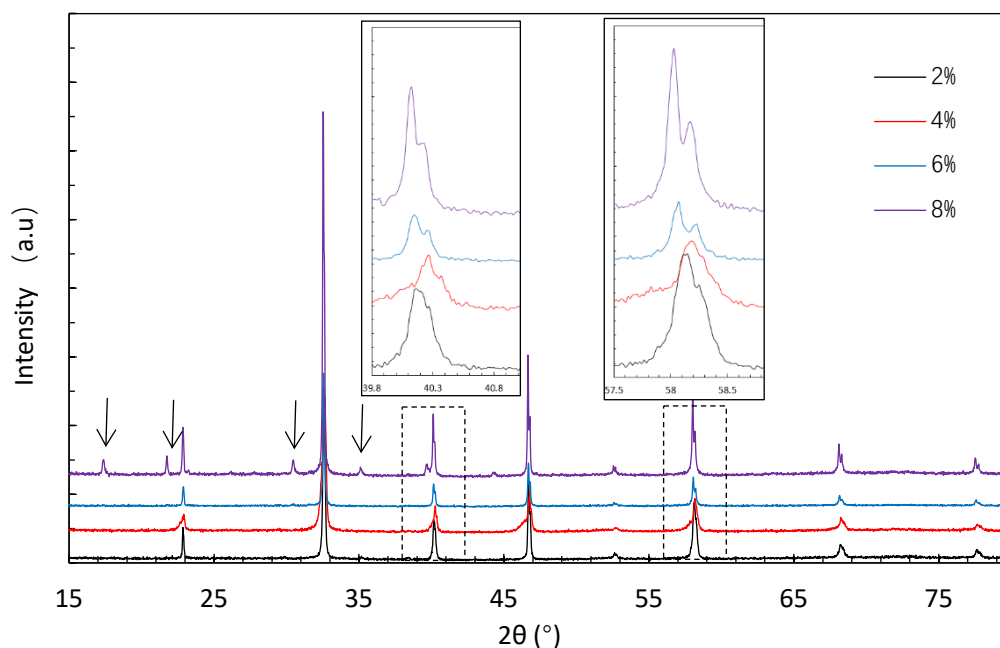


Figure 4.29. XRD patterns of ball milled NBT-BZT samples for $x=0.02, 0.04, 0.06$ and 0.08 sintered at $1150\text{ }^\circ\text{C}$.

SEM images of $x=0.04$ and 0.06 were recorded to investigate the microstructure, Figure 4.30. For the 4% sample, small areas with brighter colour were observed under the back-scattered mode, indicating the presence of an inhomogeneous distribution of reactants, incomplete reaction and/or a secondary phase. As reported by Pradal-Velázquez, BZN also reaches a solid solution limit at 4% [13]. The 6% BZT sample shows clear presence of a secondary phase. EDS studies show these areas are Zn-rich and Bi-deficient, although the XRD pattern revealed no information about the phase(s) present, Figure 4.31. Further investigation is required to identify this phase(s).

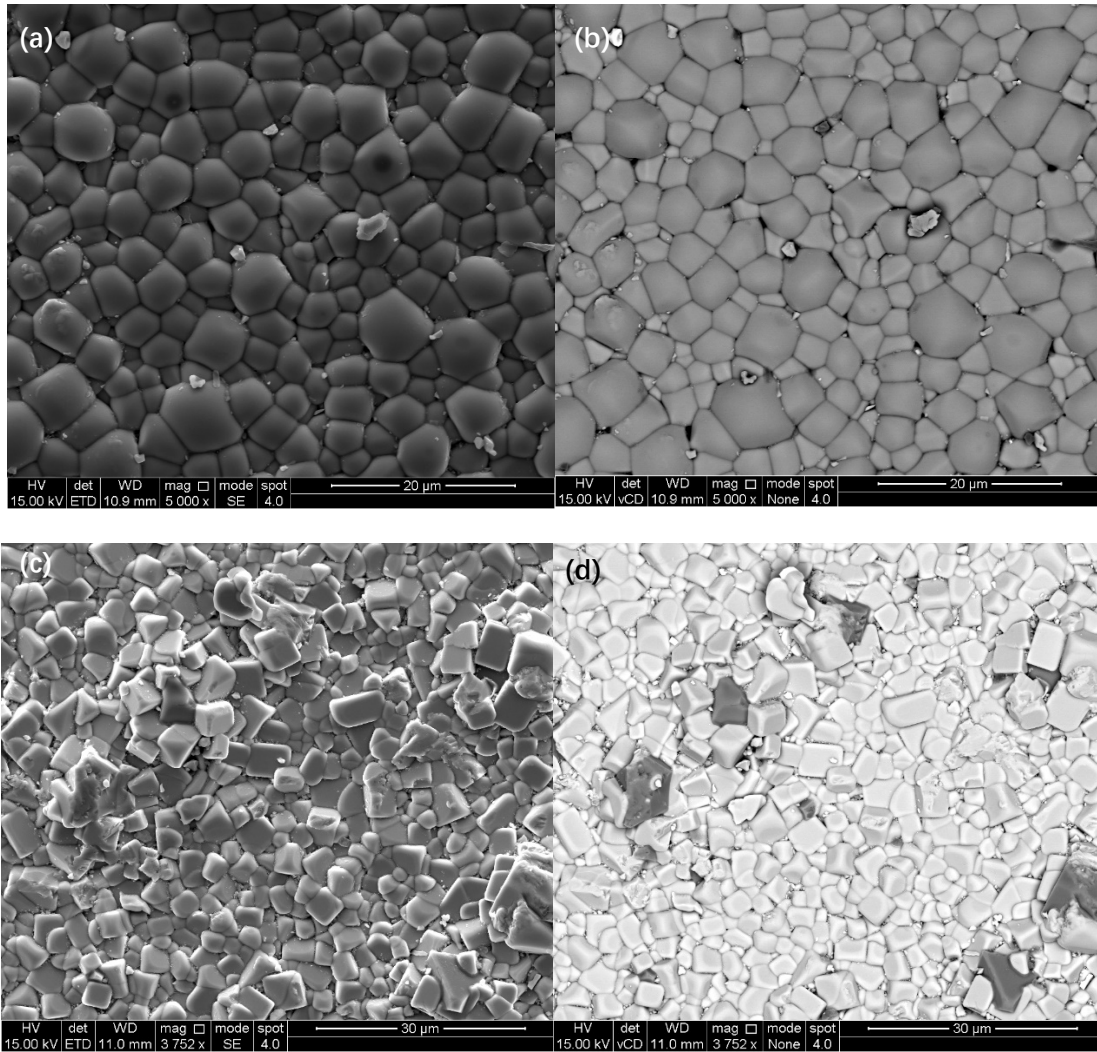


Figure 4.30. Surface SEM images of 4% (a and b) and 6% (c and d) NBT-BZT samples.

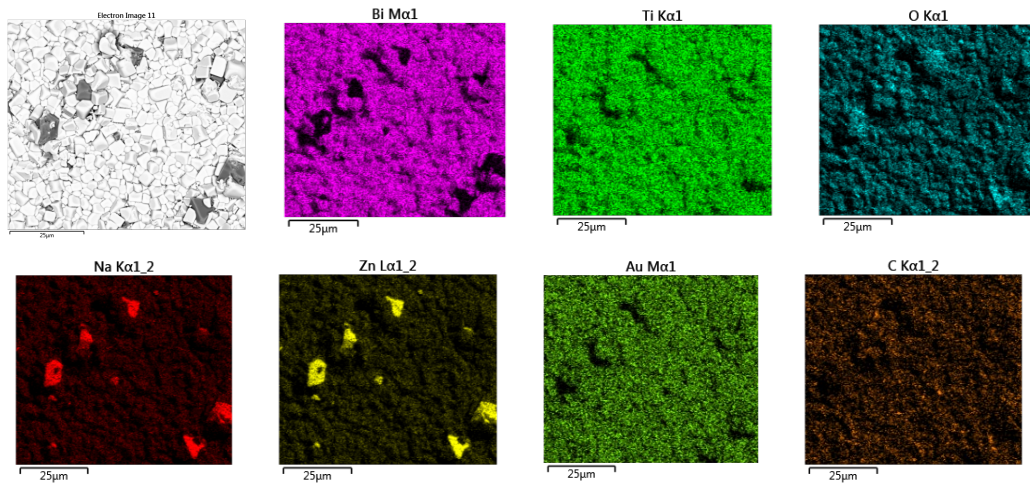


Figure 4.31. EDS mapping of a 6% BZT sample. A Na-Zn rich and Bi deficient secondary phase can be observed.

Figure 4.32 shows the temperature profile of relative permittivity and dielectric loss of NBT-BZT solid solutions for $x= 0.02, 0.04$ and 0.08 . Unlike NBT-BMT samples, the BZT samples show a clear trend. With increasing BZT content in the ceramics, the relative permittivity decreases with the peak becoming broader, also no significant shift in T_{max} is observed. The dielectric loss in the high temperature region has also been suppressed.

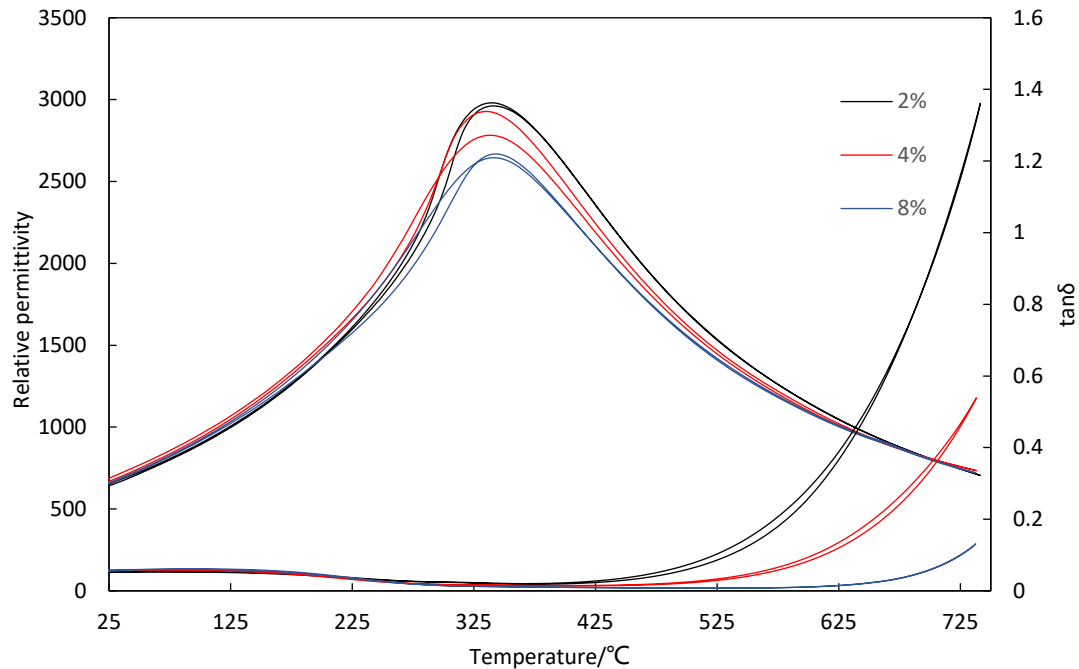


Figure 4.32. NBT-BZT solid solutions temperature profile of relative permittivity and dielectric loss at 1 MHz.

Z'' and M'' spectra and complex impedance plots are shown in Figures 4.33 and 4.34, respectively. The data are analysed using 2 parallel RC elements connected in series. For the 2% BZT sample, the M'' plot shows a single response at high frequency (50 kHz), whereas the Z'' plot shows two peaks with different heights (high frequency peak overlapped with the M'' peak at 50 kHz) suggesting the presence of an element with higher resistivity and one with lower resistivity. Based on the extracted capacitance of 1.47×10^{-10} F/cm, the M'' peak can be assumed to be the bulk response of the ceramic, whereas the lower frequency (1200 Hz) Z'' peak may indicate a grain boundary response as its capacitance is higher at 8.11×10^{-10} F/cm. For the 4% BZT sample, Z'' spectra show one major peak at lower frequency (300 Hz) and a very distorted peak at higher frequency (15 kHz). The 6% and 8% BZT samples display only one peak in both M'' and Z'' spectra that overlap at the same frequency. The capacitance values (6% = 4.12×10^{-10} F/cm, 8% = 3.72×10^{-10} F/cm) suggest this is a bulk response. A difference occurs in that the 6% BZT sample have $F_{max} \sim 25$ kHz, whereas for the 8% sample F_{max} is at 2 kHz.

The Z^* plot of 2% BZT consists of a smaller arc at lower frequency and a larger arc at higher frequency. By calculating the capacitance of the two arcs, the small arc has a higher value of 8.11×10^{-10} F/cm and may be considered as a grain boundary response, whereas the larger arc has a capacitance of 1.47×10^{-10} F/cm and is the bulk response. For $x=0.08$, only one semi-circle can be observed, where the associated capacitance is about 3.72×10^{-10} F/cm and is

assumed to be a bulk response. Similar plots and assignments for such conductive and insulating NBT samples have been observed and reported by several researchers [5] [14].

The 4% BZT sample displays more complex behaviour where the Z^* plots display two, distorted and overlapping arcs, with reversed size compared to $x=0.02$. Combined with the microstructure revealed by SEM where $x=0.04$ has grains of uneven sizes this could support the research reported by Yang et al which shows that undoped, conductive NBT ceramics tend to have large grained microstructures whereas undoped, insulating NBT ceramics have small/fine grained microstructures [14]. When there is a matrix of larger and smaller grains in a ceramic the report reveals that the current will prefer to flow through the larger grains and therefore avoid the smaller resistive grains and higher density of resistive grain boundaries. It may be possible, therefore that the M'' data for $x=0.04$ is not capturing the full bulk response of the ceramic. Another factor to consider is the change in the dominance of the charge carrier in the material. If the NBT-BZT series follows the trend reported by Yang and Pradal-Velázquez, the 2% NBT-BZT sample would be mainly an oxide-ion conductor and the 8% NBT-BZT sample would have only electronic conduction if all the oxygen vacancies have been trapped or filled [5] [13]. The 4% NBT-BZT may represent a mixed ionic-electronic conductor and these can be harder to characterise by electrical measurements. The 6% NBT-BZT sample was tested under air and nitrogen atmosphere and the impedance data are shown in Figure 4.34 (d). When measured in nitrogen the measured resistance decreased compared to an air atmosphere, confirming that 6% NBT-BZT sample contains an n-type electronic conduction mechanism.

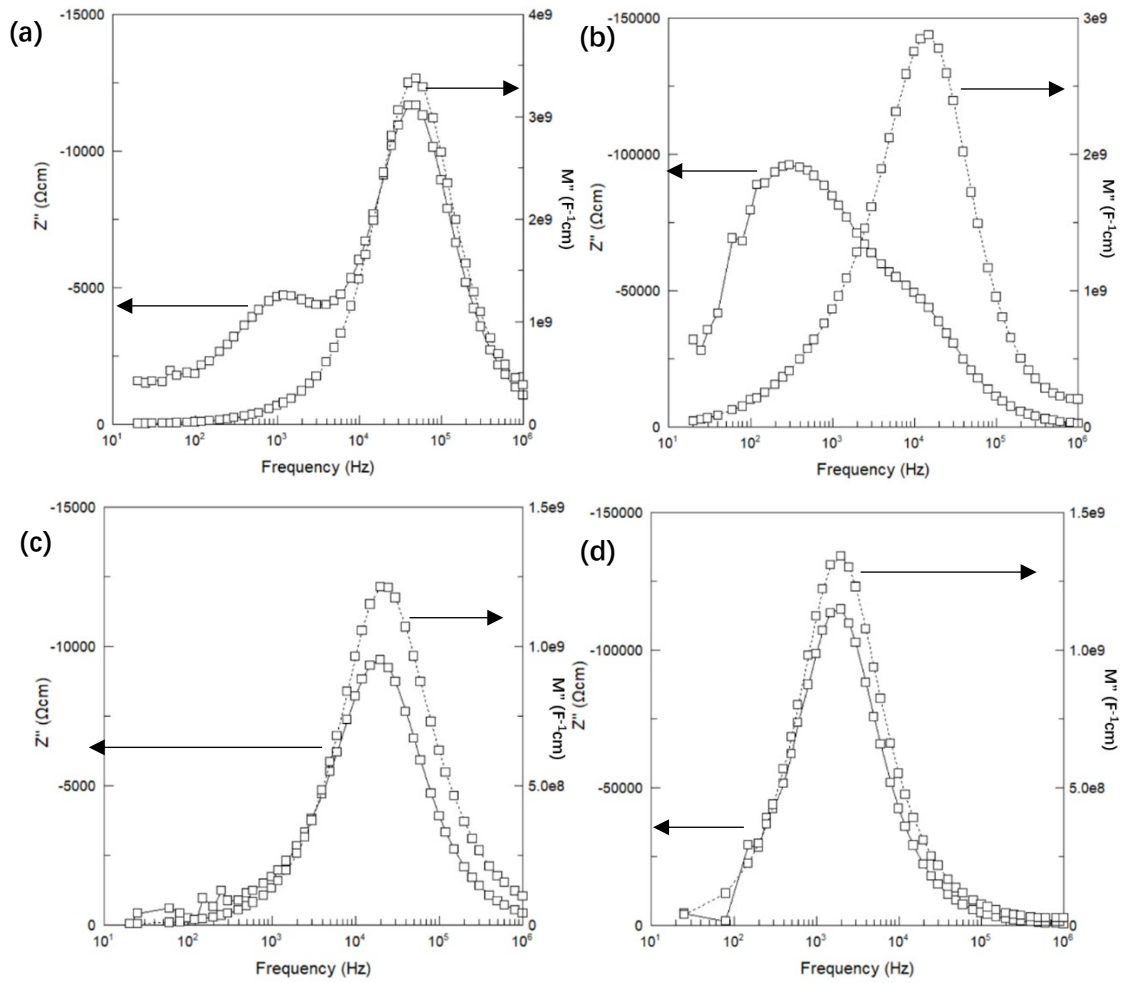


Figure 4.33. Imaginary part of impedance and modulus response for the impedance measurements of (a) NBT-BZT 2% at 489 °C, (b) NBT-BZT 4% at 499 °C, (c) NBT-BZT 6% at 662 °C and (d) NBT-BZT 8% at 577 °C.

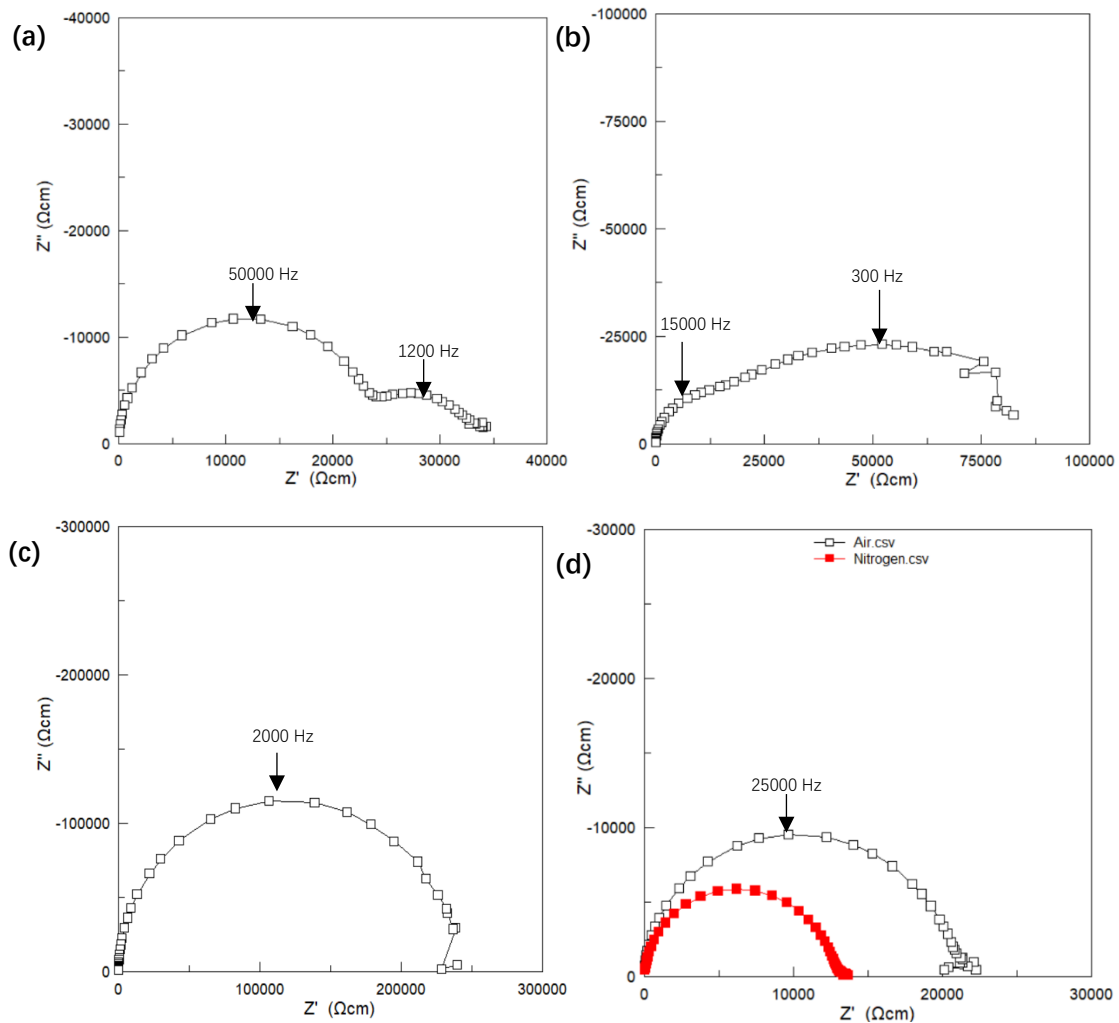


Figure 4.34. Complex impedance plots (Z') for (a) NBT-BZT 2% at 489 °C, (b) NBT-BZT 4% at 499 °C (c) NBT-BZT 8% at 577 °C and (d) NBT-BZT 6% at 662 °C. The 6% BZT sample's impedance response is measured under air (black) and nitrogen atmosphere (red). The reduction of resistance suggests the NBT-BZT 6% sample contains significant electronic conduction.

The temperature dependency of the relative permittivity of the NBT-BZT samples are shown in the form of a Curie Weiss type analysis. The relative permittivity extracted from 2% and 8% NBT-BZT samples' M'' and Z'' spectra were compared with the 1 MHz LCR data, Figure 4.35. The 2% M'' extracted data has a gradient of 2.24×10^{-6} K and T_0 at 480 K and the 2% Z'' extracted data has a gradient of 1.02×10^{-6} K and T_0 at 650 K. The 8% sample data extracted from M'' and Z'' overlapped and have a gradient of 2.87×10^{-6} K and T_0 at 540 K. The $1/\text{relative permittivity}$ extracted from the M'' data for the 2 and 8% samples and from the Z'' data for the 8% sample are very close to that for the 1 MHz LCR data. All show strong temperature dependence indicating all three responses can be assumed to be a bulk material response. The 2% Z'' extracted data shows far less temperature dependence, suggesting possible grain boundary behaviour. Thus, the 2% NBT-BZT sample shows grain and grain boundary type behaviour but the 8% sample shows a bulk response dominated in both M'' and Z'' spectra.

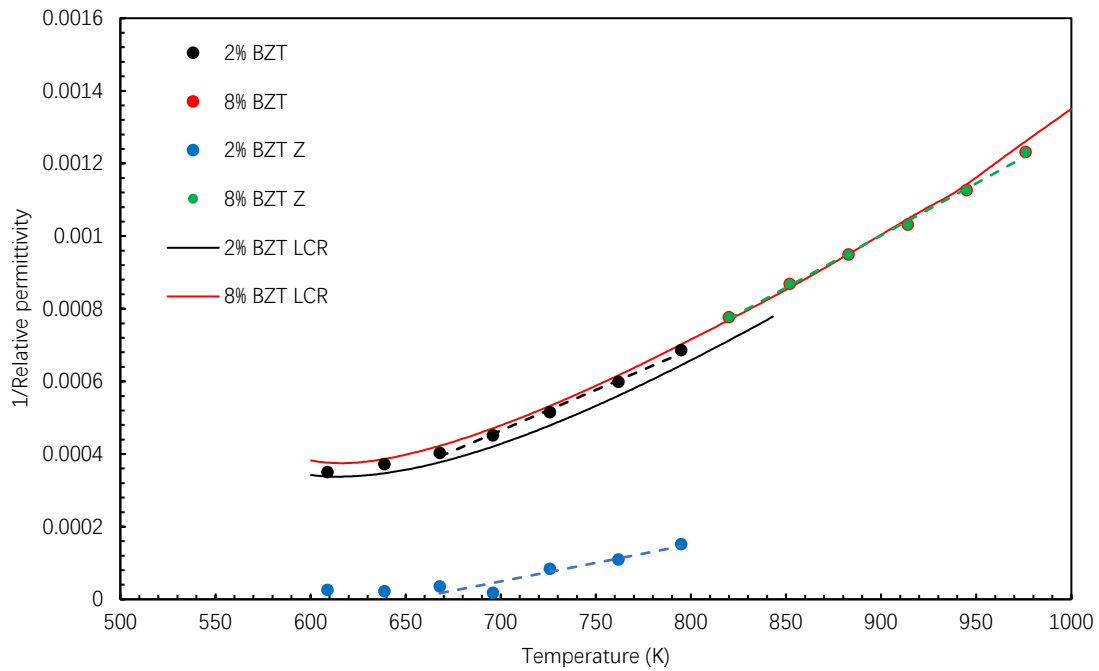


Figure 4.35. 1/relative permittivity versus temperature plots for 2% and 8% NBT-BZT samples. The capacitance data were retrieved from the impedance measurements (via M'' and Z'' plots) for 2 and 8% NBT-BZT samples. 1MHz LCR data are also included.

Arrhenius plots of conductivity have been constructed from the M'' and Z'' plots of these samples and are shown in Figure 4.36. Despite the 4% BZT sample's M'' data may not be the complete bulk response, it is still used for a preliminary inspection. The bulk conductivity of the samples decreases with increasing BZT content in the solid solutions. The activation energy also increases from 2%'s 0.73 eV to 1.63 eV for the 8% sample. The 8% sample has conductivity similar to the insulating bismuth-rich NBT. This is similar to what Yang and Pradal-Velázquez reported [5] [14], i.e. that the NBT-BZN solid solution can reach the insulating level of NB0.51T.

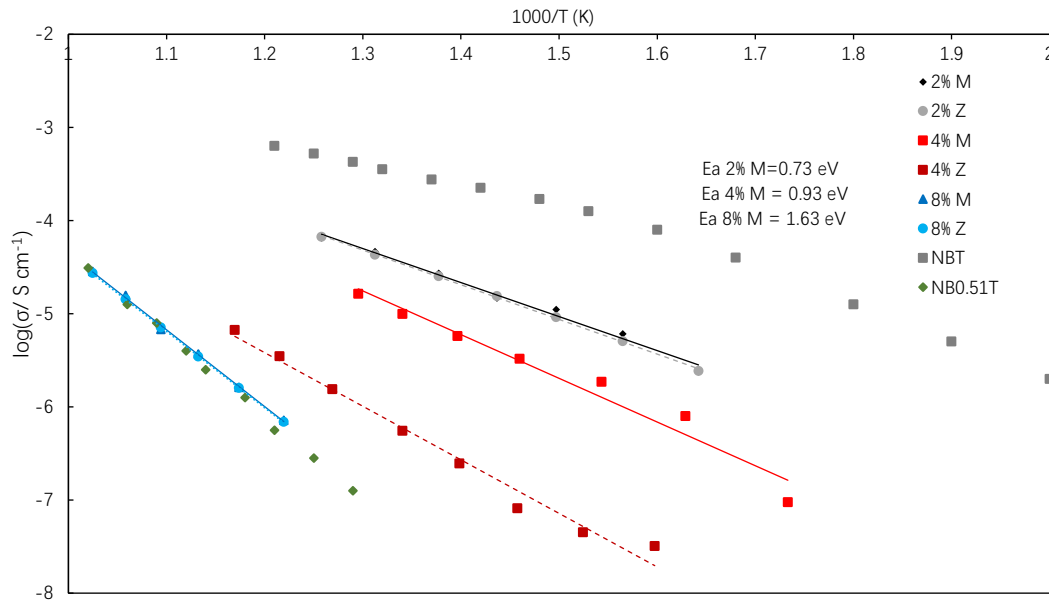


Figure 4.36. Arrhenius plots of conductivity for NBT-BZT solid solutions. Data calculated from the Z''(Z) and M''(M) peaks in the impedance data. Conductivity for insulating NB0.51T and conductive NBT from work by Li et al [4] are included for comparison.

BZT vs BMT comparison at the same doping level

A comparison of conductivity and F_{max} values between the NBT-BMT and NBT-BZT systems is shown in Figures 4.37 and 4.38, respectively. All the conductivity values are extracted from M'' spectra thus representing the bulk conductivity of each composition, Figure 4.37. The NBT-BMT data chosen are from ball milled samples. Both 2 and 8% BZT samples show lower conductivity than the BMT samples. The F_{max} analysis in Figure 4.38 allows us to make some deductions about any bulk compositional changes in the NBT-BMT and NBT-BZT samples. Based on an assumption that the permittivity behaviour of the bulk response doesn't show a dramatic change in magnitude for the various samples then we can attribute any changes in F_{max} to changes in the bulk conductivity (and therefore composition) between the samples. The assumption based on the magnitude of the capacitance being similar is borne out by the LCR data where there aren't large changes in the fixed frequency permittivity responses, Figures 4.15 and 4.32. The F_{max} difference between ball milled 2 and 8% NBT-BMT bulk responses are relatively small, suggesting a low solid solution limit for the BMT in NBT system and therefore small compositional change in the bulk material. In previous studies of Mg-doping in NBT, 0.5 at% would lead to a significant enhancement of the bulk conductivity compared to undoped NBT [4]. The fact that both samples have lower conductivity than undoped NBT suggests the lowering of the conductivity may be attributed to a decrease in the Na/Bi ratio and thus leading towards less conductive samples. Although it is not possible to quantify the levels of Mg, Ti and Bi doping in these samples, it does appear that their compositions may be closely related with both Bi and Mg being incorporated into the NBT lattice and these lead to a slight overall decrease in the conductivity. In contrast, for the NBT-BZT system, the difference in F_{max} between the 2 and 8% samples is much larger than the NBT-BMT samples and this suggests the level of Zn incorporation into the NBT lattice is low

in both samples and that there is an excess of Bi in these. Furthermore, the level of Bi-excess appears to be significantly larger in the 8% BZT sample, and that compositionally it may be very similar to NB0.51T.

The NBT-BMT series suffers an issue of being very sensitive to sintering temperature. 2, 6 and 8% BMT showed co-existence of insulating and conductive elements from M'' and Z'' data. For ball milled NBT-BMT, each composition's sintering temperature should be determined very carefully to achieve electrical homogeneity.

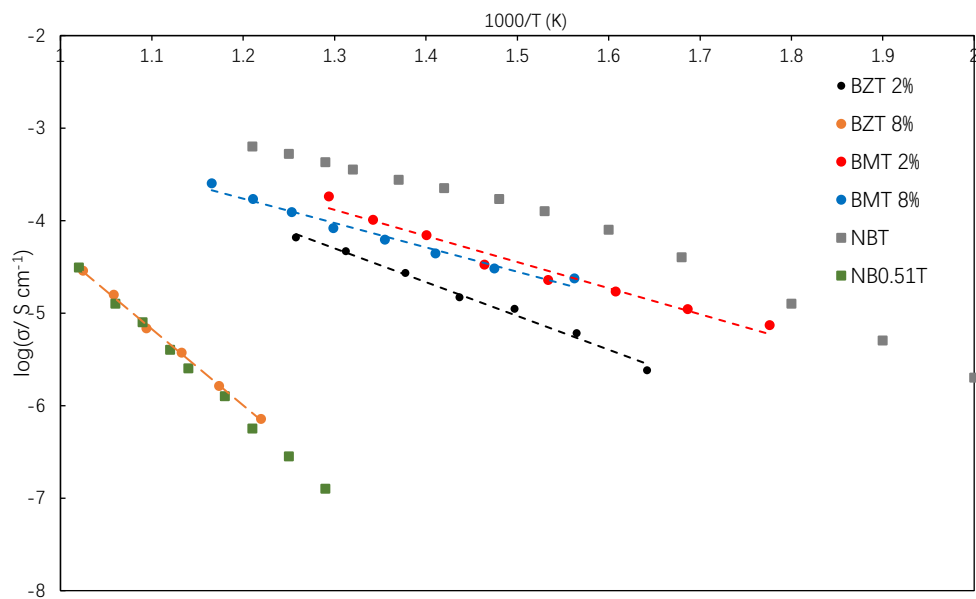


Figure 4.37. Arrhenius conductivity plots for NBT-BMT (2, 8 %) and NBT-BZT (2, 8%), data extracted from M'' plots. Conductivity for insulating NB0.51T and conductive NBT from work by Li et al [4] are included for comparison.

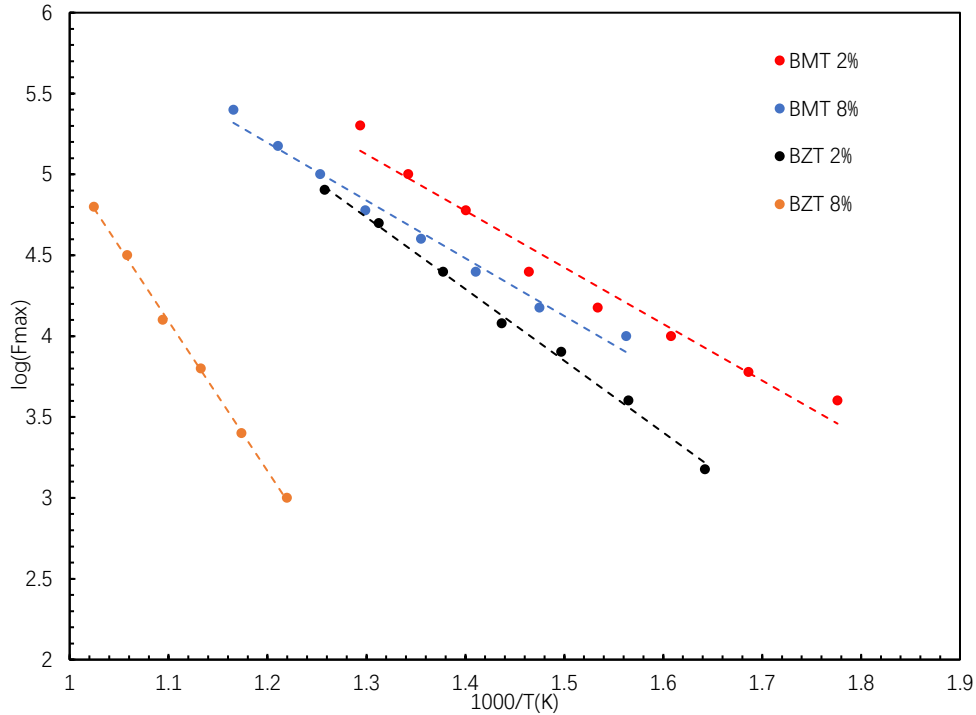


Figure 4.38. $\log(F_{\max})$ versus $1000/T$ plots for ball milled NBT-BMT and NBT-BZT samples at the same composition. The F_{\max} value is located from the peak position in M'' plots of the corresponding samples.

4.3 Conclusions

The NBT-BMT series has undergone two processing methods, hand grinding and ball milling. Samples prepared by the two methods have different electrical properties. The hand ground samples show very insulating behaviour when the BMT content increased beyond 2%. SEM images revealed the presence of Mg rich secondary phase in the insulating hand ground BMTs. This indicates possible inhomogeneous mixing of the reactants. SEM images of the insulating hand ground BMT ceramics show large grains embedded in a small grain matrix. This could be another example to support Yang et al's discovery of the inhomogeneous grain size effect on electrical properties in the NB0.51T system [14]. Ball milling was therefore chosen as the preferred mixing method. Although NBT-BMT 2% has lower conductivity than stoichiometric NBT, further increasing the BMT content to 8% resulted in a dual electrical response that suggested the presence of both conductive-type NBT (presumably Mg-doping) and insulating-type NBT (presumably Bismuth-rich content). This may be similar to the situation shown in Yang et al's NBT grain size effect study [14] or potentially a case of core-shell effects associated with the heterogenous distribution of BMT content in the NBT matrix. This may also be a processing issue and requires further investigation.

The ball milled BMT series is particularly sensitive to sintering temperature. A decrease from 1150 to 1100 °C can suppress the conductivity of the 6% BMT sample to become more insulating. Capacitance-temperature dependence analysis also revealed the 6% NBT-BMT sample contains two types of NBT material forming a composite ceramic structure, as the M'' and Z'' spectra captured the electrical response from two different NBT materials with high

and low conductivities. Another aspect to note is the starting reactant's physical form, as the hand ground NBT-BMT used pellets of MgO whereas ball milled NBT-BMT used a powder form of MgO. There could be a strong relationship between reactant particle size and the sintered ceramic's electrical properties. The data gathered for now does not support direct comparison of the trapping power of Al, Mg and Zn as dopants into the NBT system.

It is also clear that processing samples in this study proved more challenging than that reported by Pradal-Velazquez which indicates that Nb^{5+} ions may play a significant role in the ease of homogeneous solid solution formation. The NBT-BMN system shows a clearer trend in decreasing conductivity with increasing BMN content, and a homogenous distribution may be achieved. NBT-BMT at 8% still shows no obvious decrease in conductivity and NBT-BMT 6% shows sheets and squares of Mg-rich areas, therefore Nb^{5+} ions could be assisting the distribution of Mg into the solid solution. The NBT-BZT samples show an obvious trend in decreasing conductivity as the BZT content increases.

At this stage, only a few compositions of NBT-BMT and NBT-BZT solid solutions have been prepared by ball milling and examined by XRD, SEM and impedance measurements.

The covid-19 pandemic arrived and lockdown measures took place, thus experimental work was suspended. During the lockdown period, the research focus switched from synthesis and characterising functional ceramics to finite element modelling and simulations of impedance spectroscopy, as discussed with my supervisors. Thus, experimentation on the NBT-BMT and NBT-BZT series was terminated. Here I would like to appreciate the help from Dr Wang Ge who gathered several SEM images on hand-ground NBT-BMT samples, as I was overseas and unable to visit the campus. Several aspects need to be addressed if this work is continued by other researchers.

The priority of the possible future work would be as follows. First, prepare more compositions so that the NBT-BZT system should have $x=0.01$ to 0.08 , to ensure any possible trends in properties could be established. For NBT-BMT, further processing of the samples in this series is required in attempts to resolve the occurrence of insulating and conductive NBT within the ceramics. The precise sintering temperature of each composition should be determined carefully. Other synthesis methods such as solution-based methods are worthy to try and investigate the resulting ceramic's electrical properties to gather more understanding in preparing the NBT-BMT system. More in-depth analytical electron microscopy is required to better establish the levels and types of physical heterogeneity in these systems as this would assist with interpretation of the electrical data.

Second, use other methods such as ion transport number measurements and changing the oxygen partial pressure during impedance measurements to investigate the possible change of conduction mechanism(s) in the samples, as reported by Li et al and Yang et al [5] [14], when NBT changes from being conducting to insulating. The conduction mechanism changes from oxide-ion conduction to intrinsic electronic conduction. If microstructural (grain size) effects are present in this system then undertake micro-contact Impedance measurements to

study the influence of percolation pathways on impedance spectroscopy data. It is very important to verify the conductive and dielectric behaviour in NBT-BMT and NBT-BZT samples as there are many dielectric materials being developed that are based on two or three end member perovskites where the electrical behaviour is poorly understood.

4.4 References

- [1] E. Aksel and J. L. Jones, "Advances in Lead-Free Piezoelectric Materials for Sensors and Actuators," *Sensors*. 10(3) pp. 1935-1954, 2010.
- [2] D. Damjanovic, N. Klein, J. Li and V. Porokhonsky, "What can be expected from lead-free piezoelectric materials," *Functional Materials Letters*. 3(1). pp. 5-13, 2010.
- [3] K. Reichmann, A. Feteira and M. Li, "Bismuth Sodium Titanate Based Materials for Piezoelectric Actuators," *Materials*. 8, pp. 8467-8495, 2015.
- [4] M. Li, M. J. Pietrowski, R. A. De Souza, H.-r. Zhang, I. M. Reaney, S. N. Cook, J. A. Kilner and D. C. Sinclair, "A family of oxide ion conductors based on the ferroelectric perovskite $\text{Na}_{0.5}\text{Bi}_{0.5}\text{TiO}_3$," *Nature Mater*. 13, pp. 31-35, 2014.
- [5] F. Yang, P. Wu and D. C. Sinclair, "Suppression of electrical conductivity and switching of conduction mechanisms in 'stoichiometric' $(\text{Na}_{0.5}\text{Bi}_{0.5}\text{TiO}_3)_{1-x}(\text{BiAlO}_3)_x$ ($0 \leq x \leq 0.08$) solid solutions," *J. Mater. Chem. C*. 5, pp. 7243-7252, 2017.
- [6] H. Nagata, T. Takenaka, I. Ueda and S. Ikegami, "Lead-free piezoelectric ceramics of $(\text{Bi}_{1/2}\text{Na}_{1/2})\text{TiO}_3$ - $1/2$ $(\text{Bi}_2\text{O}_3$ - $\text{Sc}_2\text{O}_3)$ system," *Jpn. J. Appl. Phys.* 36, pp. 6055-6057, 1997.
- [7] H. Yu and Z.-g. Ye, "Dielectric, ferroelectric, and piezoelectric properties of the lead-free $(1-x)(\text{Na}_{0.5}\text{Bi}_{0.5})\text{TiO}_3$ - $x\text{BiAlO}_3$ solid solution," *Appl. Phys. Lett.* 93, p. 112902, 2008.
- [8] J.-h. Wang, Y. Li, N.-n. Sun, J.-h. Du, Q.-w. Zhang and X.-h. Hao, "Bi($\text{Mg}_{0.5}\text{Ti}_{0.5}$) O_3 addition induced high recoverable energy-storage density and excellent electrical properties in lead-free $\text{Na}_{0.5}\text{Bi}_{0.5}\text{TiO}_3$ -based thick films," *J. Eu. Ceram. Soc.* 39, pp. 255-263, 2019.
- [9] C. Chen, H. Zhang, X. Zhao, H. Deng, L. Li, B. Ren, D. Lin, X. Li, H. Luo, Z. Chen and J. Su, "Structure, Electrical, and Optical Properties of $(\text{Na}_{1/2}\text{Bi}_{1/2})\text{TiO}_3$ -1.5at.%Bi($\text{Zn}_{1/2}\text{Ti}_{1/2}$) O_3 Lead-free Single Crystal Grown by a TSSG Technique," *J. Am. Ceram. Soc.* 97, pp. 1861-1865, 2014.
- [10] T. Liu, H. Zhang, J. Zhou, A. Chang and H. Jiang, "Novel thermal-sensitive properties of NBT-BZT composite ceramics for high-temperature NTC thermistors," *J Am Ceram Soc.* 103, pp. 48- 53, 2019.
- [11] X.-f. He and Y.-f. Mo, "Accelerated materials design of $\text{Na}_{0.5}\text{Bi}_{0.5}\text{TiO}_3$ oxygen ionic conductors based on first principles calculations," *Phys. Chem. Chem. Phys.* 17, pp. 18035-18044, 2015.
- [12] K. Meyer and K. Albe, "Influence of phase transitions and defect associates on the oxygen migration in the ion conductor $\text{Na}_{1/2}\text{Bi}_{1/2}\text{TiO}_3$," *J. Mater. Chem. A*. 5, p. 4368, 2017.
- [13] E. Pradal Velazquez, "Structure-property relations in Sodium-Bismuth Titanate related

materials," (Doctoral dissertation) University of Sheffield, 2019.

- [14] F. Yang, J. S. Dean, Q. Hu, P. Wu, E. Pradal-Velázquez, L. Li and D. C. Sinclair, "From insulator to oxide-ion conductor by a synergistic effect from defect chemistry and microstructure: acceptor-doped Bi-excess sodium bismuth titanate $\text{Na}_{0.5}\text{Bi}_{0.51}\text{TiO}_{3.015}$," *J. Mater. Chem. A*, 8, pp. 25120-25130, 2020.

Chapter 5: Finite Element Modelling of a Homogenous Model with a Crack

5.1 Introduction

During the Covid 19 pandemic, the experimental work based on NBT-BMT and NBT-BZT solid solution had to be stopped due to laboratory closure. The focus of this project shifted to a finite element modelling based study on the effect that microstructural defects and surface layers have upon the electrical properties of ceramics. This research could be conducted remotely and as such was less affected by the pandemic.

Conventional Impedance Spectroscopy measurements uses electrodes that covers the entire sample's top and bottom surface and the electrical response gathered is an average across the full sample [1]. This is particularly useful when extracting 'bulk' properties of a sample. If an area with interesting local features is located on the sample surface, micro-contact impedance spectroscopy (mclS) is needed to probe the local electrical properties. As reported by Fleig, 75% of the electrical response from a mclS is generated from a region that extends from the surface a distance of approximately 4 times that of the micro-contact radius. Local features can therefore be probed with an appropriate micro-contact set up [2]. There exist numerous reports on using mclS to extract local electrical properties, such as grain and grain boundaries, thin films, thermal barrier coatings and many other areas [3] [4] [5]. While the sample may not always be structural intact, cracks and other structurally defects could develop with heat treatment, mechanical and/or electrical load [6] [7] [8] [9]. mclS can be applied to the defective area to reveal local electrical property changes. The electrical response from the defective sample could be very different to that of an intact, pristine sample [10] [11]. Understanding the effect of structural defects such as cracks on the impedance data measured, would be valuable knowledge to add to the field.

In this thesis, a specific experimental problem that we aim to solve was posed by a former member of the functional materials and devices group at the University of Sheffield, Richard Veazey [12]. In his experiments, pristine SrTiO₃ samples had undergone irradiation damage and the result was an amorphous surface layer appeared on the irradiated sample surface. When annealed at temperatures over 300 °C, microcracks were developed on the irradiated surface layer. Micro-contact impedance measurements revealed the impedance data of a microcrack rich area was significantly different from an intact surface area. More details of this experiment are presented in the literature review in Chapter 2. It is important to understand the effect of microcracks on the measured impedance data. FEM is the useful tool to predict this by reproducing the experimental scenario. This is achieved through using an in house finite element package, Elcer [13], that solves Maxwell's equations to predict the electrical response arising from various electrical microstructures.

Although the overall goal is to understand the effect of microcracks and resistive surface layers on a single crystal (SrTiO₃) sample, we have divided this problem into three parts to better understand all the factors that could affect the impedance data. The first step is representing a crack type structure in a single crystal material and to investigate how the crack influences the impedance spectra. The second step is to understand the effect of a resistive surface layer on the impedance data through a two-layered model without any crack(s). This is a representation of the amorphous/annealed surface layer on SrTiO₃ single crystal. The final step is to combine the crack and resistive layer features into a single model to achieve the

highest fidelity of the experimental set up of radiation damaged SrTiO₃. Based on this final model, a reproduction of the experimental measured micro-contact impedance data could be achieved.

Chapter 5 is the first step to tackle the problem. In this chapter, a cubic finite element model assigned with SrTiO₃'s electrical properties is created. The relative permittivity of the model is set as 162 and the conductivity fixed at $1.355 \times 10^{-5} \text{ Sm}^{-1}$. These values were experimentally determined for a SrTiO₃ single crystal at 300 °C with macroscopic top and bottom electrodes as measured by conventional Impedance Spectroscopy. The model is constructed through a scripting process, using the open-source CAD software Gmsh [14]. The basic script generates a cube with a side length of 200 μm. Two micro-contacts are formed on the top with a separation S , and defined radius, $r = 5 \text{ μm}$ as shown in figure 5.1(a).

Two types of crack structure are implemented into the script to modify the upper surface of the model. The first is a meshed crack that can be assigned with various levels of resistivity (MC). The second is where no structure or materials is assigned to that region, which we denote as a physical void crack (PVC). The user-controlled script can then be used to generate models with varying widths and the depths of the crack, with values set from 10 to 90% of the micro-contact separation, and 1 to 8 times of the micro-contact radius respectively. An illustration of the model is shown in Figure 5.1.

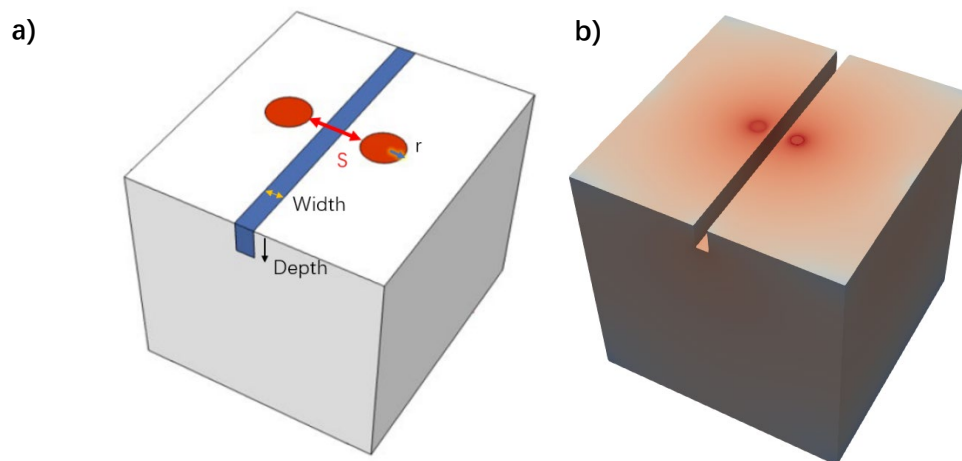


Figure 5.1. (a). Schematic illustration of the FEM model created for chapter 5. The cubic model contains two micro-contacts (red circles) on the top surface, radius is indicated as r , the distance between the micro-contacts is separation denoted as S . The blue region between the micro-contacts is a volume that can be assigned as a meshed crack (MC) or as a physical void crack (PVC), with width and depth direction indicated. (b). Current density distribution result generated from Elcer [13] from a PVC model visualised in ParaView [15] software. Red indicates high current density while blue means low current density. The dense red circles on the top surface are micro-contacts where current density is high, the blue regions at the corners have low current density.

The script then allows controllable microstructures (crack depth, crack width and micro-contact separations) which are then simulated for their impedance response. The measured electrical properties based on the impedance spectra are extracted and compared with the input intrinsic electrical properties from the models. The effect(s) of the crack on the impedance data can therefore be quantified. The spreading resistance equation is also used to verify its applicability in the presence of a crack. Current density distribution plots and line scans are used to understand the distribution status of the current in the model. Visualisation and extraction of this type of data is achieved by ParaView [15].

5.2 Result and discussion

5.2.1 Current density distribution of cracked model

Before simulating impedance measurements, static current distribution simulations are used to obtain a general understanding of the current density distribution when a crack is introduced to a homogeneous system with two micro-contacts on the upper surface.

As a start, we used models with $S/r = 2$, as this set up produces the strongest current interference between the electrodes and therefore creates the highest current density. First, the crack depth was varied from 5 to 40 μm to investigate the depth effect of the crack. The crack width was fixed at 5 μm for all models. These models were denoted as D5 to D40. The line scan was plotted in the central z axis from the top to the bottom surface of the homogeneous system, using ParaView [15]. The model lay out and results are shown in Figures 5.2 and 5.3, respectively. At the crack's tip surface, the current density decreases with increasing crack depth which is consistent with the crack tip moving away from the high current density volume between the electrodes.

The current density versus depth profile from the D40 model is the highest, suggesting the extended crack depth of the D40 model has caused the current density underneath the crack region to increase. At a depth of 40.1 μm , the D40 model shows a current density of 0.0069 A/m^2 , whereas the D5 model shows only 0.0009 A/m^2 . This surge in current density is consistent with the current having to detour around the crack to reach the opposing electrode. Also, in model D40, we consider there is a significant confinement effect as the crack depth is 20% of the total side length of the homogeneous system.

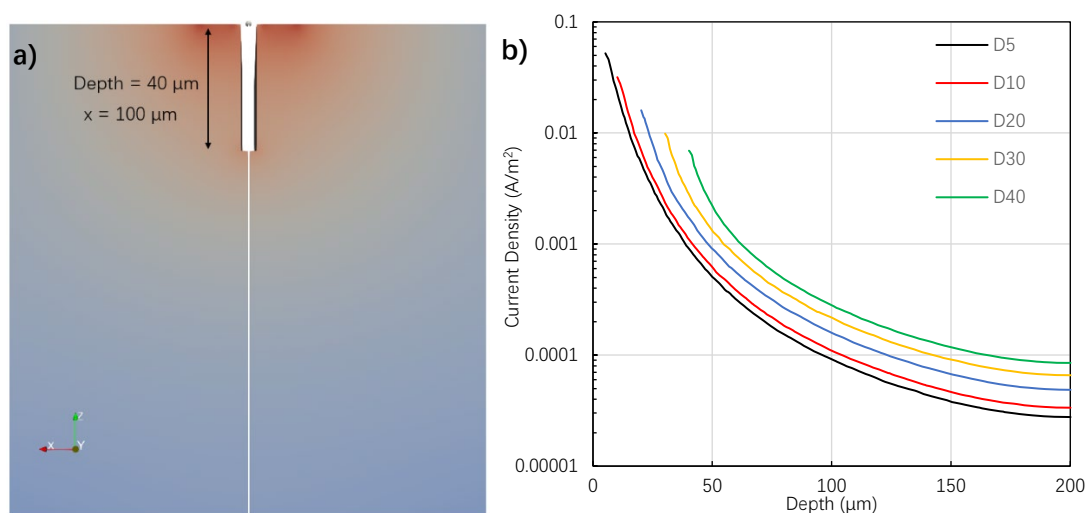


Figure 5.2. (a) Illustration of line scan position at $x = 100 \mu\text{m}$. The radius of micro-contact is 5 μm , separation is 10 μm , crack depth is 40 μm (indicated by the black arrow), crack width is 5 μm . The dense red areas near the crack are directly underneath the two micro-contacts. The scan path is shown as the white vertical line. (b) Current density (log scale) versus depth (z-axis) for models with crack depth of 5, 10, 20, 30 and 40 μm , fixed crack width of 10 μm , denoted as model D5 to D40 respectively.

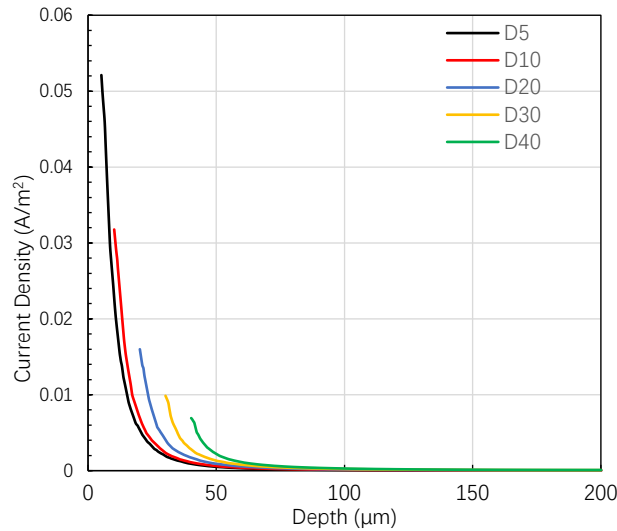


Figure 5.3. Same line scan data retrieved from models D5–D40 as Figure 5.2(b), but with the current density plotted on a linear scale.

Line scans at off-centre positions between the electrodes were conducted to confirm if confinement occurs in other regions. Selected positions were set at 10 and 20 μm along the x axis away from the crack centre. This first position is defined as one of the micro-contact's centres, the scan position and results are shown in Figure 5.4. Directly under the micro-contact, the current density of each model is slightly different with model D5 showing the highest value. The differences between the models become indistinguishable until a depth of 14 μm into the cube where the current density of each model diverges. After this depth, model D40 has the highest current density at almost all depths.

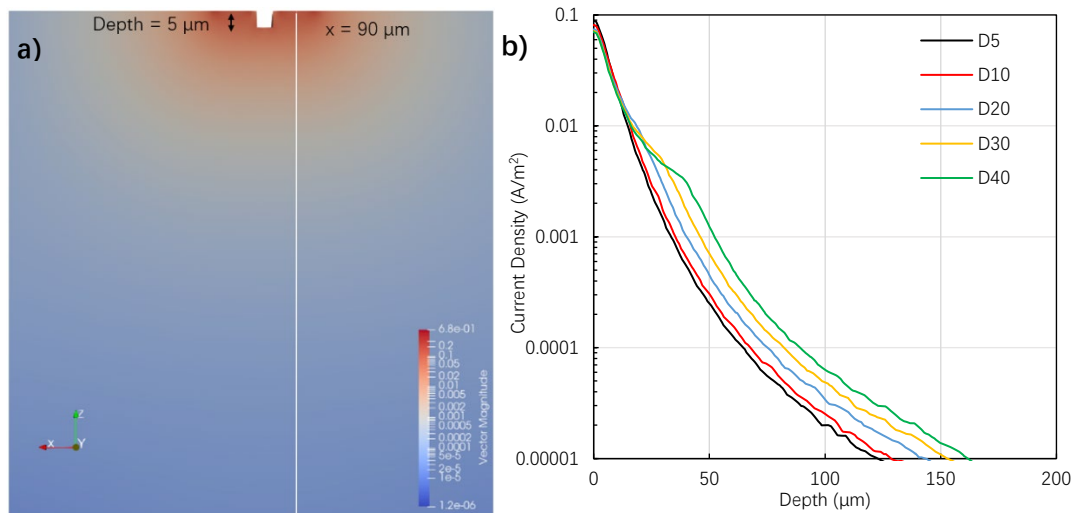


Figure 5.4. (a) Illustration of the line scan at an x axis position of 90 μm (at the right electrode centre) in D5 model, scan path shown as the white vertical line, (b) current density (log) versus depth plots for models D5 to D40.

Line scans at 20 μm away from the surface centre are shown in Figure 5.5 and show similar results as Figure 5.4. When the line scan takes place directly underneath the top surface, the difference in current density of each model is smaller than that in Figure 5.4. However, the current densities after a scan depth of 14 μm are still different, suggesting the confinement effect of increased crack depth also exists for scans at off-centre positions.

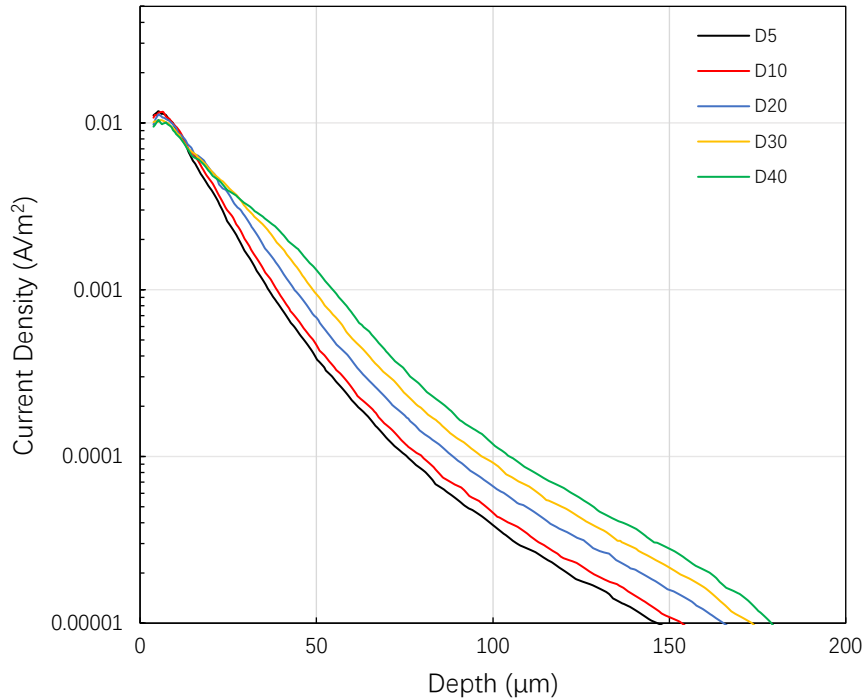


Figure 5.5. Line scan at an x axis position of 80 μm (10 μm right from the right electrode centre) and (log) current density versus depth plots for models D5 to D40.

In Figure 5.2-5.5, the line scans are along the z axis. Next, line scans were conducted along the x axis at a fixed depth to show how current density changes across the model. Results are shown in Figure 5.6 for a depth of 2 μm . As the crack depth increases, the current density near the crack wall decreases and the current density at the outer regions increases. This shows how the local current near the crack detours around the (resistive) obstacle and thus causes a decrease in current density. The increase of current density at the outer regions demonstrates confinement caused by a deep crack.

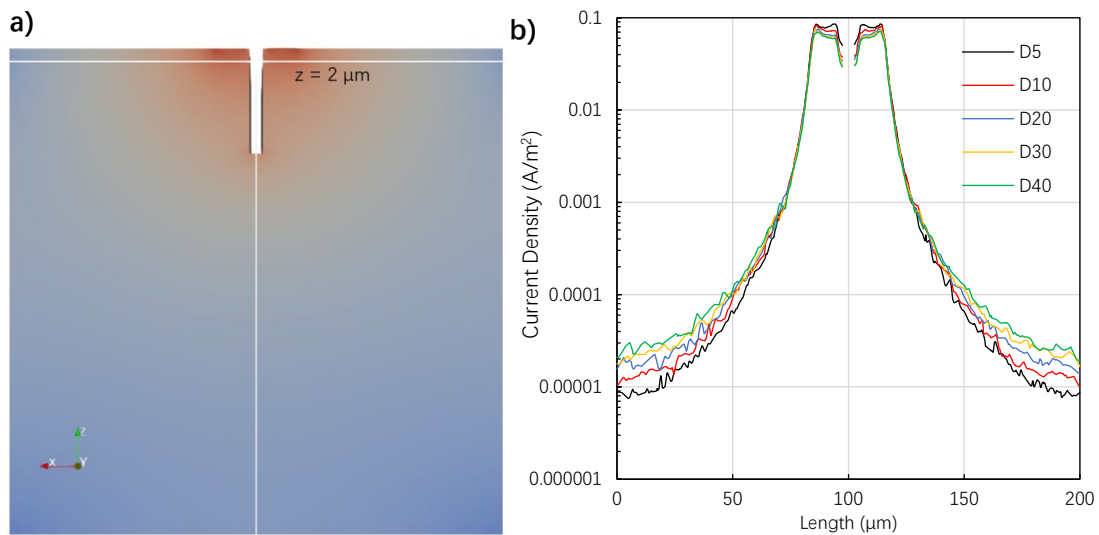


Figure 5.6. (a) Illustration of line scan position of models D5 to D40 at 2 μm deep along the x axis, which is z position at 2 μm . (b) Current density (log) versus length plots for models D5 to D40.

We made an assumption that there exists a mathematical relationship between increasing crack depth and current density at the crack tip. In order to assist our understanding, we used Irwin's stress intensity associated with an edge crack on a finite plate (Equation 5.1) [16]. The stress intensity factor K_i describes the state of stress at the crack tip caused by a remote load. σ is the applied stress at the crack tip and a is the crack length. Y is a dimensionless geometric constant based on the equation described below (Equation 5.2). The philosophy of using a stress intensity factor related term is that in our static current distribution model there exists an electric field which is an electrical equivalent concept to a stress field in a mechanical system. The line scan in Figure 5.2 revealed the current density value along the crack tip. This equation could therefore be used as an analogy to describe the change in current density. Moreover, it might help to explain the current confinement generated from deep cracks.

To apply Irwin's equation, we assumed $K_i=1$, and after re-arranging, Equation 5.1 becomes Equation 5.3 and this allows the applied stress at the crack tip at a given crack length to be calculated.

$$\text{Equation 5.1. } K_i = Y\sigma\sqrt{\pi a}$$

$$\text{Equation 5.2. } Y = 1.12 - 0.231\left(\frac{a}{W}\right) + 10.55\left(\frac{a}{W}\right)^2 - 21.72\left(\frac{a}{W}\right)^3 + 30.39\left(\frac{a}{W}\right)^4$$

$$\text{Equation 5.3. } \sigma = \frac{1}{Y\sqrt{\pi a}}$$

We use the crack depth as 'a' in Equation 5.3 and the side length of the homogeneous cube as W ; the crack depth of models D5 to D40 are 5, 10, 20, 30 and 40 μm , respectively. A plot of σ against a/W is shown in Figure 5.7. It is clear that with increasing a/W , the applied stress at the crack tip decreases.

The current density (CD) value at the bottom surface of the crack for models D5 to D40 are overlaid with the σ plot. The current density at the crack tip falls with increasing crack length, since a/W reflects the change in crack length. The σ and CD data show very similar trends from the 5 models used. Best fit lines are added and their difference is mainly on the coefficients.

It is interesting how this equation which is used in fracture mechanics can be used to facilitate the construction of an electrical relationship between crack length and current density. This is attributed to the same principles behind the equation, i.e. as the crack tip moves away from the source of stress/electric potential, the measured stress level or current density naturally attenuates.

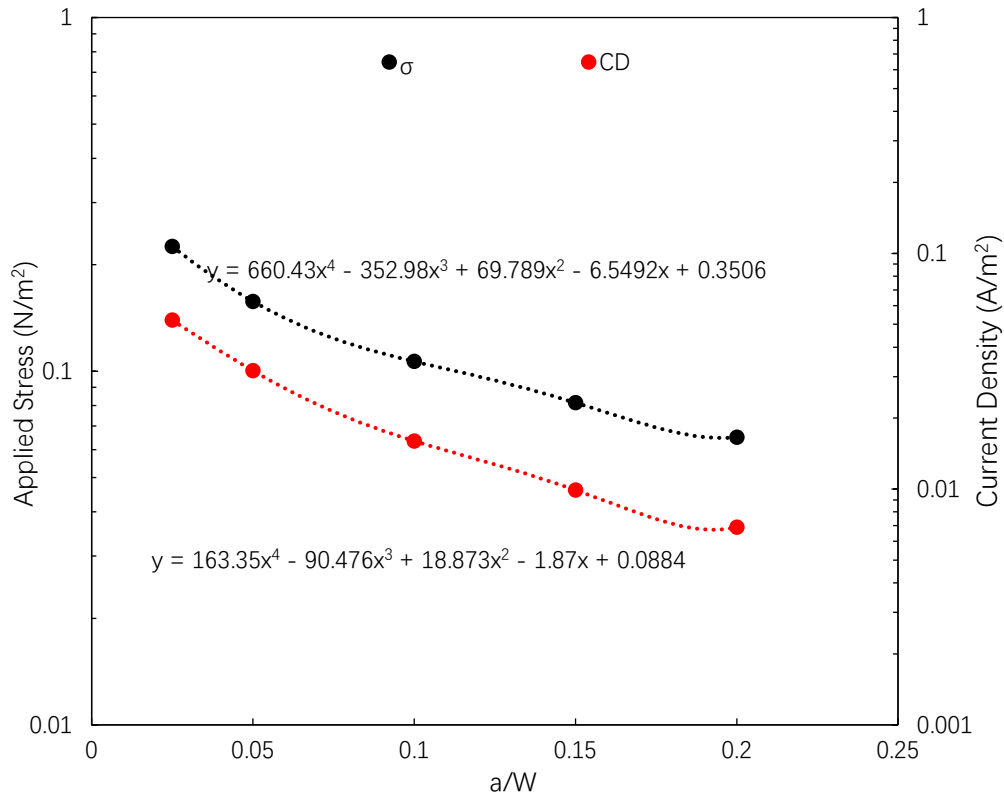


Figure 5.7. Overlaid plots of Current Density (CD) for each model and the applied stress σ value using the corresponding model's crack depth (a) and side length (W), plotted as (log) applied stress versus a/W and (log) current density versus a/W .

Equation 5.3 can assist in predicting the current density at the crack tip, yet it is not effective in explaining the increase of current density at the outer regions in the model. As shown from Figure 5.2 to 5.7, a large crack depth can induce confinement in the model. Next, we investigate the influence of the crack width on the distribution of the current density.

Models with crack widths of 1, 3, 5, 7 and 9 μm and the same crack depth of 10 μm (denoted as W1-W9 respectively) were processed with the line scan tool and the results plotted in Figure 5.8. Unlike increasing crack depth, the increment in crack width has a minor local effect on the current density only near the crack wall regions. This is attributed to the relatively small changes in crack width compared to the total side length of 200 μm , thus no significant confinement is caused by increasing the crack width.

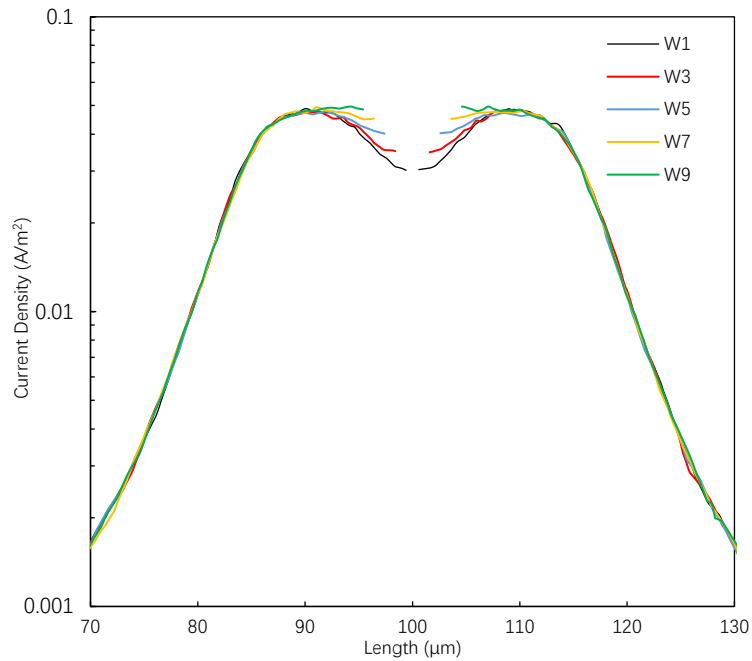


Figure 5.8. Line scans along the x axis at a depth of 5 μm , plotted as current density versus length, in models with crack width of 1, 3, 5, 7, 9 μm , fixed crack depth of 10 μm , denoted as W1-W9. The result is zoomed in the crack tip region to illustrate the minor differences between the results from the models.

Other than the decrease of current density in the bottom surface of the crack, increasing crack width has little effect over the current density on the z axis, as shown in Figure 5.9. In contrast to increasing crack depth, changing crack width does not show any significant increase in the average current density.

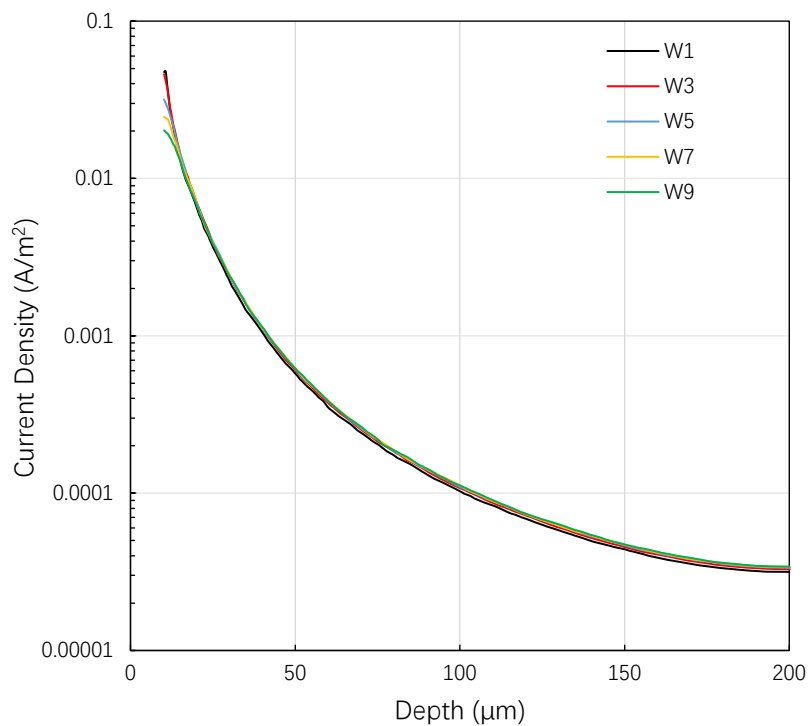


Figure 5.9. Line scan along the z axis of models with increasing crack width for models W1 to W9, plotted as (log) current density versus depth.

In conclusion, increasing crack depth induces confinement in the system. As a result, the current density at the outer regions of the model will increase, yet we consider the extent of the confinement effect to be acceptable. Increasing the crack width does not show any obvious confinement effects. Also, a commonly used fracture mechanics equation has been used to deduce a relationship between crack depth and current density at the crack tip and is a good fit to our simulated results. The next section presents impedance results for a series of models with different crack geometries.

5.2.2 Impedance results of high interference models, $S/r=2$

In this section, impedance spectroscopy data for a series of homogenous models with a physical void crack (PVC) will be shown. The models can be categorised into two groups: the high current interference model and the low current interference model. The high interference model has the following set up: electrodes separation = 10 μm , electrode radius = 5 μm , $S/r=2$. For the low interference model, $S/r = 10$. Data from the high interference model are presented first.

For $S/r=2$ models, the influence of crack depth on the impedance results are shown in Figure 5.10 and the extracted electrical values summarised in Table 5.1. The results for a pristine model without a crack, and models with a crack depth of 5, 10, 20, 30 and 40 μm are overlaid together, the models are labelled as D5-D40, respectively; all the cracks have a width of 5 μm .

In Figure 5.10 (a), a single semi-circle in Z^* plots is shown for each model, meaning only a single response is obtained. Although the crack has the properties of air, its response is not reflected in the Z^* plots. In Figure 5.10 (b) Z'' spectra show a single Debye peak for all models. All six F_{max} values are the same at 1526 Hz, which agrees well with the theoretical value of 1500 Hz. The 40 μm crack depth model has the highest Z'' value of $3.751 \times 10^9 \Omega$, whereas the homogenous (no crack) model has the lowest value of $2.539 \times 10^9 \Omega$. The extracted resistance increases with increasing crack depth.

A similar trend is observed in the corresponding M'' spectra in Figure 5.10 (c), since the lowest M'' value comes from the homogenous model and the highest comes from the model with deepest crack. It is worth mentioning that the Z'' and M'' values experienced a sharp rise from a crack depth of 5 to 20 μm , but the increase in value is reduced after the crack depth goes beyond 20 to 40 μm . This suggests the crack depth effect on the impedance results is greatest when the crack depth is 20 μm or less. Another possible hypothesis is after a crack depth of 20 μm , the confinement by a large crack depth causes the current density to increase in regions away from the crack, restoring some portion of current flow.

In Figure 5.10 (d), C' vs frequency plots are shown. Increasing crack depth causes the measured capacitance to decrease. The homogenous model has a capacitance value of 2.090×10^{-14} F, which is the highest, and the crack depth=40 μm model has the lowest capacitance value of 1.415×10^{-14} F. For this series of models, the F_{max} does not deviate from the theoretical value and the change in capacitance and resistance is caused by the varying crack depth.

Model type	R (GΩ)	Z'' (GΩ)	M'' (F ⁻¹)	Frequency (Hz)	C' (pF)
Pristine	5.08	2.54	2.39x10 ¹³	1526	0.02090
D5	5.84	2.92	2.75x10 ¹³	1526	0.01817
D10	6.46	3.23	3.04x10 ¹³	1526	0.01645
D20	7.08	3.54	3.33x10 ¹³	1526	0.01501
D30	7.32	3.66	3.45x10 ¹³	1526	0.01449
D40	7.50	3.75	3.53x10 ¹³	1526	0.01415

Table 5.1. Table showing the calculated electrical properties extracted from impedance spectroscopy data for the pristine model and models with a crack of various depths.

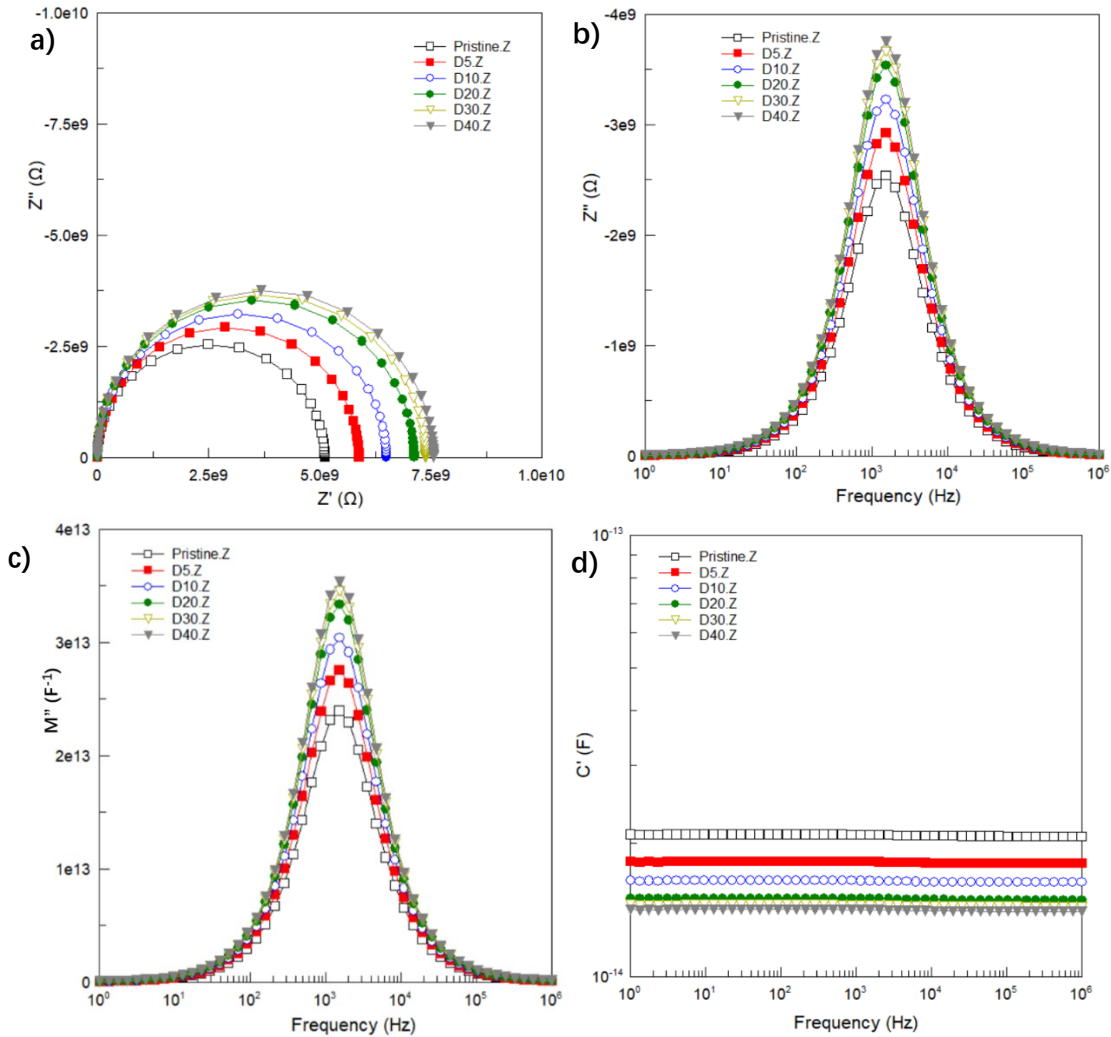


Figure 5.10. Impedance data for the pristine (no crack) model and models with crack depths of 5, 10, 20, 30 and 40 μm (denoted as D5-D40, respectively), (a) Z^* plots, (b) Z'' spectra, (c) M'' spectra and (d) C' spectroscopic plots.

After investigating the crack depth effect in Figure 5.10, the crack width effect on the impedance data is shown in Figure 5.11, the models have crack width of 1, 3, 5, 7 and 9 μm , fixed depth at 5 μm , denoted as model W1-W9. In 5.11(a), a semi-circle response in Z^* plots is shown for each model. This is the same as in Figure 5.10(a). The crack is not identified as a secondary response and hence only a single semi-circle response is observed for all models. In 5.11(b), all models show a single Z'' peak at 1526 Hz and therefore no deviation from the

theoretical value. The highest Z'' value of $3.185 \times 10^9 \Omega$ is obtained from the $9 \mu\text{m}$ crack width model, whereas the homogenous no crack model has the lowest value of $2.539 \times 10^9 \Omega$. It is clear that the Z'' value increases with increasing crack width. The same trend occurs for the M'' spectra in 5.11(c). In Figure 5.11(d), the C' spectra show the measured capacitance decreases as the crack width increases. The crack width $9 \mu\text{m}$ model has the lowest capacitance of $1.410 \times 10^{-14} \text{ F}$, whereas the homogenous model shows the highest value.

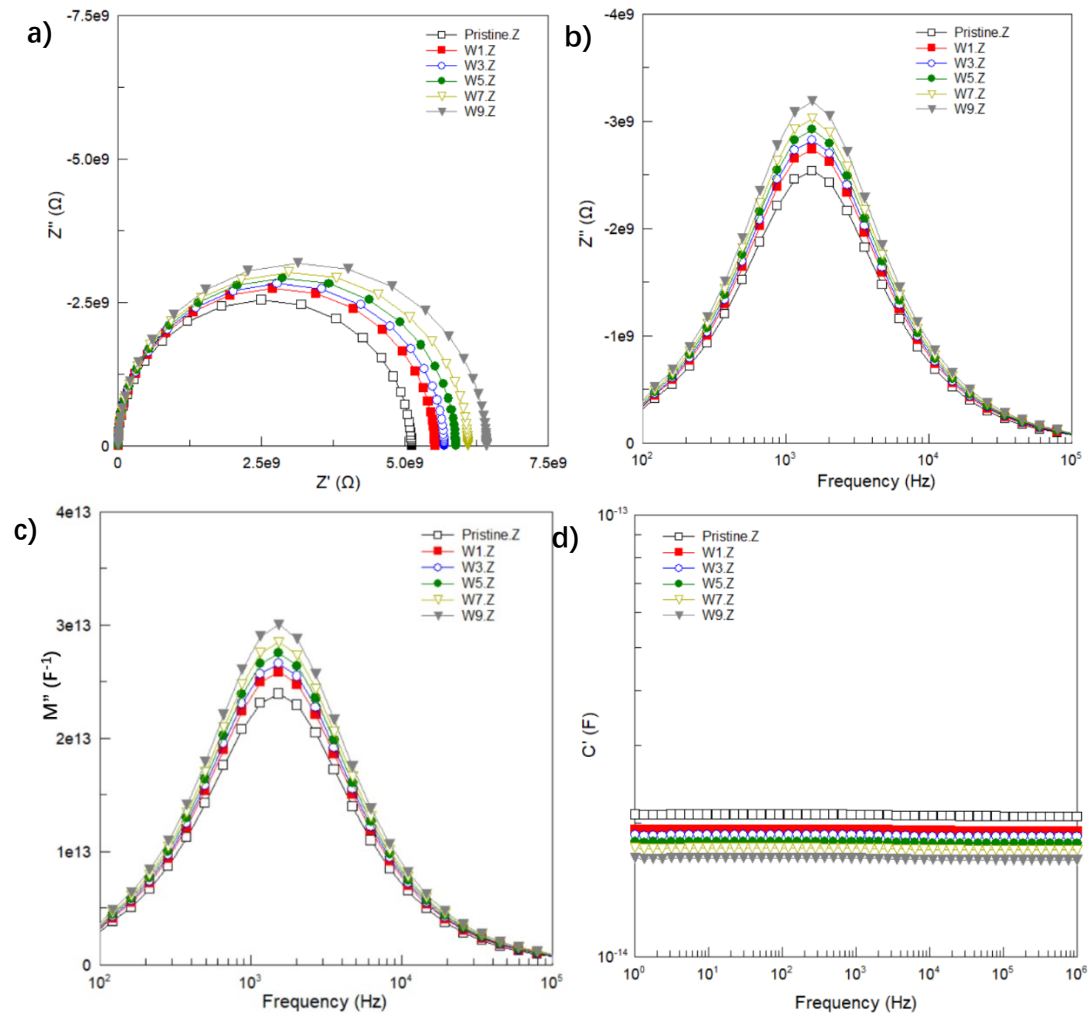


Figure 5.11. Impedance data for the pristine no crack model and models with crack widths of 1, 3, 5, 7 and $9 \mu\text{m}$, crack depth is fixed to $5 \mu\text{m}$, labelled as W1-W9. (a) Z^* plots, (b) Z'' spectra, (c) M'' spectra, (d) C' spectroscopic plots.

From Figures 5.10 and 5.11, it has been established that expanding the crack depth or width will increase the measured Z'' value and therefore the overall measured resistance from the model will increase. It is important to quantify the relative increase of resistance with the increase in crack size. To achieve this, the impedance spectroscopy data are processed in the following method: the peak reading in Z'' spectra are taken as the raw impedance results with a magnitude of $R/2$. A pristine model is where a homogenous cube is formed without a crack and is used as a baseline for comparison. With changing crack geometry, all models with cracks are compared with the pristine model.

The calculation formula is:

$$\text{Equation 5.4 } \left[\frac{(\text{PVC Model } Z'' \text{ peak value} - \text{pristine model } Z'' \text{ peak value})}{\text{pristine model } Z'' \text{ value}} \right] = \%R.$$

The processed impedance results from each model are plotted in Figure 5.12 where the effect of crack width on the results is investigated. The y axis shows each model's relative % increase in R compared with the pristine model value. The x axis shows the percentage increase in crack width over the total electrode separation. In other words, narrow cracks on the left-hand side and wide cracks on the right-hand side. The labels D10-D50, indicate the crack depth of each model series. 1X to 8X indicate the corresponding multiples to the electrode radius.

For a given crack depth and electrode radius, increasing crack width results in an increase in %R, Figure 5.12. The increase in %R is directly linked to increased crack depth. When the crack depth is 40 μm into the cube, the overall impedance of the model increased more than when the crack depth is shallower. When the crack width is fixed at 10% of total separation, a crack depth of 40 μm can produce a 38.80% increase in R but a crack with depth of 5 μm can only increase it by 7.77%. Fixing the crack depth at 40 μm and increasing the crack width from 10 to 90% of the total separation (i.e increasing the crack width from 2 to 9 μm) increases %R from 38.80 to 59.37%.

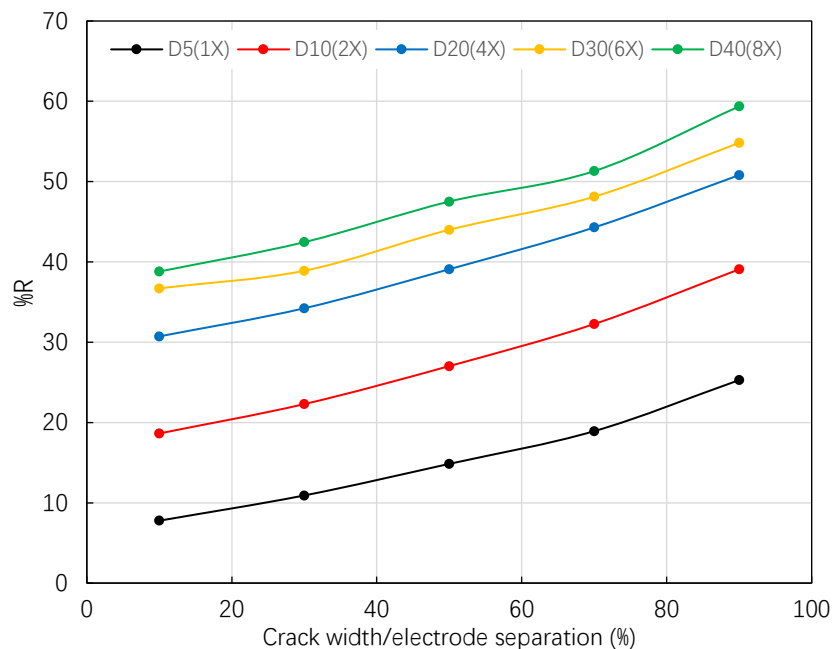


Figure 5.12. A plot of %R versus %(crack width/electrode separation) to show the crack width effect in the strong interference model. A minimum increase in Z'' of 7.77% occurs for the minimum crack dimensions of width = 10% separation and depth at 1X of the electrode radius. The maximum %R occurs for the largest crack dimensions with width 90% of electrode separation and depth at 8X of the electrode radius. Lines are shown to guide the eye.

Since the crack width is an experimentally measurable feature, the results obtained here could be used to establish crack depth which is difficult to obtain by direct measurements. Also, in micro-contact experiments, the S/r ratio is set when electrodes are printed on a sample. With both of these variables fixed, the crack depth to electrode radius ratio can be calculated based on the simulated results.

Results from models with different electrode set ups ($r=10, S=20$ and $r=5, S=10$) but with $S/r = 2$ are shown in Figure 5.13. Although from different electrode set ups, the data series are grouped together according to their crack depth/electrode radius ratio. For example, $r5(2X)$

and r10(2X) (solid and dashed red lines, respectively) both have D/r of 2. The difference between the values in the two plots is about 2%. This 2% originates from the different meshing between the models and can be regarded as a systematic error. In Figure 5.13, the S/r ratio is fixed to 2 during a simulation, the approximate crack depth can be estimated by comparing results measured with a crack and a pristine sample on an area without cracks.

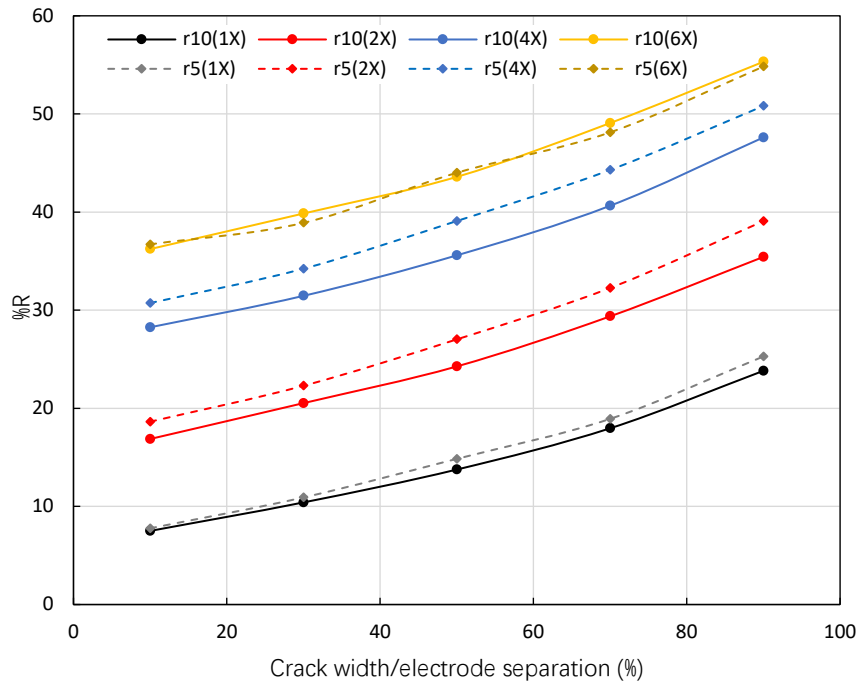


Figure 5.13. A plot of %R versus %(crack width/electrode separation) for two series of models with electrode radii of 5 and 10 μm . All models have S/r = 2. When the depth/radius ratio is 1 and 6, the results from the r5 and r10 series almost overlap. However, the average difference between r5(4X) and r10(4X) is about 3.5%.

A finer meshed model comparison was conducted to show that the 3.5% difference between model r5(4X) and r10(4X) originates from the mesh settings in the models. Initially, the models have the same mesh setting with different crack geometries. The mesh size is set at an intermediate level to achieve a balance between processing time and simulation accuracy. Thus, r5(4X) and r10(4X) were assigned with a finer mesh size. Reducing the attractor mesh size by 1 doubles the number of elements in the models. With the finer meshed models, %R between r5(4X) and r10(4X) reduces to 2.3%. This suggests that the percentage difference between these two series is based on the different mesh size in the models and can be reduced with finer meshing. However, the cost to reduce the percentage error extends the processing time. To achieve this 1.2% extra accuracy, the models needed over 90 hours to be processed, whereas the original model only required 48 hours. In consideration of the overall pace of the project, the original model settings were chosen to continue to serve in all models.

5.2.3 Applying the spreading resistance equation

We can predict the depth of the crack by comparing the measured Z'' peak value against the pristine model. This method does not require further processing of the Z'' value measured. In the opposite situation, when the crack's geometry is determined by SEM or TEM, how can we extract accurate bulk conductivity values? The effect of a crack on the impedance results needs to be considered.

The spreading resistance equation is chosen as the primary tool to extract bulk conductivity values when micro-contacts are used [17]. The first stage is to evaluate its effectiveness in the situation when cracks exist in the model. The equations used are listed below.

σ is the calculated conductivity, r is radius of the micro-contact, R is the measured resistance that can be extracted from Z'' peak values via a supplementary Equation 5.5.

$$\text{Equation 5.5. } R = -2Z''_{\max}$$

$$\text{Equation 5.6. } \sigma = \frac{1}{2rR} \text{ [17]}$$

The spreading resistance equation was proposed to calculate impedance results when micro-contacts are used for pristine samples without defects. It also has the requirement where the electrical properties of the sample are homogeneous with no resistive layers or electrical heterogeneity existing between the two electrodes. We have applied the spreading resistance equation to the impedance results with cracks present to calculate the conductivity of each model. The method requires two steps, first, extract the Z'' peak value to get the measured resistance, R , via Equation 5.5, then substitute into Equation 5.6 to extract the calculated conductivity of the model.

The calculated conductivities of the cracked models are compared with that of the homogenous model to illustrate the percentage change between cracked and homogenous models. The results are plotted in Figure 5.14. With increased crack width, the calculated conductivity of the models decreases. When the crack depth to electrode radius increases to 6 ($D/r=6$), all crack width models show the lowest calculated conductivity compared to their homogenous counterpart. Thus, increasing the depth and width of the crack will decrease the measured conductivity of the model, in comparison with the homogenous model without a crack. This is attributed to the interruption that the crack has on the flow of current. From the plot it can be seen that caution is required when applying the spreading resistance equation to calculate conductivities when a crack is present, as there exists systematic percentage differences from the pristine sample value. These can vary between $\sim 10 - 35\%$. For reference, the pristine model's calculated conductivity is 1.970×10^{-5} S/m, which is higher than the material property assigned to the model as 1.355×10^{-5} S/m. This overestimated conductivity value is a result of high current interference between the closely placed micro-contacts.

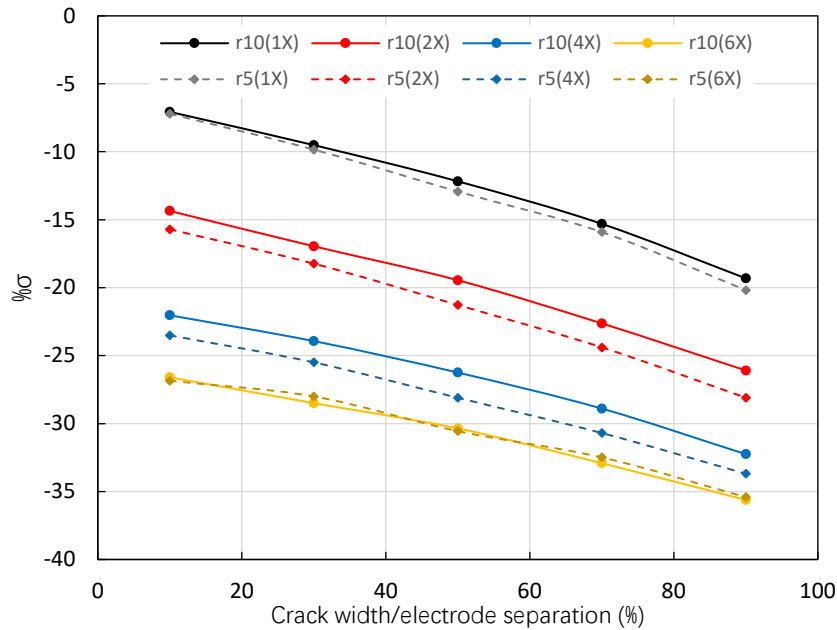


Figure 5.14. A plot of $\% \sigma$ versus $\%(\text{crack width}/\text{electrode separation})$ for models with radii of 5 and 10 μm . The conductivity value of each model is extracted using the spreading resistance equation. Lines are shown to guide the eye.

Next, the accuracy of the geometric factor equation was investigated as it is widely used in conventional impedance measurements. Impedance results listed in Figure 5.13 were processed with the geometry factor (GF) equation, $GF=L/A$. Since the crack has width and depth, L is assigned with the depth of crack, and A is the area of the electrodes. The final conductivity results from geometric factor corrections are on average 10 times greater than the materials property. For example, when a crack is 20 μm deep and wide in a model with electrode radius 10 μm and separation 20 μm , a geometric factor correction gives a conductivity of 1.470×10^{-4} S/m, whereas the spreading resistance equation gives a value of 1.440×10^{-5} S/m. The material property assigned to the cube is 1.355×10^{-5} S/m. Thus, under a high current interference set up when $S/r=2$, the spreading resistance equation gives results of better accuracy, despite the over estimation of conductivity when the electrode separation is small. It has previously been suggested that to have accurate conductivity results measured with micro-contacts an S/r of at least 8 is needed [18]. In some situations, the presence of a crack therefore counter balances the effect of strong interference from the electrodes, thus bringing the calculated conductivity value closer to the intrinsic value assigned to the model.

In Figure 5.14, the calculated conductivities of cracked models are compared with the pristine model, also called the homogenous (no crack) model, to show how the conductivity values progressively deviate away from the pristine model. However, the pristine model itself exhibits high current interference and its calculated bulk conductivity significantly deviates from the actual material property assigned to the model. The conductivity of each crack set up is therefore compared to the actual material conductivity assigned (1.355×10^{-5} S/m) and the results shown in Figure 5.15. From this comparison, the effectiveness of the spreading resistance equation can be better evaluated.

When compared with the actual conductivity instead of the pristine model conductivity, the percentage difference range has extended to both positive and negative deviations. When the difference is positive, the overestimation of current originates from the interference effect

of the electrodes. When the crack's geometry becomes wider and deeper, the crack's hindrance (confinement) over current flow offsets the overestimation of conductivity. When the crack width takes 70% of electrode separation and depth of 4 times the electrode radius a 0.58% difference between the calculated and actual value is obtained. As the crack's geometry continues to expand, the calculated conductivity becomes smaller than the actual conductivity. If we consider values within 10% of the actual value to be acceptable, then the spreading resistance equation can be accurate in a few cases. When the crack depth to electrode radius ratio is 4 and above, almost every model with any crack width could give a relatively accurate conductivity result. It is clear that models containing a crack with $D/r=1$ at any width cannot give an accurate result but when the crack depth is doubled, models with a crack width of 70% and above can provide accurate results.

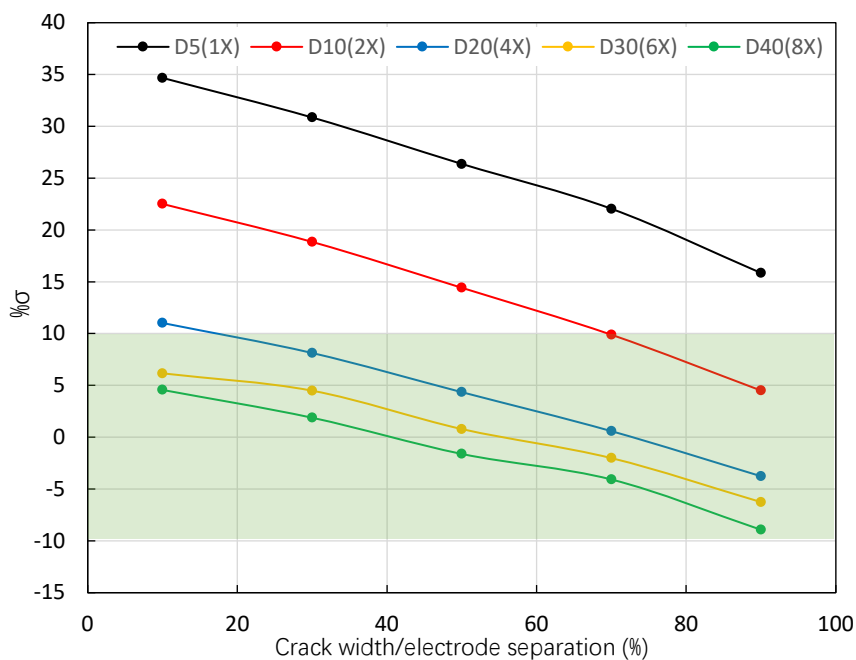


Figure 5.15. A plot of $\% \sigma$ versus $\%(\text{crack width/electrode separation})$ for models with $S/r=2$, to show how crack geometry affect the measured conductivity of the model compared to the actual conductivity assigned to the model. Results are grouped by different depth to radius ratio, $D/r=1$ has a crack depth of $5 \mu\text{m}$, $D/r=8$ has a crack depth of $40 \mu\text{m}$. The green shaded area indicates where the spreading resistance equation gives results within $\pm 10\%$ of the input value.

5.2.4 Impedance results of Low Interference model, $S/r=10$

With the high current interference situation studied, we moved onto investigating the crack effect when there is low current interference between the electrodes.

The low interference models have electrode separation of 50 and radius 5 microns giving an $S/r=10$. The crack width effect plot (Figure 5.16) is generated in the same manner as Figure 5.13. The most obvious change in the low interference model from the high interference model is the much lower percentage change at all crack depths. This is attributed to the decrease of current density in the region between the electrodes, since the electrodes have S/r of 10. Less current is passing in the volume where the crack is placed, as a consequence the geometry of the crack has less effect on the impedance results. Nevertheless, the general

trend of wider and deeper cracks having a greater influence on the relative impedance change still holds up.

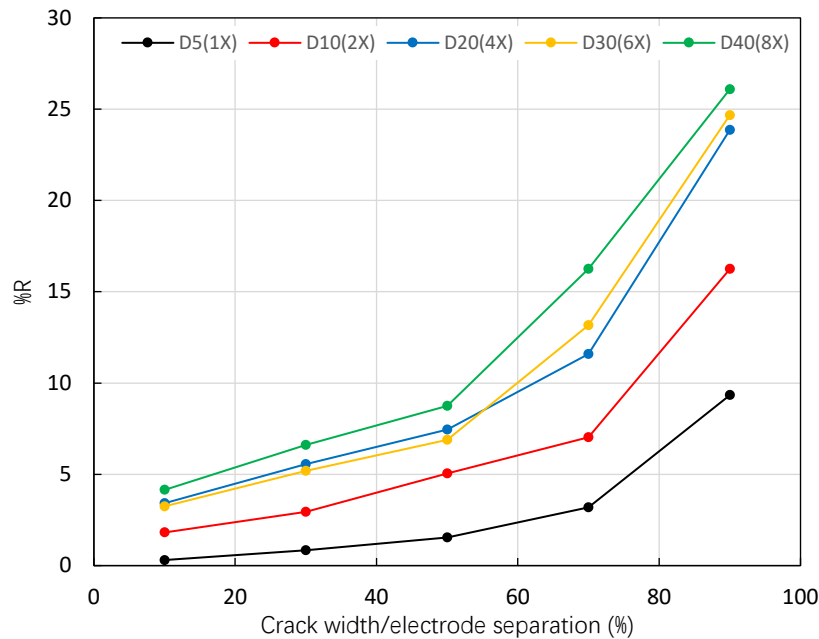


Figure 5.16. A plot of %R versus %(crack width/electrode separation) for $S/r=10$ models. The Z'' peak value of models with a crack are compared to the homogenous model result. Lines are shown to guide the eye.

The impedance results are then calculated using the spreading resistance equation in the same process as the $S/r=2$ models. Figure 5.17 shows impedance results calculated using the spreading resistance equation and compares the percentage difference from the actual material conductivity assigned (1.355×10^{-5} S/m). In particular, it shows the crack width effect on the calculated conductivity.

It is clear that the decrease of the crack's effect over the current flow shown in Figure 5.16 is also reflected in Figure 5.17. In other words, when the S/r ratio is increased to 10, the crack has become very ineffective in compensating the current interference from the electrodes. Although $S/r=10$ is considered as a set up with lower current interference than $S/r=2$, the over estimation effect still remains in the system. Most of the cracks created are no longer able to compensate the over estimation (interference) effect. Only when the crack width is at 90% of total separation, models containing a crack with D/r of 2, 4, 6 and 8 can give results close to the material value. However, at $S/r=10$, 90% of the total separation means the crack is $45 \mu\text{m}$ wide and 9 times that of the electrode radius, the practicability of such a crack's presence is clearly questionable.

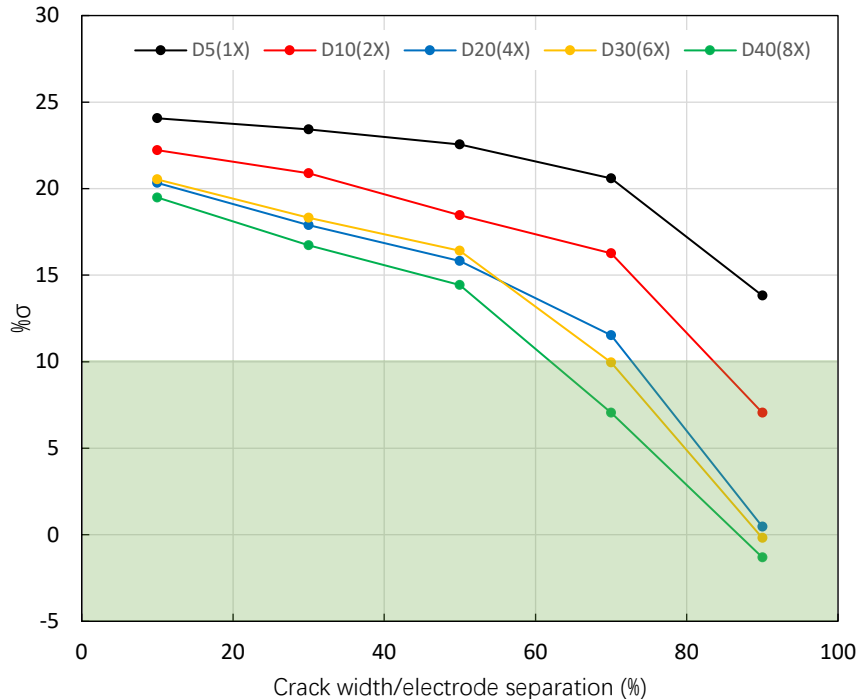


Figure 5.17. A plot of $\% \sigma$ versus $\%$ (crack width/electrode separation) for $S/r=10$ models. The calculated conductivity of the model is obtained using the spreading resistance equation. Light green shaded area indicates conductivity values within $\pm 10\%$ of the assigned actual conductivity value. Only the models at the bottom right corner can give relatively accurate conductivity values calculated using the spreading resistance equation.

5.2.5 Cross S/r ratio comparison

With $S/r=2$ and 10 data sets studied closely, we investigated the transitional S/r ratios between 2 and 10 to have a better understanding of the crack's effect on the impedance results. First, we used the line scan tool on the current density models for different S/r ratios, along the x and z axes. The models listed are $S/r=2, 4, 6, 8, 10$ and 12. To investigate the effect of a crack, pristine models without a crack are also scanned. All the cracked models have the same crack depth of $20 \mu\text{m}$ and the crack width is set at 50% of the electrode separation. This should reveal a clear distribution of current density in the model, and reflect the crack's effect on the current flow. The results are shown in Figures 5.18 and 5.19.

In Figure 5.18(a), the models scanned contain cracks of equal depth at $20 \mu\text{m}$ and width of 50% of the electrode separation. At a depth of $1 \mu\text{m}$ under the top surface, the models show a sharp decrease in current density at the side walls of the crack. The $S/r=2$ model shows the highest current density in the central region, directly underneath and between the micro-contacts, and the current density underneath the electrodes is at a similar level for each model. As the S/r ratio increases, in regions away from the centre, the current density shows a different trend. The $S/r=2$ model's value is the lowest among all 6 models, whereas $S/r=12$ shows the highest current density in regions away from the micro-contacts. This abnormality could be related to the confinement effect of the model walls; as S/r increases, the micro-contacts are moving closer to the boundary of the model, causing a build-up of current density. In Figure 5.8, extending the crack width without moving the micro-contact position does not induce any significant increase in current density at the outer regions. The positioning of the micro-contacts within the model is a factor in creating confinement.

Figure 5.18(b) reveals the effect of a crack on the distribution of the current density. The models scanned are $S/r=2$ models with and without a crack (denoted as $S/r=2P$). It is obvious that introducing a crack to the structure causes the current density near the crack wall to decrease due to the insulating nature of a void. At the outer regions away from the micro-contacts, the current density increased in cracked models. This phenomenon is presumably related to the confinement effect caused by the crack.

In conclusion, increasing the micro-contact distance will cause the current density in the central region to decrease slightly but to increase in the outer regions. Adding a crack between the contacts will have the same effect on the current distribution, this is the effect of confinement due to the presence of a crack.

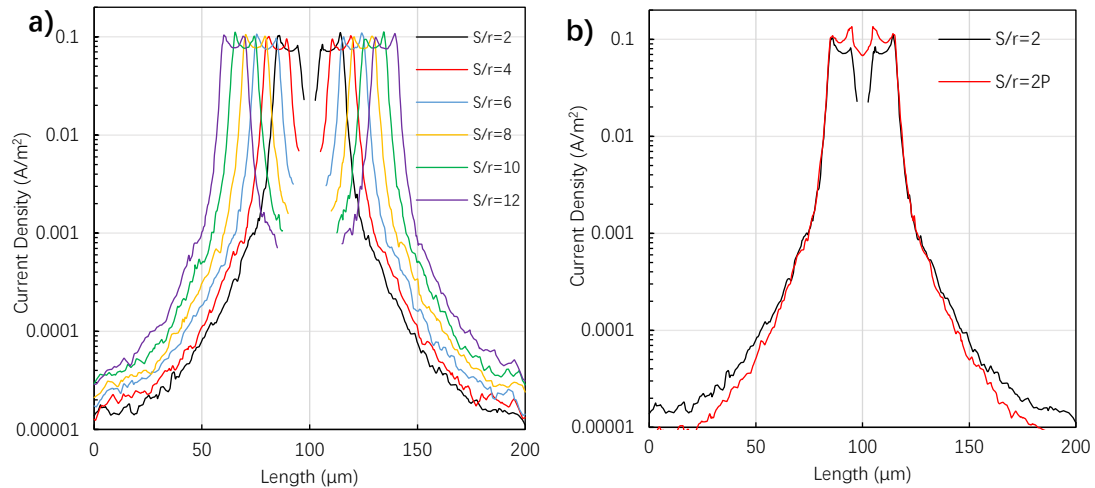


Figure 5.18. Line scan results along the x axis. (a) Different S/r models with a crack scanned at a depth of $1 \mu m$. (b) Close comparison of $S/r=2$ models with ($S/r=2$) and without a crack ($S/r=2P$).

In Figure 5.19(a), the line scan takes place along the z axis from the top surface centre to the bottom surface centre. The models scanned are a pristine cubic structure with no cracks. When the scan distance is within around $23 \mu m$ from the top, the current density falls with increasing micro-contact separation. As the scan depth goes beyond $23 \mu m$, the trend is reversed, the highest current density comes from the $S/r=12$ model. This reversed trend suggests the strong current interference is localised near the top of the model when S/r ratio is small.

When scanning in the same manner on the cracked models, in Figure 5.19(b) the trends observed are exactly the same; however, the current density trend reverse point is increased to a depth of $37 \mu m$. This is related to the crack with depth of $20 \mu m$, as the presence of crack induced confinement effect, which may counterbalance the interference effect from closely placed micro-contacts.

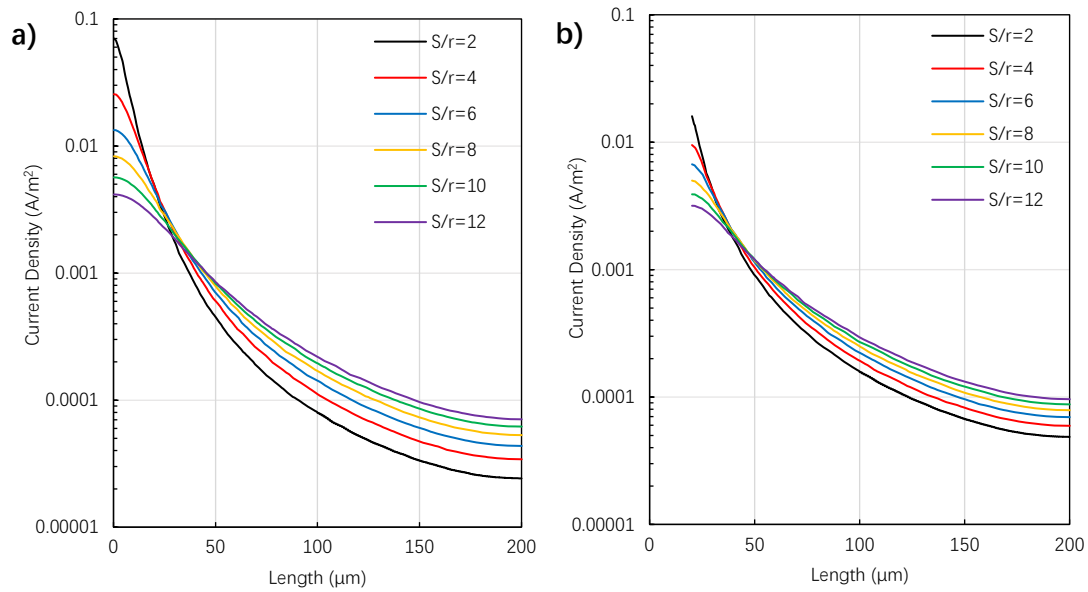


Figure 5.19.(a) Line scan results along the z axis of the pristine model with no cracks at different S/r ratios. (b) Same line scan process for cracked models at different S/r ratios. The current interference effect from the micro-contacts is persistent in the system, but weakened when a crack is present.

From the line scan results, the crack's effect over current distribution is known. Now we compare the impedance results of models with cracks to their pristine cubic model without cracks. This should reflect the combinational effect of the crack's geometry and confinement on the current flow. The results are shown in Figures 5.20 and 5.21.

Increasing S/r gradually reduces the current interference from the electrodes. As a result, the crack's influence on the impedance results decreases with decreasing current density. However, when S/r reaches 10, the percentage changes in the impedance results are very close to S/r=12; some points even overlap. This suggests that after S/r=10, the effect of the crack's geometry on the impedance has saturated. This is attributed to the lower current density between the electrodes when they are 50 or 60 μm apart.

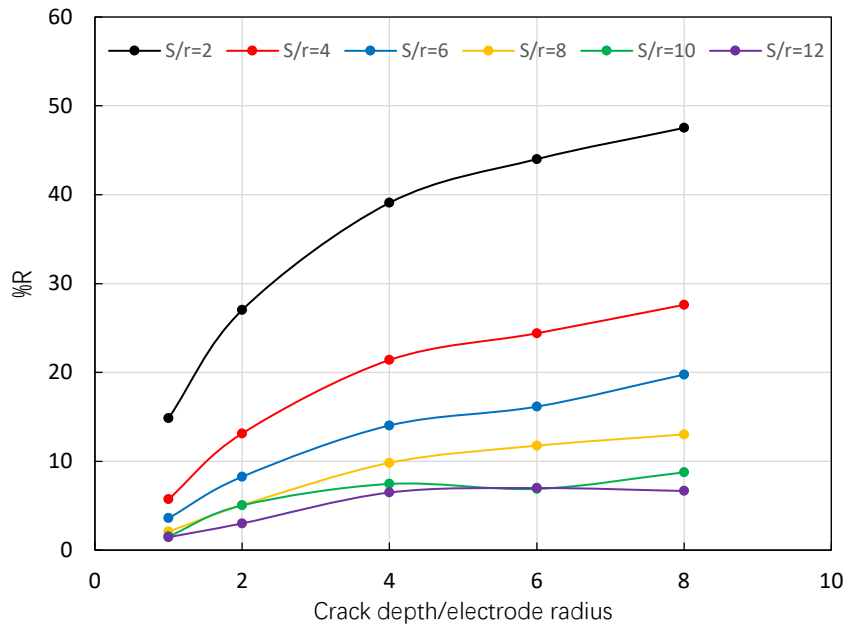


Figure 5.20. A plot of %R versus crack depth/electrode radius for models with different S/r ratios. All models have a crack width to separation percentage of 50%, instead of just comparing one point, the crack's depth has been progressively increased. When $S/r=2$, the crack's effect on the impedance results is the greatest. The effect decreases with increasing S/r ratio.

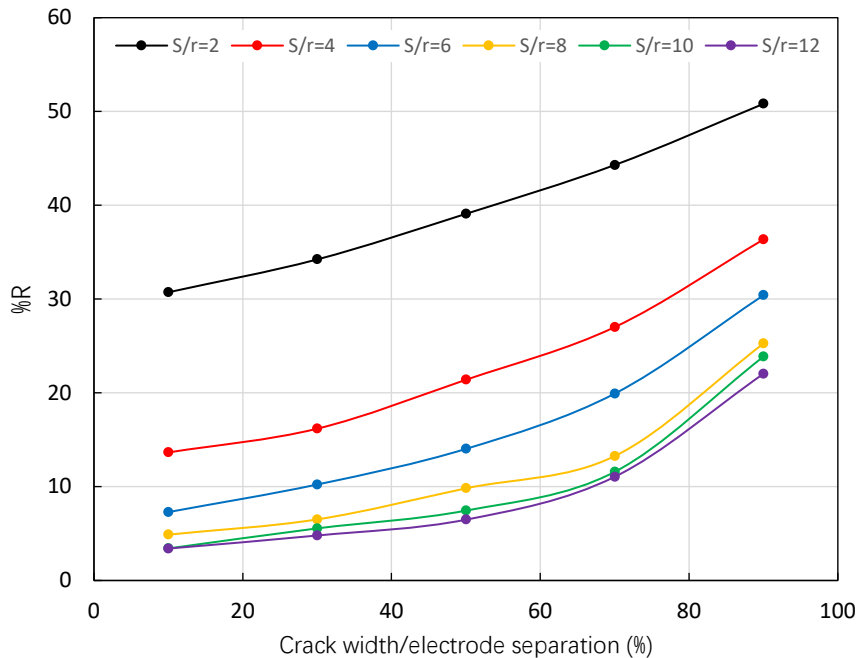


Figure 5.21. A plot of %R versus % (crack width/electrode radius) for models with different S/r ratios. All models have the same crack depth of $20\ \mu\text{m}$. Since the comparison is focused on different S/r ratios, either crack width or crack depth has to be fixed. Again, when the S/r ratio increases and the distance between the electrodes increases the effect of the crack on the impedance diminishes.

The data are then processed with the spreading resistance equation in the same manner as Figures 5.15 and 5.17. The calculated conductivity value for each model is then compared with the intrinsic assigned material conductivity of 1.355×10^{-5} S/m. This process can present the overall effect of a crack's presence and how it affects the final measured conductivity. Again, we consider $\pm 10\%$ of the intrinsic conductivity to be accurate. The results are shown in Figures 5.22 and 5.23.

In Figure 5.22, all the models are grouped by their S/r ratios. In each S/r series, the models contain a crack of fixed width of 50% of the electrode separation but increasing crack depth. Thus, Figure 5.22 shows the how crack depth can affect the calculated conductivity of different S/r groups. For S/r=2, which is the series with the strongest current interference between the electrodes, increasing crack depth has the most significant effect in reducing the calculated conductivity closer to the intrinsic value. Increasing the crack depth from 5 to 40 μm can dramatically reduce the calculated conductivity by 27%. However, as the S/r ratio increased, increasing crack depth has less effect in reducing the difference between the calculated and intrinsic values. This is attributed to the decreasing influence of the crack's effect in hindering the current flow, as current become more evenly spread with increased separation between the electrodes. For S/r=12, expanding the crack depth 8 times from 5 μm could only reduce the calculated conductivity by 6%.

Figure 5.23 shows the effect of increasing crack width in different S/r groups, all the cracks have fixed depth of 20 μm to reduce variables. Similar to increasing the crack depth, widening the crack can generate a change in all S/r groups, 18.0% change in S/r=12 and 14.8% change in S/r=2. When the crack width is 90% of electrode separation, all the S/r groups give accurate conductivity results within 10% error of the assigned intrinsic value.

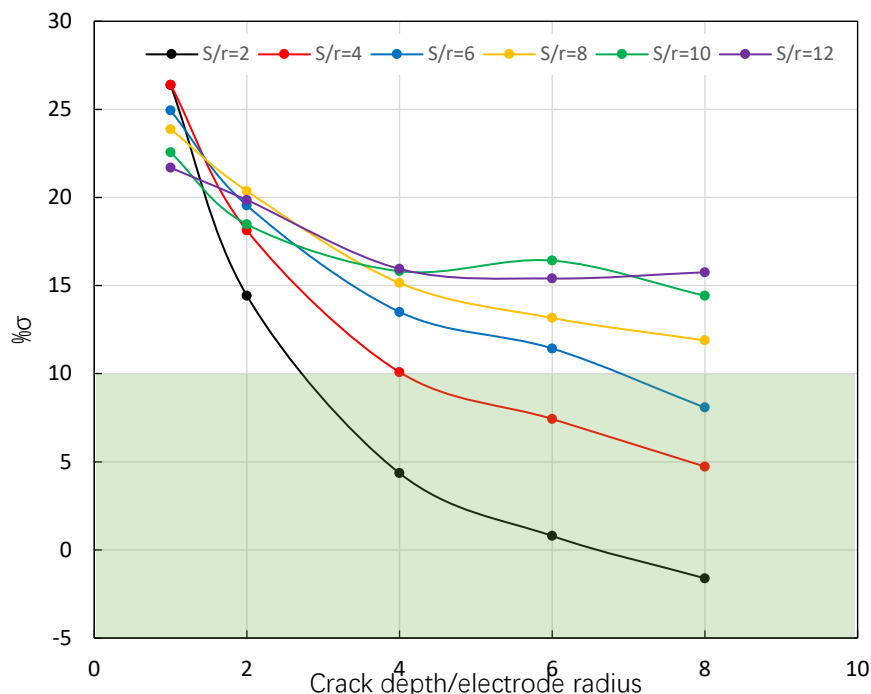


Figure 5.22. A plot of $\% \sigma$ versus crack depth/electrode radius for models with different S/r ratios. In this cross S/r comparison, models have fixed crack width of 50% electrode separation but increasing crack depth. Light green shaded area indicates conductivity values within $\pm 10\%$ of the assigned actual conductivity value.

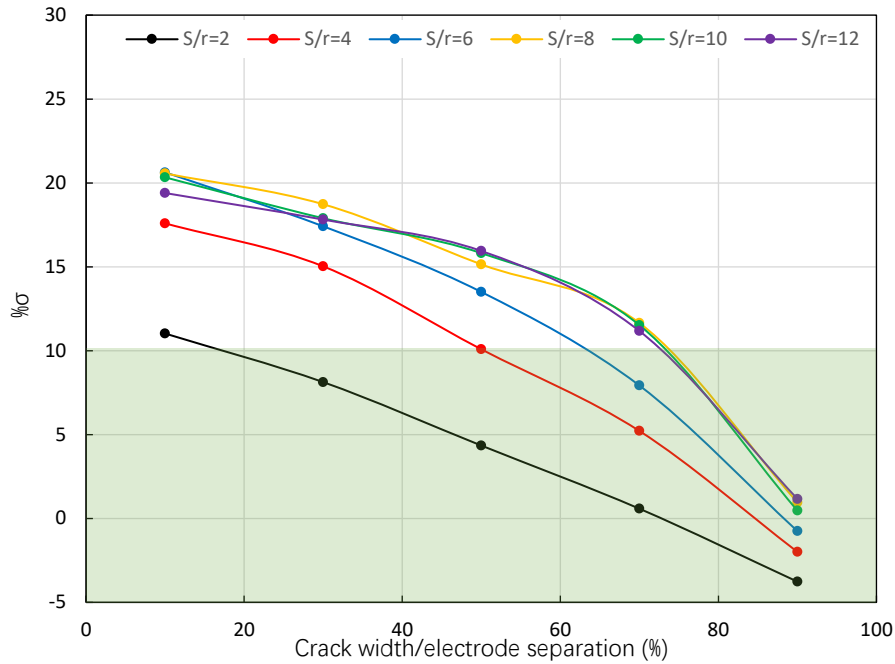


Figure 5.23. A plot of %σ versus %crack width/electrode radius for models with different S/r ratios. In this cross S/r comparison, models have fixed crack depth of 20 μm but increasing width. Light green shaded area indicates conductivity result within ±10% of the assigned actual conductivity value.

5.2.6 Crack effect versus current interference

Having completed the cross S/r models we now investigate how the current interference changes with increasing S/r ratios, and the potential effect of using crack geometry to compensate for current interference.

In Figure 5.24, we compare the crack's effect on the impedance and the over estimation of conductivity due to current interference from the electrodes when S/r is increased. To simplify the variables, the crack depth has been set to be 20 μm and its width as 10% of electrode separation. So when S/r increases, the width of the crack increase proportionally but the crack depth is fixed. Current Interference (CI) is calculated by comparing the conductivity of the homogenous model without a crack to the intrinsic conductivity assigned to the model.

$$\text{Equation 5.7. } CI = (\text{homogenous model } \sigma - 1.355 \times 10^{-5}) / 1.355 \times 10^{-5} \times 100\%$$

Due to the strong current interference between the electrodes, when S/r is small, the CI is rather high, e.g., for S/r=2 CI= 45%, (i.e. the current interference causes 45% overestimation of conductivity). The crack effect against the pristine model (CEP) measures when a crack of depth 20 μm, and 10% of electrode separation is placed into the model and how the measured conductivity changes against a homogenous model without crack, at the same S/r.

$$\text{Equation 5.8. } CEP = (\text{Cracked model } \sigma - \text{homogenous model } \sigma) / \text{homogenous model } \sigma \times 100\%$$

The CEP should indicate how much the presence of crack can affect current flow, in other words, the crack's hindrance ability. For example, when S/r=2, a crack 20 μm deep and 1 μm wide can produce a 23.5% change in terms of conductivity, compared with an intact

homogenous model at the same S/r.

The calculated conductivity with the crack effect (CCE) is calculated by comparing the conductivity of a model with a crack to the intrinsic conductivity assigned to the material. The CCE reflects the combined effect of current interference and crack hindrance of the current.

$$\text{Equation 5.9. } \text{CCE} = (\text{Cracked model } \sigma - 1.355 \times 10^{-5}) / 1.355 \times 10^{-5} \times 100\%$$

In Figure 5.24, Current Interference (CI) decreases as S/r increases from 45.13% (S/r=2) to 23.46% (S/r=12). The crack effect also diminishes (CEP) from 23.50% (S/r=2) to only 3.29% (S/r=12). Although CI and CEP both decrease by 22%, the crack effect is becoming less effective in cancelling the current interference. This is reflected in the rise of calculated conductivity (CCE). It is noteworthy that beyond S/r =6, CCE remains relatively constant at 20%.

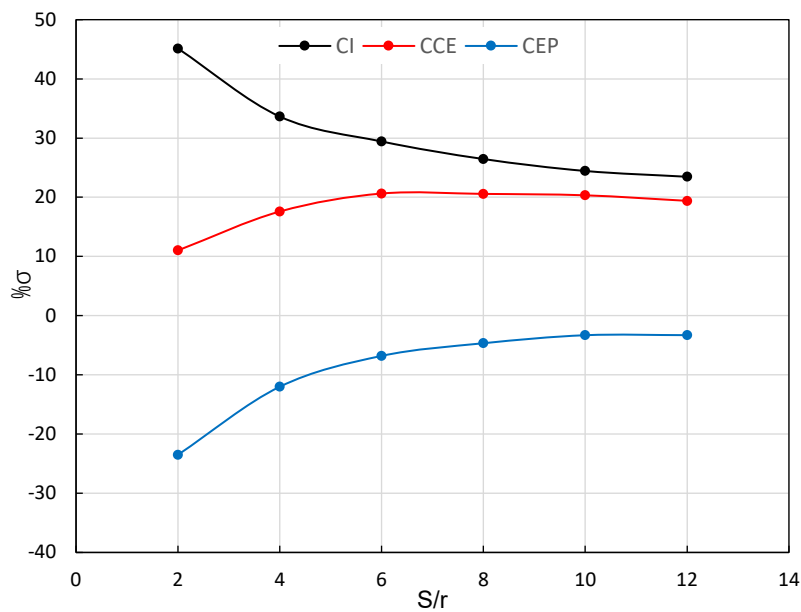


Figure 5.24. Current Interference (CI), crack effect against pristine model (CEP) and calculated conductivity with the crack effect (CCE) plotted versus S/r. The crack depth of all models is fixed at 20 μm and the crack width is fixed at 10% of the electrode separation.

In Figure 5.25, the crack's width increased from 10 to 90% of the total separation, meaning at S/r=2, the crack width is 9 μm and when S/r=10, the crack width is 45 μm. The crack depth is again fixed at 20 μm to reduce variables. This time, the proportionally wider crack is successful in compensating the current interference from the electrodes when S/r increases. The calculated conductivity is within 5% error of the intrinsic material value. However, it is a rather rare situation to find such a large width crack and to perform measurements around it.

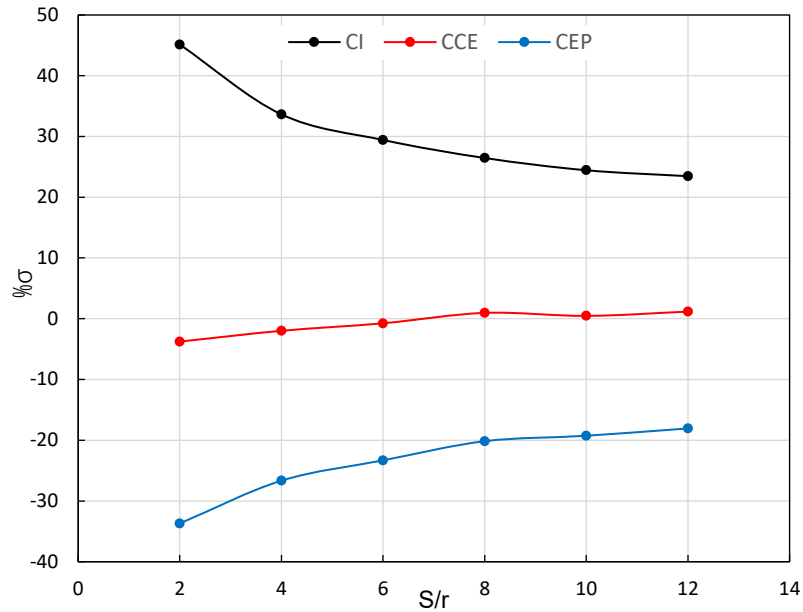


Figure 5.25. Same axes as Figure 5.24, but now all the models contain a crack with a width of 90% of electrode separation, rather than the 10% models in Figure 5.24.

5.2.7 Cross conductivity comparison

The above section shows that for fixed crack dimensions, the crack's confinement effect and current interference effect have opposite effects on the measured impedance and the final conductivity calculated can have 20% deviation from the assigned value. The study is limited to a homogenous model with conductivity of $1.355 \times 10^{-5} \text{ S/m}$ so it is necessary to investigate if these trends remain valid for a range of bulk material conductivity values. A series of models with bulk conductivities of $1.355 \times 10^{-3} \text{ (E3)}$, $1.355 \times 10^{-6} \text{ (E6)}$ and $1.355 \times 10^{-8} \text{ S/m (E8)}$ were therefore created. For each conductivity set, a homogenous model and a model containing a crack was created to calculate current interference, crack confinement and overall conductivity.

Models were created with a crack having the same crack dimensions, depth $20 \mu\text{m}$ and width $18 \mu\text{m}$. For ease of comparison, all models had $S/r = 4$, in other words, only the bulk conductivity of each set was different. The impedance results were processed using Equations 5.6, 5.7 and 5.8 to extract CI, CEP and CCE. The results are shown in Figure 5.26 and the values of CI, CEP and CCE do not change significantly for the different bulk conductivities. The crack's hindrance effect remains similar and the same applies to the current interference effect and the overall result of current interference and crack's hindrance remains unchanged. Thus, the conclusions made are valid for a range of bulk material conductivity values, as opposed to just the initial value of $1.355 \times 10^{-5} \text{ S/m}$.

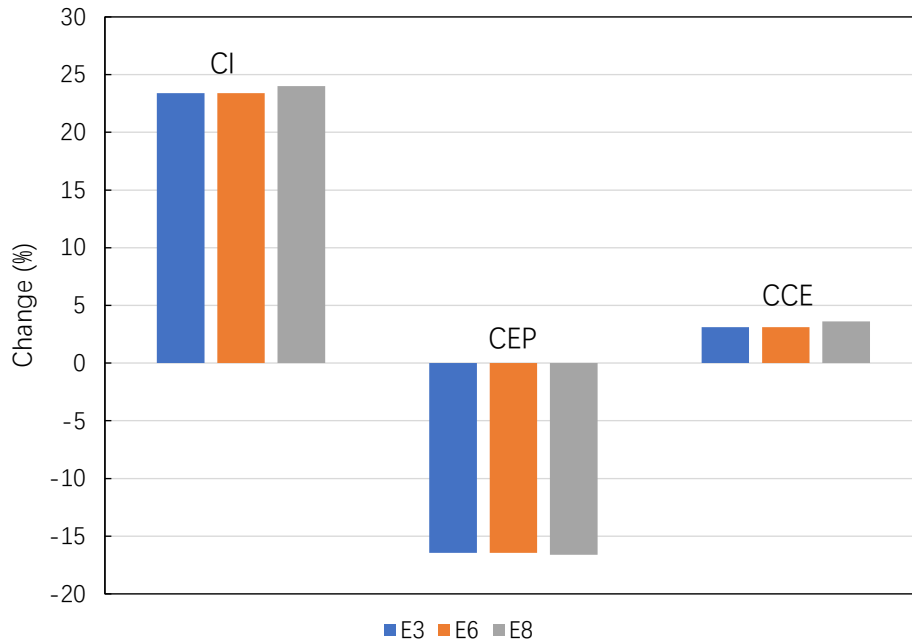


Figure 5.26. Cross conductivity comparison of CI, CEP and CCE. The material conductivity of the models was 1.355×10^{-3} (E3, blue), 1.355×10^{-6} (E6, orange) and 1.355×10^{-8} S/m (E8, grey). The three entities are calculated via Equations 5.7, 5.8 and 5.9 listed in the previous section. All models have $S/r=4$.

5.2.8 Plotting the crack effect using a \log_{10} scale

When the impedance results are calculated and compared in absolute units (S/m), the change caused by a crack can be 20-50% but after plotting the conductivity of each model on a \log_{10} scale, the difference between the crack containing and homogenous models is small, Figure 5.27. Increasing the crack depth by 8 times only inflicts about 0.1 change in the \log_{10} scale for all crack widths. Similarly, widening the crack from 10 to 90% of electrode separation, a 0.7 increase is observed on a \log_{10} scale.

Plotting the conductivity from the models on a logarithmic scale provides a perspective of how experimentalists would view the influence of a crack on conductivity Arrhenius plots. The effect on conductivity of crack geometry should be inferior to changes in temperature or material composition or adding a resistive surface layer, as the later factors can change the conductivity by more than 1 order of magnitude.

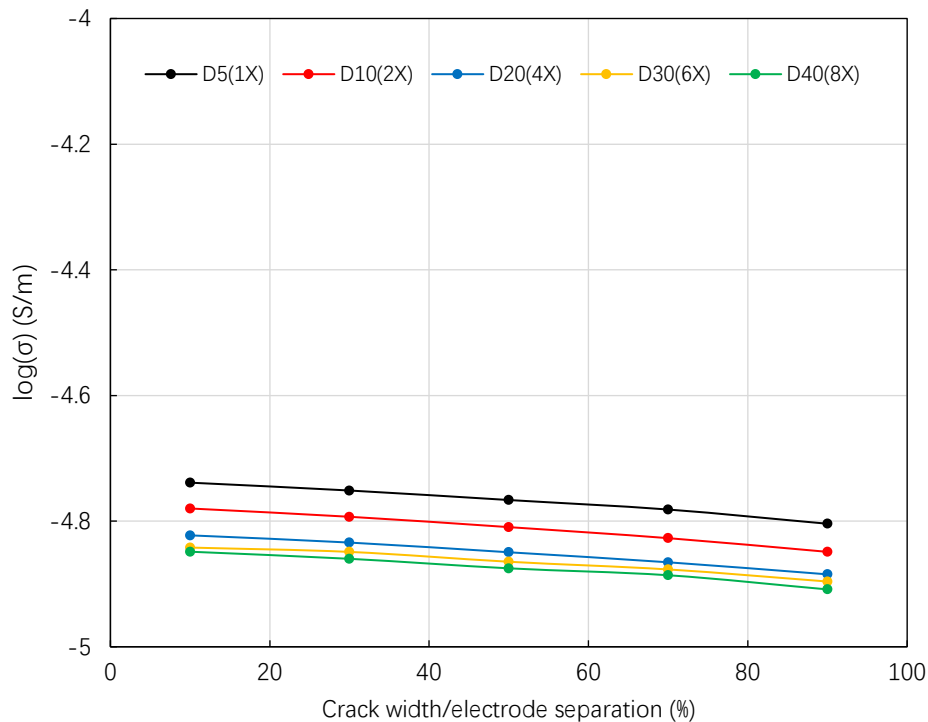


Figure 5.27. The conductivity of models containing a crack plotted on a \log_{10} scale versus crack width/electrode separation. The models are grouped by their crack depth. The y axis scale is expanded between -4 and -5 to show the relatively small differences in the conductivity values.

5.3 Conclusions

A number of key points have been made within this chapter, these are:

1. Increasing crack width and depth results in higher impedance from top-top micro-contact electrode measurements. The maximum increase in the Z'' peak value and therefore resistance is 59%, at $S/r=2$, crack width 90% of total separation and crack depth 8 times the electrode radius.
2. The geometric factor is not suitable for calculating conductivity. Under certain situations, the spreading resistance equation (SRE) can be used. In the $S/r=2$ set up, when the crack depth to electrode radius ratio is between 4 and 8, the SRE can be used to calculate the conductivity of the material at any crack width. The calculated results are within a $\pm 10\%$ error range of the input value.
3. For $S/r=2$, the crack effect (current confinement) can counterbalance the current interference from closely placed electrodes. As S/r increases, the crack effect diminishes more rapidly than the decrease in current interference. The crack's effect therefore becomes less effective in cancelling the current interference effect.
4. Line scans of current distribution show adding a crack between the micro-contacts will lower the current density between the electrodes, but the current density in the outer regions will increase.
5. When the calculated bulk conductivities of models are plotted on a \log_{10} scale, the effect of a crack of any dimensions is very limited. The maximum deviation caused by a crack is only 0.1 on a \log_{10} scale of conductivity.

5.4 References

- [1] J. T. S. Irvine, D. C. Sinclair and A. R. West, "Electroceramics: Characterization by Impedance Spectroscopy," *Adv. Mater*, 2, pp. 132–138, 1990.
- [2] J. Fleig, "Local conductivity measurements on AgCl surfaces using microelectrodes.," *Solid State Ionics*, 85, pp. 9–15, 1996.
- [3] M. Shirpour, R. Merkle, C. Lina and J. Maier, "Nonlinear electrical grain boundary properties in proton conducting Y–BaZrO₃ supporting the space charge depletion model," *Phys. Chem. Chem. Phys.*, 14, pp. 730–740, 2012.
- [4] J.-S. Lee, J. Fleig, J. Maier, D.-Y. Kim and T.-J. Chung, "Local Conductivity of Nitrogen-Graded Zirconia," *J. Am. Ceram. Soc*, 88, pp. 3067–3074, 2005.
- [5] N. Wu, K. Ogawa, M. Chyu and S. X. Mao, "Failure detection of thermal barrier coatings using impedance spectroscopy," *Thin Solid Films*, 457,2, pp. 301–306, 2004.
- [6] H. G. Beom, K. M. Jeong, J. Y. Park, S. Lin and G. H. Kim, "Electrical failure of piezoelectric ceramics with a conductive crack under electric fields," *Eng. Fract. Mech*, 76,15, pp. 2399–2407, 2009.
- [7] C. Q. Ru and X. Mao, "Conducting cracks in a piezoelectric ceramic of limited electrical polarization," *J Mech Phys Solids*, 47, 10, pp. 2125–2146, 1999.
- [8] V. Heyer, G. A. Schneider, H. Balke, J. Drescher and H.-A. Bahr, "A fracture criterion for conducting cracks in homogeneously poled piezoelectric PZT-PIC 151 ceramics," *Acta Mater.*, 46, 18, pp. 6615–6622, 1999.
- [9] C.-X. Zhang, C.-E. Zhou, S.-K. Gong, H.-F. Li and H.-B. Xu, "Evaluation of thermal barrier coating exposed to different oxygen partial pressure environments by impedance spectroscopy," *Surf. Coat. Technol.*, 201, 1, pp. 446–451, 2006.
- [10] J. W. Byeon, B. Jayaraj, S. Vishweswaraiah, S. Rhee, V. H. Desai and Y. H. Sohn, "Non-destructive evaluation of degradation in multi-layered thermal barrier coatings by electrochemical impedance spectroscopy," *Mater. Sci. Eng. A*, 407, 1, pp. 213–225, 2005.
- [11] S. -H. Song, P. Xiao and L. -Q. Weng, "Evaluation of microstructural evolution in thermal barrier coatings during thermal cycling using impedance spectroscopy," *J. Eur. Ceram. Soc.*, 25, 7, pp. 1167–1173, 2005.
- [12] R. A. Veazey, "Probing Radiation Damage in Fe-doped SrTiO₃ using Micro-contact Impedance Spectroscopy," PhD thesis, The University of Sheffield, 2019.
- [13] J. S. Dean, J. H. Harding and D. C. Sinclair, "Simulation of Impedance Spectra for a Full Three-Dimensional Ceramic Microstructure Using a Finite Element Model," *J. Am. Ceram. Soc*, 97, pp. 885–891, 2013.
- [14] C. Geuzaine and J.-F. Remacle, "Gmsh: a three-dimensional finite element mesh generator with built-in pre- and post-processing facilities.," *Int. J. Numer. Methods Eng.*, 79(11), pp. 1309–1331, 2009..
- [15] "ParaView Homepage <https://www.paraview.org/>," [Online]. [Accessed 1 5 2021].
- [16] H. Tada, P. C. Paris and G. R. Irwin, *The stress analysis of cracks handbook*, Del Research Corporation, Hellertown, 1973.
- [17] L. E. Dickens, "Spreading Resistance As A Function of Geometry And Frequency," Johns Hopkins University Carlyle Barton Laboratory, Baltimore, Maryland, USA, Technical Report No. NAS-1, p. 7, 1965.

- [18] R. A. Veazey, A. S. Gandy, D. C. Sinclair and J. S. Dean, "Modeling the influence of two terminal electrode contact geometry and sample dimensions in electro-materials," *J Am Ceram Soc*, 102, pp. 3609– 3622, 2019.

Chapter 6: Two-layer (heterogeneous) Model

6.1 Introduction

In chapter 5, the effect of adding a crack into a homogenous cube on the current distribution and on impedance spectroscopy data was studied. The addition of a crack alone is not sufficient to replicate the experimental impedance results obtained by Veazey as described in Chapter 2. The next factor to be investigated is the effect of a resistive surface layer on the homogenous cube model. Although the origin of this study is from Veazey's experiment of two-layer radiation damaged SrTiO₃-based samples, it is not limited to this particular issue. Two-layer ceramic systems have been widely studied and applied to the manufacturing sector, such as functional oxide thin films. Measuring the electrical properties in a two-layer system by micro-contact impedance spectroscopy (mclS) is an important factor to fully understand the materials. Compared with conventional impedance measurements, mclS can detect impedance responses at the surface of the material as the majority of the current distribution is within a small volume near the micro-contact. Moreover, it allows to probe particular areas or features of interest, by setting micro-contacts in the interested area. For example, Taibl et al [1] presented impedance spectra of a two-layer system, containing an Fe-doped SrTiO₃ resistive thin film deposited on a highly conductive Nb-doped SrTiO₃ substrate. mclS was used to retrieve the electrical properties of the resistive thin film, micro-contacts with radius of 50-150 μm were prepared on the thin film while platinum electrode covers the entire bottom surface of the substrate, a micro-top full-bottom configuration was used. The measured impedance spectra revealed the existence of bias induced ion motion in the thin film, although the ionic current measured is negligible compared to the electronic current [1]. Joo and Choi used mclS to investigate YSZ thin film's conductivity on Pt substrate. The YSZ films with thickness between 200 nm to 1.5 μm were deposited by pulsed laser deposition on the Pt substrates. A Pt micro-contact with area of 0.05 cm² was sputtered on the surface of thin film. The impedance data showed both the across-plane and the in-plane conductivities of YSZ thin film are very close to the YSZ bulk specimen [2].

mclS is also widely used in characterisation of thermal barrier coatings (TBC) on super alloys. The TBC generally has lower conductivity than the superalloy substrate which can be considered as a two-layer or multi-layer system. A study on 3Gd₂O₃-3Yb₂O₃-4Y₂O₃ co-doped ZrO₂ (GY-YSZ) thermal barrier coating was conducted by Zhang et al [3]. In this experiment, the GY-YSZ coating of 100 μm thickness was deposited on superalloy, micro-electrodes were prepared in micro-top top configurations. The mclS study revealed an increase in measured resistance of the thermal barrier layer after heat treatment at 1100 °C, which is linked to the compositional change in the layer itself. This case is selected for simulation in chapter 8 of this thesis to prove the versatility of our models.

Developing a two-layer FEM model of a ceramic system and the ability to provide a method to extract accurate surface layer electrical properties could be a useful addition in this field. For example, in assisting the experimentalist to extract more reliable conductivity values and/or for calibrating their measurements with known samples.

The primary research method is the same as chapter 5, to produce simulated impedance data for various models and to extract the conductivity of each in order to compare with the known input values assigned to those regions. The simulations have the following fixed variables: the micro contact radii of all models are $10\ \mu\text{m}$; the side length of the cubic model is maintained at $200\ \mu\text{m}$; the relative permittivity of each layer is set as 162; the conductivity of the bulk layer is fixed at $1.355 \times 10^{-5}\ \text{Sm}^{-1}$. Figure 6.1 shows the structure of the two-layer model used for this chapter.

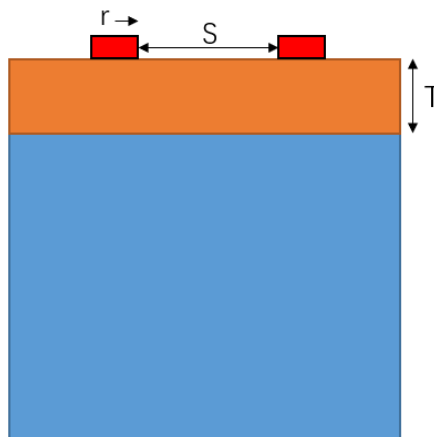


Figure 6.1. Illustration of the two-layer model used in this chapter. The radius of micro-contact, $r = 10\ \mu\text{m}$. The surface layer thickness and separation between the micro-contacts are also shown.

There are three variables to be modified: (i) the surface to bulk layer resistivity ratio (R_s/R_b); (ii) the thickness of the surface layer, T , and (iii) the separation between the micro-contact electrodes, S .

For (i) the resistivity of the surface layer was set to 2, 5, 10, 100 and 1000 times that of the bulk layer. For (ii), the surface layer thickness T was set at 1.25, 2.5, 5, 10, 20 and $30\ \mu\text{m}$, to maintain the thickness of the surface layer to micro contact radius ratios (T/r) of 0.125, 0.25, 0.5, 1, 2 and 3. This T/r range is chosen as we aim to complete the range omitted by Veazey et al [4] where they provided solutions for T/r smaller than 0.1 and larger than 10. For (iii), the electrode separation was set so the electrode radius ratio (S/r) was 1, 4 and 8. $S/r=1$ is chosen as it is a common practical setting when measuring fine features between two neighbouring micro electrodes without the presence of a crack. $S/r=8$ is chosen as our group has previously reported this to be the lowest separation required to obtain results within an acceptable $\pm 10\%$ error range based on input values. Lower S/r ratios induce current interference between both electrodes and results in an overestimation of the conductivity [4]. The combination of variables is listed in Table 6.1.

Rs/Rb	Surface layer thickness (T)	Separation/contact radius (S/r)
2	1.25, 2.5, 5, 10, 20, 30	1, 4, 8
5	1.25, 2.5, 5, 10, 20, 30	1, 4, 8
10	1.25, 2.5, 5, 10, 20, 30	1, 4, 8
100	1.25, 2.5, 5, 10, 20, 30	1, 4, 8
1000	1.25, 2.5, 5, 10, 20, 30	1, 4, 8

Table 6.1. All combinations of the variables used in this chapter. For each Rs/Rb ratio, all 6 T are simulated and for each T, all three S/r ratios are simulated. Therefore, for each Rs/Rb ratio, 18 simulations were performed.

The simulated impedance data are used to analyse the conductivity of a surface layer and a bulk layer. Data are shown for three S/r ratios based on two variables: (a) increasing surface layer thickness and (b) increasing the surface layer resistivity. From previous results [5] and from the previous chapter, it is known that in a single layer (homogenous) model, small separation distances between electrodes can induce an overestimation of conductivity (so called interference effect) as the micro-electrodes have a strong localising effect on the current [5]. It is therefore important to vary S/r to establish the influence of interference effects in a two-layer system.

6.2 Results

6.2.1 Current density distribution and impedance data

We first inspect the impedance data based on homogenous material models (i.e. $R_b = R_s$) with S/r of 1, 4, 8, 30. The properties of both layers are set to be the same; the conductivity is $1.355 \times 10^{-5} \text{ Sm}^{-1}$ and the relative permittivity is 162. In Figure 6.2(a), Z'' spectra show a single peak for each S/r model. All three F_{\max} values are the same at 1526 Hz, which agrees well with the theoretical value of 1500 Hz. This shows the FEM model generated works well. The $S/r=30$ model has the highest Z'' value of $1.777 \times 10^9 \Omega$, the $S/r=8$ model has a value of $1.737 \times 10^9 \Omega$, whereas the $S/r=4$ model has $1.624 \times 10^9 \Omega$ and the $S/r=1$ model has the lowest value of $1.394 \times 10^9 \Omega$. The extracted resistance therefore decreases with decreasing S/r , this trend agrees well with the Z^* plots in Figure 6.2(b).

In Figure 6.2(c), the C' spectra are shown and now the same trend is observed for the extracted capacitance values with varying S/r . The $S/r=1$ model has a capacitance value of $3.80 \times 10^{-14} \text{ F}$, which is the highest. The $S/r=4$ model has a value of $3.27 \times 10^{-14} \text{ F}$, the $S/r=8$ model has capacitance value of $3.05 \times 10^{-14} \text{ F}$ and the $S/r=30$ model has the lowest capacitance value of $2.98 \times 10^{-14} \text{ F}$. For this homogenous material model, the F_{\max} does not deviate and the changes in capacitance and resistance are only influenced by the separation between the electrodes, i.e. the relationship $\omega_{\max} RC = 1$ holds for the Z'' Debye peak, (where $\omega_{\max} = 2\pi F_{\max}$)

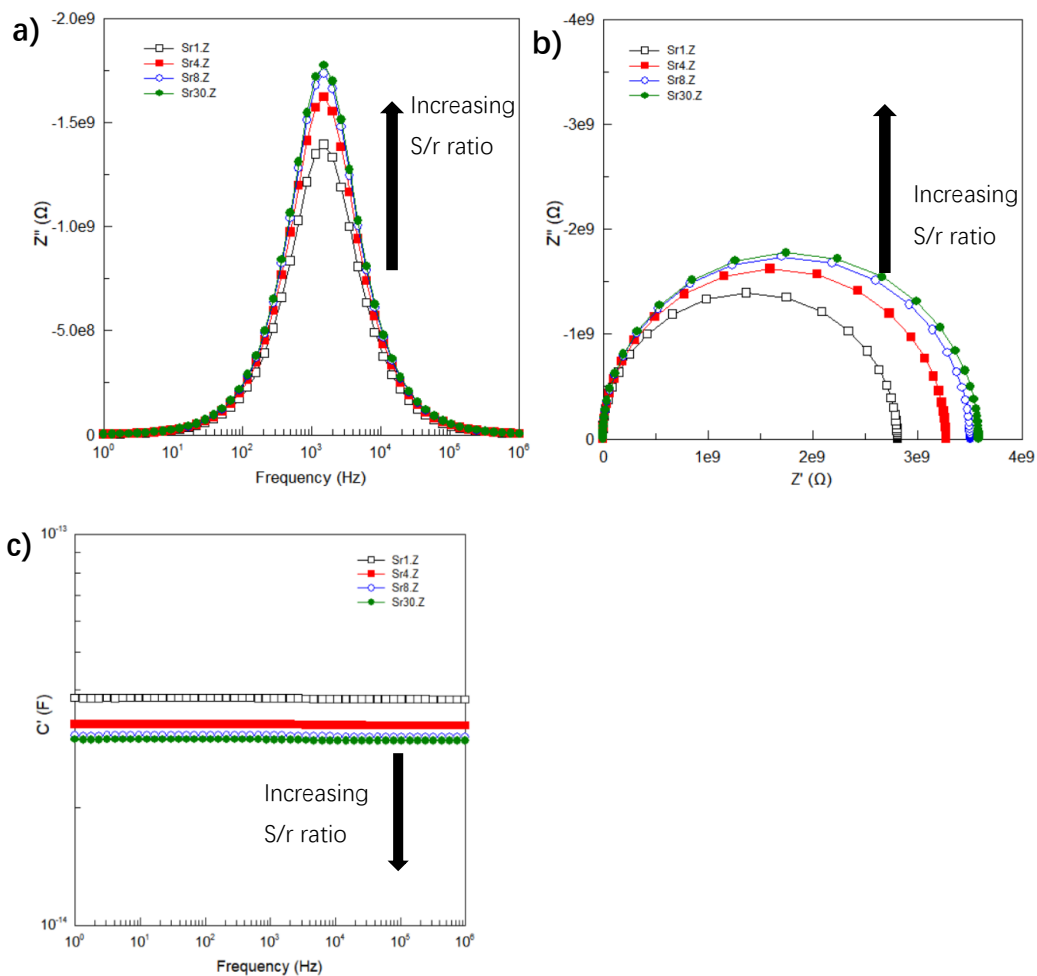


Figure 6.2. Impedance for the homogenous materials model ($R_b = R_s$) with S/r ratios of 1 (black), 4 (red), 8 (blue) and 30 (green). (a) Z'' spectra, (b) Z^* plots and (c) C' plots.

For the heterogeneous models, we started with a surface to bulk layer resistivity ratio of 100X to perform a direct comparison with Veazey et al's results [4]. In this model, the surface layer resistivity (R_s) is 100 times larger than the bulk resistivity (R_b) and therefore has a conductivity of $1.355 \times 10^{-7} \text{ Sm}^{-1}$ ($R_s/R_b=100$).

6.2.2 Line scan results for $R_s = 100R_b$ models with different surface thickness

First, line scans of current density distribution are studied to gain a fundamental understanding of the effect of a resistive surface layer on distribution of the current. In Figure 6.3, the line scan takes place in a two-layer model with a surface layer thickness of $10 \mu\text{m}$. The scan results at various depths are shown. When the scan is taken within the surface layer ($z=1 \mu\text{m}$), the current distribution shows the same shape as the homogenous model shown in chapter 5. The current interference between the electrodes is high and the central region of the distribution curve has a steep valley. The two peaks at $x = 25$ and $175 \mu\text{m}$ is the result of the coarse mesh size in this region away from the surface centre, where the more conductive bulk layer element intruded the surface layer, causing an increase in the measured current density. As the mesh attractors are placed in the model's surface centre where the mesh size is required to be the smallest, the scan resolution is the highest for x-axis positions between 50 to 150 μm .

As the scan depth moves into the underlying bulk layer, which is 100 times more conductive than the surface layer, the current density at $z = 12 \mu\text{m}$ is higher than that of the surface layer. This is as a result of the surface layer being more resistive, resulting in more current detouring around the top layer and travelling underneath into the bulk material.

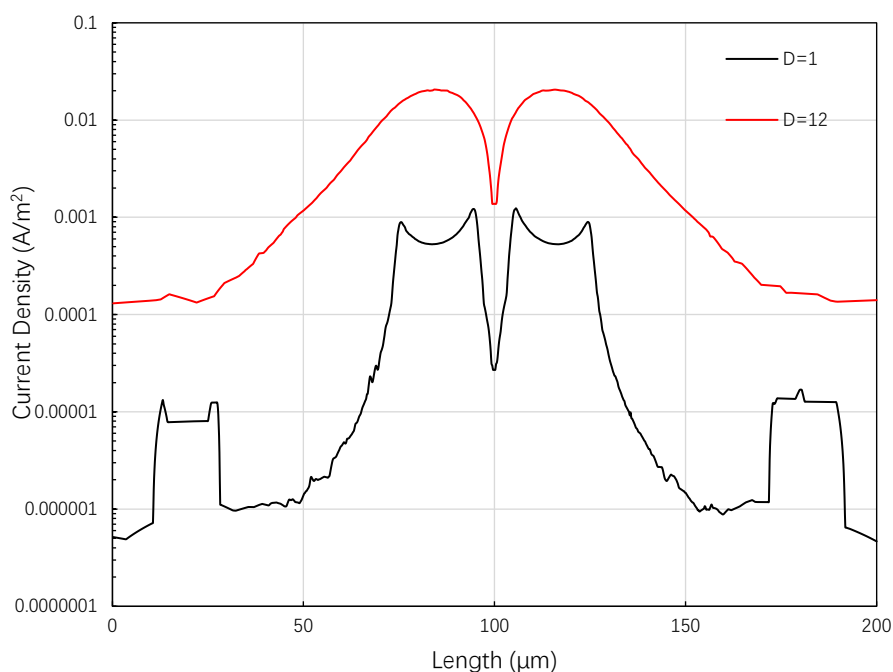


Figure 6.3. Line scan results plotted as current density versus length, scan depth at $z = 1$ and $12 \mu\text{m}$ in a two-layer model with $S/r=1$ and a surface layer thickness of $10 \mu\text{m}$. The surface layer is 100 times more resistive than the bulk layer.

In Figure 6.4, line scans for three models with $S/r=1, 4$ and 8 reveal how the S/r ratio affects the current distribution in a two-layer model set up. From Figure 6.4(a), increasing the separation between the electrodes causes the current density in the central section of the model to decrease. This is due to the reduced current interference from the electrodes. The line scans in Figure 6.4(b) take place in the bulk layer ($z = 12 \mu\text{m}$) and the current density in the central region shows the same trend as in the surface layer. However, using the $S/r=1$ model as an example, the highest current density in the bulk layer is about 20 times higher than that of the surface layer.

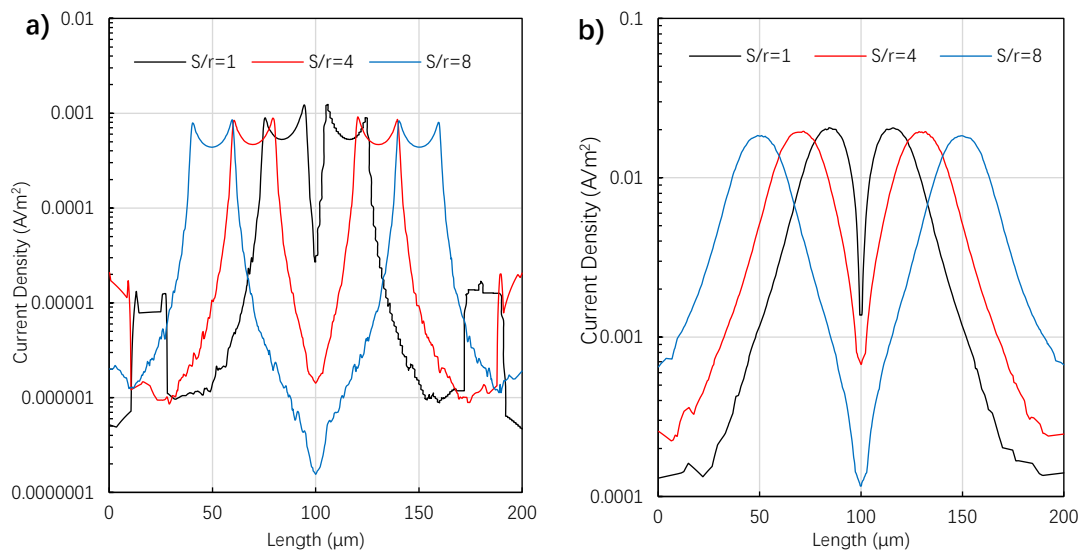


Figure 6.4. (a) Line scan data for models with $S/r=1, 4$ and 8 at a depth of $1 \mu\text{m}$ under the top surface and therefore in the surface layer. (b) Line scans for the same models at a depth of $12 \mu\text{m}$ and therefore in the bulk material.

Figure 6.5 shows models with $S/r=1$ where the line scan takes place along the z -axis to show how current density changes with the surface layer thickness. $T=0 \mu\text{m}$ corresponds to a surface layer thickness of $0 \mu\text{m}$, thus the model is a homogenous bulk material; the $T=200 \mu\text{m}$ model corresponds to a homogeneous surface layer material of $200 \mu\text{m}$. The $T=0 \mu\text{m}$ model shows the upper limit of the current density level and the $T=200 \mu\text{m}$ model shows the lower limit. In the $T=0 \mu\text{m}$ model, the current density is highest at the top surface of the model, 0.004 A/m^2 and gradually falls to 0.0006 A/m^2 at the bottom surface. When a resistive layer is added, the current density within the surface layer is reduced by 10 times, e.g., when $T=1.25 \mu\text{m}$, the current density at the top surface is only 0.0003 A/m^2 but it rapidly returns to the same level as the $T=0 \mu\text{m}$ model, when scan depth is within the underlying bulk layer. When the surface layer thickness is more than $5 \mu\text{m}$, the lowest current density is at the top surface layer and the lowest value merges with the $T=200 \mu\text{m}$ model, which is the homogenous model made with only the surface layer material. The transition between the lowest and highest current density takes place at the interface between the surface and bulk layers.

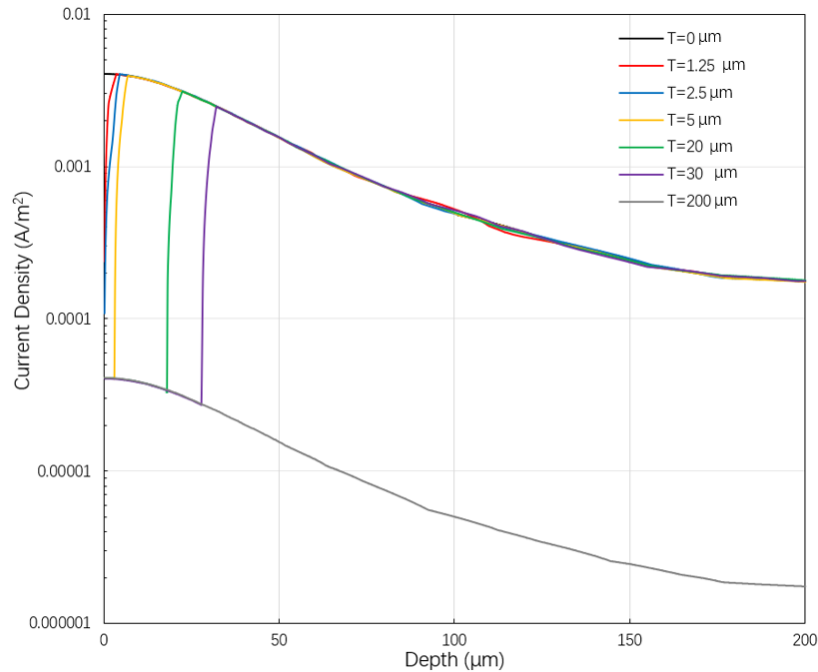


Figure 6.5. Line scan data for models with increasing surface layer thickness, T , from 0 to 200 μm , along the z axis, plotted as current density versus depth.

Since $R_s/R_b=100$ and the relative permittivity of both layers is 162, the time constant of the surface layer is 100 times larger than that of the bulk layer, therefore the impedance response from the surface layer is expected to be in the lower frequency range, using equation $\omega RC=1$, with the expected F_{max} for the associated Z'' peak at ~ 15 Hz in the Z'' spectrum.

Figure 6.6 shows impedance results from a series of simulated models with the following nomenclature: T1.25 corresponds to a surface layer thickness of 1.25 μm , electrode radius 10 μm and electrode separation 10 μm . In Figure 6.6(a)-(c), the impedance response from Z'' plots are shown for $S/r = 1, 4$ and 8 versus T , respectively. Only a single Debye peak at 15 Hz can be observed for each thickness model, meaning the surface layer response dominates the spectra. For all S/r values, the Z'' peak response increases with increasing surface layer thickness, therefore the resistance of the surface layer response also increases.

Figure 6.6 (d) shows the M'' spectra for $S/r = 4$ versus T . One set of M'' peaks increase in height with increasing surface layer thickness at 15 Hz. This is the response originating from the surface layer. At ~ 1500 Hz, another set of peaks decrease in height with increasing surface layer thickness. This response is associated with the bulk layer. The M'' peak at higher frequency becomes harder to distinguish after the surface layer thickness reaches a thickness of 20 μm ; therefore, the bulk layer conductivity is only extractable from M'' spectra for $T < 20$ μm . Nevertheless, the consistency of the F_{max} values associated with the surface and bulk layer responses indicate that the data are reliable for analysis.

The M'' spectra in 6.6(d) show a similar change in the peak height both at low and high frequencies as reported by Veazey et al [4]. For example, in Figure 2.12, measurement B (large

density of visible crack) shows a decrease in the height of the lower frequency M'' peak and an increase in height of the higher frequency M'' peak, compared with measurement A (lower density of visible cracks). In Figure 6.6(d), this trend can be observed when the surface layer thickness is reduced. Using the $T = 5$ model (open blue circle symbols) and the $T = 2.5$ model (filled red squares) as an example, the change in M'' peak heights from a surface layer thickness of 5 to 2.5 μm is very similar to that observed in Veazey's experiment. This means a change in surface layer thickness could be an important variable that is responsible for altering the observed impedance results in Veazey's experiment. Furthermore, the Z'' spectra in (a)-(c) also reflect the same trend shown in Figure 2.12; when the surface layer thickness is reduced the Z'' peak height is reduced.

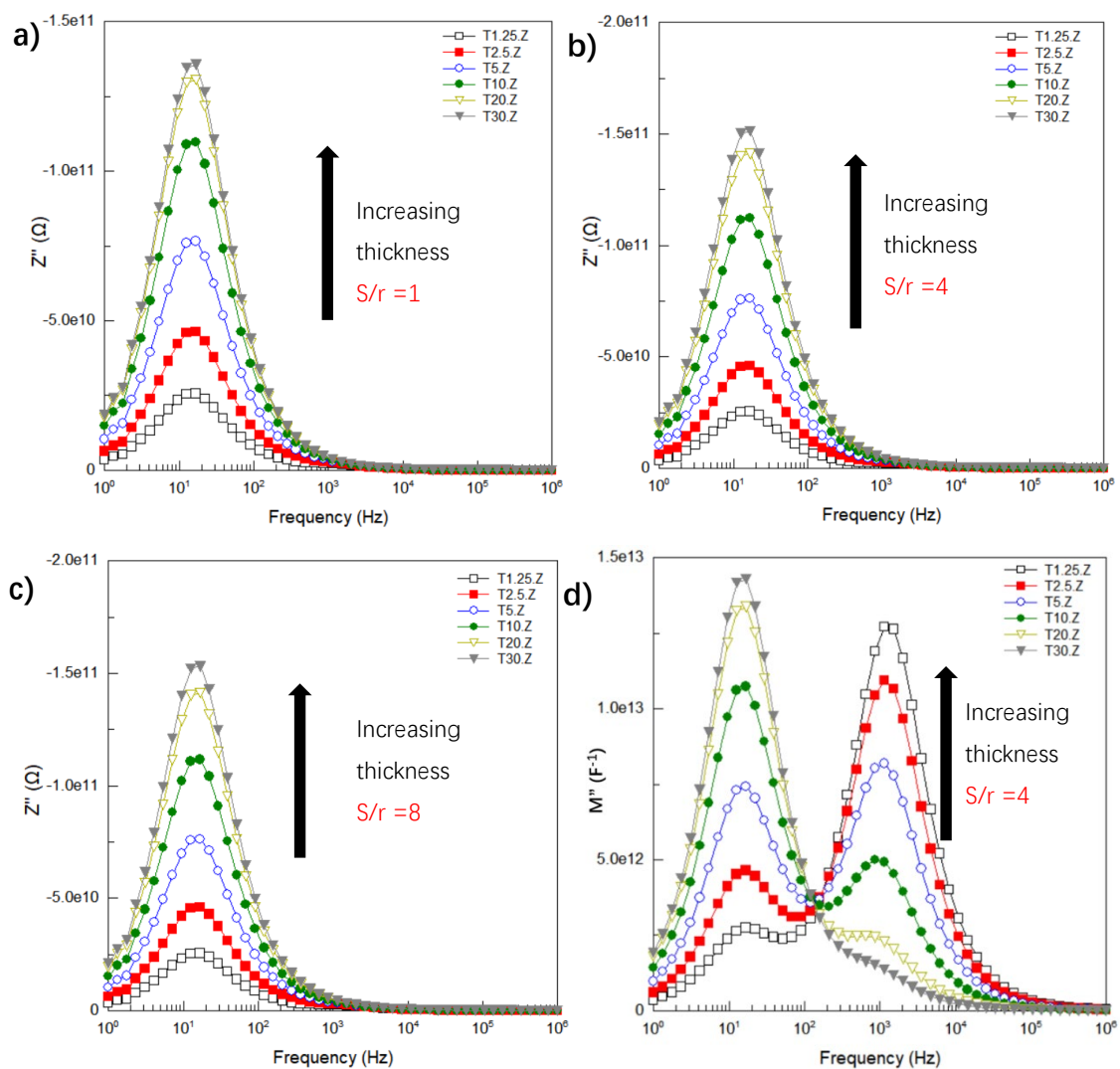


Figure 6.6, Impedance Spectroscopy data for the $R_s/R_b = 100$ model with different electrode separations. (a) Z'' spectra for models with S/r ratio of 1 with increasing T . Corresponding Z'' spectra for models with $S/r=4$ (b) and $S/r=8$ (c). (d) M'' spectra for models with $S/r = 4$ for a range of T values. Black arrows indicate the increasing surface layer thickness.

6.2.3 Data processed with the original Spreading Resistance Equation

The extracted surface layer resistance value for each S/r model versus T/r is shown in Figure

6.7 (a) and the spreading resistance equation (Equation 5.5) is used to calculate conductivity, Figure 6.7 (b). The x-axis in Figure 6.7 uses the ratio of surface layer thickness over the electrode radius (T/r) instead of the surface layer thickness alone so that we can combine surface layer thickness together with electrode radius. Since the electrode radius is set at $10\ \mu\text{m}$, combining these two parameters can effectively reduce the variables that is required to be consider. The resistance of each S/r ratio increases rapidly with thickness until the surface layer thickness reaches $10\ \mu\text{m}$ and the increase rate then slows down after that. In Figure 6.7(b), the spreading resistance equation (Equation 5.5) proposed by Veazey et al is applied to calculate the surface layer conductivity for each surface thickness set up. r is the radius of the micro-electrode and R_{spr} is the extracted surface layer resistance value using the maxima in Z'' plots. With the intrinsic conductivity value of the surface layer being $1.355 \times 10^{-7}\ \text{Sm}^{-1}$, all the calculated results using the original spreading resistance equation are overestimated, especially for low T/r values where it can be close to an order of magnitude higher. In addition, even for larger $T/r = 3$ the difference is at least a factor of two and is largest for $S/r=1$.

The results shown in Figure 6.7 illustrate the spreading resistance equation to be inappropriate for calculating surface layer conductivity in a two-layer heterogeneous system when the surface layer thickness is between 0.125 to 3 times of the micro contact radius ($0.125 < T/r < 3$). These results agree well with what has been reported previously, i.e. this equation is only accurate when the separation to electrode radius ratio is 10 or greater, providing there is no resistive layer between the electrode and the material [6]. This inaccuracy is the reason why Veazey et al limit the spreading resistance equation's applicable range to $T/r \geq 10$. Although the results calculated in Figure 6.7 deviate significantly from the input value, there is a trend, i.e. the slopes of the curves for each S/r are comparable. This indicates the original spreading resistance equation may be modified to be used in a two-layer system. This allows us to achieve the goal of simplifying the two limiting equations proposed by Veazey et al [4] into one equation and that is the aim of developing an two-layer spreading resistance equation.

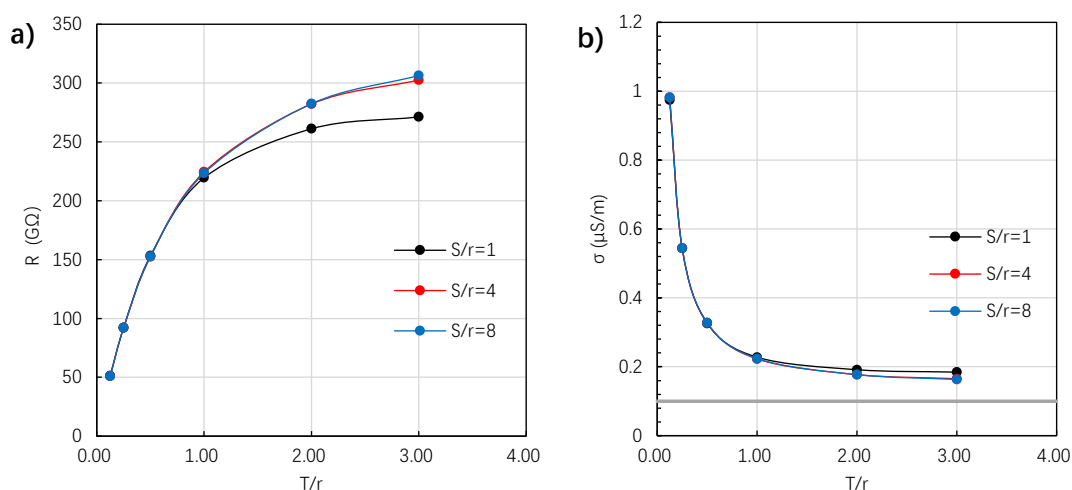


Figure 6.7. Calculated resistance (a) and conductivity (b) of the surface layer plotted against surface layer thickness/electrode radius, using the spreading resistance equation. The input value of surface layer conductivity is the horizontal grey line at $0.135\ \mu\text{S/m}$.

6.2.4 Introducing the two-layer spreading resistance equation

So far in this project, the detailed method to extract the measured conductivity can be summarised as:

- (i) Use Z'' and M'' spectra to identify surface and bulk layer responses where appropriate
- (ii) Extract R and C values for the surface and bulk responses using the $wRC=1$ relationship associated with Debye responses in the spectra

(iii) Correct R values (in units of Ω) using the original spreading resistance equation $\sigma = \frac{1}{2} \frac{1}{rR_{spr}}$

(Equation 5.5) to obtain a conductivity, s (in units of S/m).

- (iv) Establish where this equation is valid and gives conductivity values that are $\pm 10\%$ of the input value.

In chapter 5, it was shown that the spreading resistance equation can be relatively accurate for calculating a materials conductivity when the S/r ratio is low, and the crack depth is at least 4 times the electrode radius. However, the spreading resistance equation requires that no resistive obstacle is placed between the two micro-contacts. Now in chapter 6, a resistive layer is placed between the two micro-contacts and some modification of the spreading resistance equation is required. Veazey et al had proposed a set of equations with multiple boundary conditions for models with a resistive surface layer [4]. We aim to provide a method to calculate surface layer σ using only one equation that is applicable over a wider range. The core principle of our method is to adjust the spreading resistance equation with simulation data, listed as (v).

- (v) Replace $\frac{1}{2}$ in the spreading equation with a prefactor X to extend the use of the spreading resistance equation, i.e. $\sigma = X \times \frac{1}{rR_{spr}}$ (Equation 6.1)

The modifying process begins with the homogenous material model, i.e. $R_s = R_b$. This proposal of using a homogenous model is to set up a baseline for calculations based on a bi-layer model when Equation 6.1 is used.

The prefactor X 's value in Equation 6.1 is calculated by comparing simulated conductivity with the intrinsic conductivity assigned to the model, and the reciprocal of the difference between the two values being the Two-layer spreading resistance equation. The results for $R_s=R_b$ are shown in Figure 6.8. Four horizontal lines for X from different S/r ratios are generated based on the simulated results. The $S/r=30$ model data gives an X value of 0.48, which is very close to original spreading resistance equation's numerical value of 0.50. The $S/r=8$ line has an X value of 0.47, which is also very close to the original value of 0.5, suggesting Veazey et al's previous finding is correct [5]. Veazey et al suggested that to ensure the extracted conductivity is within $\pm 5\%$ error of the intrinsic value set in the model, a minimum electrode separation to electrode radius ratio (S/r) of 28 is needed [5]. For the error requirement to be within $\pm 10\%$ of the intrinsic value, the S/r ratio can be reduced to 8.

Decreasing the S/r ratio from 8 to 4 shifts the X value down by 0.026. S/r =4 and 1 are used to test the influence when current interference from the electrodes become significantly higher than the 10% error of the S/r=8 set up. Apart from this reason, S/r=1 is chosen to explore the experimentally lower limit achievable and its effect on the calculations. For S/r=1, the X value is 0.38. This difference is attributed to overlap of the high current density zones underneath each electrode and the resulting effect of the overestimation of current density.

Using the homogenous models as a baseline, three sets of two-layer models were constructed where the surface layer is 100 times more resistive than the bulk but at different S/r values. The calculated X values from the simulated impedance results are shown in Figure 6.8. When T/r is low, the X value for all 3 S/r sets is low, eg < 0.20 but it increases substantially with increasing T/r. Although the X value retained the order of being highest for S/r=8 and lowest for S/r=1, the difference in the X value is small when T/r is less than 1. With increasing T/r, the X values from the 100X model with S/r= 1, 4 and 8 rise closer towards their corresponding homogenous model X values. From this trend, we can assume that with a thick enough surface layer, the prefactor X value of all three models will intercept with the baseline value of the corresponding homogenous model. At that point, the impedance response of a two-layer system with a large surface layer thickness and thin bulk layer should be identical to a single layer model with homogenous surface layer material properties.

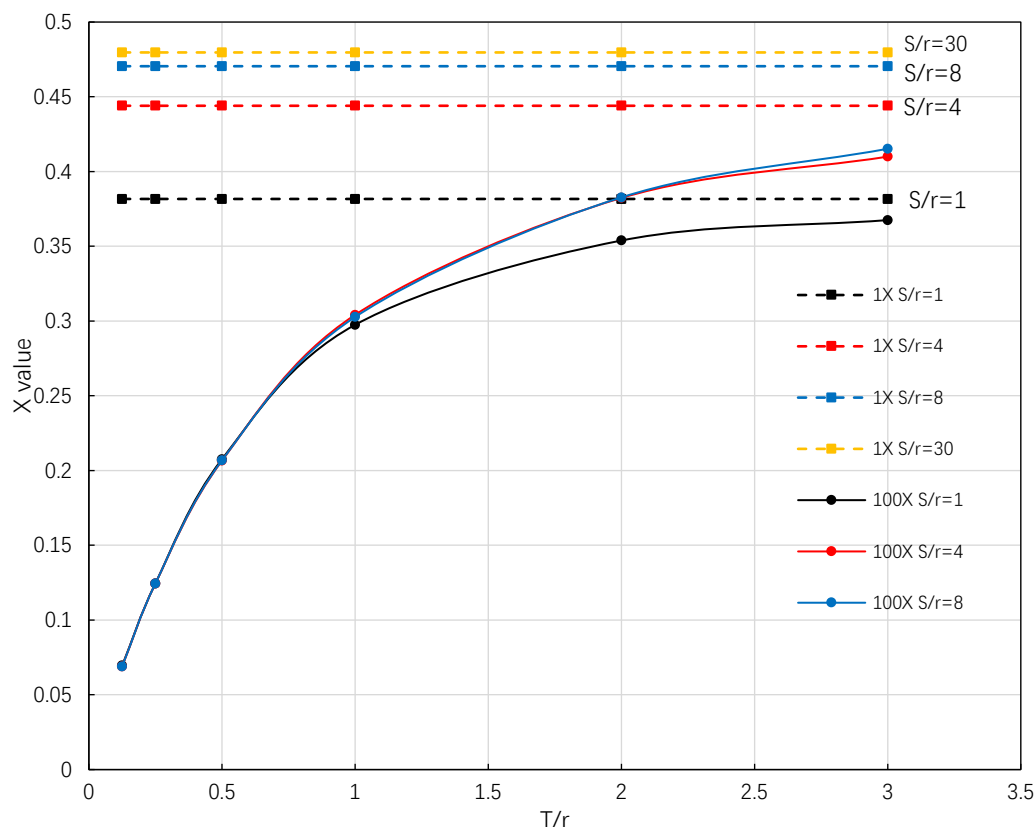


Figure 6.8. Two-layer spreading resistance's prefactor X value against surface thickness/micro contact radius (T/r). Three sets of models with different Rs/Rb ratios are chosen. The 1X set (Rs = Rb) contains four different S/r ratios of 1, 4, 8 and 30. The 100X models (Rs/Rb=100) contains S/r ratios of 1, 4 and 8.

6.2.5 Instructions on how to use the two-layer spreading resistance equation in calculations

To use the two-layer spreading resistance equation, one should first establish the experimental set up used. Firstly, confirm the electrode separation to electrode radius ratio. Next, establish the surface layer thickness if known, or conduct probing methods such as TEM to confirm the surface layer thickness. This allows the surface layer thickness to electrode radius ratio to be calculated.

For example, with a micro-contact radius of 10 μm , a surface layer thickness of 5 μm and $S/r = 1$, the prefactor X value reading from Figure 6.8 is 0.207. Substitute 0.207 into Equation 6.1 as the x variable, the equation becomes,

$$\sigma = 0.207 \times \frac{1}{rR_{spr}}$$

Then insert the r and R_{spr} values retrieved from experiments and the conductivity of the surface layer can be calculated.

The influence of the micro contact radius on the calculated conductivity values is investigated now that the novel two-layer spreading resistance equation is established. This is because the micro contact radius is an important parameter in Equation 6.1 and is something that will vary between different research groups depending on their electroding facilities. In Figure 6.9 below, X values of 4 models with different micro contact radius from 2.5 to 10 μm are summarised for the conditions of $R_s/R_b = 100$ and $S/r = 4$. All prefactor X curves overlap across the entire T/r range, suggesting that the new two-layer spreading resistance equation is independent across this micro contact radius range.

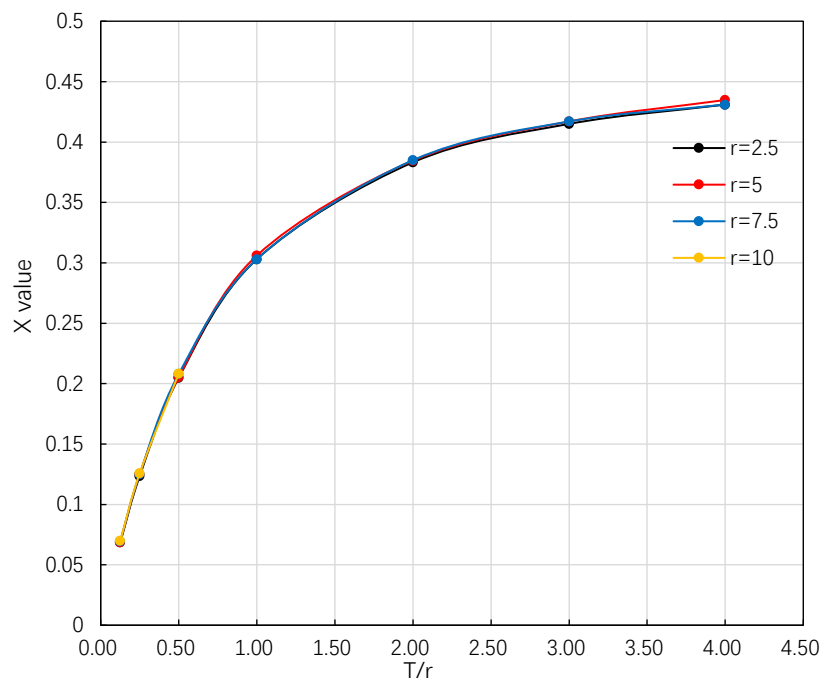


Figure 6.9, Two-layer spreading resistance's prefactor X value versus T/r for models with different micro contact radius of 2.5, 5, 7.5 and 10 μm . All models have $R_s/R_b = 100$ and $S/r = 4$.

6.2.6 The influence of the surface to bulk layer resistivity ratio

The aim now is to expand the applicability of the two-layer spreading resistance equation to other surface to bulk layer resistivity ratios (R_s/R_b). In experimental applications, various R_s/R_b ratios are likely to occur and it is instructive to use the two-layer spreading resistance equation to explore the guidelines or boundary conditions to be aware of in calculating surface layer conductivity when the R_s/R_b ratio is not 100.

Line scans were applied to models with different R_s/R_b ratios and the results are shown Figure 6.10. Line scans along the z axis reveal the current density distribution at all depths. The models scanned have a surface layer thickness of $5\ \mu\text{m}$, the R_s/R_b ratios are 1X, which is the homogenous model without a surface layer, 5X, 10X and 100X. As the surface layer resistivity increases the current density in the surface layer decreases. Once the scan depth is beyond the surface layer and into the bulk material, the current density of all models overlaps onto a single curve. Thus, the surface layer to bulk layer resistivity ratio can only affect the current density in the surface layer. The material underneath is not affected regardless of how resistive the top layer is.

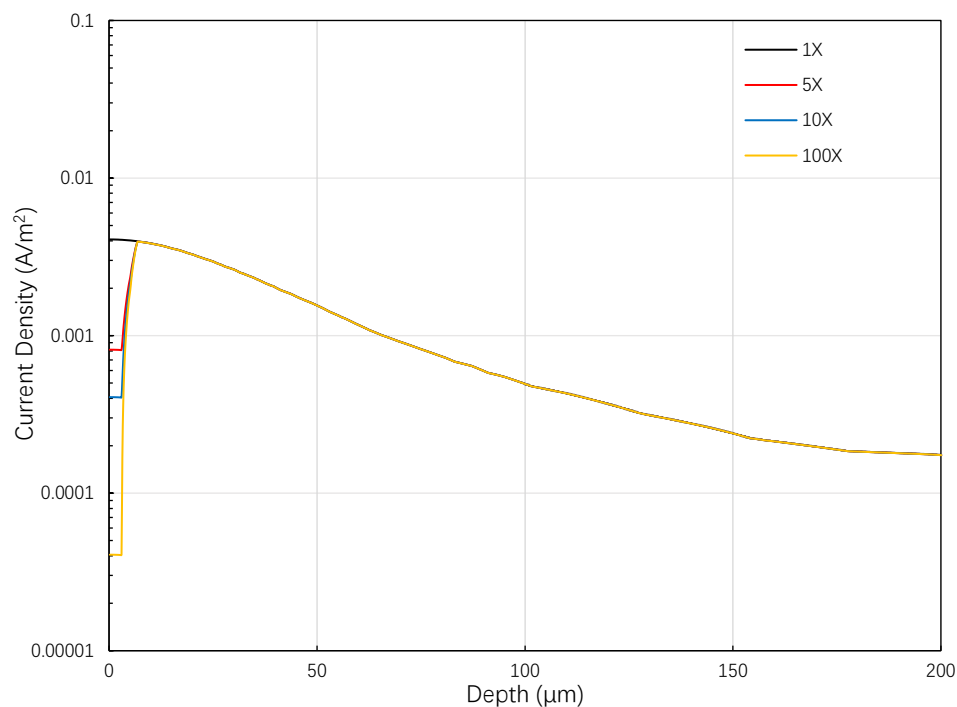


Figure 6.10. Line scan data of models with different R_s/R_b values along the z axis direction, plotted as current density versus depth. All models have a surface layer thickness of $5\ \mu\text{m}$.

The next step is to generate impedance results for different R_s/R_b models and then process with the two-layer spreading resistance equation. The first attempt was to lower the R_s/R_b ratio from 100 to 10; the surface layer's conductivity of this series of models is $1.355 \times 10^{-6}\ \text{Sm}^{-1}$. The relative permittivity value of the surface and bulk layers remains at 162. Three sets of models with $S/r = 1, 4$ and 8 were constructed. In each set the surface layer thickness increased from 1.25 to $30\ \mu\text{m}$.

In Figure 6.11, Z'' spectra from three sets of simulated models are shown. The F_{max} of the Debye peak in all plots for all surface layer thicknesses is 160 Hz compared to the theoretical value of 150 Hz; therefore, a 6.67% deviation from the theoretical value in the time constant is observed. Considering the impedance simulation is limited to use 50 points to cover a large frequency range, the accuracy of each point could be affected. A 6.67% deviation is considered acceptable (i.e. < 10%) and thus the result is considered accurate for this set of simulations.

Closer inspection of the data for the $T=1.25 \mu\text{m}$ model in the $S/r=8$ series shows a secondary, small peak near 1500 Hz. 1500 Hz is the theoretical value of F_{max} for the Debye peak associated with the bulk layer, as the intrinsic conductivity of the bulk layer was set at $1.355 \times 10^{-5} \text{ Sm}^{-1}$. This small secondary peak is the response from the bulk layer. In other words, when the surface layer is thin at $1.25 \mu\text{m}$, an impedance response from both the surface and bulk layers can be observed. The secondary peak become less visible when the surface layer thickness increases.

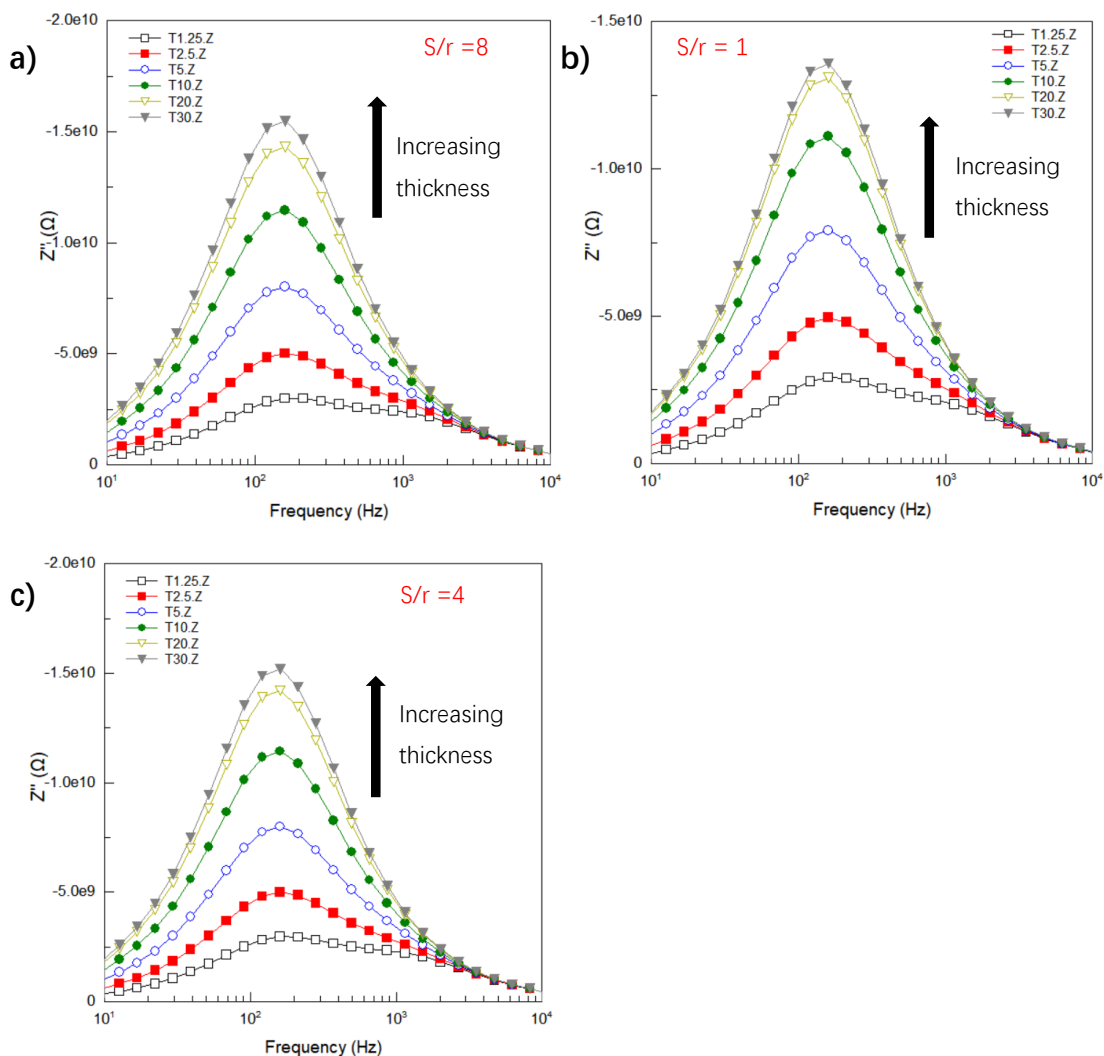


Figure 6.11. Impedance (Z'') spectra data for $R_s/R_b=10$ models. (a) $S/r=8$, (b) 1, and (c) 4, respectively. Black arrow indicates increasing surface layer thickness. The presence of high frequency peak is associated with bulk material when surface layer thickness is small.

The two-layer spreading resistance equation is now applied to the simulated results despite the deviation in the F_{max} values of the spectra from the models. The results are shown in Figure 6.12. For ease of comparison purposes, only results of $S/r=4$ for $R_s/R_b=10$ are shown. Results for $R_s/R_b=100$ with $S/r=4$ are shown for direct comparison to observe the influence when the surface to bulk layer resistivity ratio is reduced by a factor of 10. The prefactor X value curve of the $R_s/R_b=10$ model shifts upward slightly compared to the $R_s/R_b=100$ model for all T/r values. The prefactor X 's numerical difference between the two sets is around 0.01 for all T/r . In the raw impedance data analysis, only when the surface layer thickness is $1.25\ \mu\text{m}$, can a secondary small peak from the bulk layer be observed. However, after processing data via the two-layer spreading resistance equation, it seems the interference from the bulk layer could be affecting the impedance response of the surface layer for all thicknesses as in all T/r values the $R_s/R_b=10$ results shift upward, despite no secondary peak being observed for the larger surface thickness.

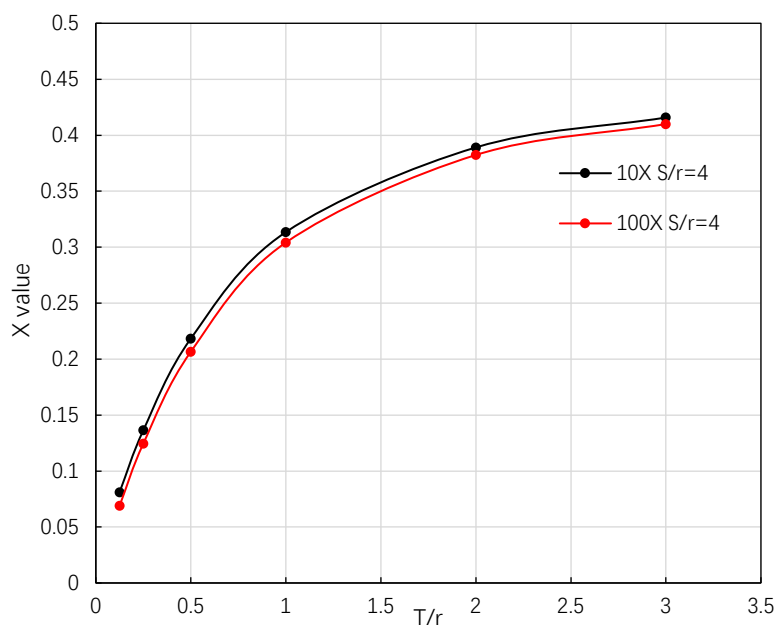


Figure 6.12. Prefactor X value versus T/r for models of $R_s/R_b=10$ and $R_s/R_b=100$, both have S/r ratio of 4. A small up shift of X value for $R_s/R_b=10$ is seen through the entire T/r range.

After exploring the two-layer spreading resistance equation with models of $R_s/R_b=10$, the R_s/R_b ratio is further reduced to 5 to investigate the impact on the extracted results when the surface layer over bulk layer resistivity ratio is lower. The surface layer conductivity is $6.775 \times 10^{-6} \text{ Sm}^{-1}$. The relative permittivity of each layer remains as 162. The impedance results of simulated models are shown in Figure 6.13. A visible deviation of F_{max} for the Debye peaks is observed for all S/r ratios. Using the $S/r=8$ series as an example, when the surface layer thickness is $1.25 \text{ }\mu\text{m}$, F_{max} is 656 Hz whereas the theoretical F_{max} is 300 Hz, a deviation of 218%. The degree of deviation in F_{max} decreases with increasing surface layer thickness. For $T=30 \text{ }\mu\text{m}$ F_{max} is 281 Hz; the F_{max} deviation from the theoretical value is only 6.7%. Although F_{max} deviation occurred for all surface layer thicknesses, no secondary peak associated with the bulk layer is visible. The F_{max} deviation value for all three S/r series is the same, therefore differences in separation between the electrodes has no influence on the shift of the Z'' Debye associated with the surface layer.

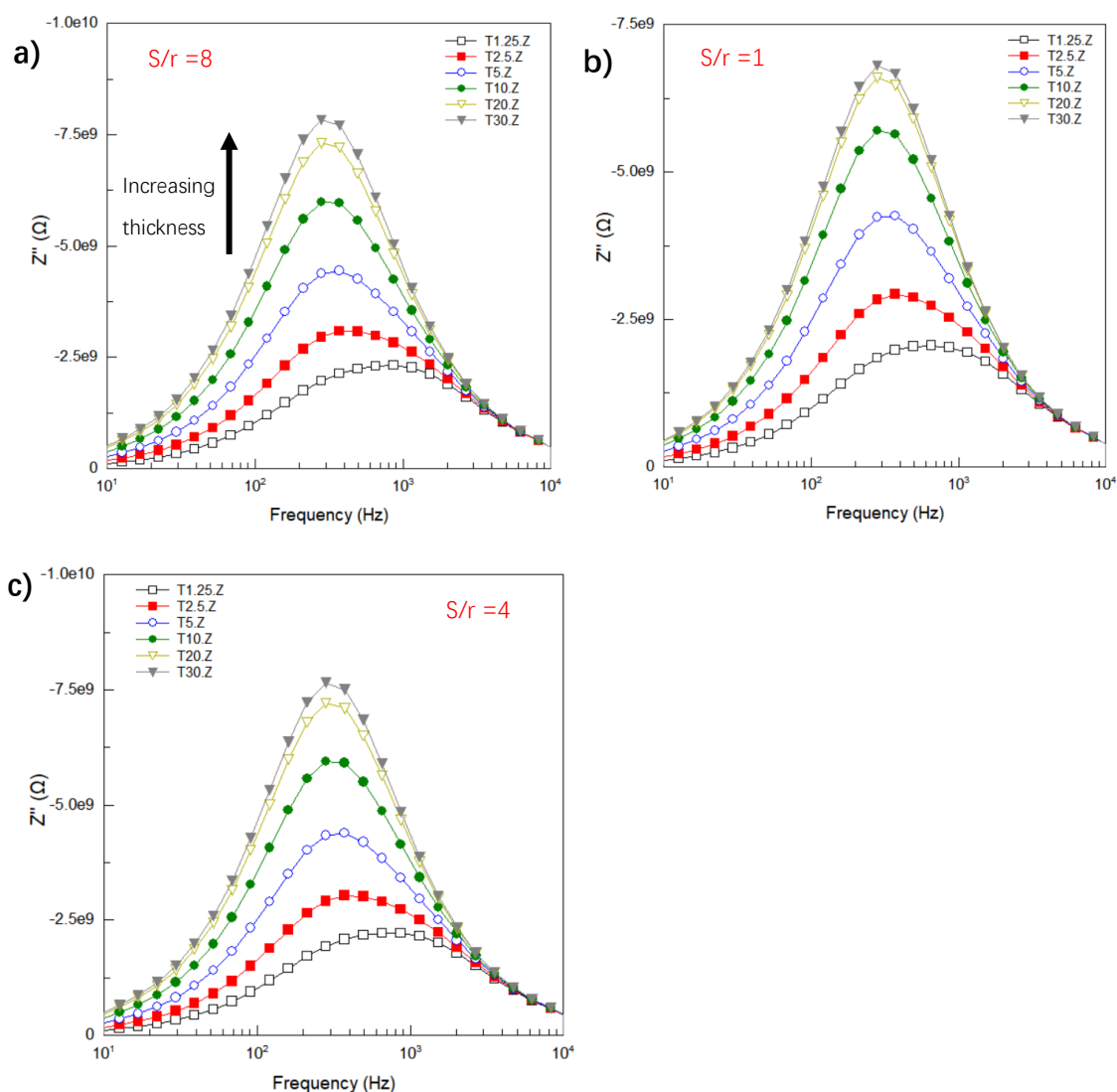


Figure 6.13, Impedance (Z'') spectra for $R_s/R_b=5$ models, (a) $S/r=8$, (b) $S/r=1$, (c) $S/r=4$. F_{max} deviation of the Debye peaks is observed. Black arrow corresponds to increasing surface layer thickness.

The two-layer spreading resistance equation was applied to the $R_s/R_b=5$ models and the results are shown in Figure 6.14. All three S/r series from $R_s/R_b=5$ are plotted. The $R_s/R_b=100$ and $S/r=4$ results are used as a reference to represent impedance data that show no F_{max} deviation(s). The prefactor X value of $S/r=4$ and 8 from the 5X series shift upward from the 100X curve across all T/r values. The $S/r=1$ curve from the 5X models is above that of 100X when T/r is less than 1. The influence of the S/r ratios on the $R_s/R_b=5$ prefactor X value is identical to the $R_s/R_b=100$ models introduced in the previous section. Note that, the numerical difference between the 100X $S/r=4$ and 5X $S/r=4$ curve is relatively large when the T/r value is low, and the 5X $S/r=4$ curve slowly converges toward the 100X $S/r=4$ with increasing surface layer thickness. This trend coincides with the degree of F_{max} deviation in the $R_s/R_b=5$ models. When the surface layer is thin, the F_{max} deviation in the Debye peaks of the Z'' spectra is large. The F_{max} deviation decreases with increasing surface layer thickness. Another thing to note is the 5X $S/r=1$ curve, which deviates away from the 100X $S/r=4$ severely when T/r increases. This is a consequence of high current interference between the closely placed electrodes, as the same trend is observed in Figure 6.8 where $R_s/R_b=100$.

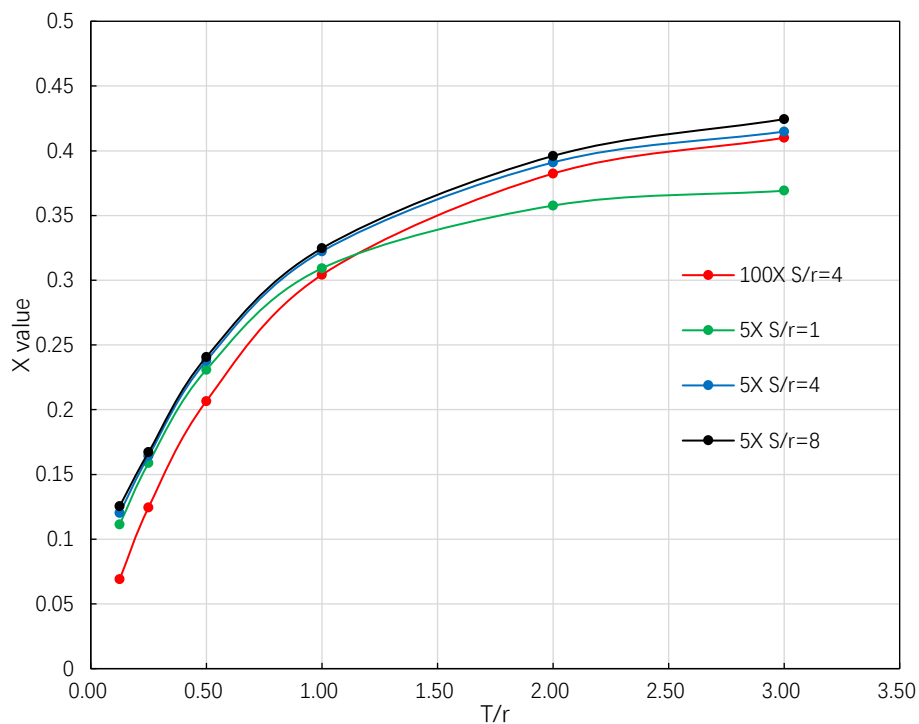


Figure 6.14. Prefactor X value curves of $R_s/R_b=5$ models with S/r ratios of 1, 4 and 8, the 100X $S/r=4$ values are plotted as a reference to investigate the influence of decreasing R_s/R_b ratio on the X values. A deviation from 100X $S/r=4$ curve occurs when the T/r value is low. This low T/r range corresponds with the deviation in F_{max} position in Figure 6.13, when the surface layer thickness is small.

6.3 Discussion

In this chapter we have established when the two-layer spreading resistance equation is reliable to calculate surface layer conductivity. This new method works well when R_s/R_b is large, e.g 100, therefore sufficient difference in the time constants of the two layers (eg, $\times 100$) can ensure good resolution of the responses using impedance spectroscopy. Then the reliability of the two-layer spreading resistance equation was examined by reducing the R_s/R_b ratio between the two layers (with relative permittivity of both layers being the same). This reduces the time constant difference between the two layers thus lowering the resolution obtained using impedance spectroscopy. This is reflected in the prefactor X value's curves, as those from $R_s/R_b=10$ and 5 deviate away from that of $R_s/R_b=100$.

In $R_s/R_b=5$ models, the M'' spectra for the surface layer showed large F_{max} deviations from the theoretical value. Prefactor X's value affected by severe F_{max} deviation will produce low reliability in calculations. The resolution achievable using impedance spectroscopy in analysing a bilayer layer system depends on the difference between the time constants of the electroactive materials in the system. When the time constant difference between two elements is small, typically < 100 , it becomes increasingly difficult to separate the responses (and therefore extract R and C values) for the two layers.

Thus, upon applying the two-layer spreading resistance equation in experimental calculations, it is important to have some expectation of the time constant difference between the two layers to be measured. This is possible to achieve when creating a desired coating or thin film on a substrate, as the properties of the bulk material of the surface layer could have been examined by conventional impedance spectroscopy. The basic electrical properties of the surface layer and substrate could be used as a guide to determine a preliminary R_s/R_b ratio. If the R_s/R_b ratio is larger than 100, then the results obtained by new method should have relatively high reliability.

The S/r ratio can be easily altered when conducting mCIS measurements, especially when the micro-contacts are coated or printed in a pattern of arrays. The size of micro-contacts can also be determined before being printed on the sample surface. If the measurement is in a scenario similar to growing a thin film on a substrate, the thickness of the surface layer could be controlled and determined easily. It is more of a difficulty to retrieve surface layer thickness in situations similar to radiation damaged samples. In such cases TEM is needed to measure the thickness of a surface layer and also to establish if the layer thickness is homogenous. With the T/r , S/r and R_s/R_b known, the Two-layer spreading resistance equation method can then be applied to extract surface layer conductivity and other electrical properties at a higher accuracy than the original spreading resistance equation, as the later equation will only work for a homogenous material.

Using the Fe-doped $SrTiO_3$ thin film on a Nb-doped $SrTiO_3$ substrate [1] as an example, we could propose a way to use the Two-layer spreading resistance equation method to extract conductivity of the Fe-doped $SrTiO_3$. The thickness of surface layer is determined by TEM, and the micro-contacts radius is also known. Their measurement was conducted in the top-down

configuration as micro-contacts on top and full bottom underneath the substrate, as their interest is the properties of the Fe-doped SrTiO₃ surface. The measurement can be changed to be between micro-contacts on the surface layer only. Placing the two micro-contacts on the surface layer could reduce the impedance response from the bulk substrate underneath, thus less interference from the substrate. The Two-layer spreading resistance equation method can be used to extract the surface layer electrical properties with higher accuracy.

6.4 Conclusions

A new way of extracting surface layer properties in a two-layer ceramic system is created, called the two-layer spreading resistance equation. The theoretical reliability of the method is examined by progressively lowering the time constant difference between the two layers. The limits of where the new method is reliable is thus determined. There exist various possibilities to apply this method in experimental measurements, as the examples listed previously [1] [2] [3], awaiting to be proved beyond simulations.

This method is reliable and the prefactor X's values can be used to calculate surface layer conductivity in the following situations:

- (a) when Rs/Rb ratio is equal to or larger than 100, the surface layer conductivity can be calculated for any surface layer thickness.
- (b) when the Rs/Rb ratio is less than 100, only when the surface layer thickness to electrode radius ratio (T/r) is larger than 3 can the surface layer conductivity be calculated.

Compared to solutions proposed by Veazey et al [4], the new method does not require to switch equations as it is only a single equation. This closes the thickness range reported by Veazey et al, and the applicable T/r range can be extended if corresponding simulation data are prepared and prefactor X's values could be calculated based simulation results. Although not perfect, it is usable when the surface layer to bulk layer resistivity ratio is changed, whereas Veazey's solution was not tested and/or verified in this aspect.

6.5 References

- [1] S. Taibl, G. Fafilek and J. Fleig, "Impedance spectra of Fe-doped SrTiO₃ thin films upon bias voltage: inductive loops as a trace of ion motion," *Nanoscale*, 8, pp. 13954-13966, 2016.
- [2] J.-H. Joo and G.-M. Choi, "Electrical conductivity of YSZ film grown by pulsed laser deposition," *Solid State Ionics*, 177, 11–12, pp. 1053-1057, 2006.
- [3] D.-H. Zhang , H.-B. Guo and S.-K. Gong, "Impedance spectroscopy study of high-temperature oxidation of Gd₂O₃-Yb₂O₃ codoped zirconia thermal barrier coatings," *Trans. Nonferrous Met. Soc. China*, 21(5), pp. 1061-1067, 2011.
- [4] R. A. Veazey, A. S. Gandy, D. C. Sinclair and J. S. Dean, "Finite element modeling of resistive surface layers by micro-contact impedance spectroscopy.," *J Am Ceram Soc.*, 103, pp. 2702– 2714., 2020.
- [5] R. A. Veazey, A. S. Gandy, D. C. Sinclair and J. S. Dean, "Modeling the influence of two terminal electrode contact geometry and sample dimensions in electro-materials.," *J Am Ceram Soc.*, 102, pp. 3609– 3622., 2019.
- [6] J. Fleig, "Microelectrodes in solid state ionics.," *Solid State Ionics*, 161, pp. 279–89, 2003.

Chapter 7: Finite Element Modelling of Two-layer System with a Crack

7.1 Introduction

We have presented processed impedance results of a homogenous cube with a crack inserted in the top surface and the general influence of the crack's geometry on the impedance response. In this chapter, we develop the complexity of this model to incorporate both a resistive surface layer along with a crack. This is to represent all the key features highlighted in the experiments performed by Richard Veazey [1]

Based on the model used in chapter 5, a resistive surface layer is added, where its thickness is set to equal the depth of the crack. This means the crack only penetrates the surface layer and we denoted this as a through-thickness crack model. The surface layer has conductivity of 1.355×10^{-7} S/m, 100 times less conductive than the bulk material. The relative permittivity of both the bulk and the surface layer is 162. In Figure 7.1, two types of models with a crack are shown. In Figure 7.1(a) the crack region is meshed and the model can be treated as a homogenous surface layer model, serving as a baseline to investigate the effect of a crack in the top layer. Figure 7.1(b) shows a two-layer model with an unmeshed crack region. This is the main model used throughout this chapter.

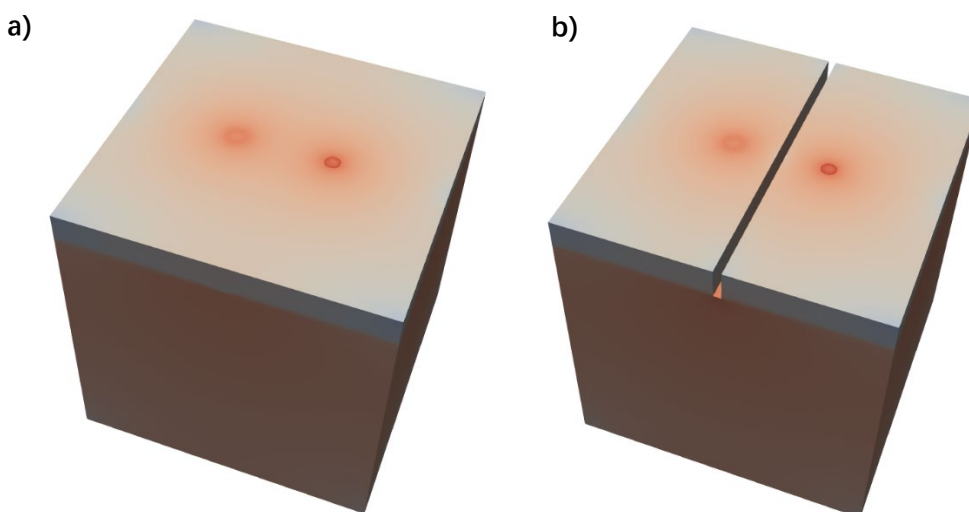


Figure 7.1. Illustration of the 2-layer model with the crack region (a) meshed and (b) unmeshed.

Before further analysis is performed, the differences in the models between chapters 5, 6 and 7 should be made clear.

In chapter 6, the model created consisted solely of a cube with $200 \mu\text{m}$ side length. As no crack geometry was used, the physical entities in the model were reduced, allowing a much finer mesh to be created. This model presented in chapter 6 is structurally simpler than that used in chapters 5 and here in chapter 7 as it has higher precision in simulating a two-layer model without a crack.

In this chapter, the complexity of the model returned to that used in chapter 5 with the crack taking up additional physical volume, therefore reducing the number of elements that can be used. To accommodate a crack feature, the mesh setting of the models in this chapter are coarser than chapter 6 but the same as in chapter 5. In chapter 6 most attractor mesh values were below 1, but in chapters 5 and 7 the lowest attractor mesh value is 1 with most of them being 2 and above.

Figure 7.2 below compares two models from chapters 6 and 7 with the same surface layer thickness, micro-contact radius and separation but different mesh size and physical volume components. The finer meshed chapter 6 model which has 220k elements, shows a higher Z'' reading of $2.25 \times 10^{11} \Omega$, whereas the chapter 7 model of the same geometry with 120k elements has a value of $1.75 \times 10^{11} \Omega$. Although the difference in mesh setting generates deviation in the impedance results between chapters 6 and 7, the coarser mesh setting in this chapter is optimised to achieve wider crack geometries (i.e. deeper and wider), thus it is retained throughout the two-layer cracked model analysis. Any measurement made through Fmax is unchanged by this increasing of mesh size. Also, due to the change of the peak height, the resistance values extracted from the models in chapter 7 and models in chapter 6 are not compared. The resistance values from the cracked models and the pristine model of the same meshing were compared, in this way the general trends of effect from cracks can be discussed.

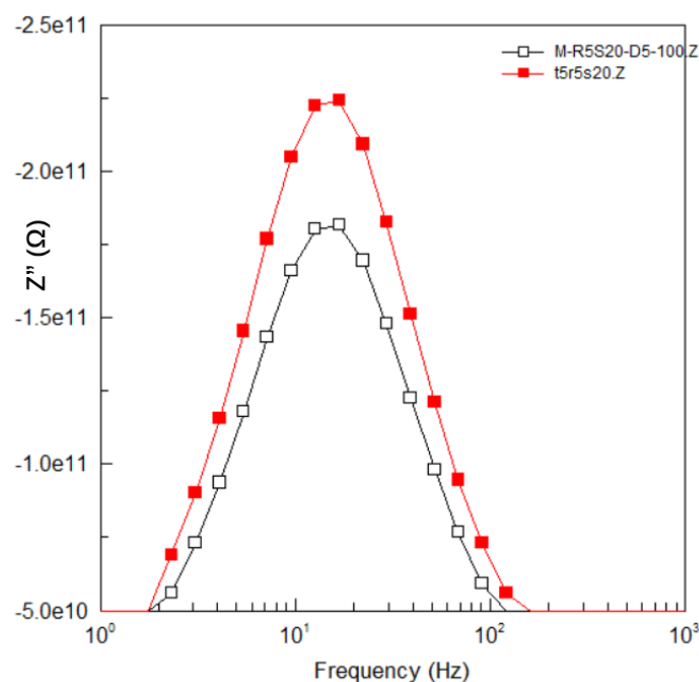


Figure 7.2. Z'' spectroscopic plot of chapter 6 and 7's two-layer model with the same surface layer thickness, micro-contact radius and separation but different mesh size. Red line is the fine meshed model from chapter 6 (220k elements at least), the black line is the model from chapter 7 (120k elements).

7.2 Results and discussion

7.2.1 Current density distribution and impedance results of $S/r=2$ models

As a start, we investigate the strong interference model, where the electrode radius is $5 \mu\text{m}$ and separation is $10 \mu\text{m}$, $S/r=2$. To investigate the current density distribution in the two layer

model with a crack, line scans were conducted in a model with a crack depth of 10 μm and a width of 5 μm . In Figure 7.3, the line scan position is along the z axis, the $x=0$ scan passes the centre point of the model, whereas the $x=10$ scan takes place at a position 10 μm away from the centre along the x axis, as shown in Figure 7.3(a). Figure 7.3(b) shows the scan results. When scanning through the centre point, no surface layer is measured as the crack exists in this region and the current density is highest on the surface of the bulk layer. When scanning at the position that is 10 μm to the right of the centre point, the scan starts in the resistive surface layer, thus the current density is reduced, with a minimum value of $3.73 \times 10^{-6} \text{ A/m}^2$ at a depth of 8.8 μm . The current density increased rapidly after the scan moves into the more conductive bulk layer but is lower than that of the central line scan. As the scan depth increases beyond 75 μm , the current density at similar depths merge to give the same values.

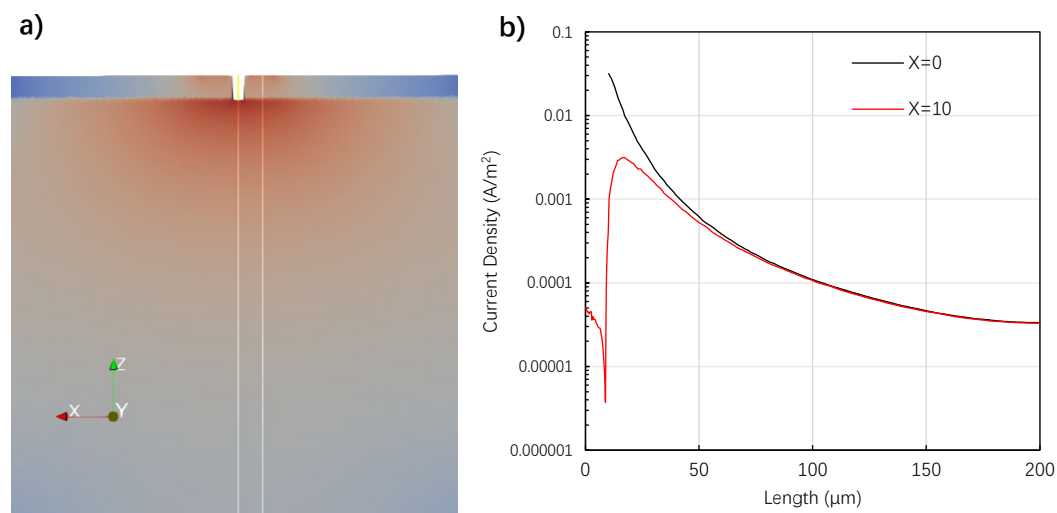


Figure 7.3. (a) Illustration of the line scan positions for a two-layer model with a crack width of 5 μm and a depth of 10 μm . The white lines in the left figure indicate the line scan path. (b) Line scan results for the two positions along the z axis: the model centre response (black line) and 10 μm to the right on the x axis response (red line).

Figure 7.4 shows line scan positions along the x axis at 4 different depths, 1, 5, 12 and 20 μm . From the line scan results, scans at a depth of 1 and 5 μm are both within the surface layer. The scan $D=5$ shows lower current density near the crack wall but higher current density in regions away from the crack when compared to the $D=1$ scan. This is similar to the findings in chapter 5 and is a result of confinement of current flow caused by the presence of the crack. Scans $D=12$ and 20 take place in the bulk layer, thus the current density is on average 10 times greater than the scan in the surface layer. Nevertheless, the confinement-based trend is still observable in the scan even in the bulk layer.

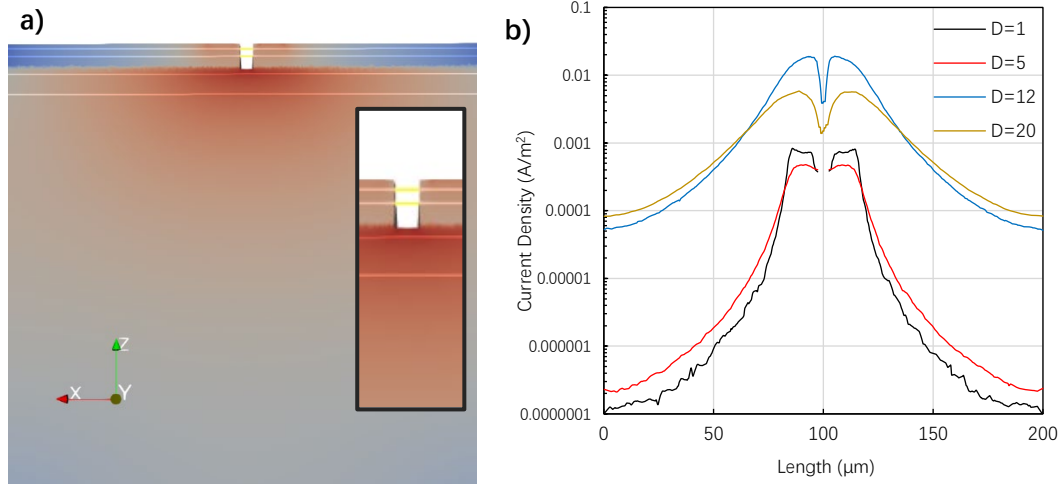


Figure 7.4. Illustration (a) and result (b) of line scans from the same model in Figure 7.3, at a depth of 1, 5, 12 and 20 μm along the x axis. The four horizontal white lines show the line scan path. The image inset shows a zoomed in version showing the position of the line scans.

In Figure 7.5, results are shown from line scans applied to multiple models with increasing crack depth, from 5 to 40 μm , denoted as D5-D40. For the z axis scan in Figure 7.5 (a), the maximum current density of the model decreases with increasing crack depth, since the scan start point is on the top of the bulk material under the crack. Increasing crack depth is equivalent to increasing the distance from the micro-contacts and the current density should decrease. However, when the scan depth reaches beyond 41 μm , the D40 model has the highest current density through the remaining depth until it reaches the bottom surface. This trend was also observed in chapter 5 for models of a homogeneous material and was attributed to a crack confinement effect: it is not affected by the presence of a resistive layer. Figure 7.5 (b) shows line scans along the x axis at a depth of 2 μm in the surface layer. As the crack depth increases, the current density near the crack walls decreases but the trend is reversed at regions away from the crack. This is additional proof of the confinement effect caused by the crack. For example, the D40 model has the deepest crack yet the highest current density at the edge of the model.

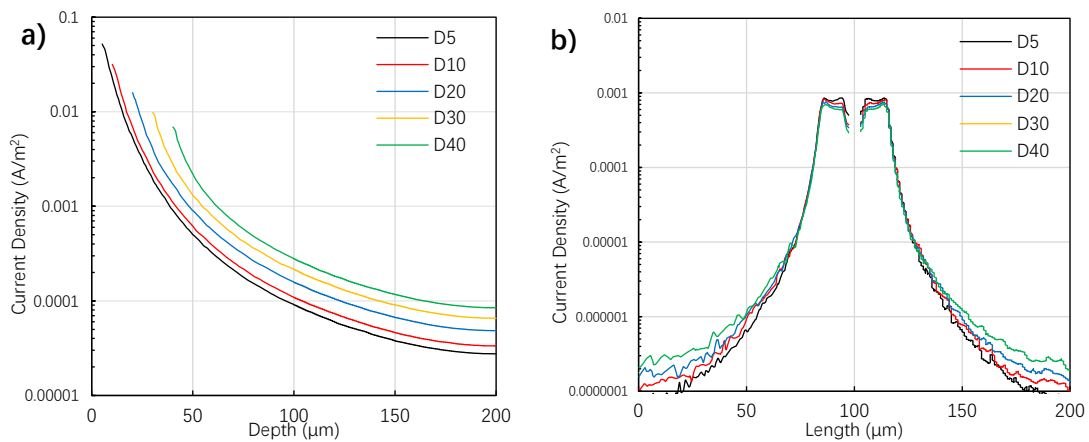


Figure 7.5. Line scan results for models D5 to D40. (a) Current density along the z axis at the model centre. (b) Current density along the x axis at a depth of 2 μm underneath the top surface.

Figure 7.6 shows line scans from models with different crack widths of 1, 3, 5, 7 and 9 μm . In Figure 7.6(a), line scans take place along the z axis from the top to bottom surface. As all models have a crack depth of 10 μm , the current density starts from 10 μm . Increasing the crack width by 2 μm only induces a change in the current density of less than 0.01 A/m^2 between each model, e.g., W9 has a current density of 0.02 A/m^2 , W7 has 0.025 A/m^2 and W3 has 0.045 A/m^2 . However, the current density of all 5 models quickly collapses onto a single trendline after a scan depth of 15 μm . The confinement effect observed in Figure 7.5 is not observed. Figure 7.6 (b) plots the results of line scans at a depth of 2 μm along the x axis. The change in current density is localised in a region near the crack edges, whereas no visible change takes place in other regions. Thus, changing the crack width from 1 to 9 μm does not generate any significant confinement effect, which is the same result as the single material model.

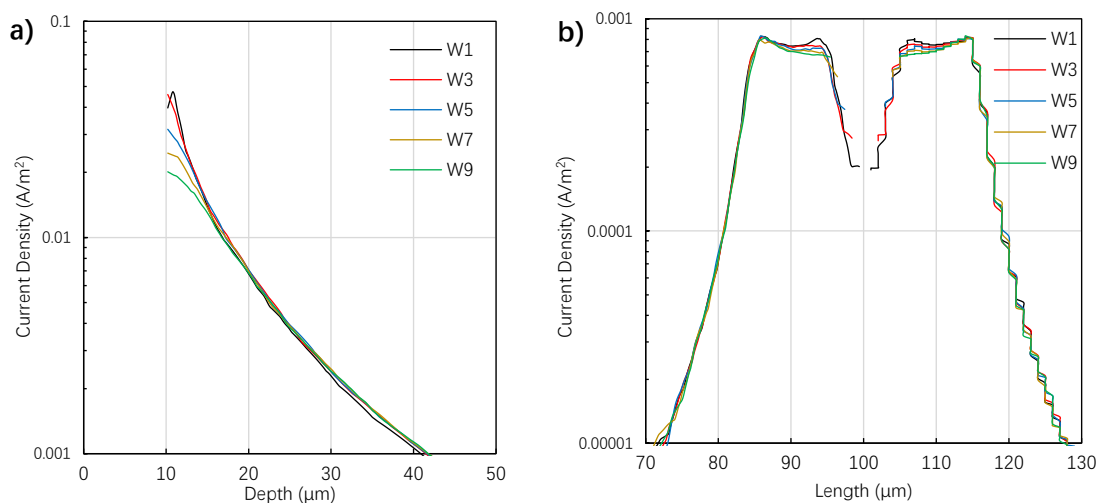


Figure 7.6. Line scan results of models with crack width from 1 to 9 μm (W1-W9). (a) Current density along the z axis at the model centre. (b). Current density along the x axis at a depth of 2 μm underneath the top surface.

The impedance results from different crack geometries are processed and grouped in a similar manner as the homogenous cubic model in chapter 5. Figure 7.7 shows the impedance results of models with crack width of 1, 5 and 9 μm . The surface layer thickness is the same as the crack depth of 5 μm . For comparison, a model with a homogenous surface layer of depth 5 μm is added. The effect of placing a through-thickness crack in the surface layer can therefore be investigated. The extracted electrical properties of each model are summarised in Table 7.1.

To assist in the results that follow a nomenclature was developed. As an example, M-R5S10-D5-100 is a model that has a meshed crack (M), homogenous surface layer, micro-contact radius of 5 μm , separation of 10 μm , surface layer depth of 5 μm (D5), the -100 indicates it is a two-layer model.

A second example, V-R5S10-D5W1-100 indicates a model that has a physical void crack (V), the same electrode configuration as the previous model, crack depth of 5 μm and a width of 1 μm . Since it is a two-layer model, the surface layer thickness is also 5 μm .

In Figure 7.7(a), two distorted semi-circles are shown in Z^* plots for each model, meaning two responses are measured. This matches with the bulk and surface layers having different electrical properties. Also, increasing the crack width causes the measured total impedance to increase. In Figure 7.7(b) Z'' spectra show a single Debye peak for all models. All 4 F_{max} values are the same at 16 Hz, which is very close to the theoretical value of 15 Hz for the surface layer. The 9 μm crack width model has the largest Z'' value of $2.034 \times 10^{11} \Omega$, whereas the homogenous surface layer model has the lowest value of $1.831 \times 10^9 \Omega$. Note that, in (a) and (b), the response of the homogenous surface layer model and the crack width of 1 μm are overlapped, thus we are unable to distinguish the two from Z^* plots and Z'' spectra. In the M'' spectra in Figure 7.7(c), two responses from the four models can now be distinguished. All four models show peaks at 16 and 1156 Hz; the lower frequency peak corresponds to the resistive surface layer, and the higher frequency peak is the response of the more conductive bulk layer underneath. With increasing crack width, the value of M'' from both peaks increased. Comparing the homogenous surface layer model and crack width of 1 μm model, adding a narrow crack of 1 μm would not change the height of the low frequency response; however, the peak at higher frequency increased from 7.188×10^{12} to $8.760 \times 10^{12} \text{ F}^{-1}$. In Figure 7.7(d), C' spectra are shown; two plateaus can be seen for each model. With increasing crack width, the capacitance associated with the two plateaus decreases.

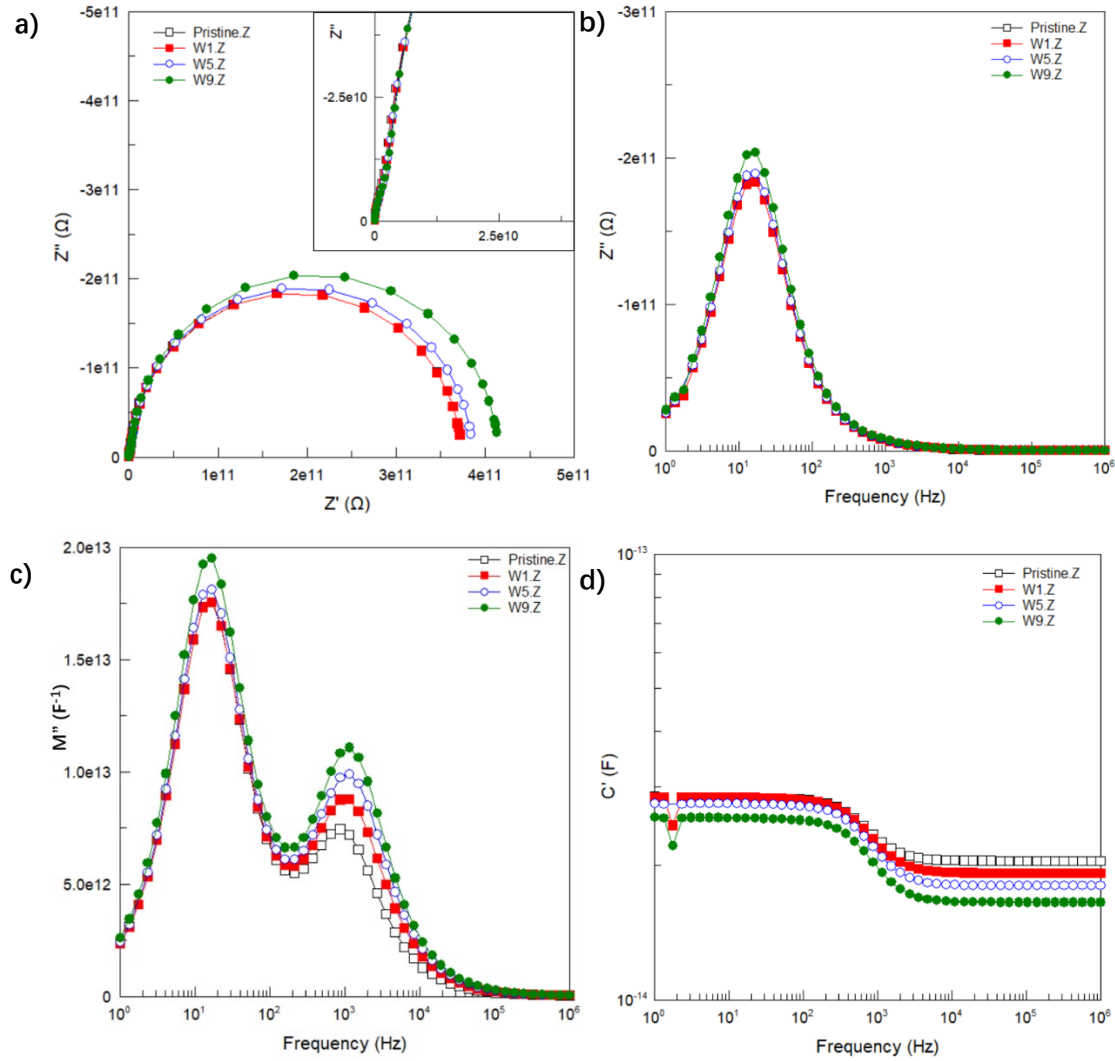


Figure 7.7. Impedance spectroscopy data for the homogenous surface layer model (pristine) and models with a crack of width 1, 5 and 9 μm (W1-W9 respectively). (a). Z^* plots, with an expanded view of the distorted arc at low resistivity. (b). Z'' spectroscopic plots. (c). M'' spectroscopic plots. (d). C' spectroscopic plots.

Model	$f_{\text{max, Surface}}$ (Hz)	$f_{\text{max, Bulk}}$ (Hz)	Surface Z'' (GΩ)	Bulk Z'' (GΩ)	Surface R'' (GΩ)	Bulk R'' (GΩ)	Surface M'' (F^{-1})	Bulk M'' (F^{-1})	Surface C' (pF)	Bulk C' (pF)
Pristine	16.8	1151.0	182.0	5.970	364.0	11.940	1.752×10^{13}	7.183×10^{12}	0.0286	0.0696
W1	16.8	1151.0	183.1	6.080	366.2	12.160	1.753×10^{13}	8.760×10^{12}	0.0284	0.0570
W5	16.8	1151.0	189.0	6.328	378.0	12.656	1.811×10^{13}	9.890×10^{12}	0.0276	0.0505
W9	16.8	1151.0	203.4	6.837	406.8	13.674	1.954×10^{13}	1.111×10^{13}	0.0257	0.0451

Table 7.1. Calculated electrical properties extracted from impedance spectroscopy data for the homogenous surface layer model (pristine) and models with a crack of width 1, 5 and 9 μm (W1-W9, respectively).

After investigating the crack width effect in a resistive surface layer, the next step is to study the effect of crack depth in a two-layer model. As the crack is set through the surface layer thickness, increasing the crack depth increases the surface layer thickness. A study of non-through thickness cracks will be introduced at the end of this chapter.

Figure 7.8 shows impedance data from models with a crack of increasing depth, from 5 to 40 μm . No homogenous surface layer model is added for comparison, since the listed models do not have the same surface layer thickness, unlike in Figure 7.7. The electrical properties of the models are summarised in Table 7.2.

In Figure 7.8(a), a large semi-circle in Z^* plots can be seen for all crack depths, suggesting the response from the resistive surface layer is the dominant response. The measured resistivity increases with crack depth. In Figure 7.8(b), each crack depth model shows one Z'' peak, all have $F_{\text{max}}=16.8$ Hz, this again confirms the surface layer response dominates the spectra. Figure 7.8(c) shows the M'' spectra of the models. A series of peaks at 1151 Hz are observed with decreasing height with increasing crack depth and surface layer thickness. This series of peaks correspond to the bulk layer. The other series of peaks at 16.8 Hz increase in height with increasing crack depth and this series of peaks are associated with the surface layer. Figure 7.8(d) shows the C' spectra of listed models. With increasing crack depth and surface layer thickness, the two capacitance plateaus decrease, so does the height difference between the plateaus. This suggests the measured capacitance of both the surface and bulk layers decrease with increasing crack depth and surface layer thickness.

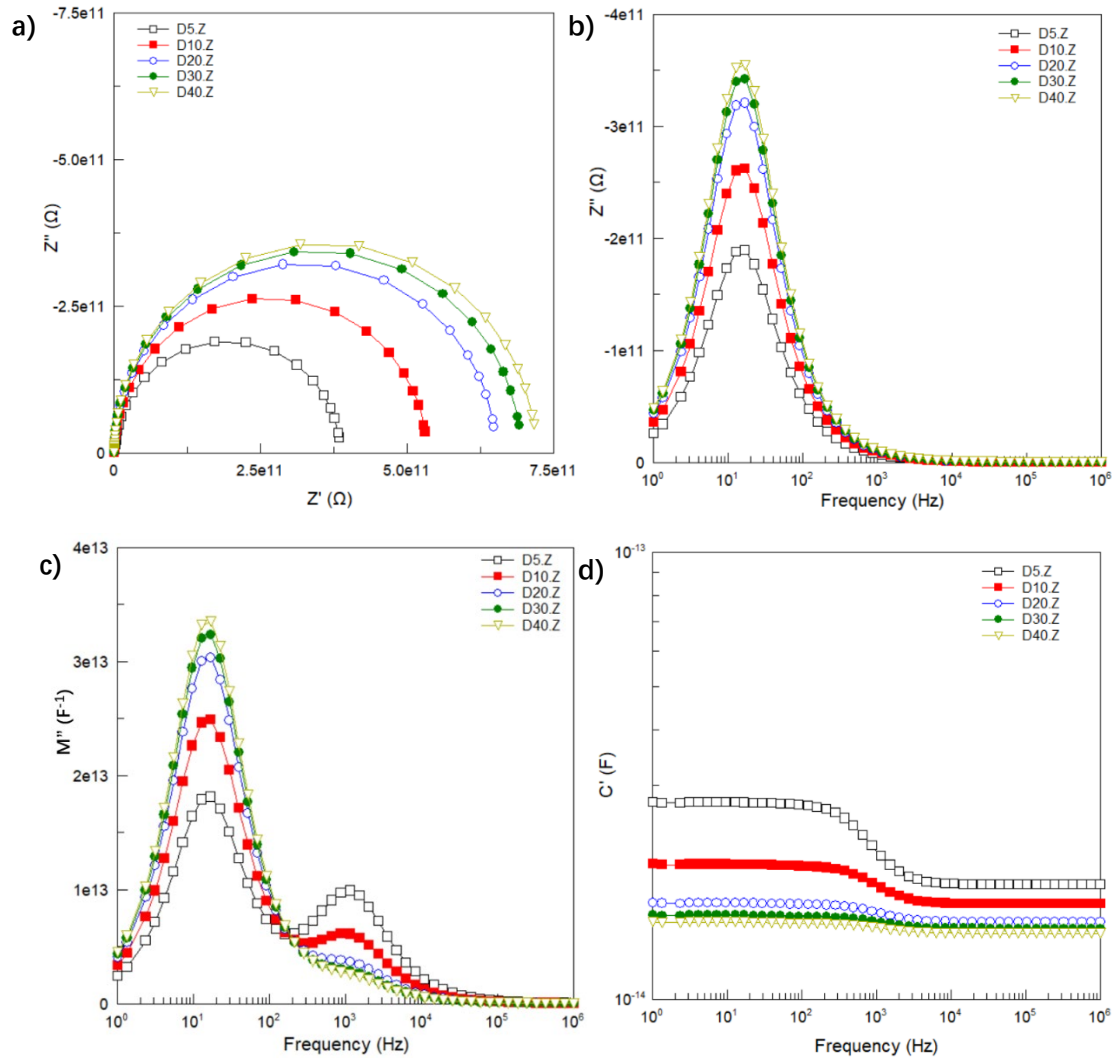


Figure 7.8. Impedance data from two-layer models with a crack of depth 5, 10, 20, 30 and 40 μm (D5-D40, respectively). The surface layer thickness is the same as the depth of the crack. (a) Z^* plots. (b) Z'' spectroscopic plots. (c) M'' spectroscopic plots. (d). C' vs frequency plots. All models have a surface layer thickness 100 times more resistive than the underlying bulk material.

Models	Fmax, Surface (Hz)	Fmax, Bulk (Hz)	Surface Z" (G Ω)	Bulk Z" (G Ω)	Surface R" (G Ω)	Bulk R" (G Ω)	Surface M" (F $^{-1}$)	Bulk M" (F $^{-1}$)	Surface C (pF)	Bulk C (pF)
D5	16.8	1151	189	6.33	378	12.66	1.81E+13	9.89E+12	0.0276	0.0209
D10	16.8	1151	262	7.69	524	15.38	2.49E+13	6.09E+12	0.0200	0.0177
D20	16.8	1151	321	8.86	642	17.72	3.03E+13	3.66E+12	0.0165	0.0155
D30	16.8	1151	342	9.3	684	18.6	3.23E+13	2.87E+12	0.0154	0.0148
D40	16.8	1151	355	9.58	710	19.16	3.35E+13	2.57E+12	0.0149	0.0144

Table 7.2. Calculated electrical properties of models with a crack depth of 5 to 40 μm (denoted as D5-D40), extracted from impedance data.

After extracting the electrical properties of the two-layer models with a crack, the next step was to investigate the effect of the crack geometry on the measured resistivity. The method

is the same as detailed in chapter 5. The peak readings from the Z'' spectra are taken as the raw impedance results. A homogenous surface layer model without cracks is used as a baseline for comparison for each thickness. With changing crack geometry, all the models with cracks are compared with the homogenous surface layer model. Please note, for each series of models with the same crack depth, it requires a specific homogenous surface layer model as a baseline for comparison (shown as the model in Figure 7.1(a)), whereas in the previous section, all the models with cracks are compared with the same pristine cube model. The extracted Z'' value of the model is processed via Equation 7.1.

Equation 7.1. $(\text{Cracked Model } Z'' \text{ peak value} - \text{homogenous surface layer model } Z'' \text{ peak value}) / \text{homogenous surface layer model } Z'' \text{ value} = \%R$

The processed impedance results for each model are shown in Figure 7.9, where the effect of crack width on the impedance results is investigated. The y axis shows each model's relative increase in Z'' (%R) compared with the pristine model value. The x axis shows increasing crack width/total electrode separation as a percentage. In other words, narrow cracks on the left-hand side and wide cracks on the right-hand side. The labels D5-D40, indicate the crack depth of each model series.

Figure 7.9 summarises the influence of adding a resistive surface layer. The general influence of the cracks' geometry on the impedance results is the same: increasing crack width leads to an increase in the Z'' peak value when compared to the model with an intact resistive surface layer. The deeper the crack into the cubic model, the larger the Z'' peak value. For a crack depth of 5 μm , a 1 μm wide crack only alters the Z'' value by 0.72%; therefore, the crack's presence has little to no effect on the impedance.

When the crack depth is increased to 40 μm , which is 8 times the electrode radius, a narrow crack width of 1 μm can increase Z'' by 32.17%. Since $-2Z'' = R$, an increase in the Z'' peak value means the overall resistance measured has also increased. The existence of a 40 μm deep and 1 μm wide crack hinders the current flow when the resistive surface layer is 40 μm . Moreover, increasing the crack width has a significant effect on the Z'' value for a fixed crack depth. When the crack depth is 40 μm , increasing the crack width from 1 to 9 μm increases the percentage change from 32 to 51%.

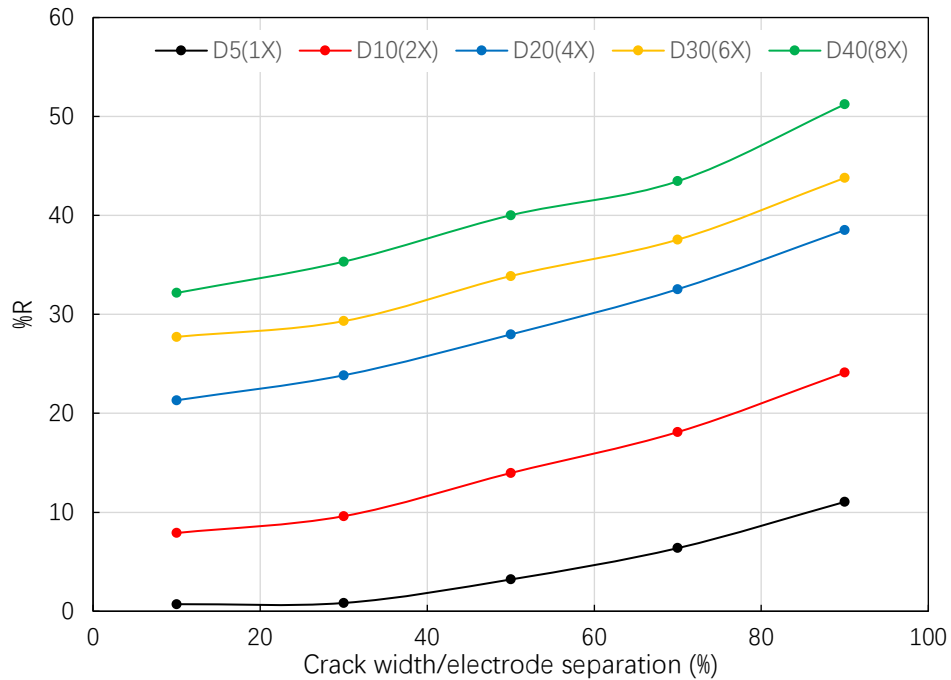


Figure 7.9. Plot of %R versus %(crack width/electrode separation) for two-layer models with different crack widths and depths. On the left-hand side the cracks are narrow and the right-hand side corresponds to wide cracks. The lower series in the black line is where cracks are as shallow as 5 μm deep. The upper most series in the light green line correspond to cracks with a depth of 40 μm .

7.2.2 Cross comparison between a homogenous cube and two-layer models with the same crack geometry

From Figure 7.9, the effect of crack geometry on the impedance results is similar to the homogenous material models but the scale of influence for the same crack set up is reduced in the two-layer models. A comparison between homogenous and the two-layer models is shown in Figure 7.10. When the crack has a width of 9 μm and depth of 40 μm , which is the top right corner point, the model shows a 51% increase compared to a model without a crack. For a homogenous system, a model with the same crack geometry shows a 59% increase in Z'' peak value, thus there is an 8% decrease. When the crack depth is 5 μm and the width is 9 μm , there exists a 14% difference between the 2 layer and homogenous models. Therefore, a crack of the same geometry in a homogenous layer can induce the Z'' peak value to increase by 25% compared with the same model without a crack, but once a resistive surface layer is added to the system, a crack with the same geometry can inflict only a 11% change in Z'' , compared with a two-layer model without a crack in the surface layer. Adding the resistive surface layer has therefore reduced the influence of the crack on the Z'' peak results, compared with the homogenous material models. This could be attributed to the drop of current density in the resistive layer with current detours around the surface layer and bypassing the crack at the same time.

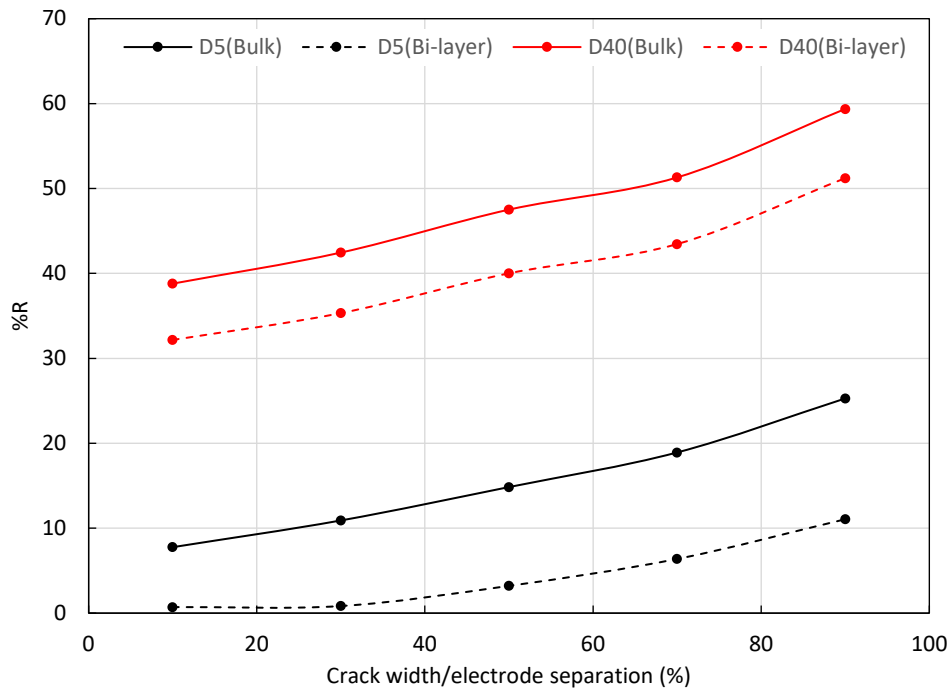


Figure 7.10. Plot of %R versus %(crack width/electrode separation) for two-layer models (Bi-layer) and homogenous model (Bulk) with different crack widths and depths. The two-layer model is created based on the homogenous model by adding a surface layer with conductivity of 1.355×10^{-7} S/m. When a resistive layer is added to a homogenous material the effect of cracks on the Z'' values has been reduced. Lines are shown to guide the eye.

Line scans of a single material model and a two-layer model were conducted to verify our assumption. In Figure 7.11 below, a single material model and a two-layer model with the same crack geometry were created. The crack depth and width were both 5 μm . The first comparison takes place along the z axis through the centre point in the model. The results are noted as Bi-layer X = 0, and Bulk X = 0. The Bi-layer X = 0 is from the two-layer model, and Bulk X = 0 is from the single material model. As the scan takes place at the centre point, it does not encounter the surface layer and that is why the reading begins at a depth of 5 μm . Both curves overlap each other, suggesting the current density distribution is the same, regardless of the presence of resistive surface layer.

When line scans take place at a position of 10 μm away from the centre point (a shift along the x axis) the scans now encounter the surface of the models. It is clear the Bi-layer X=10 model has much lower current density (2.39×10^{-6} A/m²) in the resistive surface layer, compared to that of the single material model (minimum 1.39×10^{-3} A/m²). After a scan depth beyond 5 μm , which enters the bulk layer of the two-layer model, the current density of two models overlap again. This is direct evidence that the current density in the resistive surface layer is reduced. The resistive layer does not affect current density in the bulk layer underneath.

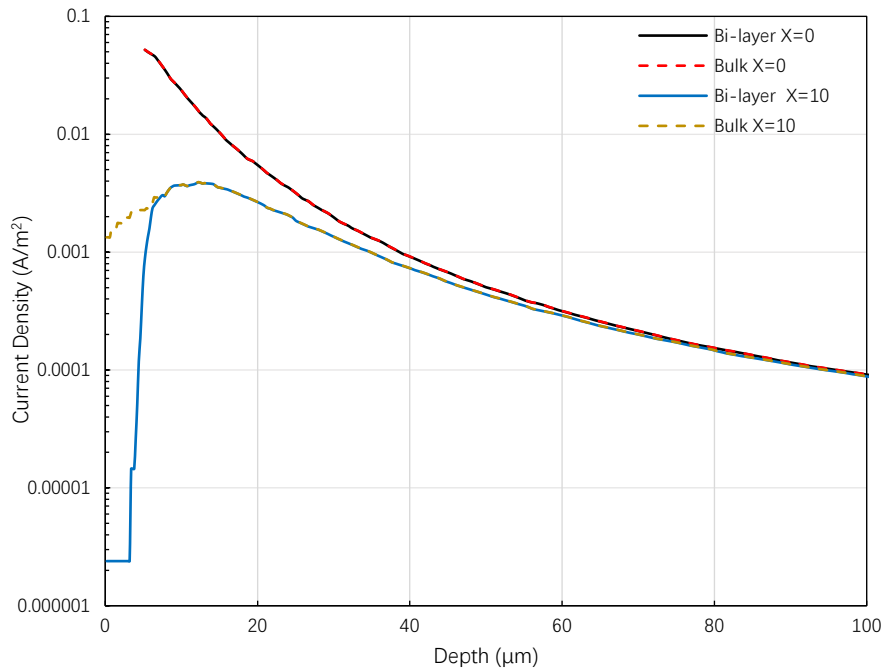


Figure 7.11. Line scan results of current density for two models with the same crack geometry, depth 10 and width of 5 μm . The bi-layer model has a resistive surface layer of 10 μm thick, whereas the bulk model is made of a single material. The scan positions are along the z axis. The $x=0$ scan takes place along the model centre point, whereas the $x=10$ scan takes place at 10 μm away from the model centre in the x axis.

7.2.3 Current density and Impedance results of $S/r=10$ models

After investigating the strong inference set up, a series of models with $S/r=10$ was created to establish how the crack affects the impedance results when less current interference takes place and a resistive layer is present. In Figure 7.12, the Z'' peak value of models with a crack is compared with their homogenous model counterpart, and the percentage change is plotted in the order of increasing crack width, grouped under different crack depths.

When the crack depth is 5 μm a crack width below 9 μm cannot generate more than 1% change in the impedance results. Similarly, for other crack depths, when the crack width is less than 90% of total separation, the effect of the crack on the impedance is relatively small. The largest change occurs when the crack depth is at 40 μm and the width is 90% of electrode separation; there is a 23.72% rise in the Z'' value. Compared with $S/r=2$ models, a crack of the same dimensions caused 51.22% change in the Z'' value. Thus, increasing the electrode separation drastically reduces the crack's effect on the impedance results. This is attributed to the decrease in current density between the electrodes.

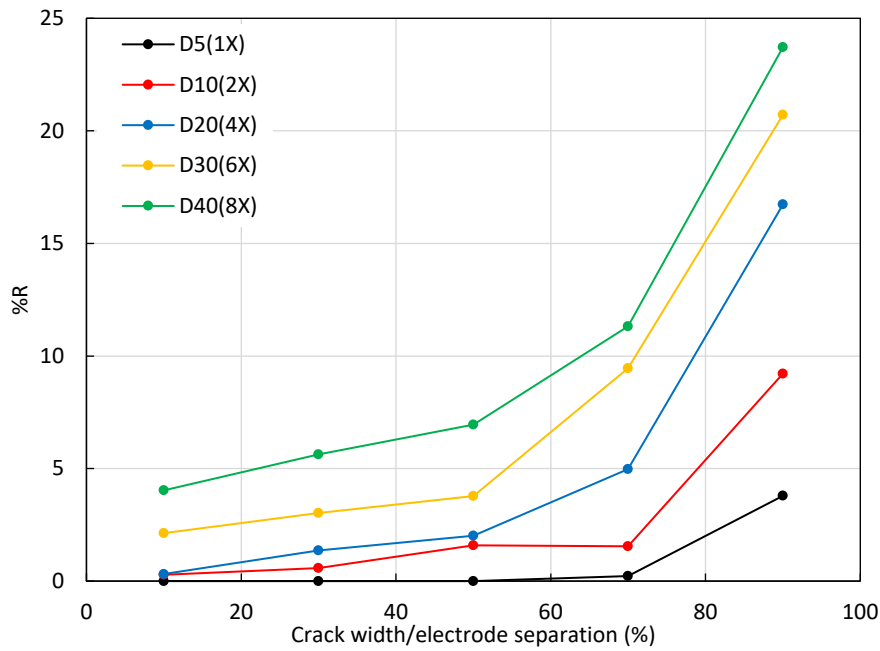


Figure 7.12 Plot of %R versus %(crack width/electrode separation) for two-layer models with $S/r=10$. The overall trend is similar to when $S/r=2$; however, a crack with the same dimensions has far less effect over the measured impedance results when compared to $S/r=2$ results. Lines are shown to guide the eye.

7.2.4 Cross S/r ratio comparison

Next, we investigated the transitional S/r ratios between 2 and 10 to understand the diminishing influence of the crack effect on the impedance results with increasing micro-contact separation. The impedance results of models with cracks are compared with their intact surface layer models. This reflects the influence of the crack on the current flow. The results are shown in Figures 7.13 and 7.14.

Similar to models without a surface layer, increasing the separation to radius ratio will reduce the current interference from the electrodes. The crack's influence on the impedance results decreases with decreasing current density. In Figure 7.13, all models have a crack depth of $20\ \mu\text{m}$. For $S/r=2$, the crack can increase the measured resistivity maximum by 38.52%. For $S/r=10$, the maximum change caused by the crack is reduced to 16.73%. Note that these maximum increases in resistivity only take place when the crack width is at 90% of electrode separation. When the width of the crack is 10% of the electrode separation, the effect of the crack is much smaller. If the S/r ratio is 6 and above, models with a crack width of under 70% of the electrode separation show less than a 10% increase in the measured resistivity.

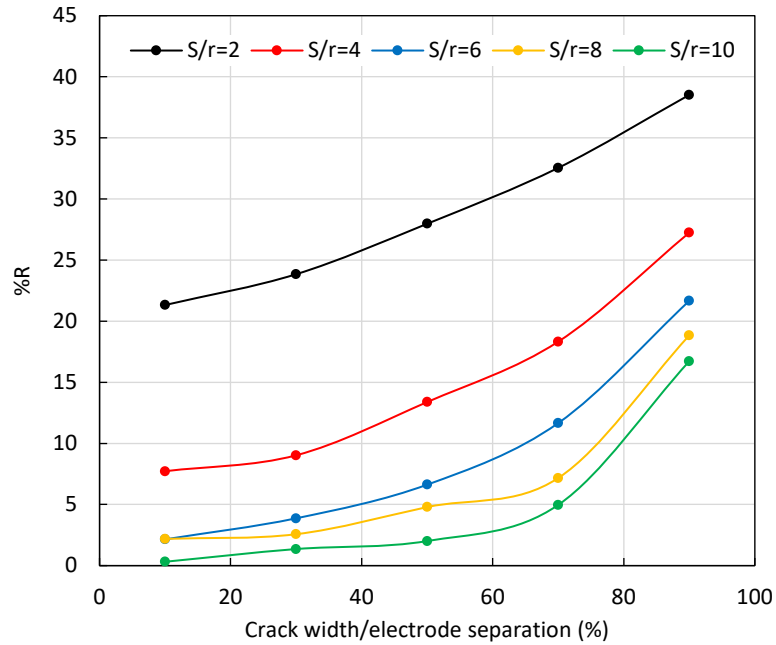


Figure 7.13. Plot of %R versus %(crack width/electrode separation) of two-layer models with different S/r ratios. The models have a fixed crack depth of 20 μm but increasing width from 10 to 90% of the electrode separation.

In Figure 7.14, the crack depth effect is summarised. In order to reduce variables, the crack width of each model is fixed to 50% of the electrode separation. In general, increasing the crack depth causes the measured impedance to increase. This effect is most prominent when the S/r ratio is 2. As the S/r ratio increases, the effect of crack depth is gradually reduced. When S/r=10, even a crack of width 25 μm and 40 μm deep can inflict only a 7% increase in the measured resistivity.

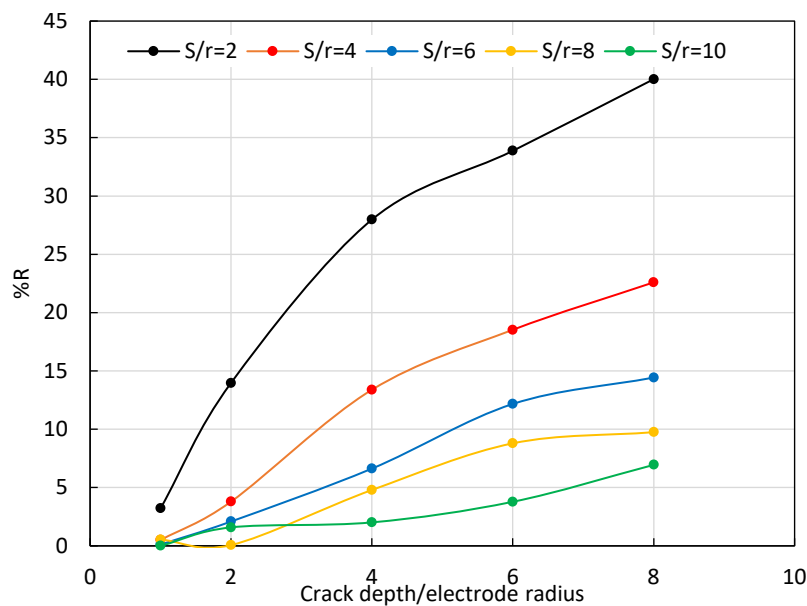


Figure 7.14. Plot of %R versus crack depth/electrode radius of models with different S/r ratios. Cross S/r comparison of models with fixed crack width of 50% of electrode separation but with increasing crack depth from 5 to 40 μm . Lines are shown to guide the eye.

7.2.5 Applying the two-layer spreading resistance equation

The spreading resistance equation cannot work when a thin resistive layer is between the two electrodes [2], it is however useful when the resistive layer is relatively thick, e.g. layer thickness is 10 times the electrode radius [3]. Thus, unlike chapter 5, we have not processed the two-layer system data with Equation 5.6 and the results are limited to raw impedance data.

However, in chapter 6, a new method called the two-layer spreading resistance equation (Two-layer SRE) was presented to compensate the effect of a resistive layer in micro-contact impedance measurements, as shown in Figure 7.15. It is instructive to apply this new method to the two-layer system data presented in this chapter with the presence of a crack to investigate if and how it works in these models/scenarios.

To apply the two-layer spreading resistance equation:

(i) calculate R from the Z'' peak as $R = -2Z''$

(ii) find the T/r value on the x axis.

(iii) Chose the trendline based on S/r for the sample and extract an prefactor X value. For example, models with a crack depth of 5 μm , width 10 μm and S/r=4, which therefore correspond to a surface layer thickness/electrode radius of 1 (T/r=1), since cracks are at an equal depth with the surface layer. The appropriate prefactor X value is 0.302.

(iv) substitute in the R value of a two-layer model with an intact surface layer as the baseline for the crack depth=5 series. The R value measured from impedance plot is $3.61 \times 10^{11} \Omega$. Then the calculated surface layer conductivity of a two-layer model with crack depth of 5 μm and width 10 μm is,

$$\sigma = \frac{0.302}{rR} = \frac{0.302}{5 \times 10^{-6} \times 3.61 \times 10^{11}} = 1.67 \times 10^{-7} \text{S/m}$$

r is micro-contact radius and R is measured resistance.

Since the assigned conductivity of the surface layer is $1.355 \times 10^{-7} \text{S/m}$, the percentage difference between the two-layer spreading resistance equation processed 2-layer model and the assigned value = $(1.67 - 1.355) / 1.355 \times 100\% = 23.56\%$

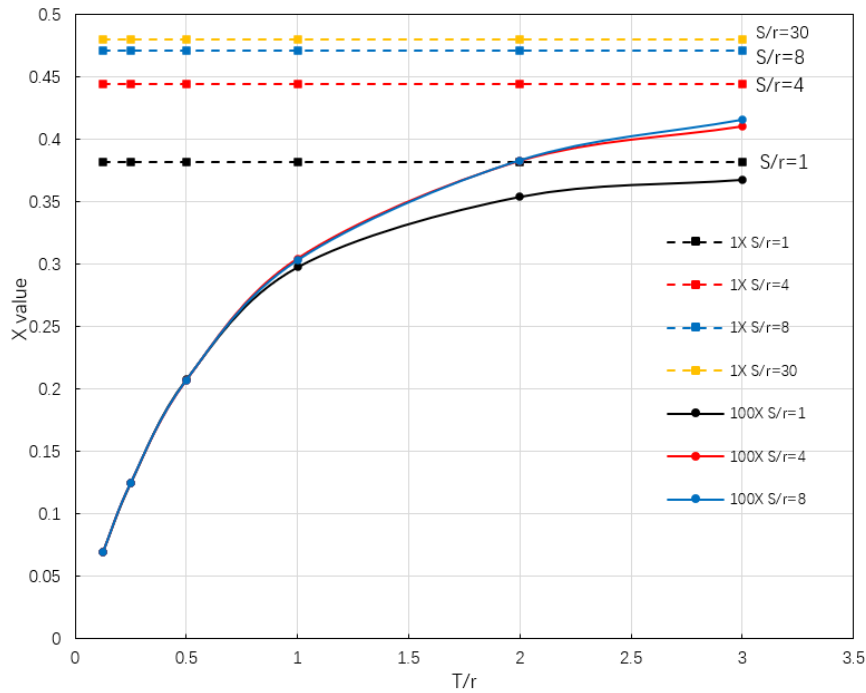


Figure 7.15. The prefactor X value of two-layer spreading resistance equation versus T/r plot. Reproduced from chapter 6.

Using the two-layer spreading resistance equation on the two-layer no crack model gives 23.56% difference from the assigned conductivity, which is considered acceptable; however, this is created by mapping simulated results with the intrinsic value and calculation of the correction factor for each surface layer geometry. There should be less than 5% difference between the calculated and intrinsic value. The 23.56% difference obtained could be partially due to the presence of the crack but other factors may be contributing to it, eg meshing of the models as these are different in chapter 6 and 7. As discussed in the beginning of this chapter, this two-layer spreading resistance equation is based on chapter 6's high precision model dedicated to simulations of two-layers whereas in this chapter the model is optimised for a variety of crack geometries.

To verify the influence of meshing in the models, two series of chapter 7's models are created with the finest mesh setting available, in order to minimise the deviation of results from the assigned conductivity of the surface layer caused by the mesh setting. Due to the limitation of file size, only crack depths of 5 and 10 μm could be simulated, the S/r ratio is 4, further crack depths could not be simulated.

The results are shown in Figure 7.16. Unlike previous plots, results from models with crack width of 0% are also shown. These are the two-layer models with an intact surface layer. Their percentage difference between the actual assigned conductivity shows the baseline simulation accuracy of the models. The impedance results of the models are processed using the two-layer spreading resistance equation and the conductivity of each model is retrieved. Their conductivities are then compared with the assigned value of 1.355×10^{-5} S/m, in order to present the effect of the crack on the overall conductivity measured. For the model series D5

(two-layer spreading resistance equation), T/r is 1, $S/r=4$, thus the prefactor X value of 0.302 is used. With increasing crack width, the calculated conductivity slowly decreases; however, it rapidly decreases when the crack width is $> 70\%$ of the electrode separation. When the surface layer thickness is doubled, the decrease of the measured surface layer conductivity occurs earlier at a crack width that is 50% of the electrode separation. When the crack width is 0, the D5 and D10 models show 8.8% and 9.8% difference from the actual assigned conductivity, suggesting at the finest mesh setting, impedance results generated by chapter 7's model have less than 10% difference from chapter 6's dedicated two-layer model.

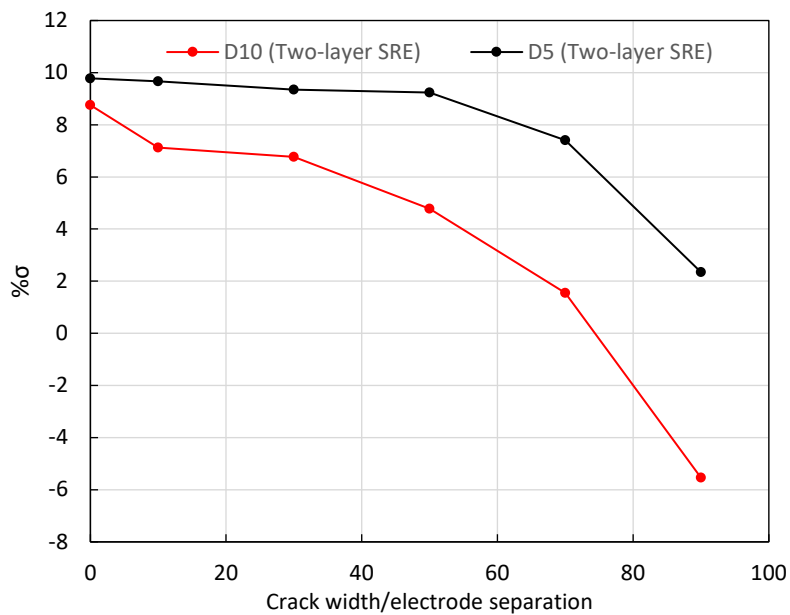


Figure 7.16. Plot of $\% \sigma$ versus $\%(\text{crack width/electrode separation})$ of two-layer cracked models with the finest mesh setting available. The Z'' peak value of each model is processed using the two-layer spreading resistance equation (Two-layer SRE) to retrieve the corresponding conductivity. The calculated percentage difference from the intrinsic conductivity value is then assigned to the model and reflected in the plot.

We now examine the effectiveness of the two-layer spreading resistance equation to extract surface layer conductivity. The original spreading resistance equation is also used to extract surface layer conductivity. This comparison between the two-layer spreading resistance equation and the original spreading resistance equation will enable verification of whether or not the new equation is an actual improvement. In Figure 7.17, impedance results from the higher precision chapter 7's D5 and D10 series are processed using the original SRE. When the crack width is 0, the surface layer is intact. Using the original SRE gives 82% error from the assigned value whereas the new equation's result is within 9.8%. It is clear that the new equation can provide more accurate values to calculate surface layer conductivity, when a resistive surface layer exists. This method is therefore an improvement on the original SRE.

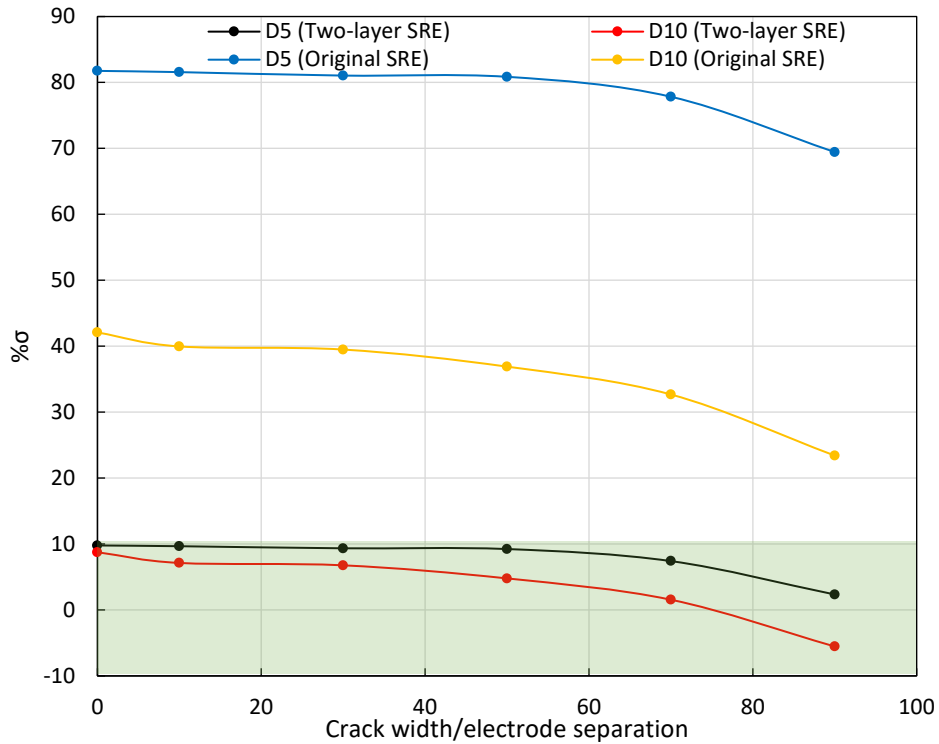


Figure 7.17. Plot of $\% \sigma$ versus $\%(\text{crack width/electrode separation})$ of two-layer cracked models with the finest mesh setting available. The Z'' of the models' impedance plot is processed by the two-layer spreading resistance equation (Two-layer SRE) and the original SRE to extract the corresponding conductivities. Through this comparison of conductivity extracted from both equations, it is clear that the two-layer spreading resistance equation provides more accurate surface layer conductivity results. Light green shaded area indicates results within $\pm 10\%$ of the intrinsic conductivity value.

The effect of crack geometry on the extracted σ is also reflected in Figure 7.17. If we subtract the baseline change for a crack width=0 (intact two-layer model) from the crack model's percentage change, the result should reflect the crack's influence over the measured conductivity. In Table 7.3, deviations in the crack model results from the intact two-layer model are shown for a crack depth of 5 μm . Little change occurred in the measured σ when the crack width is less than 70% of the electrode separation. When the crack width is 90% of the electrode separation, a 7.44% decrease in extracted σ is obtained. In the D10 model series, where the crack depth increased to 10 μm , the effect of the crack becomes more significant with a maximum decrease of 14.29% in extracted σ . Thus, from the D5 (Two-layer SRE) and D10 (Two-layer SRE) series, the extracted surface layer conductivity decreases with increasing crack width and crack depth/surface layer depth, but using the two-layer spreading resistance equation, relatively accurate conductivity values can be extracted.

	W10%	W30%	W50%	W70%	W90%
D5 (Two-layer SRE)	-0.11	-0.43	-0.54	-2.37	-7.44
D10 (Two-layer SRE)	-1.63	-1.99	-3.97	-7.20	-14.29

Table 7.3. Deviation of cracked model from intact surface layer model, based on the results shown in Figure 7.17.

7.2.6 Non-through thickness crack

Apart from the scenarios shown in the previous sections, other features with the cracked model have been explored. The first is a three materials layered crack study. As the name suggests, the crack has been divided into three physical volumes, i.e., the crack is meshed and assigned with different material properties for each (of the three) portion(s).

Figure 7.18 shows illustrations of different crack layout. The model consists 6 volumes, as shown in Figure 7.18(a), volume 1, 2 and 3 form the crack region. Volume 5, 6 are for the surface layer, then volume 4 is assigned as the bulk material underneath the crack and surface layer. In Figure 7.18(b), (c) and (d) shows three different configurations of the model. In (b) shows a homogenous resistive surface layer model, volume 1, 2, 3, 5 and 6 are assigned with conductivity of 1.355×10^{-7} S/m, and volume 4 is assigned with conductivity of 1.355×10^{-5} S/m as the bulk material. In (c), the crack region (volume 1, 2, 3) is assigned with a conductivity of 1.355×10^{-9} S/m, 100 times less conductive than the rest of the surface layer (volume 5, 6), relative permittivity is set to 1, to simulate an insulating crack. In (d), the bottom 4 μm of the insulating crack (volume 3) is assigned with the normal surface layer (volume 5, 6) properties, therefore a pathway for leakage underneath the crack is formed. The bulk layer (volume 4) properties remained unchanged: conductivity was 1.355×10^{-5} S/m and the relative permittivity was 162 for all 3 models.

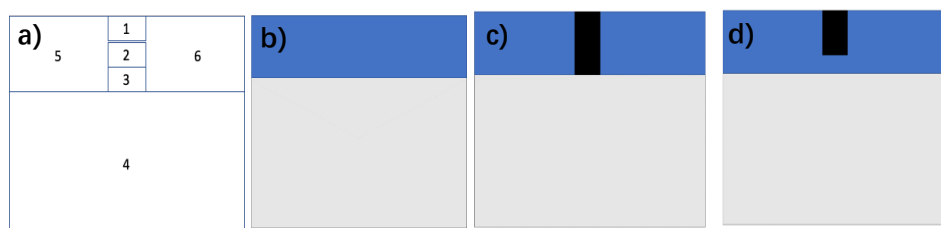


Figure 7.18. (a) Structural illustration of three materials layered crack model. (b) Configuration for homogenous surface layer model, (c) Configuration for insulating meshed crack model, (d) Configuration for non-through thickness insulating meshed crack model. The region underneath the insulating meshed crack has the same properties as the rest of the surface layer, acting as a tunnel for current to flow.

Line scans of current density were tested for all three models with the results presented in Figure 7.19. The scans take place in the z axis from the model centre. The homogenous model shows the highest current density in the surface layer but the lowest in the bulk layer. D6 and D10 have a similar surface layer current density distribution. Both are 2 orders of magnitude lower than the homogenous model but they have slightly higher current density in the bulk layer. In terms of crack depth, the models can be seen as homogenous=D0, D6 and D10. As crack depth increases, the confinement effect of the crack increases, thus the current density in the bulk layer increases according to crack depth.

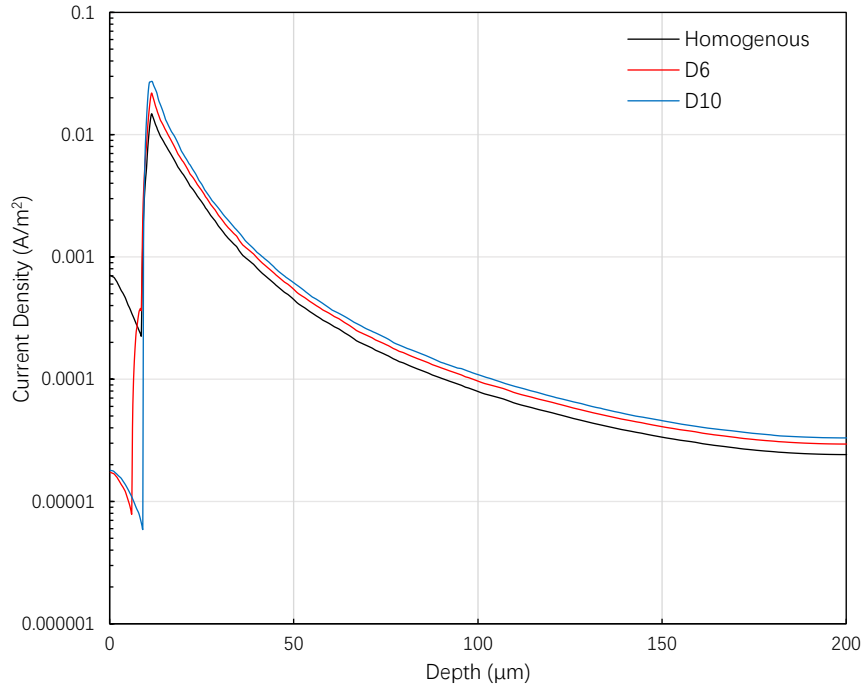


Figure 7.19. Line scan results of current density versus scan depth plot. The scan takes place in the three models shown in Figure 7.18, along the z axis through the model centre. The homogenous model has no insulating crack in the surface layer. The D10 model has an insulating crack with the same thickness as the surface layer. The D6 model reduced the insulating crack depth to 6 μm , thus the 4 μm underneath the crack has the same properties as the surface layer.

The impedance results of these three models are shown in Figure 7.20. First, identify the 3 series of data: Black, homogenous top layer without crack structure. Blue, D10, top layer with a through thickness insulating crack. Red, D6, top layer with a non-through thickness insulating crack, the bottom 4 μm of the crack provides a pathway for current.

In Figure 7.20(a), all 3 models show a dominant semi-circle in Z^* plots. The model with no crack has the lowest measured impedance value. When the insulating crack is meshed in the surface layer, the overall impedance increased. The difference between a through thickness and non-through thickness model is minor and barely distinguishable. Figure 7.20(b) shows M'' spectra for all three models. Compared with the homogenous surface layer model, adding an insulating crack in the top layer gives an increase in both the lower and higher frequency peaks in the M'' (blue) spectrum. Meaning the response from both the surface layer and bulk layer increased. When a pathway for leakage is created underneath the crack, a decrease of peak height from 5.96×10^{12} to $4.83 \times 10^{12} \text{ F}^{-1}$ occurs for the higher frequency M'' peak (red spectrum) but it's still higher than the no crack model ($2.77 \times 10^{12} \text{ F}^{-1}$), M'' (black) spectrum.

The increase in height of the M'' response at higher frequency on introducing a crack suggests the current pathway in the surface layer is effectively blocked by the insulating crack structure and therefore detours underneath the crack, increasing the current flow in the more conductive bulk layer. When the lower 4 μm of the crack is changed to the same property as

the surrounding surface layer, a pathway is constructed for the current to flow and this explains the decrease in the height of the higher frequency M'' peak at 1151 Hz.

The Z'' spectra in Figure 7.20(c) also revealed the measured overall resistivity increases when an insulating crack is placed in the surface layer. Finally, in the C' spectra in (d), originally there exists two plateaus of 0.027 and 0.021 pF. Placing an insulating crack of depth 10 μm , causes the two plateaus to decrease to 0.020 and 0.018 pF. Providing a leakage tunnel of 4 μm under the crack retains the capacitance values as 0.020 and 0.018 pF. This suggests the insulating crack body in the surface layer is the dominating factor in the change of low frequency impedance results, since introducing a tunnel for current only slightly alters the results.

Through this comparison study, it can be concluded that introducing an insulating object in the surface layer will effectively increase the impedance response from the underneath more conductive bulk layer but the insulating object also causes the response from the surface layer to surge. This should explain why adding a crack in the surface layer alone will not reproduce the impedance change in Veazey's experiment.

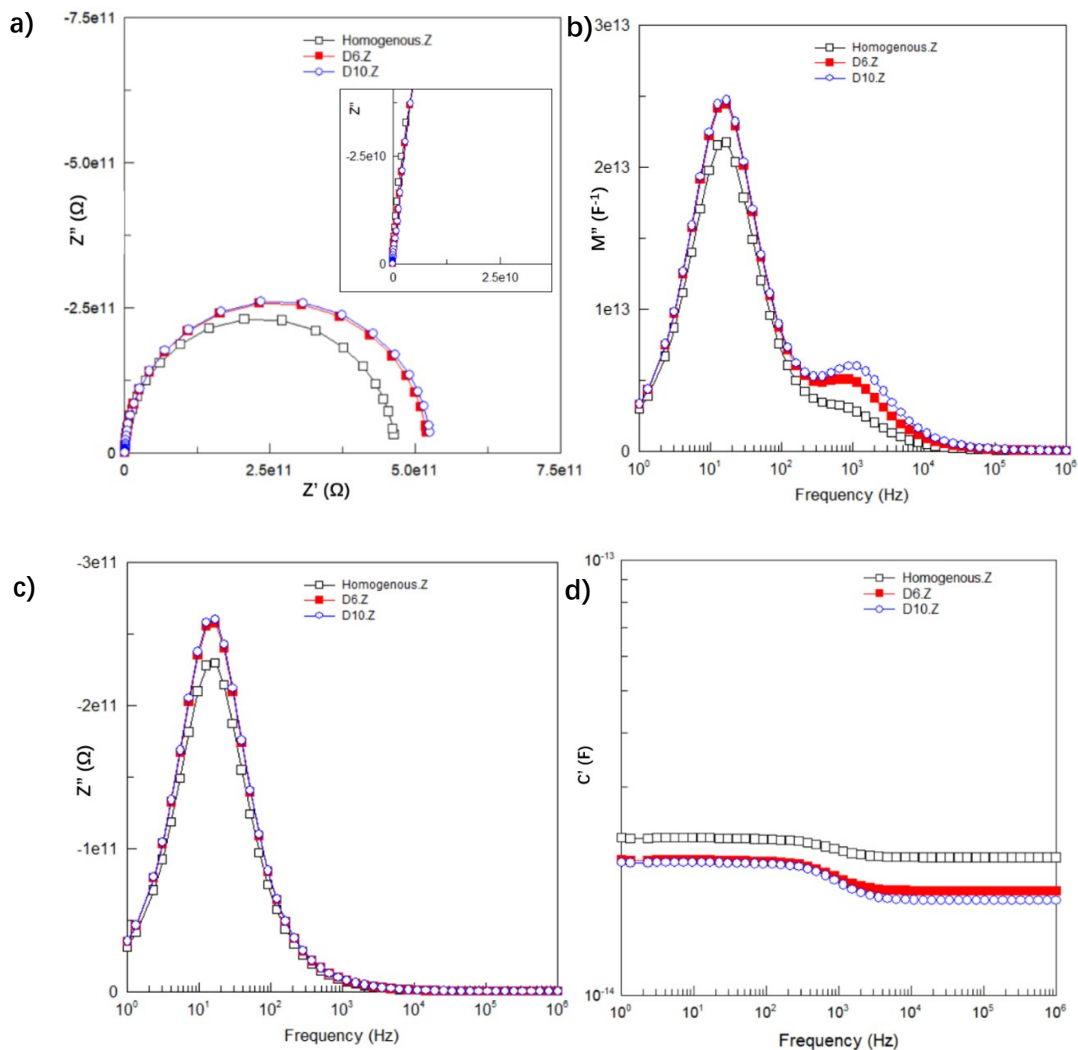


Figure 7.20. Impedance spectroscopy data for 3 two-layer models with different crack configurations: a homogenous surface layer with no crack (Black); a through-thickness crack

(D10, blue); and a non-through thickness crack (D6, red). (a) Z^* plots. (b) M'' spectroscopic plots. (c) Z'' spectroscopic plots. (d). C' vs frequency plots.

7.2.7 Non-through length crack

Throughout this project, all the cracks in the model have the same length as the model and the current could only detour into the bulk layer underneath. This specific set up is based on the microscopy images of the Veazey experiment, where the visible crack density was high between the two micro-contacts. This set up also reduces the variables to investigate. As the crack's depth and width effects on the impedance response have been studied, it is now appropriate to investigate length effects associated with a crack.

The model structure was modified to construct a crack of variable length, but no change was made in the meshing and attractor settings. Figure 7.21 shows a model with crack length of $40\ \mu\text{m}$ and width of $2\ \mu\text{m}$, instead of cutting across the entire top surface of the model. The crack is only placed in the middle section where current density is high. Line scans are first conducted to understand the current density distribution when the crack length changes. For comparison proposes, two models with crack lengths of 5 and $40\ \mu\text{m}$ were constructed, denoted as L5 and L40, respectively. The line scan takes place on the top surface of the models along the x axis direction, but at different y axis positions, which are 0 , 20 and $30\ \mu\text{m}$ away from the model centre, denoted as $Y=0,20$ and 30 . The line scan results are shown in Figure 7.22.

In Figure 7.22, the current density distribution of models L5 and L40 are nearly identical when scanned along the model centre (L5-0 and L40-0). Moving away from the model centre by $20\ \mu\text{m}$, which is at the edge of the crack in the L40 model but $17.5\ \mu\text{m}$ away from the edge of the crack in L5 model, the current density in the L5 model is higher than that of the L40 model. This can be attributed to the hindrance of current flow by the crack in the L40 model, whereas in the L5 model, no obstacle exists for current to flow. Moving the line scan further to $30\ \mu\text{m}$ from the model centre, now L40's current density is higher than that of L5. This region is where the current detours around the crack edge in the L40 model, thus causing an increase in current density.

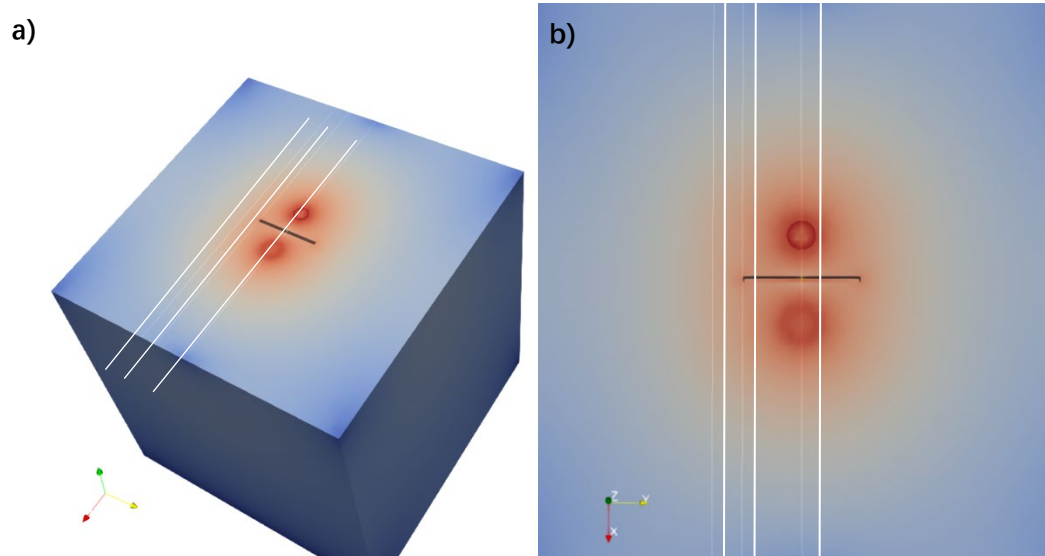


Figure 7.21. Model illustration of a non-through length crack in the surface layer. The crack is 40 μm in length, 2 μm in width and 10 μm in depth. The three white lines represent the line scan positions along the x axis. (a) Angled top view. (b) top view.

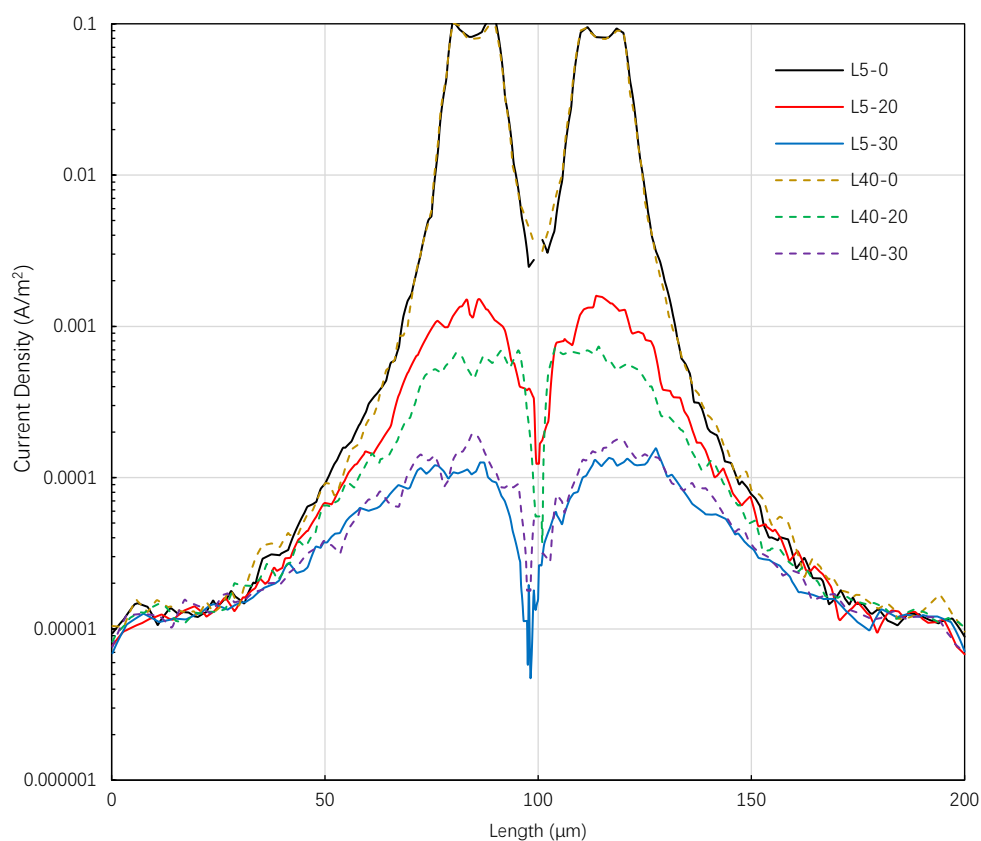


Figure 7.22. Current density versus scan length plot, showing the current density distribution of models with a crack length of 5 and 40 μm . Scan positions at 0, 20 and 30 μm along the x axis away from the model centre.

Impedance analysis of models with increasing crack length was conducted. The results are shown in Figure 7.23. The result nomenclature is: L5W2 means a crack length 5 and width 2 μm , the 3M6A homo model is where the pristine cube has no crack. Thus, the models show crack length from 5 to 198 μm , all have a crack width of 2 μm and a depth of 10 μm . From the Z'' spectra, all models have a single peak near 1526 Hz. The Z'' value increases with the crack length; however, the increase in Z'' is a minimum after the crack length extends beyond 40 μm .

In Figure 7.24, a percentage change in measured resistance versus crack length/electrode radius plot is shown. The x axis used crack length/electrode radius (L/r) instead of crack length in micro meters. The measured resistance increases when the crack length extends and reaches a maximum (7.37%) when the crack length is 40 μm , which is 8 times of electrode radius. After which, further increasing the crack length does not generate greater changes in the measured resistance of the models. This suggests a crack length of 40 μm or $L/r=8$ is effective enough to block most current flow on the top surface. The current density distribution illustration in Figure 7.21 also shows a crack with length of 40 μm , which cuts across most of the high current density area. The M'' spectra show a similar grouping of the results.

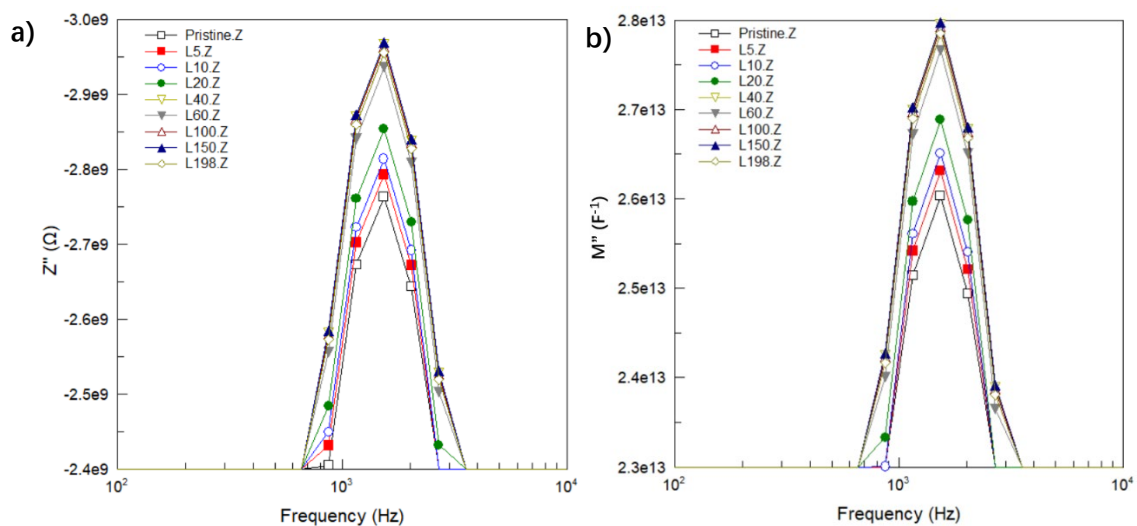


Figure 7.23. Z'' (a) and M'' (b) spectra of two-layer models with increasing crack length, from 0 to 198 μm . Pristine model has no crack but a resistive surface layer of 10 μm thick, L5-L198 model has crack length of 5 to 198 μm . For models have a crack, crack width is fixed at 2 μm and depth fixed at 10 μm thick. The electrode separation is 20 μm .

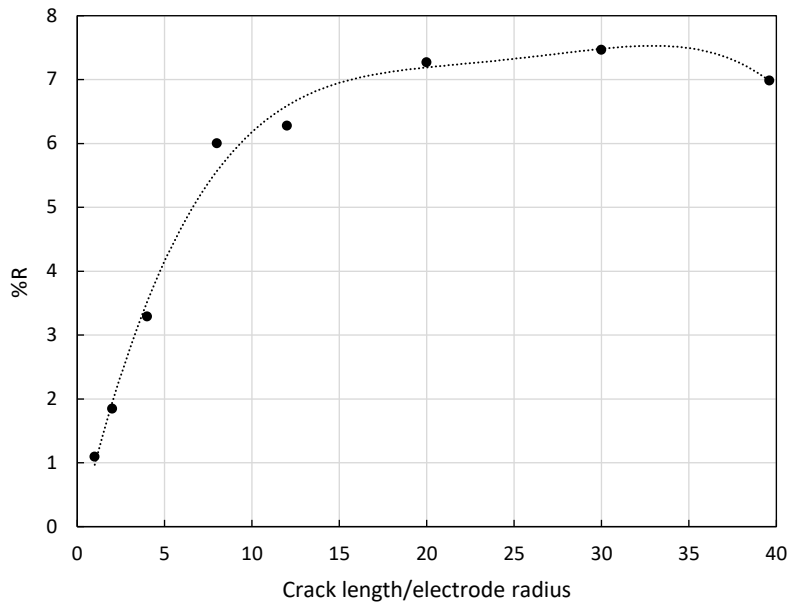


Figure 7.24. %R versus crack length/electrode radius plot for two-layer models with increasing crack length from 5 to 198 μm . The x axis used a ratio between crack length to electrode radius instead of crack length in micro meters. Line is shown as a guide to the eye.

7.2.8 Simulations of real experimental results

We have constructed a cubic model with a crack featured on the top surface, and a resistive surface layer has been included. The relationship between crack dimensions and impedance results has been investigated. The next step is to apply the findings in an attempt to simulate the micro-contact measurement results reported by Richard Veazey [1]. In this process, we would be able to have a better understanding of the possible factors causing the cracked region impedance results to be different from the intact region. To control the number of variables in the process, the crack created are through surface layer thickness and through side length.

First, we need to inspect the physical environment of Veazey's measurements, the detailed information is presented in chapter 2. The pristine SrTiO_3 samples had undergone 5 MeV Au irradiation to create an amorphous surface layer on the substrate. The samples developed crack features of various depth on the surface after 500°C heat (annealing) treatment. Veazey used TEM to study the cross section of the radiation damaged SrTiO_3 samples and determined the radiation damaged region penetrates $1.47 \pm 0.04 \mu\text{m}$ into the sample surface and this region is completely amorphous before annealing [1].

To determine the effect of the cracks on the impedance response, Veazey conducted micro-contact impedance measurements in the region shown in Figure 7.25. Measurement A took place where the number of cracks is at a local minimum, and measurement B took place at a region with a significantly higher crack density. The impedance responses were plotted in the same figure.

The results indicated that the cracks in the surface layer of the sample were the main cause

of the impedance response to be different from region A and B. When a low density of cracks was present between the micro-contacts, the two peaks at higher and intermediate frequencies in the M'' spectra have similar magnitude. However, for a high density of cracks between the micro-contacts, the higher frequency M'' peak increased and the intermediate frequency peak decreased. The Z'' impedance plots reveal that, increasing crack density causes the impedance measured to decrease slightly, as the peak near 140 Hz from measurement B is lower than that from measurement A. It appears the M'' spectra show greater change than the Z'' spectra, between measurement A and B.

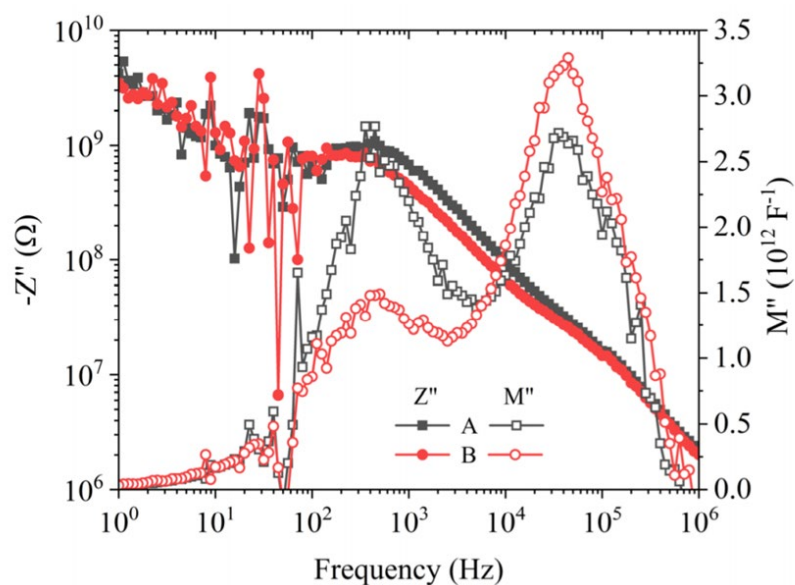
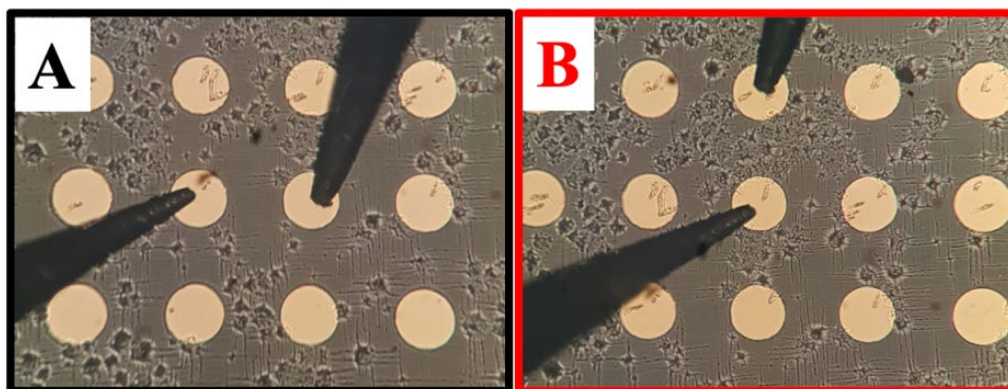


Figure 7.25. Veazey's impedance results from measurements A and B. Measurement A took place in a region with a low number of visible surface cracks, whereas measurement B took place in a region filled with visible surface cracks. The actual temperature of the sample was 310 °C and the heating had endured for 296 minutes at the time of measurement [1].

In Veazey et al's previous hypothesis, a crack in the resistive surface layer would drive the current down to the conductive bulk material layer, causing the total impedance response in the surface layer to drop (low frequency M'' peak to decrease in height) and the response from bulk layer to rise (high frequency M'' peak to increase in height), as illustrated in Figure 7.26.

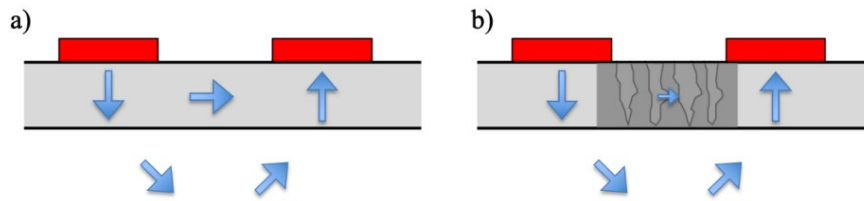


Figure 7.26. Schematic illustration of possible current flow in the sample. a) Damaged sample prior to heat treatment with an intact resistive layer on top of a crystalline bulk material. b) After heat treatment, cracks formed between the micro-contacts, hindering the current to flow through the micro-contacts [1].

Through the development of chapters 5 and 6, we have the capability to construct a crack in the resistive layer, allowing us to verify the suggested hypothesis and to try and simulate the impedance results obtained by Veazey.

7.2.8.1 Adding a crack to the surface layer at the same thickness

The first step is to add a physical void type crack (PVC) in the resistive layer and observe if the result matches with the experiments. As shown in Figure 7.27, two models with a surface layer thickness of 2.5 μm are shown. When the crack region is unmeshed, the M'' peaks at both lower and higher frequency increased. In this way, we have a partial match with Veazey's experimental results: the increase in the higher frequency peak should be a result of more current being driven into the bulk layer. However, the small increase in the low frequency peak is not understood or consistent with Veazey's hypothesis. In the Z'' spectra, adding a crack in the surface layer caused the measured impedance to increase slightly, which also contradicts with the experimental results.

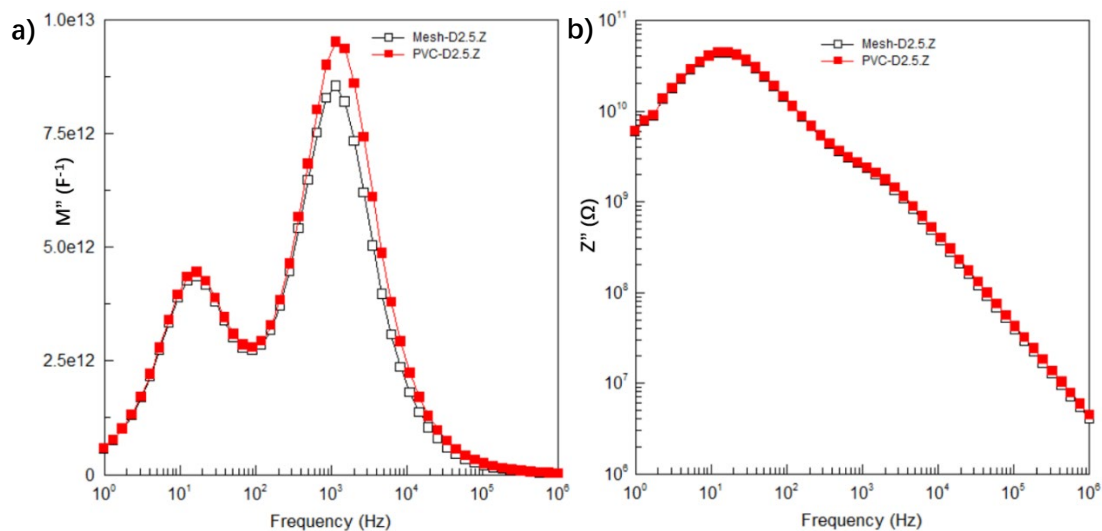


Figure 7.27. Impedance data of a two-layer model with crack (red) and a two-layer model with a homogenous surface layer (black). (a) M'' spectra. (b) Z'' spectra.

7.2.8.2 Changing the surface layer thickness

The assumption of model setting has been altered slightly. Previously we assumed the surface layer thickness between measurement A (few visible cracks) and B (intense visible cracks) conducted by Veazey is the same. However, the true surface layer thickness of both regions

is unknown. In fact, Veazey's TEM images showed the thickness of the amorphous layer not to be even ($1.47 \pm 0.04 \mu\text{m}$ in Figure 2.10 and $1.52 \pm 0.10 \mu\text{m}$ in Figure 2.11). Also, note that recrystallisation was still occurring between measurements, this adds to the uncertainty of the amorphous/recrystallised layer thickness. Therefore, we can have a new hypothesis: to achieve a low frequency peak drop but a high frequency peak rise in the M'' spectra, a crack is present but the surface layer thickness decreased. The influence from a reduced surface layer thickness is shown below, Figure. 7.28. Reducing the surface layer thickness from $5 \mu\text{m}$ (blue) to $4 \mu\text{m}$ (red), produces an increase in the high frequency peak near 1500 Hz and a decrease in height of the low frequency peak at 16 Hz . Further reducing the thickness to $2.5 \mu\text{m}$ (black), the extent of the peak increases and decreases, respectively is enhanced.

This was first discovered in chapter 6: the effect of changing surface layer thickness alone can alter the height of the two peaks in M'' spectra. The Z'' spectra change when surface layer thickness is changed, reducing the surface layer thickness would also reduce the Z'' peak height.

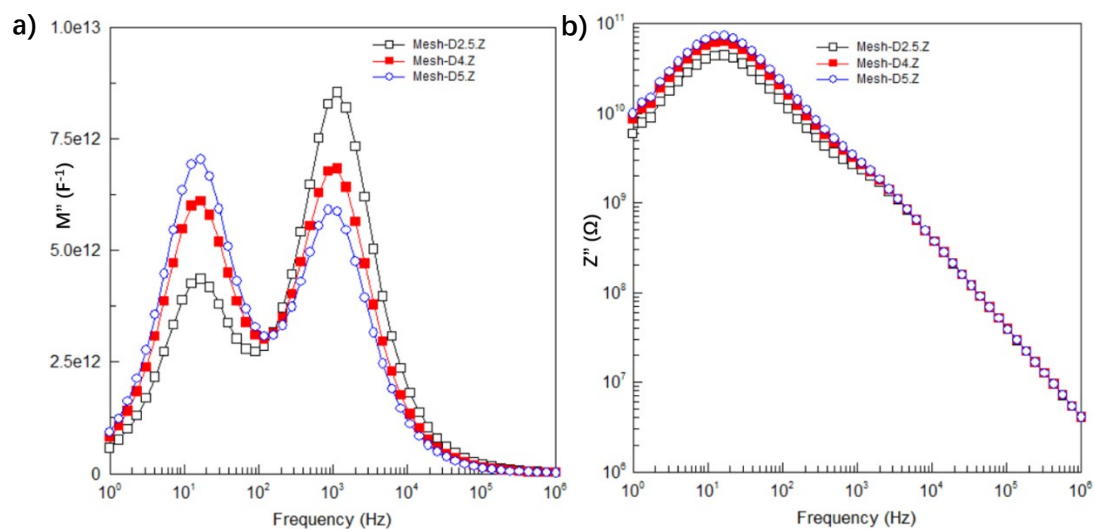


Figure 7.28. Impedance data for two-layer models with different homogeneous surface layer thickness. Black $2.5 \mu\text{m}$, red $4 \mu\text{m}$, blue $5 \mu\text{m}$. (a) M'' spectra. (b) Z'' spectra.

7.2.8.3 Combining both changes

As a final study we combine the two effects together, compared with a homogeneous two-layer model. Not only is a crack added to the model but it also has a thinner surface layer thickness than the homogeneous two-layer model. The results are shown in Figure 7.29 in the form of Z'' and M'' spectra. A homogeneous surface layer model (red) is our simulation of experiment A from Richard's report, and the cracked and reduced surface layer model (black) is our attempt to simulate what happened in experiment B. Not only do the results in the M'' spectra show the same trend as his measurements but so does the changes in the Z'' plots.

Since the result matches well with the changes shown in the experiments, it is possible our hypothesis is correct; however, there may remain other features that we have overlooked and have yet to be identified and tested. Such as delamination of the surface layer during

recrystallisation, which will generate longitudinal cracks between the surface layer and bulk material underneath, or cracks penetrating beyond the surface layer and into the bulk layer. XTEM in the recrystallised region revealed vacancy-type defects, interstitial-type defect clusters and regions with high strain were also observed [1]. These influence of such structural defects on the impedance data was not characterised in the experiment and not simulated in the models of this thesis. Also, the amorphous layer began recrystallisation at 300 °C and above. At the temperature of the measurements recrystallisation would have happened. It is unclear if the amorphous layer had uniform electrical properties in the area where mclS was conducted. Finally, there exists an amorphous to crystalline transform region from 1.47 to $1.64 \pm 0.04 \mu\text{m}$ from the surface of the sample which was suspected to contain Sr_2TiO_4 and TiO_2 secondary phases [1]. Their electrical properties have not been characterised, let alone simulated in the current two-layer model. A third layer in the model may be required to simulate the transformation region.

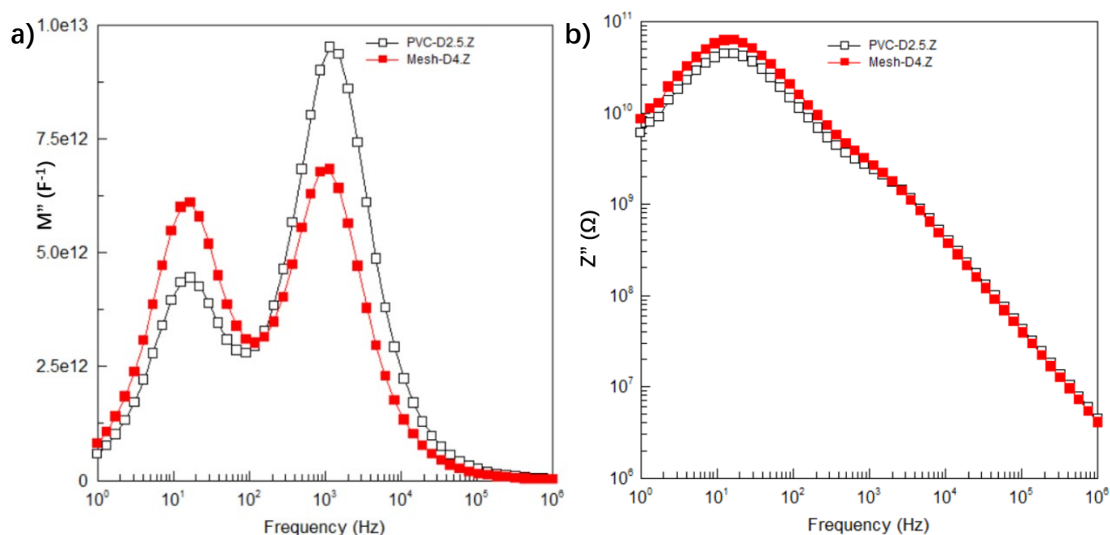


Figure 7.29 (a) M'' plots from two models. One with a thinner surface layer thickness and a crack (PVC-D2.5, black) and another with a thicker intact surface layer (Mesh-D4, red). (b) Z'' spectra from the two models.

7.3 Conclusions

Within this chapter a resistive layer was incorporated into the cracked model. The simulated impedance results revealed the confinement/hindrance effect of crack geometry in the surface layer is reduced, due to the reduced current density within the resistive surface layer.

After examination, the spreading resistance equation was not able to extract accurate surface layer conductivity, thus the two-layer spreading resistance equation presented in chapter 6 was utilised to process the measured Z'' values in an attempt to extract meaningful conductivity values. Although the two-layer spreading resistance equation is based on chapter 6's higher precision model, it was possible to extract surface layer conductivity at much higher accuracy than the original spreading resistance equation, with less than 10% deviation from the intrinsic assigned value. In contrast, the original spreading resistance

equation yields deviations of 40-80% from the intrinsic assigned value.

A non-through surface layer thickness crack and non-through side length crack models were also investigated. For a non-through surface layer thickness crack, a conductive tunnel is created underneath the insulating crack in the surface layer. The crack's hindrance/confinement effect was reduced and the impedance response from bulk layer underneath was also reduced.

In the situation of a non-through length crack, various crack length models were created. It was shown that the measured resistance increased with increasing crack width but when the crack length reached 40 μm or 8 times of the electrode radius and above, the increase in the measured resistance was minimal, even for a crack length of 198 μm . This means when placing a crack between the micro-contacts, a crack length of 8 times of the electrode radius is very effective in blocking the current flow in the surface layer.

In an attempt to resolve Veazey's micro-contact impedance measurements on damaged and annealed SrTiO_3 were made. Adding cracks in the surface layer causes the M'' peaks associated with surface and bulk responses to rise. This is only in partial agreement with the experimental results. A new hypothesis was proposed where the surface layer thickness between the two measurements may be different. The simulation results presented support the new hypothesis; reducing the surface layer thickness decreases the M'' peak value at lower frequency but increases the M'' peak at high frequency. Also, the change in Z'' spectra show the same trend as observed in the experiments. Combined with the effect of a crack, the hypothesis proposed here matches with the experimental results obtained by Veazey.

7.4 References

- [1] R. A. Veazey, "Probing Radiation Damage in Fe-doped SrTiO_3 using Micro-contact Impedance Spectroscopy," PhD Thesis, University of Sheffield, 2019.
- [2] J. Fleig, "Microelectrodes in solid state ionics," in: Alkire RC, Kolb DM, eds. *Chapter 1 in Advances in Electrochemical Science and Engineering*, Weinheim, Wiley-VCH, 2002, pp. 1-87.
- [3] R. A. Veazey, A. S. Gandy, D. C. Sinclair and J. S. Dean, *J Am Ceram Soc*, 103, pp. 2702-2714, 2020.

Chapter 8: Conclusions

8.1 Conclusions

The initial aim of this thesis was to investigate the electrical properties of $\text{Na}_{1/2}\text{Bi}_{1/2}\text{TiO}_3$ (NBT)-based dielectric materials. During the first year of the project, NBT- $\text{BiMg}_{1/2}\text{Ti}_{1/2}\text{O}_3$ (NBT-BMT) and NBT- $\text{BiZn}_{1/2}\text{Ti}_{1/2}\text{O}_3$ (NBT-BZT) systems were synthesized and characterised.

There are noticeable differences between the two types of NBT-based solid solutions studied in this work. For the NBT-BMT series, two different mixing methods were used which were hand grinding and ball milling. The hand ground samples change from conductive to insulating when BMT content increased to 2%, further increasing the BMT content results in marginal suppression in conductivity and the 8% NBT-BMT sample has conductivity similar to NBT0.51T. Mg-rich secondary phase(s) were observed via SEM when the BMT content is 2% or higher. The insulating hand ground NBT-BMT samples showed large grains embedded in a small grain matrix, which could link to Yang et al's finding of grain size effect on electrical properties in NBT0.51T [1]. As a comparison, ball milling was used in order to achieve higher homogeneity in reactant distribution than hand grinding. The resultant samples showed complex electrical properties. Increasing the BMT content from 2 to 8% percent did not achieve a decrease in conductivity, but the 8% sample showed dual electrical response, indicating the presence of both insulating and conductive materials. An investigation on 6% NBT-BMT sample revealed the ball mill NBT-BMT could be very sensitive to sintering temperature. Further study is needed on the NBT-BMT system to fully understand the structural and electrical property relationship. The NBT-BZT system showed a clear trend as the bulk conductivity decreased with increasing BZT content.

After the onset of the Covid-19 pandemic, the experimental work was halted after discussions with the supervisors. The research focus was then shifted to a simulation-based finite element modelling (FEM) study on micro-contact Impedance Spectroscopy (mclS) and its application on ceramic systems with defects, namely surface layers and/or cracks (physical voids). The FEM section of the work contains an investigation on the effects that surface layers and cracks can have on mclS results. A novel method to accurately extract surface layer conductivity in a two-layer ceramic system was developed and a successful simulation on radiation damaged SrTiO_3 mclS experimental results from the models was constructed.

In chapter 5, a (homogeneous or pristine) model with the electrical properties (at $\sim 300^\circ\text{C}$) of SrTiO_3 was created. Two types of crack features were constructed on the cubic model's top surface. A meshed region assigned with very high resistivity as a crack (MC) and a physically void region as a crack (PVC). The crack's width and depth were altered to investigate the influence of crack geometry on the impedance results.

The simulated data show that increasing crack width and depth results in higher impedance from top-top micro-contact electrode measurements on a homogenous material. The maximum increase in the Z'' peak value and therefore resistance is 59%, at $S/r=2$, crack width 90% of total separation and crack depth 8 times the electrode radius. The geometric factor is

not suitable for calculating conductivity. Under certain situations, the spreading resistance equation (SRE) can be used. In the $S/r=2$ set up, when the crack depth to electrode radius ratio is between 4 and 8, the SRE can be used to calculate the conductivity of the material at any crack width. The calculated results are within a $\pm 10\%$ error range of the input value. For $S/r=2$, the crack effect (current confinement) can counterbalance the current interference from closely placed electrodes. As S/r increases, the crack effect diminishes more rapidly than the decrease in current interference. The crack's effect therefore becomes less effective in cancelling the current interference effect. Line scans of current distribution show adding a crack between the micro-contacts will lower the current density between the electrodes but the current density in the outer regions will increase. When the calculated bulk conductivities of models are plotted on a \log_{10} scale, the effect of a crack of any dimensions is very limited. The maximum deviation caused by a crack is only 0.1 on a \log_{10} scale of conductivity.

The FEM simulations then advanced to a two-layer ceramic system. In chapter 6, a novel way of extracting surface layer properties in a two-layer ceramic system was created. This is called the two-layer spreading resistance equation. Compared to a geometry correction factor or the original SRE, which are the two common methods to extract electrical properties from impedance spectra, the two-layer spreading resistance equation offers higher accuracy in correcting the results obtained. To examine the theoretical reliability of the method the time constant difference between the two layers was progressively lowered and the boundary conditions of where the new method is reliable was determined. When the resistivity of a surface layer is at least 100 times greater than the bulk layer, the surface layer conductivity can be extracted for any surface layer thickness. When the surface layer is less than 100 times resistive than the bulk underneath, the surface layer thickness needs to be at least 3 times that of the micro-contact radius to extract a reliable surface layer property. Despite the limitations of where to apply the novel two-layer spreading resistance equation method, its greatest advantage comes from providing an approach that uses a single equation, instead of the multiple equation solution proposed by Veazey et al [2]. Also, the two-layer spreading resistance equation can be used for thin surface layer conditions, which is unapproachable by the previously proposed method(s). The applicability of the two-layer spreading resistance equation can be extended to any desired thickness range. The novel method is also tested when the surface to bulk layer resistivity ratio is less than 100. Despite the loss of accuracy due to the small difference in time constant between the two layers, the two-layer spreading resistance equation can provide acceptable results in most simulation set ups. It is very exciting to see the application of this method in experimental measurements.

In the final results chapter, the model features were developed from chapters 5 and 6, combining and a resistive layer with a crack. The simulated impedance data revealed the confinement effect of crack geometry is reduced, as current density is reduced within the resistive surface layer.

The spreading resistance equation was tested to extract surface layer electrical properties and the results showed it is not capable of the task. The extracted electrical properties show 40-80% deviation from intrinsic values, although in chapter 5, the spreading resistance equation

can extract the electrical properties of the cracked bulk material for certain crack geometries. The two-layer spreading resistance equation presented in chapter 6 was applied to extract the surface layer electrical properties from chapter 7's model. The values extracted are within 10% deviation from the intrinsic values of the model. Thus, the two-layer spreading resistance equation is considered a valid tool to extract surface layer conductivity in a two-layer ceramic system, even with a crack existing in the surface layer.

Up to this point, the crack's width and depth effects have been studied, in order to achieve a holistic understanding of a crack's effect on impedance data. Two other types of crack geometry were investigated, a non-through surface layer thickness crack model and a non-through side length crack model. For a non-through surface layer thickness crack, a conductive tunnel is created underneath the insulating crack in the surface layer. The impedance data reveal the crack's hindrance/confinement effect was reduced and the impedance response from the bulk layer underneath was also reduced as the current now has a conductive pathway underneath the crack.

The effect of crack length on impedance data was studied by creating models with various crack lengths on the top surface. The data show the measured resistance increased with increasing crack width but when the crack length reached 40 μm or 8 times of the electrode radius and above, the increase in the measured resistance was minimal, even for a crack length at 99% of the model side length. This study shows that when a crack exists between the micro-contacts, a crack length of 8 times of the electrode radius is very effective in blocking the current flow in the surface layer.

After a systematic study on the crack's geometry effect on impedance data, the project moved to resolve an experimental problem posed by Veazey from the functional materials and devices group in Sheffield. He conducted micro-contact impedance measurements on radiation damaged and annealed SrTiO_3 single crystal samples. The impedance data showed annealed samples with a high density of cracks have different M'' and Z'' spectra from samples without a high density of cracks. In order to simulate the experimental results, the first step was to add a crack in the surface layer. This results in increased magnitude of the M'' peaks associated with both surface and bulk regions. This is only in partial agreement with the experimental results. A new hypothesis was proposed where the surface layer thickness between the two measurements may be different. The simulation results presented support the new hypothesis; reducing the surface layer thickness decreases the M'' peak value at lower frequency (resistive surface layer) but increases the M'' peak at higher frequency (bulk layer). The changes in Z'' spectra show the same trend as observed in the experiments. Combined with the effect of a crack, the hypothesis proposed here matches with the experimental results obtained by Veazey. This case study shows the models constructed in this thesis are capable of simulating two-layer ceramic systems with and without crack features.

8.2 Future work and application examples

Due to the pandemic, there remains works can be done to bring the topics discussed in this thesis into a more holistic state. For the experimental section focused on the NBT based

complex perovskite materials, the first step would be to prepare more compositions so that the NBT-BZT system should have $x=0.01$ to 0.08 , to ensure any possible trends in properties could be discovered and established. For NBT-BMT, insulating and conductive NBT grains were discovered in the structure at the same composition, also the uneven distribution of Mg in the system was found. More analytical electron microscopy is needed to understand this heterogeneity in the NBT-BMT system. If using solid state synthesis method, the precise sintering temperature of each composition should be determined carefully. Other synthesis methods such as solution-based methods are worthy to try and investigate the resulting ceramic's electrical properties to gather more understanding in preparing the NBT-BMT system.

For the FEM models, possible future works could be adding more features in the model structure to simulate more complex impedance measurement set ups. For example, adding more layers in the model could allow more gradients of electrical properties in the structure. Another aspect to look at is to apply the current FEM model to existing experimental report to verify the utility and accuracy of our models. To explore the full capability of the FEM models we have constructed a series of case studies on published mclS focused publications and the analyses are shown in the following section. The initial simulation results prove our model has significant potential to be applied to other ceramic systems. With appropriate input of the electrical properties of the materials, the models can assist experimentalists in analysing their results or to support their hypothesis.

We have selected 4 examples of mclS experiments with micro-top top (MTT) configurations, 1 example of mclS experiment with micro-top micro-bottom (MTMB) configuration and 2 examples of micro-top full-bottom (MTFB) configurations.

8.2.1 Resistive BaZrO₃ grain boundary characterisation: MTT

The first example comes from a study on grain boundary properties in large grained Y-doped BaZrO₃ polycrystalline samples by impedance spectroscopy. The major objectives were to extract grain boundary properties as using macroscopic and micro-contact impedance, with and without DC bias.

In this study, Maier et al reported that, with applied DC bias, the GB resistance and GB capacitance decreases, showing strong evidence for the presence of space charge depletion layers near the positively charged GB core. The origin of the high GB resistance of this material was determined to be the depletion of the major charge carriers in the space charge zones [3]. We will limit our simulation to the non-DC biased impedance measurements presented by Maier et al.

6 at% Y-doped BaZrO₃ was prepared by solid-state reaction starting from BaCO₃ and 6 at% Y-stabilized ZrO₂. Micro-contacts with diameter of 20 μm and 70 μm separation were printed on the samples by photolithography. Pt alloy needles with a nominal tip radius of 2.5 μm were used to connect the electrodes to an impedance analyser. The samples were placed on a heating stage and measured in a nitrogen gas atmosphere. The impedance measurements

were conducted in the frequency range from 10^6 to 0.1 Hz with an AC amplitude of 100 mV. Figure 8.1 shows the grain and micro-contact layout.

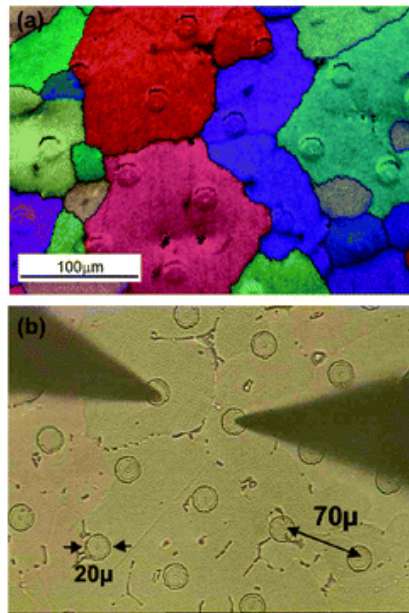


Figure 8.1. (a) Grain map of 6 at% Y-doped BaZrO₃ ceramic overlaid with SEM image of microelectrodes and (b) positioning of the needle tips on microelectrodes under the optical microscope [3].

As shown in Figure 8.2 (a), the non-DC biased AC impedance results of measurements taken in the same grain (red symbols) exhibit one semicircle in the Nyquist plot that is considered as the bulk contribution. When measurements take place across a GB, the data (black symbols) show two semicircles in the Nyquist plot (black symbols) from high to low frequencies attributed to the bulk and GB responses, respectively. The Bode plots reveal the difference between spectra inside a grain and across a GB, as in Figure 8.2(b).

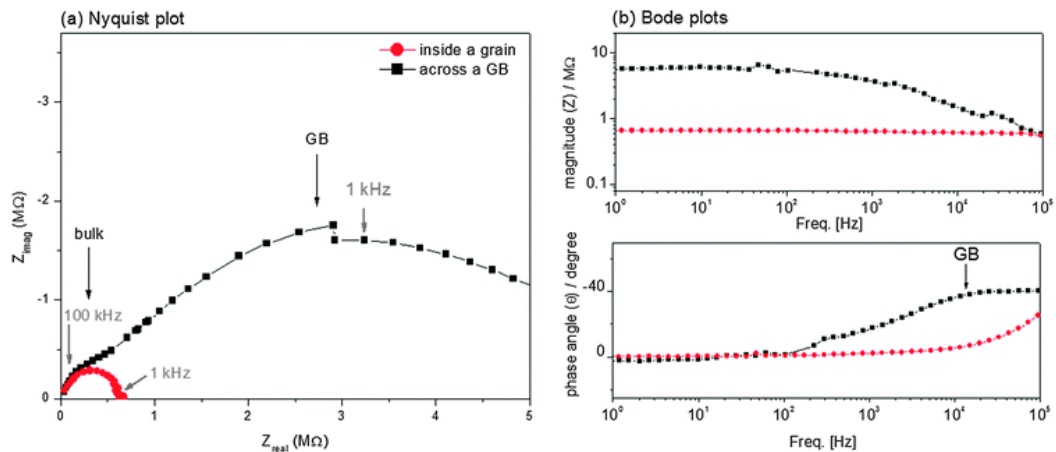


Figure 8.2. AC impedance data for a 6 at% Y-doped BaZrO₃ ceramic measured inside a grain (black symbols) and across a GB (red symbols). (a) Nyquist and, (b) Bode plots based on measurements performed at 700 °C in N₂ [3].

The resistances obtained by measurements inside grains ($R_1 = R_b$) and across the GBs ($R_1 + R_2 = R_{GB}$) at different locations are shown in Figure 8.3 (a). R_1 within a grain has a similar

value with R_1 from the measurements across a GB. The GB resistance is much higher than the bulk value. The measured resistance of the GB, $R_2 = R_{GB}$, shows a relatively even distribution.

Figure 8.3 (b) shows the variation in the peak frequency distributions associated with the bulk and GB semicircles. Maier et al interpret the narrow distribution of the individual GB peak frequencies to mean the GB's electrical properties are relatively similar, regardless of any difference in crystallographic orientations in the sample. The measured capacitance of individual GB's is ~ 10 pF. However, they did not rule out the possibility that more resistive GB's can exist and were maybe overlooked in measurements, as current could detour through surrounding grains instead of flowing through the more resistive GB pathway; therefore, the impedance response reflects this as a bulk only response with normal resistivity.

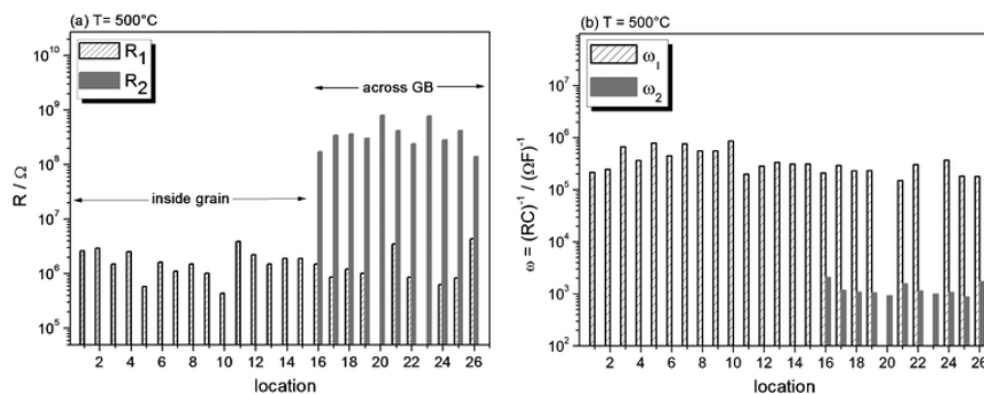


Figure 8.3. (a) Resistances and (b) peak frequencies of high-frequency and low-frequency semicircles from microcontact measurements at 500 °C on 6 at% Y-doped BaZrO₃ ceramics [3].

This study is an ideal case to illustrate the versatility of the models created in this thesis. The electrical properties can be simulated by a meshed crack in the bulk material, as shown in Figure 8.4. The micro-contacts on the top surface have a radius of 10 μm and the separation between the micro-contacts are 70 μm . The meshed grain boundary has a depth of 199 μm and width of 5 μm . The bottom layer of the cube has a thickness of 1 μm . The meshed grain boundary and bottom layer have the same electrical properties.

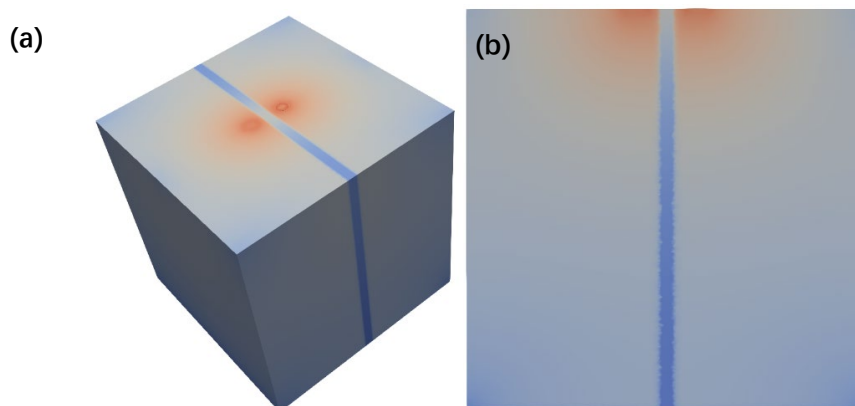


Figure 8.4. A resistive grain boundary simulation using a meshed crack (darker blue) as the GB in a more conductive bulk structure. The bottom surface has the same electrical properties as the meshed crack. (a) Angled top view. (b) Cross section side view.

The conductivity of the bulk material is set at 5×10^{-2} S/m. The conductivity of the meshed GB region and bottom layer is set at 5×10^{-4} S/m and then changed to 5×10^{-5} S/m for two trial simulations, as the resistive GB, two values are used to cover the deviation between the GB and bulk resistivity ratio shown in Figure 8.3(a). As Maier et al presented in the measurements, the conductive bulk shows resistance of $\sim 10^5 \Omega$ and the most resistive GB shows a resistance of $\sim 10^8 \Omega$. The maximum R_{GB}/R_{bulk} ratio can be as high as 1000. The relative permittivity is set at 50 as the paper reported. The simulated impedance data are shown in Figure 8.5. From the Z^* plots, the response from the bulk and GB can be distinguished in the measurements between a GB (blue and red data sets), as a large semi-circle appeared at low frequencies and an incomplete arc at the high frequency range. In contrast, only one response in the shape of an incomplete semi-circle (black data set) is observed from measurements within a single grain. The bode plots also shows a clear difference between measurements within a grain and between a GB.

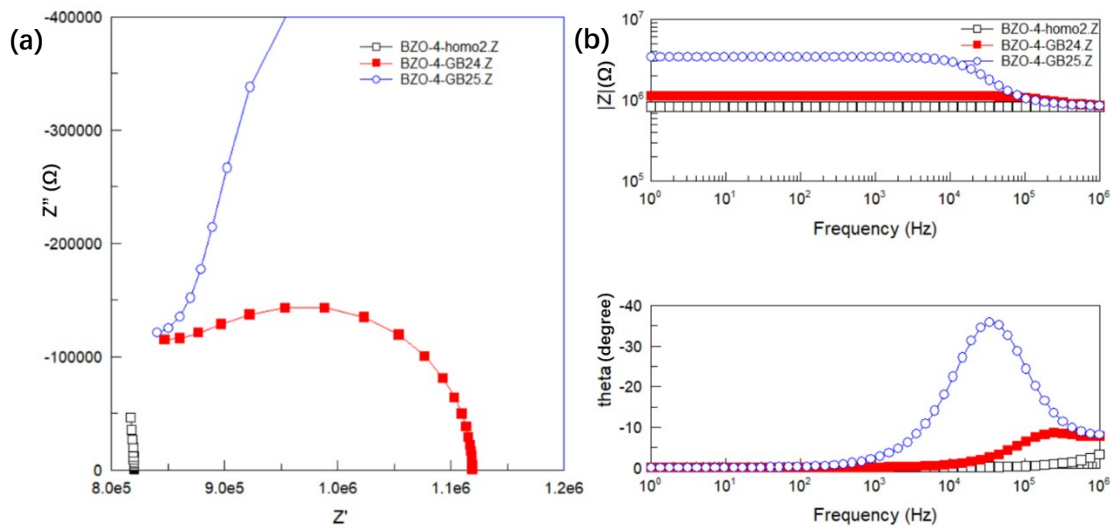


Figure 8.5. Simulated impedance data for a grain boundary model, (a). Z^* and (b) Bode plots. Black: pristine model without GB. Red: $R_{GB}=100 R_{bulk}$. Blue: $R_{GB}=1000 R_{bulk}$.

The simulated data shows similar observation as reported in the paper, note that the conductivity and relative permittivity values are only estimated values from the paper, and notwithstanding the dimensions of the grain boundaries, thus deviation from the actual impedance spectra is unavoidable. More precise data are needed to generate simulated data with higher accuracy, but this model can still be used as a proof of concept, showing our model's potential in simulating grain and grain boundary contributions to impedance spectra.

The current hindrance effect between a resistive GB and an insulating crack can be made via the data gathered in this project. Despite the physical void crack having the equivalent electrical properties of air, the maximum depth of crack simulated was only $40 \mu\text{m}$ which is equivalent to 8 times the micro-electrode radius. The results in Figure 8.6 show a maximum of 50% increase in the measured resistance, with no appearance of a second semi-circle, whereas a 100 times resistive GB in the simulation above could generate a secondary response.

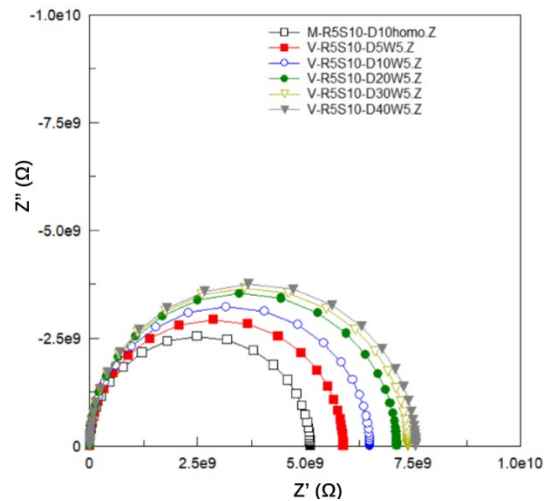


Figure 8.6. Z^* plots for the homogeneous (no crack) model and PVC models with a crack depth of 5, 10, 20, 30 and 40 μm .

Apart from the grain boundary and grain interaction scenario, we also applied the models to a dislocation enhanced electrical conductivity effect.

8.2.2 Conductive dislocation enhanced local conductivity: MTT

Bishara et al reported edge-type dislocations on the (100) surface of rutile TiO_2 single crystals can increase local conductivity of the defect-rich region by 50% [4]. The higher conductivity of dislocations in TiO_2 comes from the mixed-valence state of the Ti ions inside the dislocation core, resulting in a higher density of states at the Fermi level. Dislocations were carefully created in samples by indentation of a spherical diamond tip with a tip radius of 1 μm . An array of 5x5 indents was created with a distance of 1 μm between each indent, in order to increase dislocation density. Tungsten micro-contacts with 2 μm diameter were deposited on the dislocation and defect free areas, with a separation of 100 μm . Impedance measurements were conducted over the frequency range of 1 Hz–200 kHz using a voltage amplitude of 1 V. The set up and impedance data are shown in Figure 8.7.

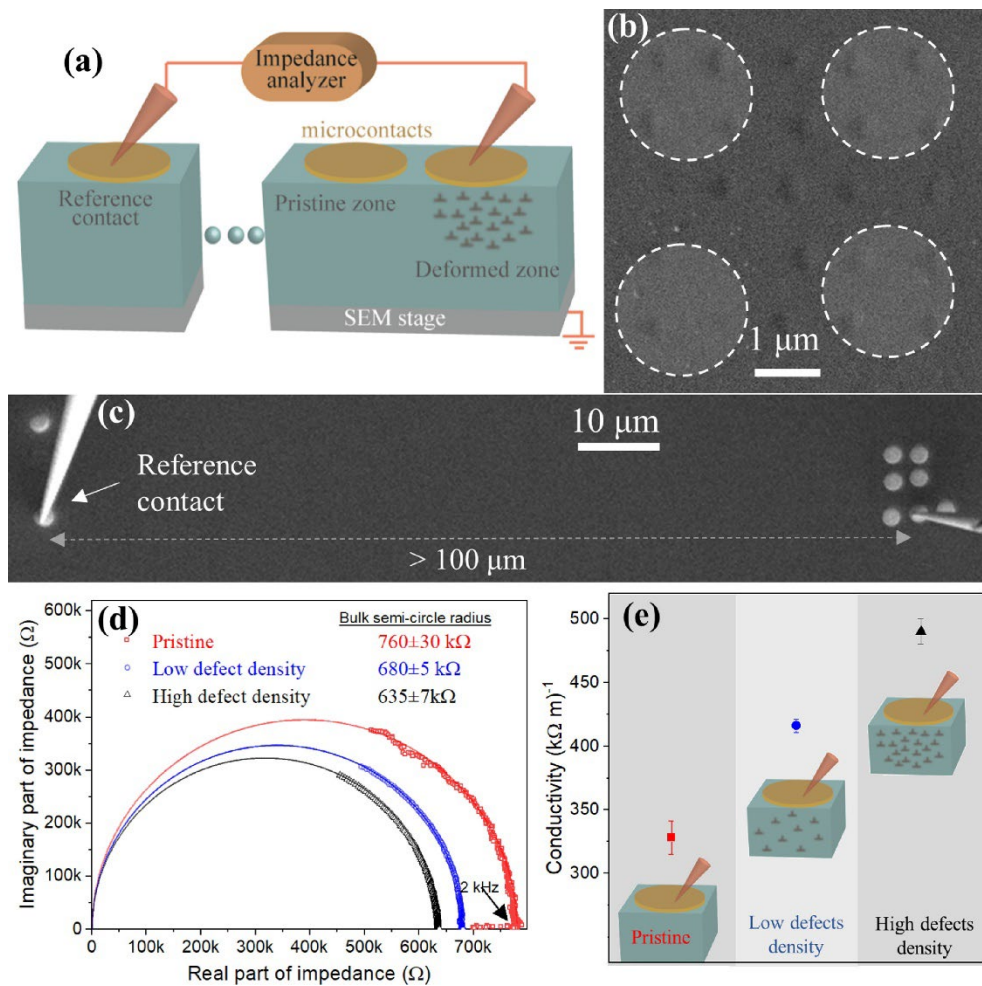


Figure 8.7. (a) Schematic illustration of the electrical measurements on indents in a TiO₂ crystal. (b) An array of indents was created to inspect the conductivity of the deformed area. Microcontacts area indicated by dashed circles. (c) Tungsten needles connect the micro contacts to perform impedance measurements. (d) Nyquist plots of pristine and deformed areas. (e) Conductivity increased up to ~50% on deformed areas compared to non-deformed areas [4].

The Nyquist plots in Figure 8.7 (d) show three semi-circles in the frequency range of 2-20 kHz. Since no second semi-circle is observed, the single arc response is considered the combined response of pristine and deformed material. Although the dislocations have higher conductivity, it is not reflected in the Nyquist plots where only an enhanced bulk response is detected. The capacitance of the measured data is about 1 pF, which corresponds to the bulk material property. A minor decrease in the capacitance from the deformed area of 0.78 pF is reported. The measured resistances of the pristine, low defect density and high defect density areas were 760 ± 30 , 680 ± 5 and 635 ± 7 kΩ, respectively, and the calculated conductivity of the measurements were 328 (kΩm)⁻¹, 416 and 490 (kΩm)⁻¹ respectively. They concluded the conductivity shows an increase up to 50%.

As the dislocations under and near the micro-contacts are volumes with higher conductivity, our model can be adopted to simulate such micro-contact impedance measurements. Two

approaches are made. First, set the meshed crack volume to have conductivity higher than the bulk material, or secondly, set the volume underneath one micro-contact to have higher conductivity than the bulk material. However, the paper did not provide details about dislocation volume nor the dislocation conductivity. We decided to use the SrTiO₃ material's properties to prove the core concept of the approaches, if a more conductive material is embedded within the model.

Figure 8.8 (a) and (b) show the first approach of a more conductive meshed region between the two micro-contacts. The meshed region has a width of 10 μm and a depth of 20 μm and the conductivity is 100 times greater than the surrounding bulk material. As the current density plot shows, the meshed region has much higher current density than the bulk material. Figure 8.8 (c) and (d) show the second approach, where the layer underneath one micro-contact is 100 times more conductive than the bulk volume. The layer has a thickness of 20 μm and 50% area of the top surface. As the figure shows, the current density is significantly higher in the layer underneath one micro-contact.

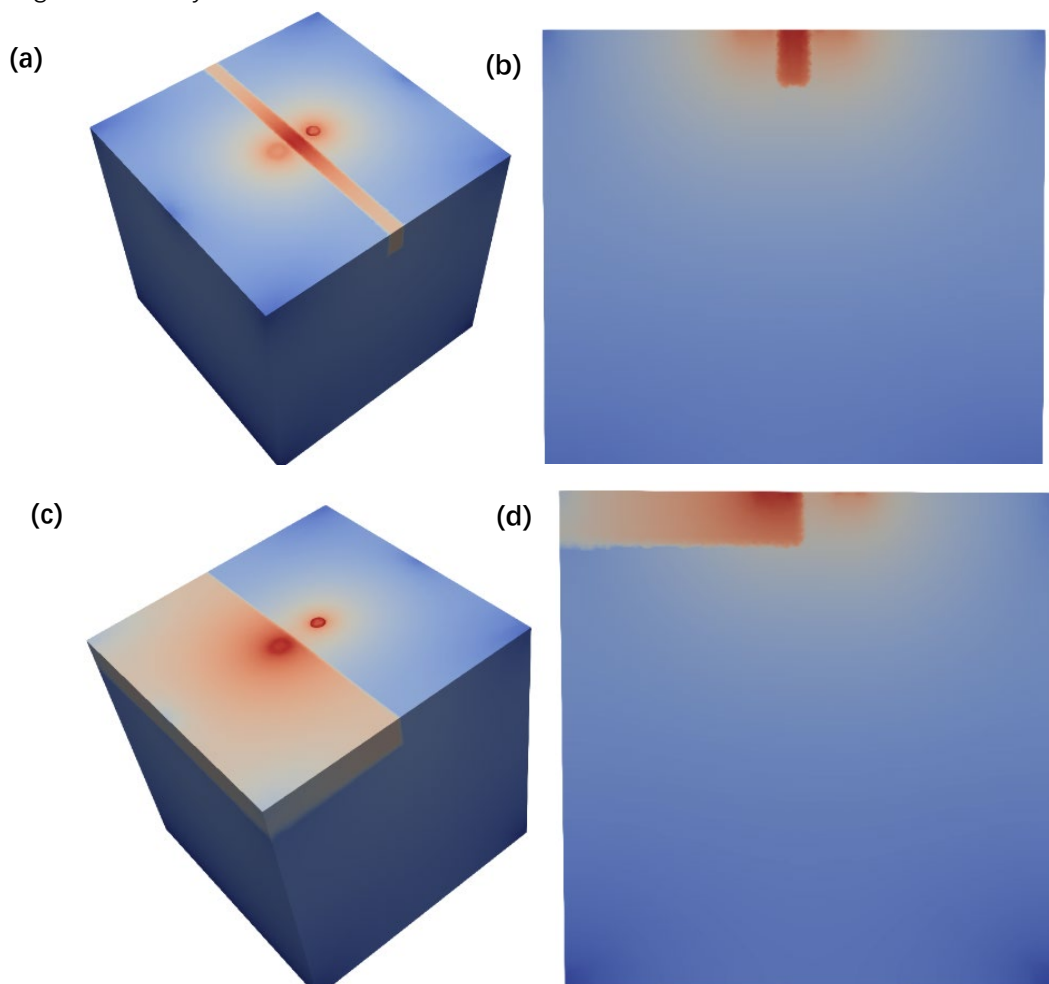


Figure 8.8. Illustration of the two approaches to simulate the dislocation enhanced conductivity effect. (a). Meshed crack region assigned with a higher conductivity model, angled top view. (b). Cross section side view. (c). Layer underneath one micro-contact with higher conductivity model, angled top view. (d). Cross section side view. The red colour indicates high current density, blue indicates low current density.

The simulated impedance data are shown in Figure 8.9. Results from three models are plotted together for comparison. The blue data indicates a pristine model without any high conductivity defects, the black data are for the model with a meshed crack of high conductivity (approach one) and the red data are for a model with a high conductivity layer underneath a micro-contact (approach two). From the Nyquist plots in Figure 8.9, all three responses consist only of a single semi-circle, which can be attributed to a bulk response. Inserting a more conductive volume in the cubic model, will cause the measured resistance to decrease. The data for the pristine model shows an intercept on the Z' axis of $5.59 \times 10^9 \Omega$. The approach one model shows an intercept of $5.18 \times 10^9 \Omega$ and the approach two model gives a value of $2.95 \times 10^9 \Omega$. It is clear that with increasing volume of conductive material in the matrix, the measured resistance decreased. Approach one's result is a closer match to the results presented in the experiment, suggesting the higher conductivity volume is small in the experiment, which fits well as there exists limited number of deformations on the sample surface.

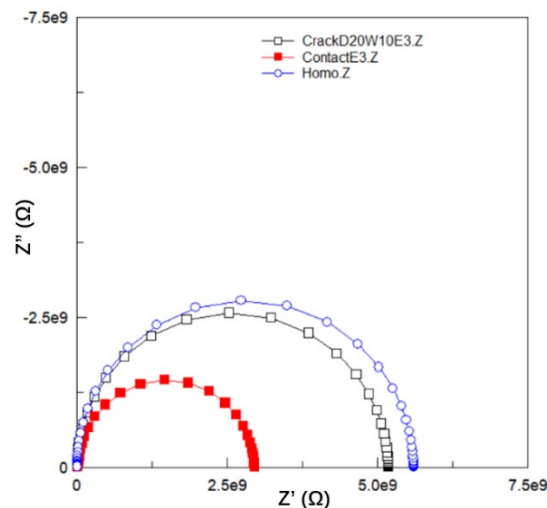


Figure 8.9. Nyquist plots for the pristine model (blue), meshed crack model (black) and high conductivity layer model (red).

8.2.3 Effect of crack on impedance in zirconia polycrystals: MTT

In chapters 5 and 7, we investigated the effect of a crack on mclS data and there exists publications highly relevant to our study. Lee et al used mclS on nitrogen-graded 2 mol% yttria-doped tetragonal zirconia polycrystals (2Y-TZP) [5]. Micro-contacts with radius of $5 \mu\text{m}$ and separation of 20 and $30 \mu\text{m}$ were applied on the sample.

Local measurements showed increasing the nitrogen concentration in TZP would decrease the local conductivity. One advantage of mclS is the ability to reveal heterogeneity in the specimen. In this study, it is reported that the distribution of precipitates and micro-cracks can influence the accuracy of the extracted conductivity.

The microstructure of the sample measured is shown Figure 8.10 (top). It is observed that nitrogen stabilisation takes place in the entire cross section, with columnar growth at a length of $950 \mu\text{m}$ from the two sides in contact with ZrN. The central region shows an equiaxed grain

structure. Impedance data of measurements across the region are shown Figure 8.10 (below), micro-top full bottom (MTFB, open symbols) and micro-top top (MTT, closed symbols) configurations are used. A conductivity profile in relation to nitrogen concentration is constructed. Both MTFB and MTT measurements show an increase in local conductivity with decreasing nitrogen concentration towards the sample centre. At the edge of the samples, the results from MTFB and MTT show observable differences. Lee et al consider this is related to the distribution of tetragonal precipitates, which is a microstructural difference. This example shows MTT could reveal more information in such a heterogeneous microstructure than MTFB, as the current is more localised between the two electrodes.

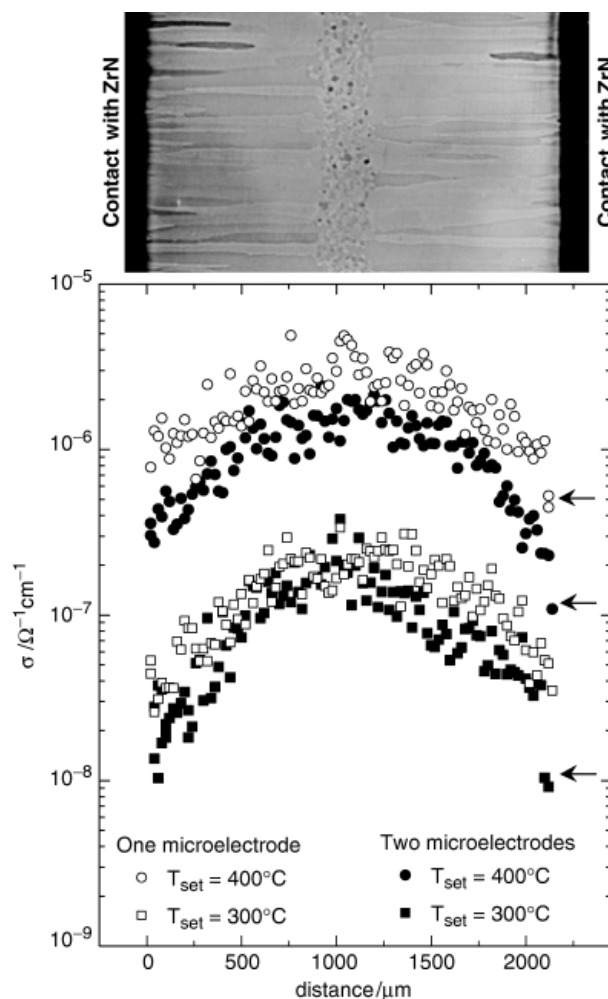


Figure 8.10. Conductivity profiles of a nitrogen graded 2Y-TZP sample (micrograph on top). Open symbols represent micro-top full bottom configuration, and closed symbols indicate micro-top top configuration [5].

The sample was then annealed at 700 °C for 10 minutes, microcracks were observed and the sample disintegrated after a few annealing cycles. The cracks are shown in Figure 8.11, indicated by the white arrows. Lee et al constructed conductivity profiles of as-prepared samples and annealed samples, shown in Figure 8.12. The scattering of the calculated conductivity is related to the random distribution of tetragonal precipitates with higher

conductivity than the matrix material. The microcracks add to the scattering of the results for annealed samples. This is in agreement with the conclusion made in chapter 5, where we demonstrated that the existence of a crack in a homogenous material would cause a deviation in the calculated conductivity, but when plotted on a \log_{10} scale, the deviation level is observable but less prominent than on a linear scale. Figure 8.13 shows the deviation of measured conductivity when different crack geometries, plotted as $\log(\sigma)$ versus crack width/electrode separation. This experimental research supports our simulation data and conclusion, justifying our confidence in applying the models to more experimental studies.

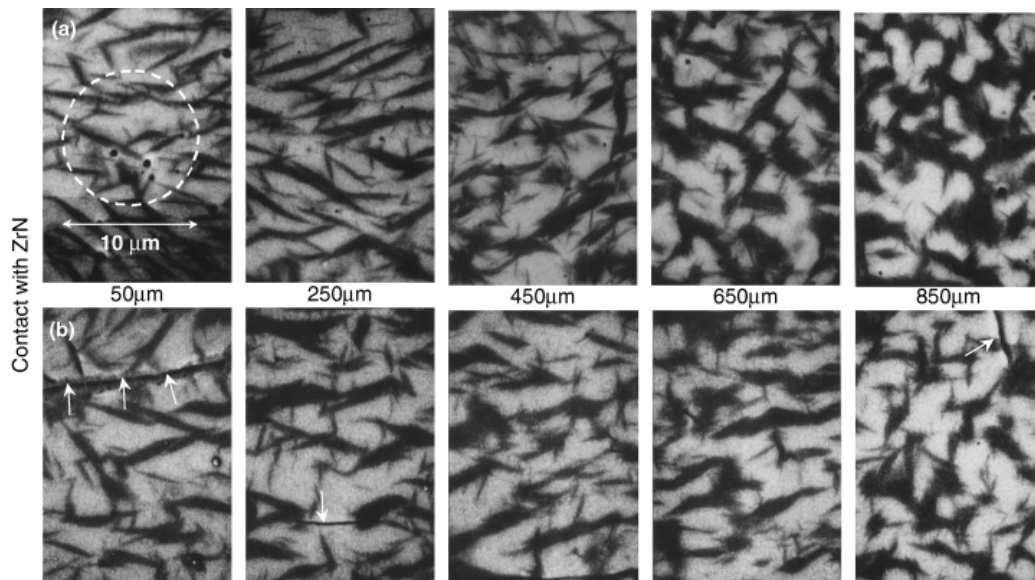


Figure 8.11. Backscattered electron SEM image of nitrogen-graded 2Y-TZP at different depths from the surface as prepared by heat treatment at 1700 °C for 4 h (a) and then annealed at 700 °C for 10 min in air (b). Tetragonal precipitates are shown in darker contrast. White colour shows the nitrogen-rich matrix. The dashed circle in (a) indicates the size of microelectrodes (radius 5 μm) on the surface of a specimen. The arrows in (b) indicate microcracks [5].

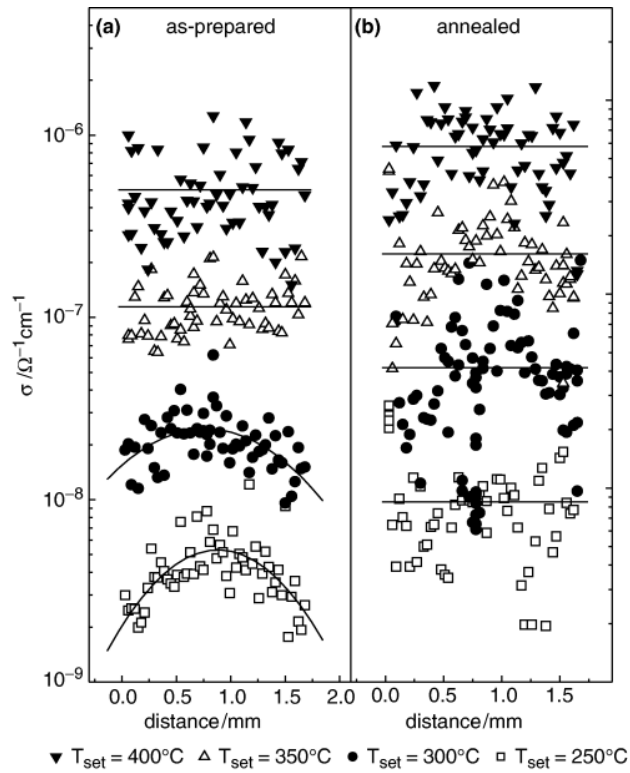


Figure 8.12. Conductivity profiles of nitrogen-graded 2Y-TZP of (a) as-prepared and (b) annealed [5].

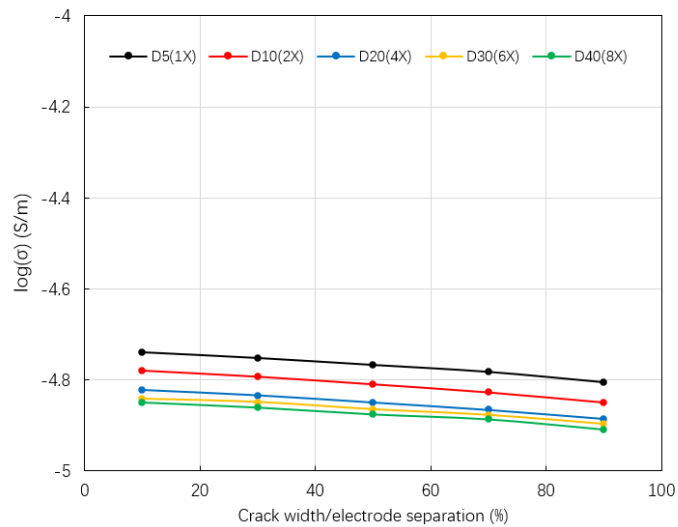


Figure 8.13. The conductivity of models containing a crack plotted on a \log_{10} scale versus crack width/electrode separation. The models are grouped by their crack depth. The y axis scale is expanded between -4 and -5 to show the small differences in the conductivity values.

8.2.4 Electrical property changes and crack generation in thermal barrier coating: MTT

To further extend the versatility of the models constructed in this thesis, an attempt to simulate mclS on thermal barrier coatings (TBC) on a superalloy is made. A mclS study on $3\text{Gd}_2\text{O}_3\text{-}3\text{Yb}_2\text{O}_3\text{-}4\text{Y}_2\text{O}_3$ co-doped ZrO_2 (GY-YSZ) thermal barrier coating is selected. In this

experiment, the GY-YSZ coating of 100 μm thickness is deposited on NiCoCrAlY bond-coated K3 superalloy [6].

The samples underwent heating at 1050 $^{\circ}\text{C}$ for 4 and 50 hours. Impedance measurements were conducted based on the set up shown in Figure 8.14. The measurement temperatures were 200, 250, 300, 350 and 400 $^{\circ}\text{C}$, respectively. AC voltage was applied to samples over a frequency range from 10^6 to 0.1 Hz.

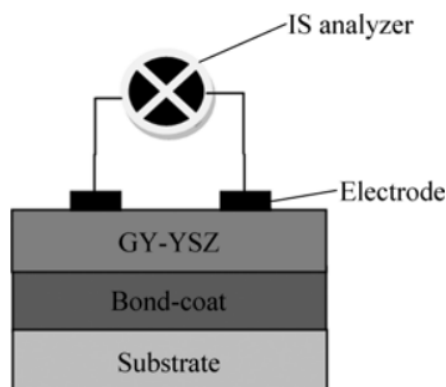


Figure 8.14. Illustration of set up used for impedance measurements for a TBC on a superalloy [6].

As the SEM cross section in Figure 8.15 shows, as-received samples contain no longitudinal cracks, but both vertical and longitudinal cracks developed in the samples oxidised at 1050 $^{\circ}\text{C}$. The number of cracks increased with prolonged oxidation. Equivalent circuits were constructed for as-received and oxidised samples to aid data analysis. For the as-received samples, the circuit consists of 3 parallel RC elements in series for grain, grain boundary and columnar grains. For the oxidised sample, an extra parallel RC component for a crack was added. The measured impedance spectra were fitted with the equivalent circuits, a typical result is shown in Figure 8.16. The oxidised sample shows higher measured impedance at all frequencies than the as-received sample. The increase in the impedance is relatively stable in the higher frequency range. When the frequency is under 1000 Hz, the difference in impedance between the two samples increased.

To investigate the origin of the increase in measured impedance of the two samples, we constructed two micro-top top models with and without a crack. Since no conductivity and relative permittivity data were presented in the paper, the models used SrTiO_3 's electrical properties, therefore the simulated data could not provide accurate replication of the experimental result; however, it can still serve as a proof of concept and shows the influence of cracks in the top coat. Both models have an electrode radius of 5 μm and separation of 100 μm . The surface layer thickness is 50 μm and has a conductivity of 1.355×10^{-7} S/m. The bulk layer thickness is 150 μm and has a conductivity of 1.355×10^{-5} S/m. Relative permittivity of both was set at 162. For the model containing a crack, a crack of width 90 μm and depth of 50 μm was created between the two micro-contacts.

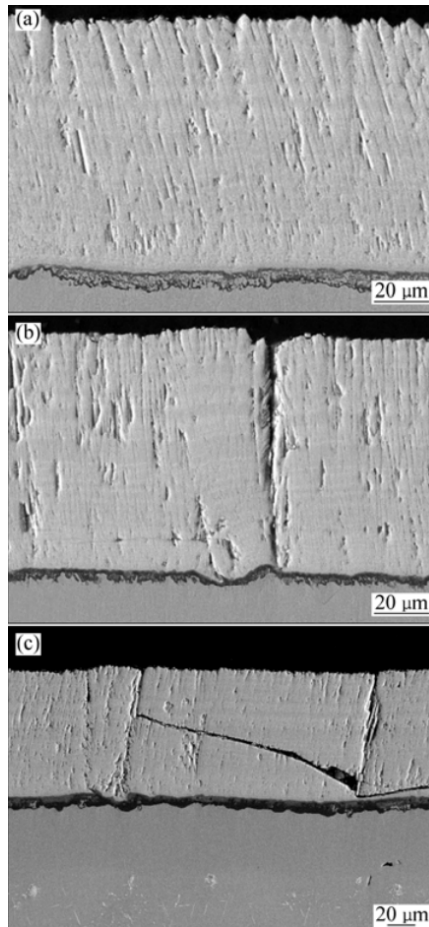


Figure 8.15. SEM images of cross-sections of (a) as-received and oxidised GY-YSZ thermal barrier coating samples in air at 1050 °C for (b) 4 h and (c) 50 h (c). Cracks developed with prolonged oxidation time [6].

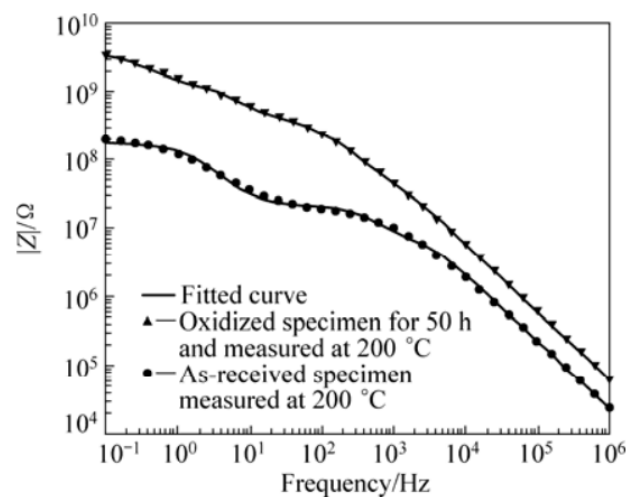


Figure 8.16. Impedance for the fitted and measured data of as-received and oxidised for 50 hours GY-YSZ samples. The fitting is achieved via equivalent circuits with various parallel RC elements connected in series [6].

The simulated impedance data for the with and without crack models are shown in Figure 8.17. Compared with the surface layer intact model, the model with a crack in the surface layer has increased impedance across the entire frequency range; however, the difference between the two models is not as large as the experimental results, where the maximum increase in impedance is about an order of magnitude. A possible reason is the top coating's material properties have changed after oxidation. The paper indeed stated two changes in the coating layer, Gd_2O_3 and Y_2O_3 diffused after oxidation and produced more oxygen vacancies and the crystal lattice was distorted due to diffusion. Thus, the surface layer/coating's electrical properties have altered compared to the as-prepared sample.

To reflect the change in the surface layer property, 4 two-layer models without a crack were selected where the surface layer has resistivity 2, 5, 10 and 100 times that of the bulk material, respectively. The simulated impedance data are shown Figure 8.18. The impedance of all 4 models are the same when the frequency is 1000 Hz and above. At the lower frequency range of below 1000 Hz, the measured impedance increases with increasing surface layer resistivity. The impedance data show the change in surface layer electrical properties could inflict greater change in the measured impedance in the lower frequency range which corresponds to the surface layer response, but the presence of a crack would affect the overall impedance measured across the entire frequency range. The oxidised sample shows the presence of longitudinal cracks and a change in the crystal structure for the top coating. Our model proves the existence of cracks and changes in surface layer electrical properties could be the origin of the impedance difference between the as-prepared and oxidised samples observed in Figure 8.16.

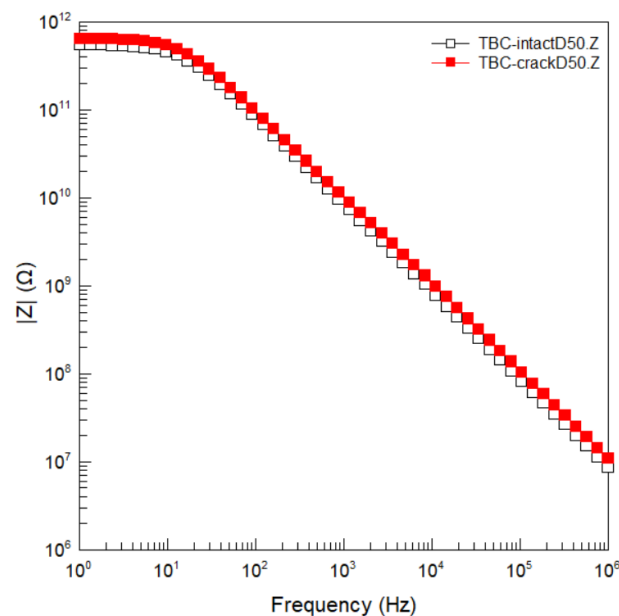


Figure 8.17. Impedance data for two-layer models with and without a crack. White symbols, two-layer model with intact surface layer with a thickness of 50 μm . Red symbols, two-layer model with a crack of width at 90 μm and depth of 50 μm in the surface layer. The resistivity of the surface layer in both models is 100 times the bulk material underneath.

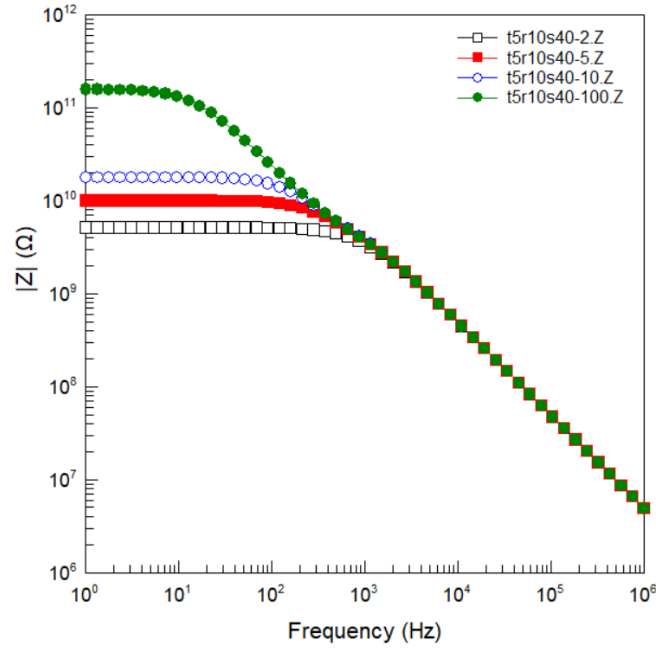


Figure 8.18. Impedance data for two-layer models with intact surface layer but different surface layer resistivity. White, $R_{\text{surface}} = 2 R_{\text{bulk}}$. Red, $R_{\text{surface}} = 5 R_{\text{bulk}}$. Blue, $R_{\text{surface}} = 10 R_{\text{bulk}}$. Green, $R_{\text{surface}} = 100 R_{\text{bulk}}$. The surface layer thickness is the same at $5 \mu\text{m}$, microcontact radius of $10 \mu\text{m}$ and separation of $40 \mu\text{m}$.

If more information on the experiments were provided, such as conductivities for the surface layer and substrate, the dimensions of typical cracks, and the detailed measurement set up parameters such as electrode radius and separation, the accuracy of the simulations could be improved. Our models could then serve as tools to extract more information on the thermal barrier coating. One potential usage could be the determination of coating layer thickness and estimation of relative crack size. Since the effectiveness and service life of thermal barrier coatings are highly related to the integrity of the coating structure, it would be invaluable for FEM models to provide information on the status of the coating.

So far, the examples selected are micro-top top configuration only, but one of the micro-contacts can be placed on the bottom surface of the model. Micro-top micro-bottom (MTMB) and micro-top full-bottom (MTFB) configurations could therefore be achieved, allowing more types of experimental data to be simulated. Due to the time limit of this PhD project, here we present the prospective application of the models with a MTMB experiment.

8.2.5 Crack and thin layer characterisation in thermal barrier coating: MTMB

MTMB is a common set up in thermal barrier coating impedance measurements, as shown in Figure 8.19. This is based on a study on failure detection of thermal barrier coatings using impedance spectroscopy by Wu et al [7]. The sample contains a $300 \mu\text{m}$ thick 8 wt.% YSZ coating on a NiCrAlY bond coating with a thickness of $100 \mu\text{m}$ and the substrate is a nickel-based superalloy. Pt electrodes with diameter of 5 mm were placed on the centre of the top and bottom of the sample. The size of the electrodes is not in the micrometre range as common mclS, but is still smaller compared with the sample size. The sample had undergone

a thermal cycle of heating at 1050 °C and then quenched in water. Cracks formed in the YSZ layer and large cracks parallel to the bond coating formed as well, shown in Figure 8.20. Similar to previous cases, the cracks formed caused the measured impedance to increase. When the sample was aged at 1100 °C, a thermally grown oxide (TGO) layer was formed between the YSZ layer and the bonding layer. This means the actual structure changed from 3 to 4 layers, the thickness of the TGO layer increased with aging time as revealed by SEM images. Impedance data in Figure 8.21 show the measured impedance was doubled when the sample was aged for 50 hours, and further increased with aging time. Three factors were proposed to explain the increase in impedance with aging time: TGO layer thickness varied; TGO layer composition changed; and the volume of defect such as cracks increased.

This example shows a potential area where our models can be applied. Two modifications of the models are needed to simulate this type of measurement on TBC samples: 1. Create another layer on top of the present surface layer, thus the crack would become embedded between the two layers. Create another layer under the bulk layer, thus a four-layer model is created, where the four layers can be assigned with different electrical properties. 2. Arrange one of the micro-contacts to the bottom of the model to construct a MTMB configuration. With the modification implied, the model can assist in understanding of each component's contribution to the measured impedance response. To verify if the three factors proposed to explain the aging effect are correct, the modified model can have various TGO layer thickness, TGO with various conductivity values and different crack volumes. The significant contributions of each component to the impedance data could then be clarified.

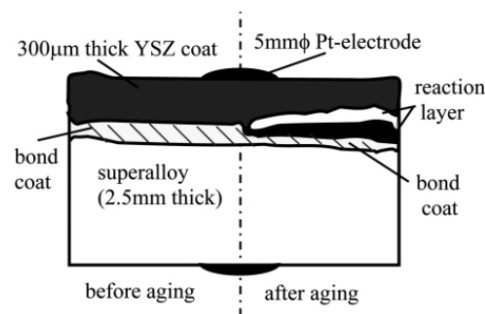


Figure 8.19. The geometry of the 8 wt.% YSZ TBC sample used for impedance measurements (left: as-received, right: thermally grown oxide formed) [7].

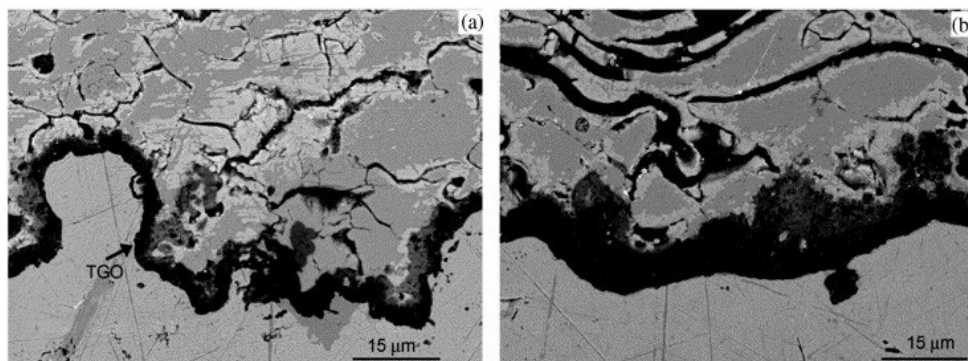


Figure 8.20. The cross-section of the 8 wt.% YSZ TBC sample after aging at 1100 °C: (a) aged for 50 h; (b) aged for 500 h. The dark region of TGO layer increased in thickness with aging time. Cracks increased in size with aging time [7].

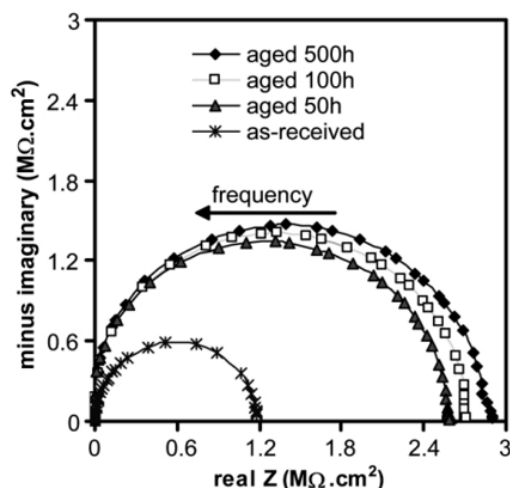


Figure 8.21. Impedance, Z^* , plots for 8 wt.% YSZ TBC sample aged at 1100 °C for 0, 50, 100 and 500 h.

8.2.6 Thin layer characterisation and micro-contact size effects: MTFB

Another common electrode arrangement in TBC impedance analysis is MTFB, with one of the micro-contacts shifted to the bottom surface and is converted into a full coverage electrode. This can be achieved with our models. The example below shows a case of TBC analysis where modified models could be useful. Research by Xiao et al explored using the mclS with MTFB configuration to characterise various properties of TBCs [8]. TBC samples consisted of an air plasma sprayed FeCrCoAlY bond coat, a Ni-super alloy and 8 wt.% YSZ top coat. The aging temperature was at 950 or 1150 °C for up to 3000 h. The polished base of superalloy was used as the full bottom electrode, while various sizes of Ag micro electrodes were fired on the 8 wt.% YSZ top surface. At first, they investigated the impedance response of samples that had undergone increased aging time. As Figure 8.22 shows, four relaxation processes were identified as grain, grain boundary, TGO layer and electrode response. They concluded the TGO layer response increased with increasing heat-treatment time. The SEM analysis supported this observation as the TGO layer thickness and integrity increased with heat-treatment time. The Ag electrode size effect was also studied, as shown in Figure 8.23, where it can be seen that the TGO layer response decreases as the Ag electrode size decreases, but the response from the YSZ grain and grain boundary were mostly unaffected.

To simulate this experiment, the modified model should have 3 intact layers to represent the YSZ top coat, the TGO layer and the superalloy substrate, each assigned with appropriate electrical properties. The size of micro-contact on the YSZ surface layer can be easily altered with different parameters, which is a strong suit of our models. Then it would be very exciting to reproduce the impedance response reported by Xiao et al, and analyse how the TGO layer thickness and electrical properties can affect the simulated impedance response. In the same study, they also revealed using one or two micro electrodes on the YSZ surface layer did not generate significant difference in the impedance response. This is another potential point of interest to be simulated with FEM modelling, providing an opportunity to understand the current density state in the TBC sample for multiple micro-contacts present on the surface

and a full bottom counter electrode on the other side.

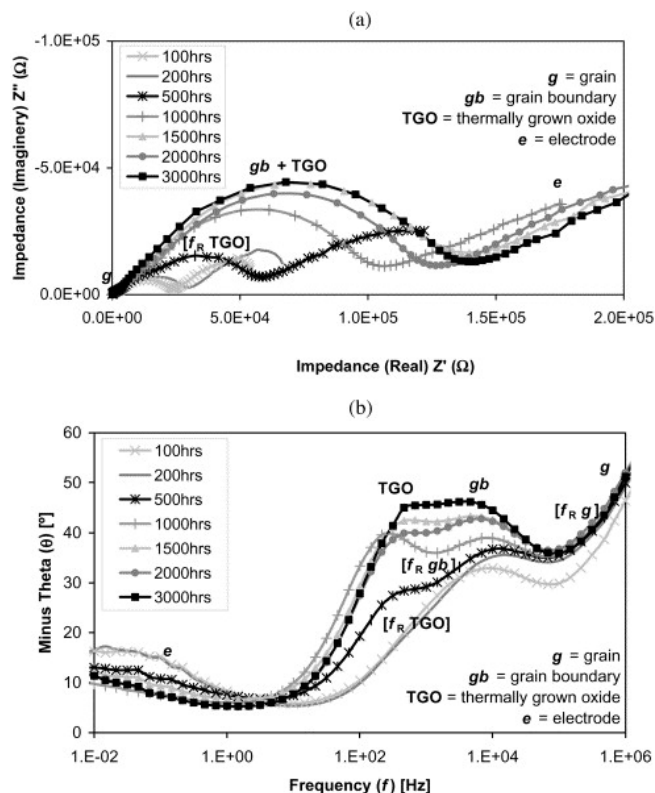


Figure 8.22. (a) 8 wt.% YSZ TBC sample aged at 950 °C with electrode size of 1 cm² Ag paste (Z'' vs. Z' spectra) (b) Phase angle vs. frequency plot of the same sample [8].

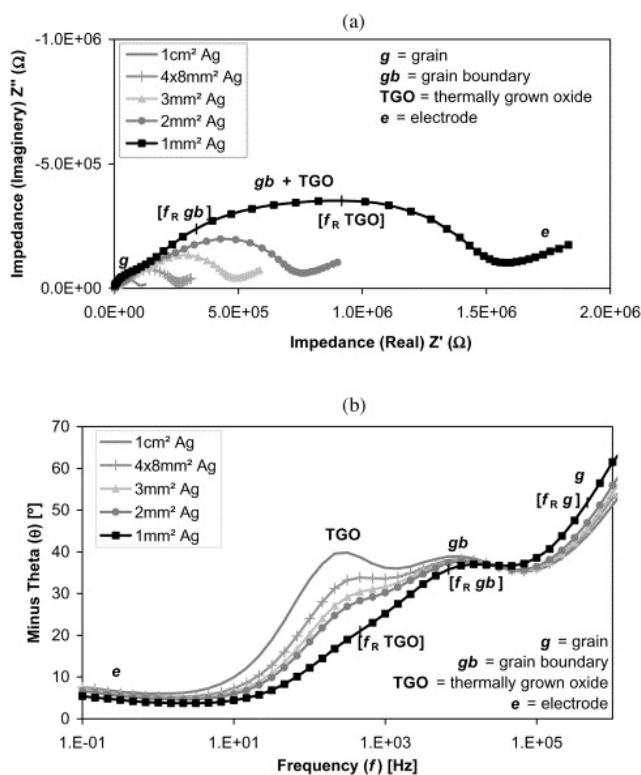


Figure 8.23. (a) Nyquist plot and (b) phase angle vs frequency plot of the TBC sample with different electrode sizes. The sample had undergone heat-treatment at 950 °C for 1000 h [8].

8.2.7 Dislocation enhanced local conductivity with 2D FEM simulation: MTFB

Apart from being perpendicular to the top surface, the meshed crack volume can be tilted at different angles. This is a feature of our model that is still under testing thus not utilised in this thesis; however, there exists areas where tilted cracks can be applied. Frömling et al presented a mclS study on dislocation-mediated electronic conductivity in rutile. The core principle is similar to a previous example of micro-top top set up case, but in this research, a MTFB set up was used [9]. Rutile single crystals were cut along the [010] direction, uniaxial compressive deformation was conducted so dislocations were created on the (011) plane. Microelectrodes with radius of 10 μm were deposited in an array to cover areas free of dislocations, areas with a medium density of dislocations and areas with a high density of dislocations. The bottom of the sample was used as the counter electrode, thus a MTFB configuration was used. The configuration is shown in Figure 8.24 (a). Impedance data are shown in Figure 8.24 (b) and (c), for a dislocation free area. The measured impedance response shows a single semi-circle with capacitance around 1×10^{-12} F, which is considered the bulk response. When measured in an area with dislocations, an additional distorted semi-circle at high frequency appeared and is considered to be the response from the highly conductive dislocations. The measured impedance from the high dislocation areas is more than an order of magnitude lower than the dislocation free area, suggesting the dislocations could enhance local conductivity.

FEM simulation was conducted with COMSOL's software. A two-dimensional geometry was created to simulate the dislocation effect in mclS measurements. The electrical potential distribution result is shown in Figure 8.25 (a). The area near dislocations has higher potential than the defect free area. Simulated impedance data show that introducing dislocations in the structure could effectively reduce the measured resistance, and an additional distorted semi-circle appeared in higher frequency range, Figure 8.25 (b). These simulations correlate with the experimental observations, Figure 8.24.

This is a particularly interesting case where a tilted, meshed crack could be useful. Since dislocation bundles could enhance local conductivity, the meshed crack volume can be assigned a higher conductivity value than the bulk material. The meshed crack volume can be tilted at 45° from the top surface to simulate the dislocation(s) along a specific plane. Previous preliminary dislocation simulations in Figure 8.8 already showed adding a conductive volume in the bulk material could cause the measured impedance to decrease. It is interesting to explore how accurate the tilted volume could simulate dislocation bundles in rutile. Another advantage of our model is it is three-dimensional, providing an extra dimension of information. Current density distribution data can be gathered and visualised enabling us to understand the state of current flow when tilted dislocations/conductive volumes are present in the bulk material.

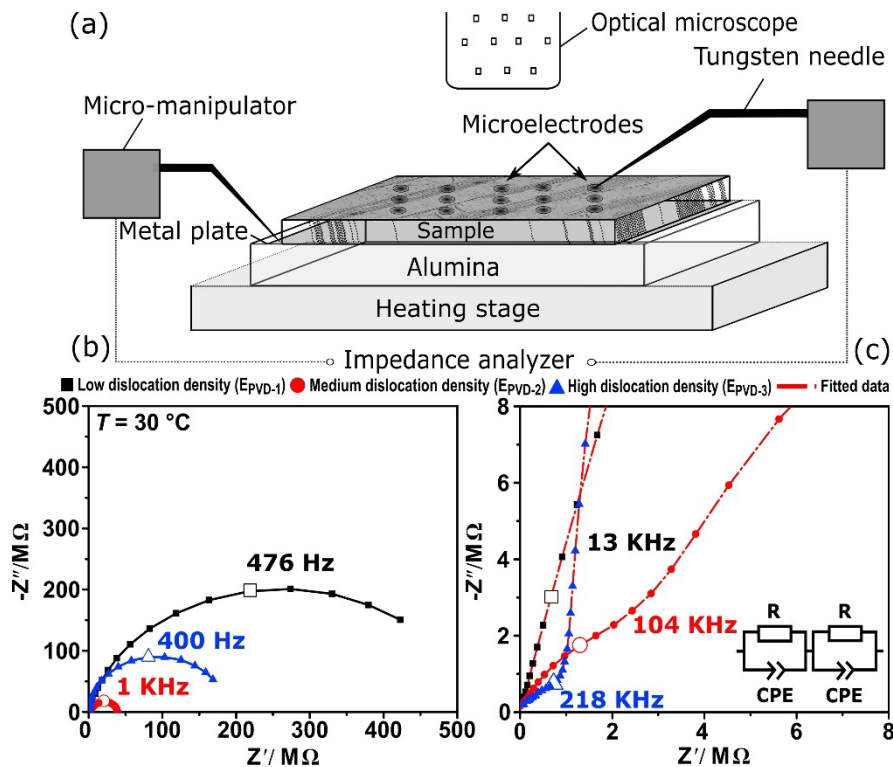


Figure 8.24. (a) Schematic of the mclS setup to measure dislocation affected local conductivity in TiO_2 (b) Nyquist plots of impedance for selected microelectrodes; onto low, medium, and high dislocation density areas. (c) Aside from the bulk response visible for all three electrodes, medium and high dislocation density electrode shows distorted semi-circle at high frequencies attributed to the dislocations. Measured data were fitted using the equivalent circuit presented in the inset [9].

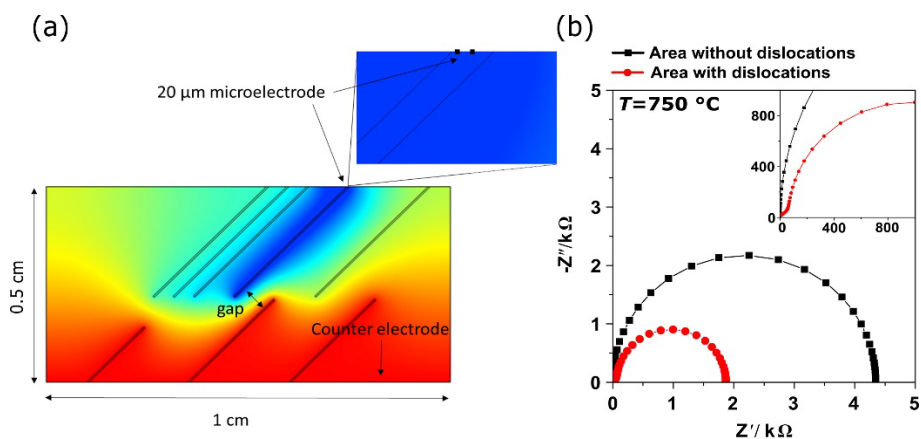


Figure 8.25. (a) Distribution of potential for a microelectrode deposited on a dislocation-rich region in TiO_2 simulated by FEM (25°C , 1 kHz). The sample has length of 1 cm and height of 0.5 cm. Dislocation bundles are illustrated as black lines and 45° from the top surface. (b) Nyquist plots of simulations for areas with and without dislocations bundles at $T = 750^\circ\text{C}$ [9].

In conclusion, the models created and developed in this thesis have been applied to simulate various mclS experimental results from different aspects. These include: grain and grain boundary interactions in large grained ceramics; dislocations with enhanced local electrical conductivity; detection of microcracks and the crack's effect on measured conductivity result scattering in nitrogen graded 2Y-TZP; characterising cracks in thermal barrier coatings on a superalloy. The preliminary simulation results show the potential of the models to be applied in a wider range of mclS studies. This is in addition to the cracked amorphous layer on SrTiO₃ single crystals via radiation damage and thermal annealing, which was the original objective in the FEM section of this thesis. Another point to note is, simulating a resistive region in the matrix is an easier path, as additional electrical response can be detected by the impedance spectroscopy. When simulating a more conductive region in the matrix, the measured impedance would be smaller than the pristine model, and no additional response can be detected, nonetheless, it can still assist in terms of estimating the volume/proportion of the conductive region in the matrix.

With more structures added to the model, it can be used to study impedance data obtained from multi-layer ceramic capacitors. Switching the electrode configuration from MTT to MTMB and MTFB can further extend the application range. Potential projects of interest are proposed, for example the MTMB and MTFB model can be used to characterise TBC on superalloys. Both models can be used to identify each structural component's contribution in the impedance spectra depending on the experimental set up. Once a tilting feature is complete, the model could be used to simulate high conductivity dislocations along certain planes in single crystal and ceramic systems to provide further understanding in dislocation enhanced local conductivity. The potential application of our model is not limited to the listed examples, more areas to be applied are awaiting discovery.

8.3 References

- [1] F. Yang, J. S. Dean, Q. Hu, P. Wu, E. Pradal-Velázquez, L. Li and D. C. Sinclair, "From insulator to oxide-ion conductor by a synergistic effect from defect chemistry and microstructure: acceptor-doped Bi-excess sodium bismuth titanate $\text{Na}_{0.5}\text{Bi}_{0.51}\text{TiO}_{3.015}$," *J. Mater. Chem. A*, 8, pp. 25120-25130, 2020.
- [2] R. A. Veazey, A. S. Gandy, D. C. Sinclair and J. S. Dean, "Finite element modeling of resistive surface layers by micro-contact impedance spectroscopy.," *J Am Ceram Soc.*, 103, pp. 2702– 2714, 2020.
- [3] M. Shirpour, R. Merkle , C. Lina and J. Maier, "Nonlinear electrical grain boundary properties in proton conducting Y–BaZrO₃ supporting the space charge depletion model," *Phys. Chem. Chem. Phys.*, 14, pp. 730-740, 2012.
- [4] H. Bishara, H. Tsybenko, S. Nandy, Q. . K. Muhammad, T. Frömling, X. Fang, J. P. Best and G. Dehm, "Dislocation-enhanced electrical conductivity in rutile TiO₂ accessed by room-temperature nanoindentation," *Scripta Materialia*, 212(15), pp. 114543, 2022.
- [5] J.-S. Lee, . J. Fleig, J. Maier, D.-Y. Kim and T.-J. Chung, "Local Conductivity of Nitrogen-Graded Zirconia," *J. Am. Ceram. Soc*, 88, pp. 3067-3074, 2005.
- [6] D.-H. Zhang, H.-B. Guo and S.-K. Gong, "Impedance spectroscopy study of high-temperature oxidation of Gd₂O₃-Yb₂O₃ codoped zirconia thermal barrier coatings," *Trans. Nonferrous Met. Soc. China*, 21(5), pp. 1061-1067, 2011.
- [7] N. Wu, K. Ogawa, M. Chyu and S. X. Mao, "Failure detection of thermal barrier coatings using impedance spectroscopy," *Thin Solid Films*, 457,2, pp. 301-306, 2004.
- [8] P. Anderson, X. Wang and P. Xiao, "Impedance spectroscopy study of plasma sprayed and EB-PVD thermal barrier coatings," *Surface and Coatings Technology*, 185, 1, pp. 106-119, 2004.
- [9] Q. Muhammad, H. Bishara, L. Porz, C. Dietz, M. Ghidelli, G. Dehm and T. Frömling, "Dislocation-mediated electronic conductivity in rutile," *Materials Today Nano*, 17, p. 100171, 2022.